

Diss. ETH No. 18587

Experimental Research into Resonant Vibration of Centrifugal Compressor Blades

A dissertation submitted to the

SWISS FEDERAL INSTITUTE OF TECHNOLOGY
(ETH ZÜRICH)

for the degree of

DOCTOR OF SCIENCES

presented by

ALBERT KAMMERER

Dipl.-Ing., Technical University of Braunschweig, Germany
born 7. October 1976
citizen of the Federal Republic of Germany

accepted on the recommendation of

Prof. Dr. Reza S. Abhari
Prof. Dr. Edoardo Mazza
Dr. Beat Ribi

2009

Acknowledgements

This thesis is the result of my research work at the Laboratory for Energy Conversion at the Swiss Federal Institute of Technology in Zürich. Throughout the course of this work I had always been looking forward to finally have the opportunity to acknowledge all who supported me in this project. Your help was vital during my time at ETH and I would like to sincerely thank you all.

First and foremost I would like to thank Prof. Abhari for providing me with an excellent working environment and for guiding me throughout the time of my PhD. Looking back I realize the unique opportunity I was given by Prof. Abhari within the laboratory to run a complex project during which I could foster a range of interdisciplinary skills. I greatly appreciate this.

I am very grateful to Prof. Edoardo Mazza for accepting the role of co-examiner and for his suggestions and corrections concerning this thesis.

Special thanks go to the industrial partners ABB Turbo-Systems AG and MAN Turbo AG Schweiz. I am very grateful for their intellectual and financial support. Providing their resources and deep expertise they made it possible to accomplish this project. I would like to thank Dr. Beat Ribi for accepting the role of co-examiner and for his suggestions and corrections concerning this thesis. I would like to thank Dr. Janpeter Kühnel, Dr. Christian Roduner, Dr. Peter Sälzle, Hans-Peter Dickmann and Urs Baumann. I would like to thank Dr. Matthias Schleer for sharing his enthusiasm and experience on the test facility RIGI. The financial support of the The Innovation Promotion Agency CTI is acknowledged.

I want to particularly thank Armin Zemp for his considerable contribution to this work. It was a pleasure to discuss the multitude of details on CFD and the experimental work. His patients, intuition and understanding of the subject made it simple to overcome all hurdles during the project. Also special thanks go to Cornel Reshef for his contribution to the development of an entirely new electronic equipment used for performing measurements on rotating components. Ein grosser Dank gebührt dem Team der Laborwerkstatt, bestehend aus Peter Lehner, Hans Suter, Thomas Künzle, Claudio Troller und Christoph Räber. Mit ihrem herausragenden Einsatz und höchster Präzision haben sie massgebend zum Gelingen dieser Arbeit beigetragen. I would also like to mention my appreciation to Dr. Michel Mansour for his support during the development of the pressure sensors. Many thanks go to Dr. Ndaona Chokani for his helpful discussions and especially the support during the pre-conference periods. I would like to express my gratitude to all members of the LEC for creating a friendly and relaxing atmosphere. It was a pleasure to spend my time in this multi-cultural environment. I enjoyed the endless discussions with Martin Bruderer on photography and it was enlightening to be shown India by Vipluv Aga.

Finally, I would like to thank all my friends here and from Germany for their support. I am particularly grateful to my parents for their continuous support. Valeria I would like to thank for her patients and understanding throughout the years and for spending the time to teach me Italian.

Abstract

The objective of this work was to study resonant vibration of high-speed centrifugal compressor blades. Low order resonant response conditions were created in a test facility in order to experimentally investigate four aspects of blade forced response: (1) inlet flow distortion, (2) unsteady blade excitation, (3) damping and (4) resonant response. These aspects were evaluated for resonance cases of the first two blade modes and a number of inlet distortion cases. The major parameters during the study were the inlet pressure and the mass flow.

Centrifugal compressors play a key role in processes engineering, propulsion and power generation. Due to the increased demands on aerodynamic performance the designs are pushed towards their mechanical limits. This is in particular the case for high cycle fatigue due to blade vibration. Resonant vibration due to forced response manifests during operation where flow disturbances upstream or downstream of the rotor cause unsteady blade excitation. Generally, aerodynamic non-uniformities are created in the flow field by diffuser vanes or mechanical obstacles in the flow field, i.e. struts or pipe bends. In some applications flow injection generates non-uniformities.

Experimental research was conducted in a closed loop test facility driven by a centrifugal compressor. The rotor used in the study featured design and performance criteria typical for turbocharging applications with highly loaded blades and a vaneless diffuser. The flow upstream of the compressor was intentionally disturbed using screens with the number of lobes equivalent to the engine excitation order. The resultant flow field was measured using a fast aerodynamic probe. Pressure sensors and dynamic strain gauges were installed on the blade surface to measure unsteady pressure and strain, respectively. The blade thickness was modified using FEM in order to generate resonant crossing conditions of the first two blade modal frequencies. Modal shapes and frequencies were verified using speckle interferometry and were found to agree very well with the predictions.

Due to intentional inlet flow distortion, the total pressure distribution varied in the range of 1% to 4% of the inlet static pressure depending on the mass flow setting. The distortion amplitude represented a case commonly encountered in applications. A one-dimensional model based on loss generation and mass redistribution was developed. It was shown that this model predicts accurately the mean levels of the distortion properties. Depending on the case, the inlet distortion caused unsteady pressure amplitudes on the blade surfaces of

1.5% of the inlet static pressure. For centrifugal compressors, typical strut installations in the inlet cause dominant EO2 and EO3 harmonics which prevail for all screen cases. The intended engine orders, i.e. EO5 or EO6, were of similar amplitude. Overall, in the course of the analysis it was shown that the relatively complex nature of centrifugal compressor flows results in a strong dependence of the excitation function on the operating point of the compressor.

A novel experimental analysis technique has been successfully developed to measure the energy transfer between the vibrating blade and the fluid. The method is generally applicable to any case of blade vibration and was shown to enable the identification of zones on the blade surface where either excitation or damping takes place during resonance. The phase angle between the blade and the unsteady pressure plays a key role in the energy exchange by determining the direction of energy transfer and by scaling the amplitude. Therefore, mass flow variations during operation affect the phase angle distribution and may cause substantial increase in modal force and therefore response amplitudes.

The dynamic response characteristic of a centrifugal blade during resonance was proved to be very well captured by a single-degree-of-freedom (SDOF) model. Based on the SDOF model damping was experimentally shown to be dominated by contribution from aerodynamic damping whereas material damping is by a factor of ten smaller. For centrifugal compressors aerodynamic damping was found to be linearly dependent on inlet pressure. In the present the researched pressure was ranging from 0.2-0.8bar. For the same range of inlet pressure the maximum vibratory amplitude at resonance increases and becomes asymptotic at approximately 1bar. Material damping becomes relevant at pressure levels around 0.3bar and below. For the first eigenmode blade damping was shown to be constant, i.e. to be independent of the operating line or resonance case. Mistuning was experimentally shown to cause a potentially hazardous increase in response amplitude and must not be neglected during design.

Kurzfassung

Das Ziel dieser Arbeit ist die Untersuchung resonanter Schaufelschwingung von Radialkompressoren. Das experimentelle Forschungsvorhaben umfasste eine gezielte Erzeugung erzwungener Schaufelschwingung niedriger Frequenzordnung, um die folgenden vier Aspekte resonanter Schaufelschwingung zu untersuchen: (1) Strömungsstörung im Eintrittsbereich, (2) instationäre Erregung von Schaufelschwingungen, (3) Dämpfung und (4) resonante Schaufelschwingung. Diese Aspekte wurden für die Eigenfrequenzen der ersten zwei Modi und eine Anzahl von Resonanzfällen untersucht.

Radialkompressoren spielen eine Schlüsselrolle in den Bereichen der Verfahrenstechnik, Antriebstechnik und der Energieumwandlung. Aufgrund derer zunehmenden aerodynamischen Belastung, steigen die mechanischen Beanspruchungen und erreichen dadurch die Materialbeanspruchungsgrenzen. Dies ist im Besonderen der Fall für Materialermüdung aufgrund von Wechselbeanspruchung bei resonanter Schwingung. Der Zustand der resonanten Schwingung wird durch Strömungsstörungen entweder im Eintritts- oder im Austrittsbereich der Laufräder verursacht. Diffusorschaukeln am Austritt oder Störkörper sowie Strömungskrümmen im Eintrittsbereich generieren einen ungleichförmigen Strömungszustand und damit eine auf die Schaufeln wirkende instationäre Druckverteilung.

Die experimentellen Untersuchungen wurden in einem Radialkompressorteststand mit geschlossenem Kreislauf durchgeführt. Das dabei eingesetzte Laufrad kennzeichnet sich durch eine hohe aerodynamische Belastung aus und schliesst an einen schaufellosen Diffusor an. Die Kompressorkonfiguration stellt eine für Turboaufladung typische Auslegung dar. Die Strömung am Laufradeintritt wurde mit segmentierten Gittern gezielt gestört. Die Anzahl der dabei eingesetzten Segmente entsprach der zu erregenden Ordnungszahl. Die Eintrittsströmung wurde mit einer aerodynamischen Sonde vermessen. Auf den Schaufeloberflächen angebrachte Drucksensoren und Dehnungsmessstreifen dienten zur Erfassung der instationären Drücke und Schaufelschwingungsdehnungen. Die Schaufeldicken wurden unter Einsatz von FEM derart angepasst, dass resonante Schwingungszustände der ersten zwei Schaufelschwingemodi mit den tiefen Erregungsordnungen möglich wurden. Die Modalformen und deren Frequenzen wurden experimentell unter Einsatz von Speckle Interferometry verifiziert und als sehr gut mit den numerischen Werten übereinstimmend gefunden.

Aufgrund der gezielten Strömungsstörung am Laufradeintritt, stellte sich ein Totaldruckprofil in Umfangsrichtung ein. Abhängig vom Massenstrom betrug die Profilamplitude 1%

bis 4% vom statischen Eintrittsdruck und stellte damit ein für reale Anwendungen realistischen Fall dar. Zur Bestimmung der Störungsamplitude wurde ein Model entwickelt, welches die Verluste und die Verblockungseffekte beim Durchströmen von porösen Gittern quantifiziert. Experimentelle Untersuchungen haben bestätigt, dass mit diesem Model die mittleren Störungsamplituden sehr gut bestimmt werden konnten und sich das Model damit zur Auslegung eignet. In Abhängigkeit vom untersuchten Fall, verursachten die Eintrittsstörung instationäre Druckamplituden von 1.5% vom statischen Eintrittsdruck. Unabhängig vom eingesetzten Störungsgitter wurde die Druckverteilung auf den Schaukeloberflächen von der zweiten und der dritten Erregungsharmonischen dominiert. Die gemessenen Amplituden der beabsichtigten Erregungsordnungen EO5 sowie EO6 waren vergleichbar. Allumfassend wurde gezeigt, dass die relativ komplexe Strömung innerhalb des Laufrades zu einer starken Abhängigkeit der Erregungsfunktion mit dem Betriebspunkt der Maschine führte.

Eine neue experimentelle Methode wurde erfolgreich angewandt, um den Energieaustausch zwischen der schwingenden Schaufel und der instationären Strömung zu quantifizieren. Die Methode kann für jeden möglichen Fall von Schaufelschwingung angewendet werden und ermöglicht es Bereiche auf der Schaufeloberfläche zu identifizieren, die entweder durch aerodynamische Dämpfung oder Erregung gekennzeichnet sind. Der Phasenwinkel der Druckverteilung spielt dabei eine Schlüsselrolle indem dieser die Richtung des Energieaustausches bestimmt und ebenso den Effekt der Erregungsamplitude skaliert. Aus diesem Grund können Änderungen des Betriebspunktes zu massiven Schwingungsamplituden führen, die darauf zurückzuführen sind, dass die damit einhergehende Änderung der Phasewinkelverteilung einen Anstieg der Modalkraft verursacht.

Im Verlauf dieser Arbeit wurde gezeigt, dass das dynamische Verhalten von Radialschaufeln während resonanter Schwingung durch ein Masse-Dämpfer-System mit einem Freiheitsgrad sehr gut abgebildet werden kann. Basierend auf diesem Ansatz wurde die Schaufeldämpfung gemessen, wobei sich ergeben hat, dass die aerodynamische Dämpfung die gesamte Dämpfung dominiert. Materialdämpfung ist um den Faktor zehn kleiner als die aerodynamische Dämpfung. Diese ist linear abhängig vom Eintrittsdruck, der in den untersuchten Fällen im Bereich von 0.2-0.8bar variiert wurde. Für diesen Druckbereich steigt die resonante Schwingungsamplitude an und wird asymptotisch für einen Eintrittsdruck von 1bar. Materialdämpfung kann bei Eintrittsdrücken von unter 0.3bar für Schwingungsamplitude als relevant betrachtet werden. Weiterhin hat sich herausgestellt, dass die Schaufeldämpfung für die erste Schwingungsform als vom Betriebspunkt und Resonanzfall unabhängig angenommen werden konnte. Der Einfluss von Mistuning führt zum markanten Anstieg der Schwingungsamplituden einzelner Schaufeln und muss damit während der mechanischen Laufradauslegung berücksichtigt werden.

Contents

1. Introduction	1
1.1. Motivation	1
1.2. Centrifugal Compressors	2
1.3. Forced Response Vibration in Turbomachinery	4
1.4. Experimental Analysis	11
1.5. Research Objectives	17
1.6. Thesis Outline	18
2. Experimental Setup	21
2.1. Test Facility	21
2.2. Compressor Performance	23
2.3. Impeller Modal Properties	24
2.4. Data Transmission and Acquisition	32
2.5. Transient Measurement Approach	33
2.6. Measurement Cases and Pressure Levels	35
3. Impeller Instrumentation	37
3.1. Fast Response Pressure Sensors	37
3.1.1. Temperature Effects	40
3.1.2. Centrifugal Force Effects	40
3.1.3. Frequency Bandwidth	41
3.1.4. Sensitivity to Vibratory Strain	41
3.1.5. Pressure Signal Calibration and Linearity	42
3.2. Dynamic Strain Gauges	44
3.2.1. Strain Gauge Installation	44
3.2.2. Resolution and Calibration	45
3.3. Piezoelectric Actuators	45
3.4. Uncertainty Analysis	47
3.4.1. Algorithm	47
3.4.2. Pressure Sensor Uncertainty	49
3.4.3. Strain Gauge Uncertainty	50

4. Inlet Flow Distortion	53
4.1. Generation of Inlet Flow Distortion	53
4.2. Inlet Flow Field Measurement	56
4.3. Flow Field without Distortion Screens	57
4.4. Flow Field with Distortion Screens	58
4.5. Summary and Conclusions	63
5. Blade Unsteady Forcing	67
5.1. Measurement Procedure	67
5.2. Unsteady Pressure without Distortion Screens	68
5.3. Overview on Measurement Cases	75
5.4. Analysis of Resonance Case Model1/EO5	75
5.4.1. Flow Field Analysis	75
5.4.2. Blade Unsteady Excitation	78
5.4.3. Comparison with CFD (OL1 case)	84
5.4.4. Pressure Wave Evolution along Blade Surface	86
5.5. Analysis of Resonance Case Model1/EO6	88
5.5.1. Spectral Functions	89
5.5.2. Harmonic Functions along Blade at Mid-Height	92
5.6. Unsteady Pressure during Resonant Response	94
5.7. Summary and Conclusions	98
6. Resonant Response	101
6.1. Transient Response and Maximum Amplitude	101
6.1.1. Modeling Transient Blade Response	102
6.1.2. Resonant Amplitude Dependency on Inlet Pressure	105
6.2. Blade Response without Installed Distortion Screens	107
6.3. Overview on Measured Resonant Response Cases	109
6.4. Results	109
6.4.1. Model1/EO5 - Dynamic Response Characteristic	109
6.4.2. Model1/EO5 - Maximum Amplitude	113
6.4.3. Model1/EO6	114
6.4.4. Mode2/EO12	114
6.4.5. Strain Amplitude Comparison	116
6.5. Effects of Mistuning	117
6.6. Summary and Conclusions	118
7. Damping	121
7.1. Blade Damping in Turbomachinery	121

7.2. Damping Measurement Methods	124
7.2.1. Frequency Analysis	124
7.2.2. Curve-Fit Method	125
7.2.3. Circle-Fit Method	126
7.2.4. Comparison between Curve-fit and Circle-fit Methods	128
7.3. Damping Measurement Results	128
7.3.1. Material Damping	129
7.3.2. Aerodynamic Damping – Mode 1	131
7.3.3. Aerodynamic Damping – Mode 2	135
7.3.4. Damping Amplitude Comparison	137
7.4. Summary and Conclusions	139
8. The Cumulative Aspects Of Forced Response	141
8.1. Modal Formulation	142
8.2. Blade Excitation, Damping and Response Amplitude	145
8.3. Mistuning Effects on Damping and Response Amplitude	151
8.4. Summary and Conclusions	154
9. Aerodynamic Work	157
9.1. Theoretical Background	158
9.2. Measurements of Aerodynamic Work and Phase	162
9.3. Summary and Conclusions	167
10. Conclusions, Summary and Future Work	169
10.1. Conclusions	169
10.2. Summary	171
10.3. Future Work	177
Bibliography	178
A. Nomenclature	189
B. List of Publications	193
C. Curriculum Vitae	195

1. Introduction

1.1. Motivation

Centrifugal compressors play a key role in processes engineering, propulsion and power generation. Their designs have been evolving towards higher efficiencies, mass flow rates and pressure ratios. However, the continuous improvement of aerodynamic attributes has been also pushing centrifugal compressor designs towards their structural limits. Of paramount importance on this subject is the requirement to ensure safe operation and avoid mechanical failure. Prominent to this concept is high cycle fatigue failure due to blade vibration which is inevitably encountered during the design of new products as well as during operation of existing machinery. From the economic perspective a quantified appreciation of the HCF problem is given in the frequently cited works by *EL-Aini et al.* [20] and *Kielb* [41]. In 1997 *EL-Aini et al.* indicate that although 90% of the potential HCF problems are covered during development testing, the remaining few problems account for nearly 30% of the total development cost and are responsible for over 25% of all engine distress events. *Kielb* mentioned in 1998 that every new development program for jet engines has about 2.5 serious high cycle fatigue problems. Furthermore, *Srinivasan* [75] states in 1997 that the U.S. Air Force estimates an expenditure of about \$100 million/year to inspect and fix high cycle fatigue related problems. It is for this reason that the datum research work addresses the subject of forced response of centrifugal compressors. The prediction of potentially critical blade vibration requires understanding and quantification of aerodynamic and structural properties for an intended configuration. Associated with it are considerable computational and experimental costs during the design phase. This work derives its motivation from the intention to relate the cause of excitation, i.e. flow distortion to blade vibration properties, namely excitation function, blade response and damping.

1.2. Centrifugal Compressors

Application of Centrifugal Compressors

The employment of radial turbomachinery in general and centrifugal compressors in specific can be found in a wide range of applications. Centrifugal compressors are considered to be robust and compact and combine these properties with comparatively high pressure ratios. For this reason a number of designs has been developed in the past integrating and adopting the properties of centrifugal compressors within the intended applications. By far the majority of applications to employ centrifugal compressors handles the compression of fluids in process engineering where fluid for example have to be transported or compressed for chemical processes. Where required, multi-stage configurations are realized to increase the pressure ratio of a single compression unit. In aerospace applications centrifugal compressors have been used for example in helicopter engines where high pressure ratios could be reconciled with the need to build compact and light-weight engines. For the same reason comparatively small turbo-prop and jet-engines have been relying on the integration of centrifugal stages to boost the pressure ratio downstream of an axial stage. In the recent decades, the market for centrifugal compressors has been growing in particular in the field of turbo-charging of conventional diesel stroke engines, i.e. for naval transportation, where considerable fuel savings can be achieved. Current designs in this field intend to push centrifugal compressors towards higher pressure ratios and mass flows.

Research on Centrifugal Turbomachinery

Traditionally, research into centrifugal turbomachinery has been focusing on aerodynamic aspects aimed to increase efficiency, pressure ratio and mass flow. This primarily involves the design of the aerodynamic flow path within the rotor and the diffuser. Unlike in axial turbomachinery, aerodynamics of centrifugal compressors is inherently characterized by rather complex three-dimensional flow field conditions. Typical research activities in this regard refer to jet-wake modeling, over-tip leakage and impeller-diffuser interaction. In order to understand these flow conditions research into this field has been intensified experimentally and computationally. In particular the advancement of computational methods and hardware capacities to deal with larger three-dimensional domains enabled valuable insight into the flow field structure of a radial compressor. Today, common practice of aerodynamic design

of centrifugal compressors involves quasi 2D layout by means of stream line curvature methods followed by 3D RANS steady-state computation. In the future it is expected to see inclusion of unsteady computation into the design process. For this reason, research focuses on solver improvement and validation. The involved complexity of fluid flow modeling necessitates experimental research for validation purposes. Recent in-house work on the subject flow field measurements has been conducted by *Stahlecker* [77], *Roduner* [66] and *Köppel* [44]. The focus of their research activity was the measurement of unsteady flow field properties in a centrifugal compressor and involved the resolution of the interactive effects between the impeller and the diffuser. In addition, development of intrusive and optical measurement techniques has been conducted among which are fast aerodynamic probe techniques and Laser Doppler Velocimetry (LDV). For example, *Stahlecker* [77] applied LDV in a vaned diffuser of a centrifugal compressor to measure the velocities during stable operation and during stall. The method allowed a plane-by-plane resolution of the flow features along the diffuser channel.

Further research focus has been intensified on compressor stability. Typically, high pressure centrifugal compressors suffer from narrow stability limits whereas customers demand improvements in both high pressure ratio as well as a wide mass flow range. Research therefore targets to advance the understanding of instability inception, stall and surge. Research work on this subject has been undertaken by *Ribi* [64] and *Schleer* [68]. Of particular interest is research into mechanisms used to extend the stability limits, among which are casing-treatment and inlet flow injection.

High Cycle Fatigue

An ever growing improvement of aerodynamic attributes has been consequently pushing centrifugal compressor designs towards their mechanical limits. Generally, on the one hand the maximum rotational speeds have been rising and on the other hand higher mass flow rates had to be realized. The latter has been facilitated through thinner and longer blades. However, the increase in rotational speed also increases the centrifugal load of the component leading to a rise in the static mean stress of the material. Through this mechanism compressor blades become vulnerable to vibration and associated with it suffer from high-cycle-fatigue (HCF) failure. The problem of HCF is illustrated in the Goodman diagram in figure 1.1 which defines an endurance limit under static and vibratory stresses. Static stresses arise from centrifugal

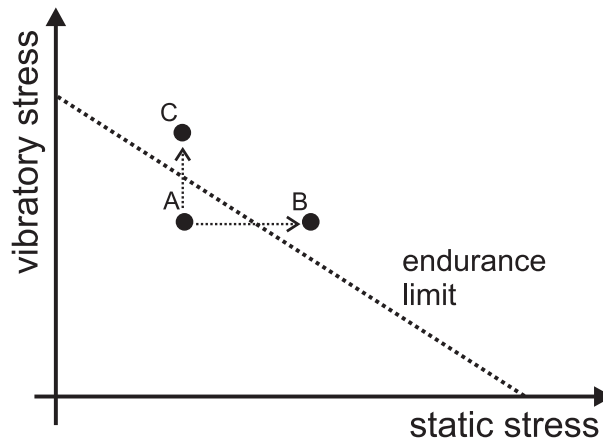


Figure 1.1.: Goodman diagram.

forces or gas ending forces acting on the structure. Vibratory stresses are introduced due to forced response from aerodynamic excitation. Depending on the amplitude of the two stress contributors the stress loading may be within the endurance limit i.e. below the endurance line as indicated by *A*. With an increase in static stress as for example due to higher centrifugal loading, the static stress may move the overall stresses into a regime where the blade would fail as indicated by *B*. In a different scenario, unsteady blade excitation may increase i.e. due to changes in operating point and may thereby cause an increase in vibratory stress as indicated by *C*. In any event, operation outside the endurance limit represents a failure mechanism that must be accounted for.

1.3. Forced Response Vibration in Turbomachinery

Blade Vibration and Sources of Excitation

Vibration in turbomachinery is an undesirable but also an inevitable mechanical phenomenon of paramount importance with respect to limitation of component life. All rotating components within a turbomachinery are subject to vibration, as for example either caused by periodic mechanical excitation or unsteady aerodynamic loading. The latter is of particular interest to blade vibration and has been subject to a number of investigations for the last decades. One aspect of research into this field was aimed towards understanding the excitation sources that cause blade vibration and their effect on

the dynamic response of the blades. The other aspect was the necessity to estimate blade damping and identify damping contributions due to various damping mechanisms present in a blade assembly. The maximum response of a vibrating structure during resonance that is subject to periodic excitation can be described by the following model

$$\eta_0 = \frac{|f|}{2\omega^2\zeta} \quad (1.1)$$

where η_0 represents a the response amplitude, f is the excitation amplitude, ζ is the critical damping ratio and ω is the eigenfrequency of the system. In order to assess stresses from vibratory motion a quantification of excitation forces as well as damping is required. For this reason blade vibration studies of forced response focus on these two quantities.

The majority of work into turbomachinery blade vibration has been carried out for axial configurations featuring blades of high aspect ratios. In addition, early experimental and analytical investigations into blade vibration were based on many simplifications with respect to geometry, often neglecting the effect of centrifugal load and coupling effects between the individual blades and the disc. With the increasing demand for higher efficiencies of radial turbomachines in the field of turbochargers and process engineering, the design of radial compressors and turbines requires a more in-depth understanding of vibratory issues.

There is a number of reasons why blade excitation occurs. Generally, two mechanisms are distinguished by their way to cause blade vibration. Blade vibration due to forced response refers to excitation by external sources acting on the blade in the form of unsteady forces. Flutter refers to a form of self-excitation where a blade undergoes unsteady deformation and thereby introduces flow instabilities. Flutter is rarely encountered in centrifugal compressors as pointed out by *Kushner* [47] and *Haupt* [27].

Forced response sources of excitation are numerous. For example, flow distortion upstream of the rotating blades may be introduced due to vanes, pipe bends, flow injection or flow separation due to struts. The experimental and computational case study by *Dickmann et al.* [11] look into blade excitation caused by flow recirculation where fluid is extracted along the shroud and then reinjected. Depending on the operating point, either near surge or near

the choke limit, the response amplitudes of the impeller blades were shown to vary considerably. Their numerical study, backed-up with response measurements, quantified and visualized the unsteady flow mechanism that caused resonant excitation. It was shown that non-axisymmetrically positioned components, i.e. the inlet duct as well as the volute tongue, have an effect on the unsteady excitation amplitude.

Flow instabilities may occur within the rotor passages depending on the operating point. In the publication by *Haupt et al.* [32] on a centrifugal compressor this source of excitation was recognized as broadband pressure fluctuations to cause strong blade vibration at part speed.

A comprehensive work was carried out by *Haupt* [27], who studied the effect of different excitation mechanisms on the response amplitude of a high-speed centrifugal compressor. In this case obstacles in the inlet section of the system were identified to cause relatively low blade response amplitudes which agreed with earlier observations for similar machines. Substantial blade response was measured due to excitation stemming from the vaned diffuser. The diffuser vane shape was shown not to affect the excitation amplitude, instead, different vane shapes altered the performance map and thereby introduced flow separation that led to excessive vibration amplitudes. Vibration due to flutter could not be identified for the centrifugal compressor. The potential of dangerous vibration due to rotating stall was shown to increase towards higher rotational speeds. Blade resonance with a frequency corresponding to the number of stall cells was not observed. During surge, blade excitation was substantially increased for the vaned diffuser case as opposed to the vaneless diffuser. Laser-based optical measurement of rotating blades at resonance showed that the blades were vibrating with an identical mode shape albeit at different amplitude. This observation could be associated with effects due to mistuning.

Blade vibration and the cause of excitation was subject to research by *Jin* [38] for a high-speed centrifugal compressor. In the studied case resonance was observed to occur due to flow recirculation along the shroud, which originated at the outlet of the rotor and propagated upstream to the blade leading edges. The associated unsteady pressure field was found to be controlled by blade vibration which was affected by the inlet flow angle. As a result of the interaction between the vibrating blades and the unsteady pressure

field, resonant vibration was measured to exceed tolerable stress amplitudes. Particularly radial compressors featuring thin blades and vaned diffusers are prone to this mechanism of excitation. Unsteady excitation amplitudes are sensitive to blade angle variation due to vibration and therefore represent a likely scenario of dangerous blade vibration. Further research was focused on blade excitation due to rotating stall and surge. During these aerodynamic instabilities, both, periodic as well as non-periodic flow conditions could be identified. Flow pulsation at the inlet were shown to cause excessive blade vibration.

Low-speed compressors were studied by *Sälzle* [73]. Response measurements during harmonic excitation showed that obstacles in the inlet flow caused negligible response with respect to failure. Dangerous excitation was identified to stem from the spiral-type volute. Unsteady pressure measurements on the rotor proved the dependence of the excitation distribution and the harmonic content on the mass flow setting. The first harmonic of the excitation spectrum was found to dominate whereas higher harmonics were by about an order of magnitude smaller.

The excitation mechanisms stemming from rotor-diffuser interaction were studied by *Gallier* [22] for a centrifugal compressor. Wall-mounted static pressure transducers and PIV were employed to quantify the pressure and velocity field in the vaneless space between the rotor exducer and the diffuser vanes. The main drivers of the unsteady exducer excitation were shown to originate from incidence variations acting on the diffuser vanes and the resultant variation in vane loading that propagates upstream. This interaction between the passing rotor blades and the vanes causes substantially higher excitation amplitudes than could be justified by a steady potential field due to the vanes.

Other sources of forced blade vibration include periodic mechanical disturbances transmitted through the shaft and the disc. Particularly high excitation amplitudes can be realized by flow instabilities encountered during stall or surge. In many applications this might cause an instant failure of blades. *Haupt et al.* [28] point out the complexity of this excitation phenomenon and the need to understand underlying mechanisms. In their later work *Haupt et al.* [33] identified stall cells to cause blade excitation. The origin of any of the sources of excitation depends on the type of application and

the mechanical and aerodynamic design of the turbomachinery. Research into forced response requires the quantification of excitation sources for example in the form of aerodynamic measurements.

Blade Damping

Damping represents a source of energy dissipation and counter balances excitation energy. In general three main contributors to damping can be identified for turbomachinery blades: material, mechanical and aerodynamic damping. The contribution of each of these damping mechanisms depends on the associated blade design properties i.e. material, fixation and shape as well as fluid properties. In the past the vast majority of work and publications in the field of vibration and the quantification of damping was carried out for axial turbines and compressors. A summary of experimental approaches and problem modeling was presented by *Srinivasan* [74, 75]. With regard to damping, in the past research has focused on the estimation of mechanical damping. This damping mechanism can be affected through mechanical implementation of dampers and rubbers. *Kielb and Imregun* [42] outline the contributors to damping and present the characteristics of mechanical damping.

The experimental research by *Srinivasan et al.* [76] revealed material damping to be minimal and could be neglected during design. The study was performed for titanium blades and experiments were undertaken for different ambient pressure settings while providing mechanical excitation.

Newman [57] performed damping measurements in a three-stage axial flow compressor. Blade response was measured for a number of inlet pressure levels caused by aerodynamic excitation. Damping was obtained for each pressure setting and then linearly extrapolated to vacuum pressure. The results clearly identified aerodynamic damping to be dominant for the bending and torsion modes. Material damping could be considered negligible.

The publication by *Crawley* [10] introduces a generalized concept to obtain aerodynamic damping of a vibrating axial blade, based on response measurements. The concept is derived from the normalization of the equation of motion into a set of decoupled equations, one for each mode. The modal force composition is then reduced to the influences of the blade itself as well as its neighboring blades. This method enabled the computation of the modal force depending on the blade response. During the experiment the blade was

excited by rotating stall cells. The passing of a stall cell caused excitation whereas the free-flow between each stall cell caused damping and a decay of the response amplitude. During the decay event a blade was only subject to aerodynamic damping with the damping force oriented such that it is in phase with the response but with an opposite sign. In a later experimental work, *Crawley* [9] presents measurements of aerodynamic damping for a transonic compressor by introducing inlet distortion and thereby causing forced response of the blades. The inlet distortion consists of injection holes placed stream-lined struts and can be shut down such that a sharp termination of the excitation can be facilitated during the transient measurement. Aerodynamic damping for the first two blade modes was found to dominate and structural damping contributed roughly 2-10% to the overall damping.

An experimental technique to measure the contributions from structural and aerodynamic damping was presented by *Jeffers et al.* [37] and applied by *Kielb and Abhari* [40] for a transonic axial turbine. The methodology relies on blade excitation through piezo actuators mounted on the blade surface while the turbine spins in vacuum conditions. Under these conditions only structural, i.e. the sum of material and mechanical damping, was present and could be quantified for a number of speeds. Structural damping was shown to be proportional to $1/RPM^2$ due to a reduction in friction as the speed increased. Despite the contribution of mechanical damping, aerodynamic damping was shown to be the dominating contributor to the overall damping for all modes and by a factor of 10 higher than structural damping.

For radial turbomachinery, where rotors are machined from a single piece, structural damping is very low and aerodynamic damping is therefore the dominant damping mechanism. Data on damping is rare in the open literature especially for centrifugal compressors. The publication by *Jin et al.* [39] quantifies damping during resonant response and was found to be by a factor of 15 higher compared to on-bench experiments of a non-rotating impeller. Two impellers were compared featuring blades of different thickness and concluded that thin blades exhibit higher damping ratios than thicker blades. Moreover damping was shown to increase for higher mass flows. The exact contribution of structural and aerodynamic damping to the overall damping could not be reported due to the lack of in-vacuum measurements.

Mistuning

The effects of mistuning are encountered in cyclicly symmetric structures i.e. bladed disk assemblies or impeller machined from a single piece of material. The root of the problem are slight variations of blade-to-blade properties that cause eigenfrequency shifts of the cyclic sectors. The effect on the response amplitude however is profound and might cause excess amplitudes with respect to HCF failure. The publication by *Lin* [51] outlines the subject of wave propagation in periodic structures, starting from ideal systems of equal entities and then presenting the dynamics of disorder structures, i.e. entities with slightly different properties. On this basis an analytical approach to describe the attenuation of wave motion and the scattering of the frequency response was given. The effects of damping and wave reflection between neighboring units were considered. Periodic structures subject to mistuning suffer from localization, in which case essentially a large amount of the total energy is concentrated within a small region. In engineering practice this phenomenon becomes evident during testing and operation as failure of single blades. For this reason the subject of mistuning has received great attention in the past. Early work by *Whitehead* [82] pointed towards the fact that although the excitation may be regular, the mistuned system has multiple resonances with a distinct scatter in amplitude and phase. Reviews in great detail were given by *Srinivasan* [74, 75] outlining that small departures in individual frequencies from a datum frequency could result in unacceptable levels of vibration. Mistuning is non-deterministic, therefore probabilistic methods have been initially adopted in order to assess the maximum response amplitude. Research into this field was largely driven by industry need to deal with this problem. As *Srinivasan* [75] underlines, mathematical analysis have been developed based on a multiparameter perturbation problem of disordered systems. For this approach a base system has to be defined about which the perturbation could be applied. Depending on the degree of coupling, either the tuned or the mistuned system was used. Due to shortcomings of these methods, later, Monte Carlo simulations have been regularly employed. In a later survey, *Slater et al.* [72] summarizes essential conclusions on the subject of mistuning and points out that mistuning has the greatest effect when coupling between the blades is weak. Even disk assemblies with ideally "tuned" blades maybe mistuned due to asymmetric friction of an assembly. Limitations have been associated with testing for the effect of mistuning, since bladed assemblies experience changes in properties during operation.

1.4. Experimental Analysis

Experimental analysis in forced response requires the use of a wide range of measurement techniques. Quantification of forced response parameters involves employment of (1) modal analysis, (2) flow field measurement techniques, (3) forcing function measurements on blade surfaces and (4) blade response measurements. Each of these aspects must be approached individually.

Modal Analysis

Experimental modal analysis is conducted with the aim to determine the modal shapes and frequencies of blade-disk configurations during vibration. Commonly the rotor is mounted on the bench and excited by a mechanical, electrical or acoustical actuator. Structural response can then be measured using either optical methods or point-to-point techniques to acquire displacement. Application of holographic interferometry was presented by *Haupt et al.* [30, 31] for a centrifugal compressor during operation for maximum speed of 20500rpm. The method enabled an optical acquisition of the modal shapes of all blades during vibratory response due to aerodynamic excitation. This visualization technique enabled to conclude that depending on the resonance case and excitation, that blades may vibrate with a single mode shape or a combination of multiple mode shapes. This condition could not be clarified using strain gauges only. Further work was conducted in this respect by *Hasemann et al.* [26] and *Hagelstein et al.* [25] to investigate the dominance of coupling effects between the blades and the disk. The investigation targeted the validation of a computational tool to predict modal shapes and it was concluded that due to the coupled nature of the higher modes, finer grid discretization should be aimed at in order to resolve the eigenfrequencies and shapes. The same experimental method was applied by *Jin* [38] to calibrate strain gauge signals with blade deflection.

Further examples for the applications of holographic interferometry can be found in the work by *Sälzle* [73] for a low-speed radial compressor. For low vibratory modes deformations could be identified as they are typical for disks and as they can be characterized by nodal lines. For higher modes however, the modal shapes became complex and could not be classified according to the number of nodal or circular lines. A classification of the modes could be performed based on the periodicity parameter which is commonly used for cyclically periodic structures for modal analysis.

Flow Field

Measurements of flow field properties aim at the quantification of the amplitude of external disturbance. A number of techniques are commonly applied that measure the pressure, temperature and velocity field upstream or downstream of the rotor. *Manwaring and Fleeter* [52] used a cross hot-wire mounted on a rotating blade to measure the inlet distortion flow field which was intentionally introduced upstream of the impeller. Using the cross hot-wire the velocity triangles could be measured facing the rotor blades. The amplitude of the intended excitation harmonic was found to dominate the flow field with higher harmonics being much smaller. In the study by *Rabe et al.* the inlet distortion pattern was measured using inlet rakes equipped with pressure sensors which could be turned circumferentially. A nearly sinusoidal total pressure distortion pattern was measured revealing fluctuations of $\pm 16\%$ from the mean value. The distortion pattern provided sufficient excitation to cause resonant response. Rake geometries were studied by *Anderson and Keller* [3] for the measurement of frequencies contained in a distorted inlet flow field. Different rake arrays were compared. In addition clocking the rakes was investigated. Based on the evaluation of the random and the systematic errors to measure inlet frequencies it was concluded that errors could be reduced by increasing the arrays or clocking the rakes. Particularly for higher excitation orders this becomes inevitable in order to accurately resolve the amplitudes. Excitation due to diffuser vanes or pressure field asymmetries in the volute is commonly measured using pressure sensors mounted on the shroud wall, as presented in the work by *Gallier* [22]. The method enabled the quantifications of the non-linear coupling between the rotor and the diffuser.

Unsteady Blade Pressure

Probably one of the most challenging experimental tasks is the measurement of the unsteady pressure acting on rotating blade surfaces. For this reason publications in this regard are sparse for axial configurations and do not exist for centrifugal compressors operating at high speeds. Measurement of excitation forces requires the installation of pressure sensing devices on rotating blades. Under these conditions pressure sensors are subject to harsh environments during measurements which may deteriorate and falsify the response signal considerably. A great deal of calibration and quantification of numerous influence parameters becomes inevitable. Early works on the technique to

measure unsteady blade pressure were reviewed by *Lakshminarayana* [48] referencing the application of strain gauge transducers or piezoelectric and film type capacitance transducers. *Chivers* [6] presented experimental techniques to measure steady and unsteady pressure for fans or large turbines using high frequency response pressure transducers inserted into the blade surfaces. The importance of measuring blade pressure distribution and its measurement in experimental heat flux research and computational predictions was reviewed in great detail by *Dunn* [17].

In a series of publications blade pressure measurements were reported for short-duration test turbines, i.e. by *Dunn et al.* [19] and *Dunn and Hause* [16]. Their work focused on the quantification of unsteady aerodynamics due to row interaction. Trailing edge shocks could be identified to cause high-amplitude unsteadiness on the rotor leading edge and to affect the heat flux. Validation of a computational tool was carried out on the basis of blade pressure measurements by *Dunn et al.* [18] and *Rao et al.* [63] for a transonic turbine. The computation was in good agreement with the measurements to predict vane generated shock impingement on the rotor surface. A comprehensive research study on the effect of vane-blade spacing on the blade surface pressure distribution was carried out by *Venable et al.* [79] and *Busby et al.* [5]. They found that the mean pressure on the rotor blade surface is not affected by the spacing, whereas the flow unsteadiness is substantially changed. The measured results were well predicted by numerical flow computation.

A detailed discussion on fast response pressure sensors based on piezo-resistive semiconductors was published by *Ainsworth et al.* [1, 2]. The application of pressure sensors focused on an axial turbine test facility operating at transonic conditions. The effects of temperature, base strain sensitivity, centrifugal force effects as well as the frequency response of piezo-resistive semiconductors were outlined. Based on the described techniques, unsteady pressure measurements in a short-duration test facility were performed by *Miller et al.* [55, 56] in order to identify blade row interaction mechanisms and to quantify their effect on the unsteady blade surface pressure distribution. Unsteady aerodynamic effects stemming from passage vortex and shock interaction between the blade rows could be identified and characterized.

The influence of temperature transients and centrifugal forces on fast-response pressure sensors was presented by *Dénos* [13] as well as correction methods

were proposed for both effects. Temperature calibrations under conditions of thermal equilibrium were found to be not well suited to correct the data obtained during transient tests. Centrifugal forces during rotation cause a constant drift proportional to the square of the rotational speed with large amplitudes that must be corrected. Measurement examples using blade-mounted pressure sensors in a blow-down turbine test facility were presented by *Dénos et al.* [15, 14] with focus on unsteady aerodynamics due to blade row interaction.

In the case of a low-speed centrifugal compressor, on-blade unsteady pressure was measured by *Sälzle* [73]. The main cause of excitation was measured to originate from the non-symmetric volute and was shown to vary significantly when changing the mass flow. Associated with this the excitation spectrum varied, albeit the first harmonic was by an order of magnitude higher than the higher harmonics.

Unsteady flow field and noise generation in a centrifugal pump impeller were studied by *Choi et al.* [7] using pressure transducers mounted in the exducer region of the rotor. Jet-wake phenomena were identified to induce strong vorticity fields near the trailing edge of each blade. The unstable nature of this vortex affected the neighboring passages and therefore the jet-wake flow pattern. As a result, the flow unsteadiness caused periodic pressure fluctuations on the blade surfaces.

A series of extensive on-blade pressure measurements were performed for an axial flow research compressor aiming at the quantification of unsteady excitation forces. Both, steady loading as well as the unsteady excitation due to inlet distortion were examined by *Manwaring and Fleeter* [52]. On the pressure side, unsteady pressure amplitudes were primarily affected by the steady loading whereas on the suction side the unsteady pressure was a function of steady loading as well as the distortion amplitude ratio. In a subsequent study *Manwaring and Fleeter* [53] measured the unsteady loading levels for two types of inlet distortion: (1) due to the velocity deficit from a 90° circumferential inlet flow distortions and (2) due to vane generated wakes. The data showed that the wake-generated forcing function amplitude is much greater than for the distortion pattern, the difference, however, decreased with increased steady loading.

Transonic compressor blades were instrumented with pressure gauges in the work by *Rabe et al.* [62] and enabled the measurement of force and moment during resonance. The fast-response pressure sensors were installed such that the suction and pressure side were measured simultaneously by a single sensor, which is a measure for the unsteady pressure force. Based on this, forces and moments could be calculated for the blade section where the sensors were installed. The results revealed a pressure wave traveling through the blade passage during a distortion traverse. For a similar setup, pressure sensors were employed by *Manwaring et al.* [54] during the successful attempt to acquire all aspects of forced response, i.e. inlet flow distortion, unsteady pressure and resonant response. The study showed, that the distortions had strong vortical, moderate entropic and weak acoustic parts.

Vibratory Response

In the past two major measurement techniques have been established to measure blade vibratory response: (1) strain gauge measurements of blade surface strain and (2) tip-timing techniques measurements of blade deflection along the shroud. In the first case, strain gauges are mounted on the surfaces of the impeller blades and measure the local strain due to blade deformation. This technique enables very reliable, high resolution measurements and is currently the primary method employed during testing of new designs. However, associated with strain gauge measurements in the rotating frame of reference are time and cost consuming installations for data conditioning and transmission which are prone to failure. Moreover, the number of strain gauges may limit the number of blades measured depending on the modes of interest. In addition, on blade installations of sensors introduces parasitic mistuning into the system as opposed to "natural" mistuning due to manufacturing tolerances.

Due to the wide-spread application of this technique no examples will be presented here, instead a short overview on the optimization of strain gauge installations should be given. For example, *Griffin* [24] proposes a method to identify the number and identity of blades for an optimal instrumentation of blades in turbomachinery. Effects of mistuning were taken into account and it was proposed to instrument those blades that show the smallest standard deviation in the measurement quantities of interest, i.e. strain or frequency. Also, the number of gauges from stage to stage should be allocated such that the measurement errors are consistent from stage to stage. A method to

choose the optimum strain gauge position was outlined by *Penny et al.* [59] for modal analysis. The approach is based on FEM modal analysis and modal reduction techniques. Then, criteria are applied to judge on the suitability of each measurement location. *Sensmeier and Nichol* [71] optimized the strain gauge location based on an optimization function which reduced the error between the experiment and the numerical modal analysis. All modes of vibration were considered simultaneously during the employment of the routine and which resulted in a considerable improvement of the correlation between the measured data and the model predictions. Blade positioning optimization was carried out by *Szwedowicz et al.* [78] based on a cyclicly symmetric model of a tuned bladed disk. Optimization criteria include sensitivity, orthogonality, gradient and gauge distance. The method was shown to efficiently select strain gauge locations.

The tip-timing technique is a non-intrusive method and measures blade passing periods along the shroud surface. The technique essentially captures the time lag due to vibration which can then be expressed in terms of blade deflection. The major advantages of this technique are its comparatively simple installation requirements and reusability. In addition, all blades can be measured simultaneously thus allowing to capture effects of mistuning. However, high blade tip speeds accompanied by low deflection requires high temporal resolutions and may render the technique unusable. Under such conditions the problem of data under-sampling must be dealt with. Moreover, computational modal analysis must be performed alongside in order to express blade deflection in terms of stress within the material. Tip-timing is restricted to modes with deflection at the tip of the blade. Also, shrouded rotor configurations cannot be studied by tip-timing. Early work on this techniques was presented by *Roth* [67] for optical sensors. In a later work *Zielinski and Ziller* [86] studied vibration of compressor rotor blades using tip-timing. Probe technologies based on the capacitance effect were applied by *Lawson and Ivey* [49]. Mathematical modeling in support of tip-timing modeling can be found in the publication by *Dimitriadis et al.* [12].

1.5. Research Objectives

The introduction presented above revealed considerable research efforts into forced response based on axial turbomachinery. Despite the broad range of applications for centrifugal compressors, forced response research in this respect has received comparatively limited attention. Therefore, the objectives of this work can be summarized in the following questions:

Suppose the blades of a centrifugal compressor experience low order excitation during operation or testing due to aerodynamic disturbances in the flow field, what are the governing parameters in forced response terms to determine the resultant resonant response amplitude?

How do the governing parameters of forced response change with changes of the operating conditions of the centrifugal compressor?

In view of these questions the objective of this research study primarily targets the quantification of forced response parameters for centrifugal compressor blades. This would enable to draw conclusions on the underlying mechanisms to affect resonant response. The results obtained could then be transferred into the design and testing practice of novel centrifugal compressor configurations. In line with the stated objectives the research work implies the realization of an experimental case study where measurements can be undertaken under engine representative conditions. Experimental analysis is essentially based on the measurement of aerodynamic quantities of the compressor flow field and the blade response. The objective herein is to propose novel experimental techniques that can be used for forced response studies. In more specific terms, the goals of the study are:

- Realize the measurement of aerodynamic and structural properties for a centrifugal compressor during resonant vibration under engine representative conditions.
- Provide and integrate an experimental methodology to intentionally distort the flow field upstream of the impeller to cause resonant response.
- Develop experimental techniques to measure unsteady pressure and strain on rotating blades.

- Develop a methodology to quantify damping and separate contributions from structural and aerodynamic damping.
- Study the excitation function, the damping and the resonant response amplitude for a series of excitation cases and mass flow settings.
- Conclude on the significance of the modal parameters on the resultant response amplitude of a centrifugal compressor blade.

The research was realized in a centrifugal compressor test facility where measurement requirements could be met in order to achieve the objectives. The rotor operates at engine representative conditions and resembles a design typical for turbocharging applications where the blades are highly loaded. The test section enabled the installation of flow distortion devices, fluid flow measurement techniques and on-blade sensor installations. Crucial to this research is the ability of the closed-loop facility to adjust the internal pressure level independently of the ambient conditions.

1.6. Thesis Outline

Chapter 1 outlines the motivation of this study, a comprehensive overview on centrifugal compressors, forced response and its analysis are given.

Chapter 2 presents the experimental setup. Details are given on the test facility with focus on the rotor properties which includes the performance and modal properties. FEM computation and an optical method based on speckle interferometry were applied to obtain the blade modal properties. Moreover, details on the measurement approach, on-impeller data acquisition and signal transmission are given.

Chapter 3 outlines the applied sensor instrumentation on the impeller blades. The development, calibration and error analysis are presented for a novel pressure sensor developed for the use on impeller blades. Also, strain gauge application for the measurement of dynamic strain and the employment of piezo electric actuators is presented.

Chapter 4 proposes a methodology to intentionally distort the inlet flow of the test facility in order to target specific excitation orders. The method represents an analytical approach to adjust the circumferential velocity deficit to

a desired amplitude. Moreover, measurements using an aerodynamic probe are presented and discussed.

Chapter 5 presents and discusses results on measurements of unsteady pressure along the blade surface. Two cases are generally distinguished, unsteady pressure measurements with and without distortion screen installation. For both cases the spectral content of the flow field is illustrated first, then specific harmonics are presented in terms of amplitude and phase angle. In addition CFD results are discussed in support of the findings based on experimental data. Finally, unsteady pressure measurements during resonance are presented.

Chapter 6 outlines details on resonant response measurements of strain during resonance. This is first done in terms of dynamic response characteristics and is then expressed in terms of maximum response amplitude. The response of the blade is compared to a SDOF dynamic system. In addition mistuning effects on the blade-to-blade variation of the maximum response underline the importance of this phenomena.

Chapter 7 deals with the measurement of blade damping, expressed in terms of critical damping ratio. The presented approach enables the measurement of the separate contributors to damping, in this case material and aerodynamic damping. Material damping is obtained from on-bench measurements whereas aerodynamic damping is measured during operation in the facility. Two different fitting methods are discussed and applied.

Chapter 8 addresses the subject of forced response by combining measurement results on response, forcing function and damping. Their dependency is expressed in the modal space. Moreover, in order to complement data analysis a method to measure local aerodynamic work on the blade surface is presented.

Chapter 9 Summarizes and concludes on the outcome of this research work.

2. Experimental Setup

2.1. Test Facility

The test facility is a single stage centrifugal compressor, termed 'RIGI'. A schematic drawing of the test facility is given in figure 2.1. The facility operates in a closed loop which allows the pressure to be adjusted independently of ambient conditions. In the present study, the pressure at the inlet of the impeller was typically varied within the range of 0.1bar to 0.9bar. The impeller is driven by a 440kW DC motor with a two stage gear box. Due to power limitations of the gear box the maximum inlet pressure is limited to 0.6bar for maximum speed. Upstream of the impeller, both the pressure and the temperature are measured and held constant to the desired levels by a control system. Downstream of the compression stage the fluid is cooled and then discharged through a throttle prior to reentering the impeller section. The throttle is used to set the mass flow rate. A standard orifice upstream of the impeller is used to measure the mass flow. In order to estimate the performance of the facility, pressure and temperature are measured upstream and downstream of the compression stage. During operation performance data is continuously acquired and stored.

Figure 2.2 illustrates the arrangement within the inlet section of the compressor. During blade strain and pressure measurements the center of the inlet section is occupied by a cylinder covering the rotary transmitter. The transmitter is mounted and centered using two rows of adjustable struts, i.e. 3 upstream and 4 downstream. The downstream struts are covered by symmetrical airfoils in order to avoid flow separation that would otherwise be generated across the rods. The distortion screen section is situated five blade heights upstream of the impeller. Their mechanical integrity assures, that the distortion screens can be exchanged without the need to dismount the rotary transmitter. Upstream of the impeller a traversing mechanism was integrated where an aerodynamic probe can be mounted in order to measure flow conditions entering the impeller. The traversing system allows probe

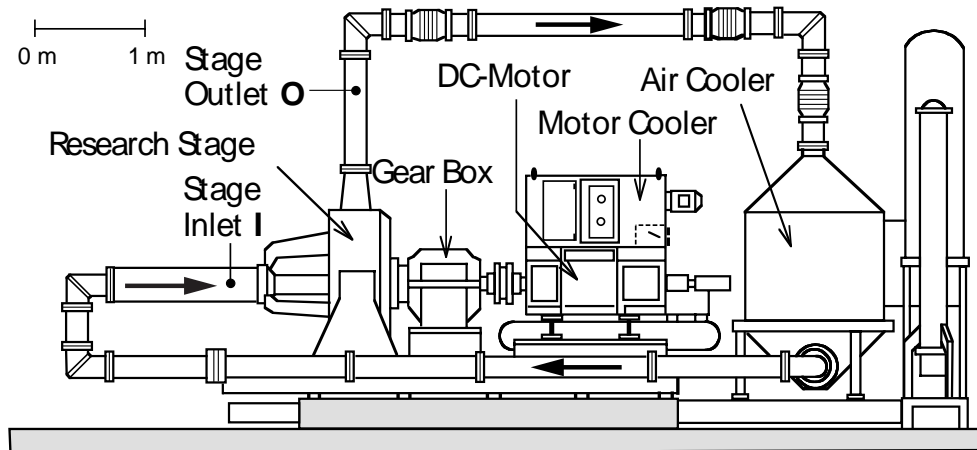


Figure 2.1.: Radial compressor research facility.

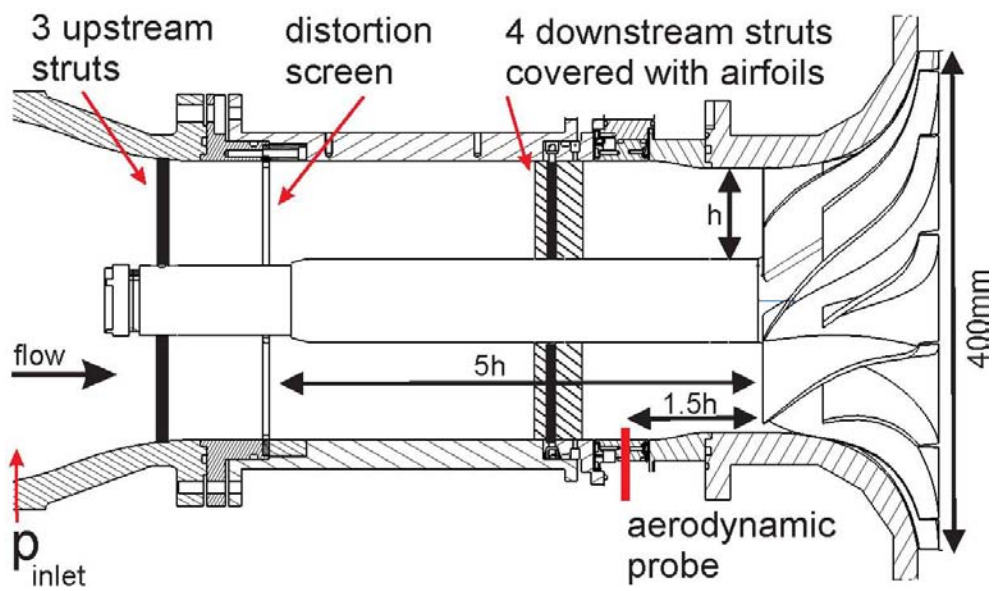


Figure 2.2.: Arrangement and dimensions within the inlet section.

traversing in the circumferential and radial direction. In addition, the probe can be rotated around its axis.

2.2. Compressor Performance

The impeller used in this study, termed *A8C41*, is a modified version of the impeller designed by *Schleer* [69], termed *A8C*. The latter has been employed in a number of experimental flow structure investigations. An in-depth description is given in *Schleer* [68]. With a design total pressure ratio of $p_{t,out}/p_{t,in} = 2.8$, the impeller consists of seven pairs of main and splitter blades with an outer diameter of 400mm. The diffuser is parallel and vaneless with an exit diameter of 580mm and a height of 15.7mm. Downstream of the diffuser the flow is discharged into a toroidal collecting chamber. The maximum rotational speed is 22000rpm.

Impeller exit diameter	400mm
Diffuser width	15.7mm
Number of blades main/splitter	7/7
Impeller material	aluminum
Tip speed	460m/s
Rotational speed	22000rpm
total pressure ratio $p_{t,out}/p_{t,in}$	2.8
inlet pressure	0.1bar ... 0.8bar

Table 2.1.: Impeller design properties.

The performance map in terms of pressure rise is shown in figure 2.3. Both, the mass flow and the pressure rise are referenced with respect to their design quantities. The performance map illustrates the regime of interest for the datum research. Since the new *A8C41* design features thinner blades than the original *A8C* configuration, the maximum mass flow passing through the blade passages increased proportionally to the reduction in blade thickness. The pressure ratio was not affected but the choke limit was increased by about 15%. With respect to rotational speed, on-impeller data was taken for a maximum speed of 18'000rpm, which is approximately 20% below the

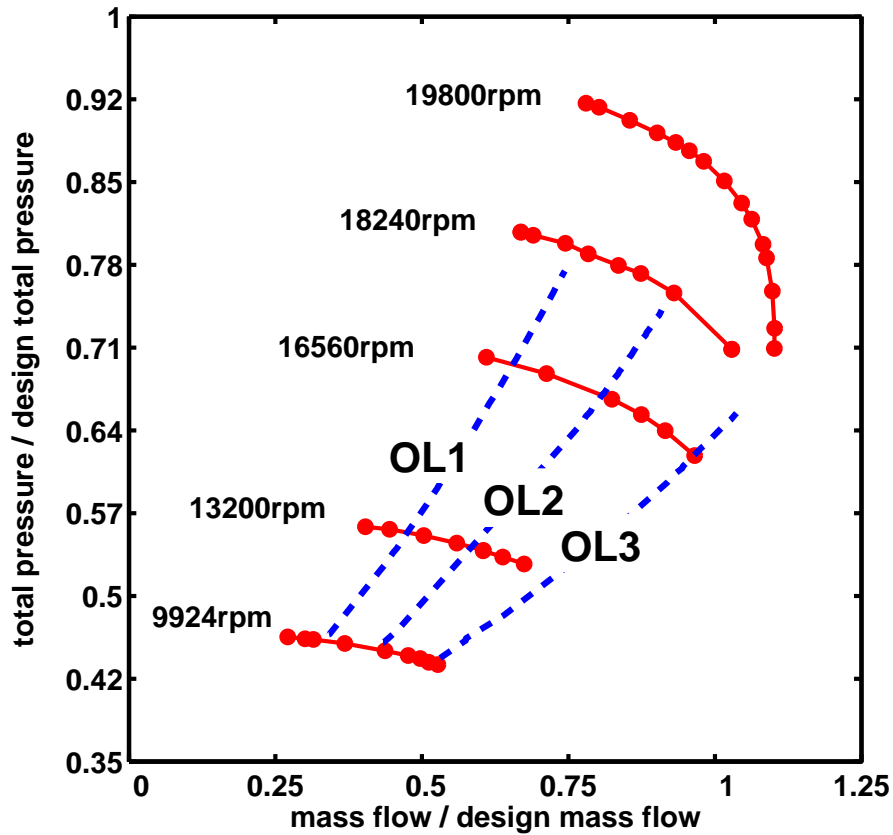


Figure 2.3.: Performance map.

design speed and pressure ratio. In accordance with the Campbell diagram in figure 2.5, all forced response data was taken at rotational speeds between 13'500rpm and 18'000rpm. Measurements were performed along three operating lines, signified with OL1, OL2 and OL3. These were chosen such, that forced response data covers the entire mass flow range for a given resonant crossing, ranging from operation near the stability limit to operation near the choke margin.

2.3. Impeller Modal Properties

Main Blade Thickness and Eigenfrequencies

In order to fulfil the requirements of the current study, the modified impeller *A8C41* design features thinner blades than the original *A8C*. Except for the blade thickness all other parameters defining the geometry of the blades and

the disc were retained as it was the case in the original design. The final impeller thickness was obtained from progressively reducing the blade thickness at the hub and tip and recalculating its modal properties using FEM. Figure 2.4 presents the dependence of the main blade eigenfrequencies on the blade thickness. In a first step the blade thickness was reduced equally at the hub and the tip from 100% thickness down to 41% as shown in figure 2.4(a). Doing so resulted in a linear reduction of the main blade modes. The linear relationship applies to all modes, however, the slope of the linear function is mode dependent and increases for higher modes. For the datum impeller the frequency of the first eigenmode, Mode 1, was reduced from 2500Hz down to 1350Hz. In a second step the blade tip thickness of the blade was increased thereby shifting the eigenfrequency towards higher values as shown in figure 2.4(b). The effect of modifying the tip thickness affects higher modes only. The first mode was not affected by this modification whereas the second eigenfrequency was shifted upwards by about 100Hz.

Resonant Conditions

The redesign focused on ensuring a number of potential resonant crossings of the first and second main blade eigenfrequencies with the low order engine excitation sources. The Campbell diagram in figure 2.5 illustrates the location of the main blade eigenfrequencies, termed Mode 1–4. The eigenfrequencies of the modes can be seen to be well separated. Given the modified blade thickness, a number of potential resonant crossings can be identified with the low engine order excitations. These were intentionally generated using distortion screens with specific distortion patterns in order to target the corresponding engine order excitation. The realized resonant cases during forced response measurements are given in the following table:

RPM at resonance	mode name	excitation order	nodal diameter ND
13500	Mode 1	EO6	1
14370	Mode 2	EO12	2
13250	Mode 1	EO5	2
17400	Mode 2	EO10	3

Table 2.2.: Resonant condition cases.

The dispersion diagrams in figure 2.6 were obtained from computing the

modal properties for a cyclicly symmetric model and the nodal diameters $ND = 0, 1, 2$ and 3 . The results show, that the frequency of the first two main blade modes is constant for all nodal diameters and is therefore not affected by the disk modal shape. Resonant crossings are marked where the excitation, dashed line, crosses the blade modes. From this the according nodal diameter of the impeller can be identified during resonance. Using the ESPI method as explained in the following paragraph, the impeller modal shapes are shown in figure 2.8 for $ND = 2$ at 2862Hz and $ND = 3$ at 2882Hz. The Mode 2 case is shown only whereas in the case of Mode 1 the nodal diameters could not be visualized. The visualization method reveals disk motion to undergo in the exducer region of the impeller. Therefore, blades are only affected at the exit of the impeller. The inducer part of the main blade, where the highest stresses occur during resonant vibration, does not appear to be affected by the disk motion.

Application of the ESPI Method

Complementary to computational modal analysis an experimental technique was applied aimed to identify the eigenfrequencies as well as to visualize the modal shapes. Electronic Speckle Pattern Correlation Interferometry (ESPI) was applied in this experimental approach which is an optical method. The method allows to visualize the displacement of vibrating structures with rough surfaces. During the experiment the impeller was harmonically excited using a piezoelectric actuator mounted on the back side of the impeller as shown in figure 3.7(b). The excitation frequency of the actuator was controlled by a frequency generator and was gradually increased until resonance was reached where an image was taken. The procedure was applied once showing the blade only and once visualizing the entire impeller.

Main Blade Modal Shapes

The experimentally obtained blade modal shapes for the first four modes are shown in figure 2.7. The pictures are orientated such that the leading edge of the impeller is on the right hand side. Black zones are areas outside of the blade surface, i.e. neighboring blades. The interferometry pattern shows lines of the same displacement. The signs \oplus and \ominus are used to indicate the direction of displacement for an instance in time. Mode 1 in figure 2.7(a) for example moves in one direction only, i.e. the entire blade vibrates in phase where the tip of the blades undergoes the highest displacement amplitudes.

The second mode in figure 2.7(b) consist of two zones that vibrate in counter phase. Between them a line of zero displacement can be identified indicated with the dashed line. As the eigenfrequency increases the number of zones of opposing sign increases. In the case of Mode 3, shown in figure 2.7(c), the nodal line moved into the tip corner of the blade revealing three distinct zones of displacement. In the case of Mode 4 in figure 2.7(d) the entire blade leading edge is displaced in the direction of the \ominus and superposed on this are two zones of opposite direction indicated with \oplus .

The experimental modal analysis shown is important for two reasons. First of all it enables to visualize the modal shape at its specific eigenfrequency which is necessary in order to allow for comparison between different impeller designs. Secondly, the results can be used for verification of FEM predictions used during the design process.

Comparison between FEM and ESPI

A qualitative comparison between the measured and predicted modal shapes is given in figures 2.9(a) and 2.9(b) for Mode 1 and Mode 2, respectively. In both cases the entire impeller is shown for the measured case whereas in the case of the computation a cyclicly symmetric section of the impeller is illustrated. The deformation pattern can be seen to be captured by the computation. For both cases, Mode 1 and Mode 2, all seven main blades can be seen to vibrate in the same pattern. This finding is in accordance with expectations for low order vibration. Generally, very good agreements between measurements and predictions are achieved for the first blade modes, which are well separated and marginally affected by coupling effects. At higher modes, i.e. above Mode 4, these agreements tend to deteriorate.

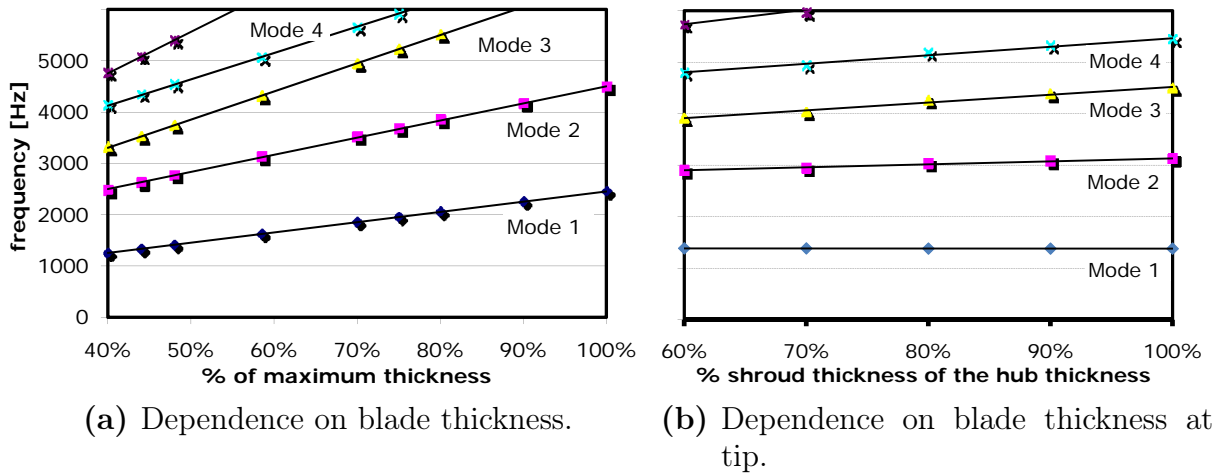


Figure 2.4.: Eigenfrequency dependence on blade thickness.

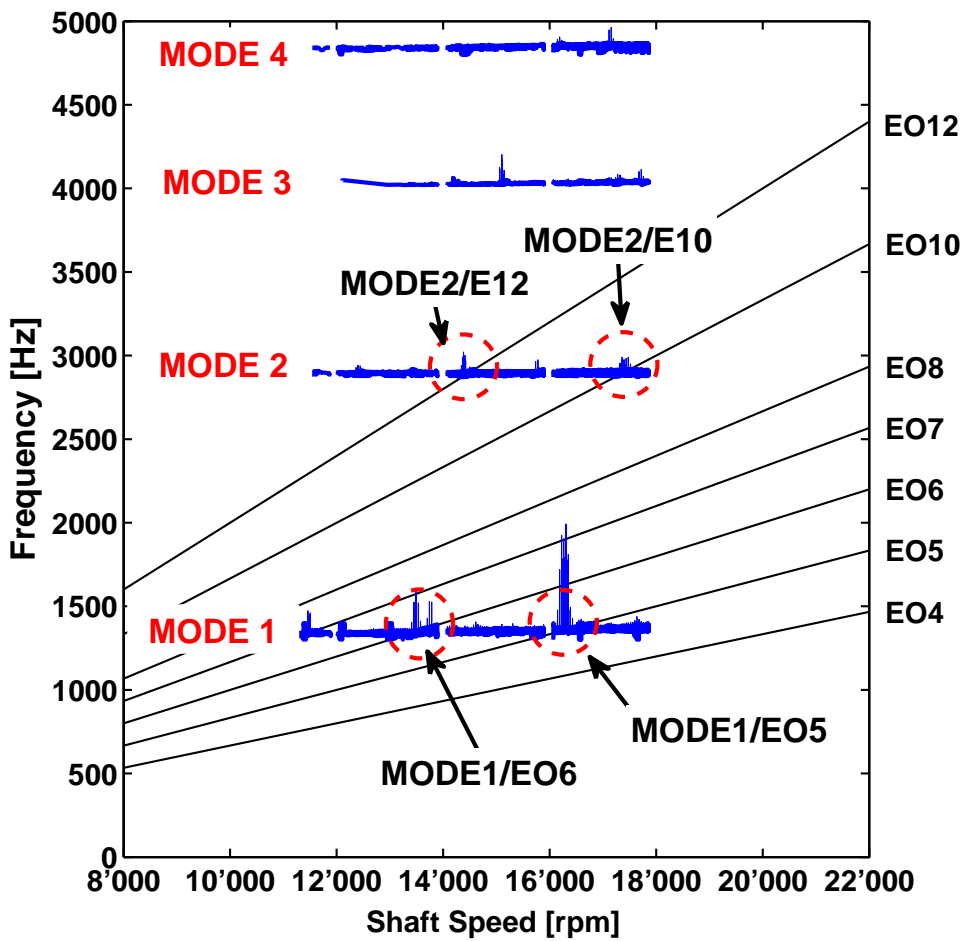
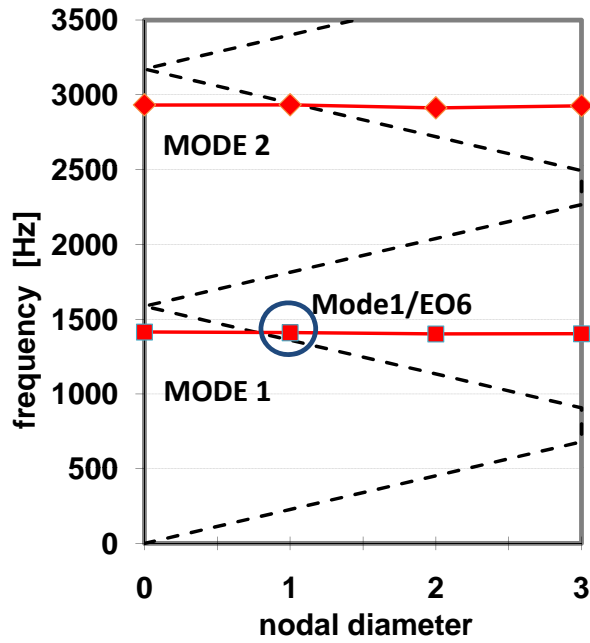
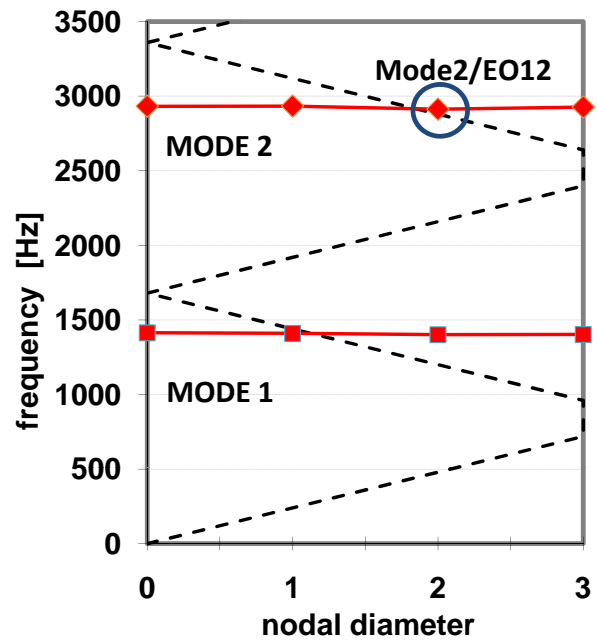


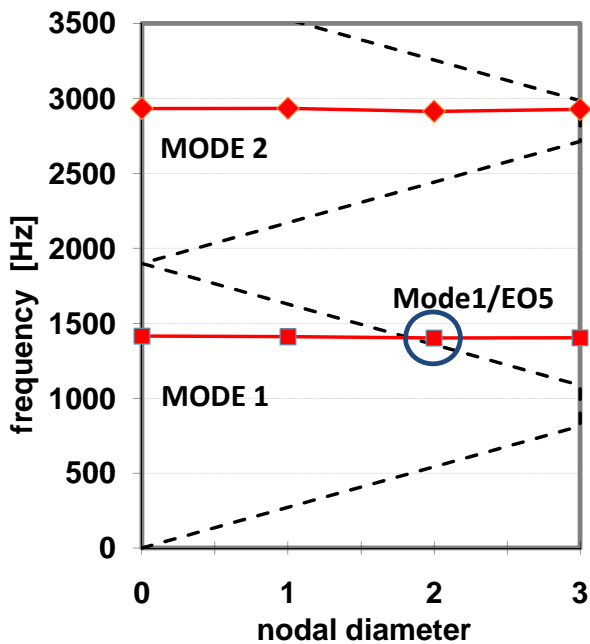
Figure 2.5.: Impeller A8C41 Campbell diagram.



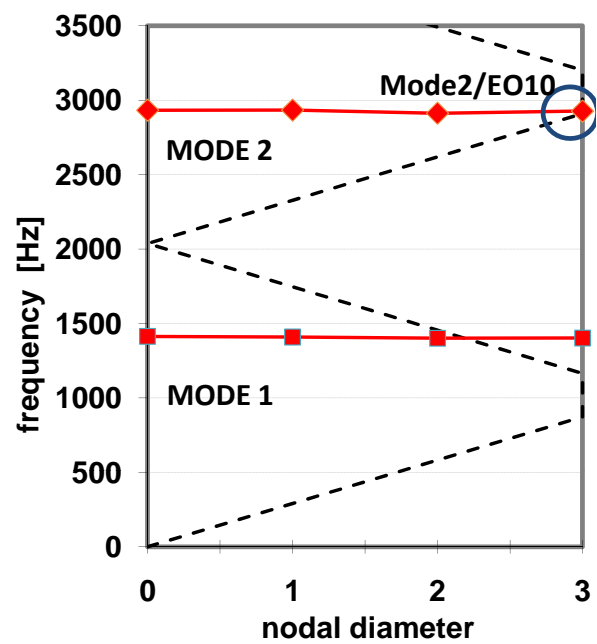
(a) Mode1/EO6 at 13500rpm.



(b) Mode2/EO12 at 14370rpm.



(c) Mode1/EO5 at 16250rpm.



(d) Mode2/EO10 at 17400rpm.

Figure 2.6.: Dispersion diagrams.

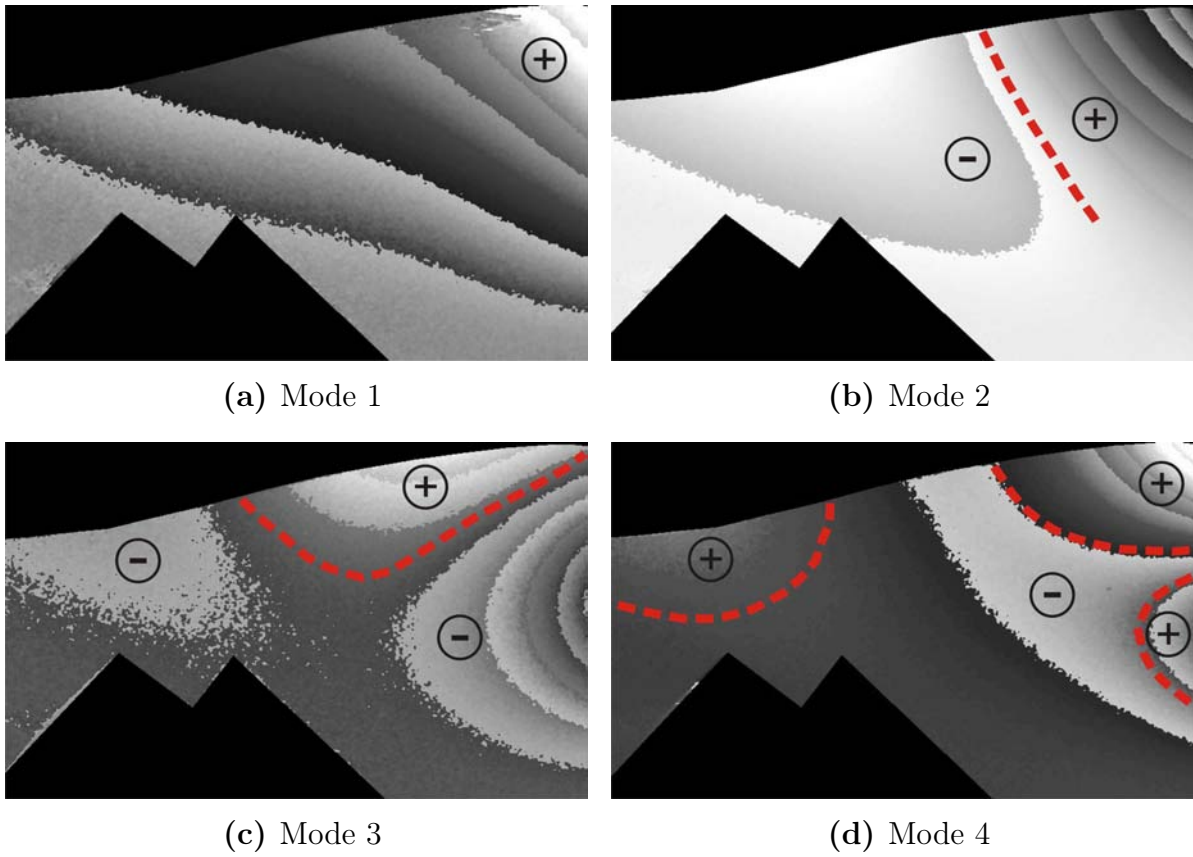


Figure 2.7.: Main blade Mode 1 – 4 modal shapes.

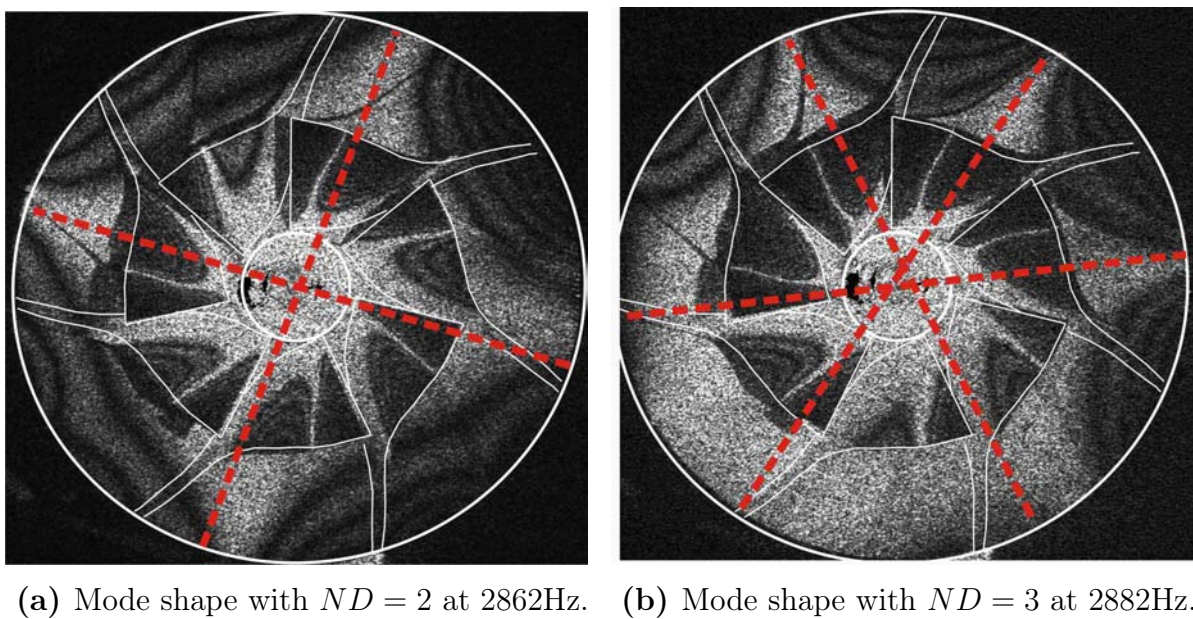
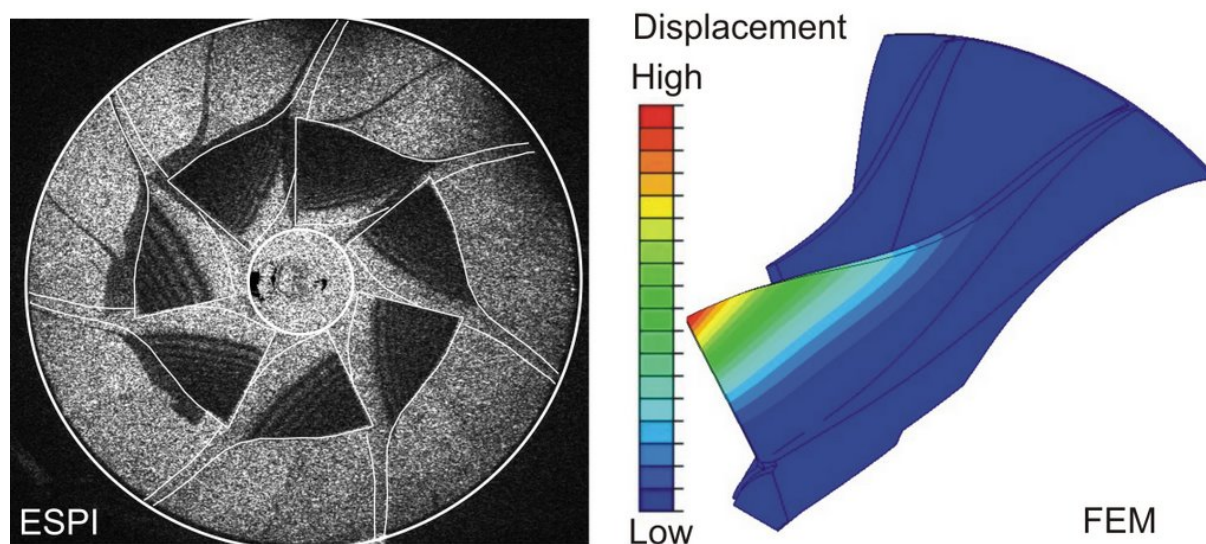
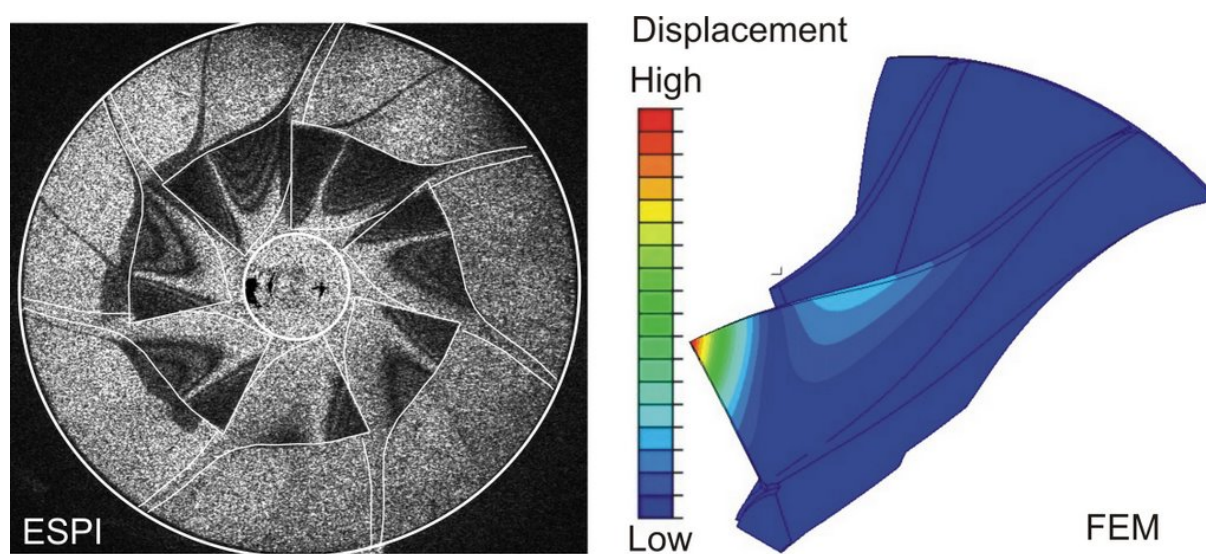


Figure 2.8.: ESPI visualization of Mode 2 nodal diameters.



(a) Mode 1



(b) Mode 2

Figure 2.9.: Modal shape comparison between ESPI and FEM.

2.4. Data Transmission and Acquisition

One of the key elements of this research work was the design of the signal transmission and acquisition systems. On-impeller signal acquisition necessitates the transmission of signals from a rotating frame of reference to the stationary data acquisition boards. Moreover, the following requirements had to be met: (1) low noise to signal ratio was considered to be crucial, (2) approximately 100 channels were considered to be necessary for a meaningful impeller sensor instrumentation, (3) the transmission system was expected to be capable of handling signals from different sensor sources, i.e. strain, pressure or temperature.

Low noise to signal ratio was achieved by employing a transmitter where mercury is encapsulated in chambers and acts as a contact between the rotating and the stationary element. Conventional slip rings generate comparatively high noise to signal ratio due to brush contacts and require lubrication for cooling purposes at the required operational speeds. This was not the case with the mercury transmitter. The signal quality in combination with the installed data acquisition system was judged to be sufficiently good so that signal amplification was not required.

In order to facilitate roughly 100 transmission channels it was decided to design a multiplexer that could be mounted on the impeller. Approaching the problem this way it was possible to reduce the cost of the transmission system considerably, considering the price per channel. The analog multiplexer, shown in figure 2.10, was electronically equipped such that all signals coming from the impeller sensors were structured into groups of a few sensors. During the measurements the groups were scanned sequentially. The multiplexer unit could be easily plugged into the impeller as shown in figure 2.10(b). Moreover, the design of the multiplexer unit was adapted to the need to transmit different signal sources. The intended flexibility allowed to change between applications with strain gauges or pressure sensors.

A schematic illustration of the signal transmission and data acquisition system is shown in figure 2.11. The rotary transmission system is used to transmit two types of signals: (1) data coming from the sensors and (2) control signal and power supply for the multiplexer. The latter feeds the multiplexer and sets the transmission channel through digital coding. In the non-rotating

frame of reference a data acquisition system was installed capable of digitizing each analog signal with a temporal resolution of 200kHz and an amplitude resolution of 24bit.

2.5. Transient Measurement Approach

During strain or pressure measurements stress levels due to resonant vibration were expected to be sufficiently high to potentially cause high cycle fatigue failure. Therefore, in order to overcome the risk of steady measurements, transient measurements were performed with respect to rotational speed, i.e. to sweep through the resonant speed regime with constant change in shaft speed. By doing so the blade was effectively excited by a forcing function of constantly changing frequency, expressed by the sweep rate. Shaft speed control was an integral part of the data acquisition system that consisted of a routine that was dedicated to control the shaft speed while performing an automatic channel switch on the multiplexer. In order to achieve near steady state response conditions the sweep rate has to be chosen sufficiently low in order to allow the structure to build up maximum response. *Ewins* [21] references the maximum linear sweep rate S_{max} prescribed by ISO standards

$$S_{max} = 3.6 f_{res}^2 \zeta^2 \left[\frac{\text{Hz}}{\text{s}} \right] \quad (2.1)$$

Using realistic values for resonant frequency, f_{res} , and critical damping ratio, ζ , for the datum application yields maximum sweep rates of approximately 7 Hz/s. Figure 2.3 shows the compressor map and the operating lines for distinct throttle settings along which blade response was measured.

For any of the measurement cases performed the data acquisition was structured into two steps. In a first step sweeping was performed along the entire operating line up to 18000rpm. In this case the sweep rate was by a factor of 4 higher than the one stated in equation 2.1. In the first step the intention was to identify resonant crossings. With respect to blade pressure measurements this enabled to capture pressure fluctuations along the entire operating line.

In a second step, refined sweeping was performed with the above mentioned maximum sweep rate in order to acquire data across a resonant response upon which data analysis was subsequently performed. Sweeping was carried out

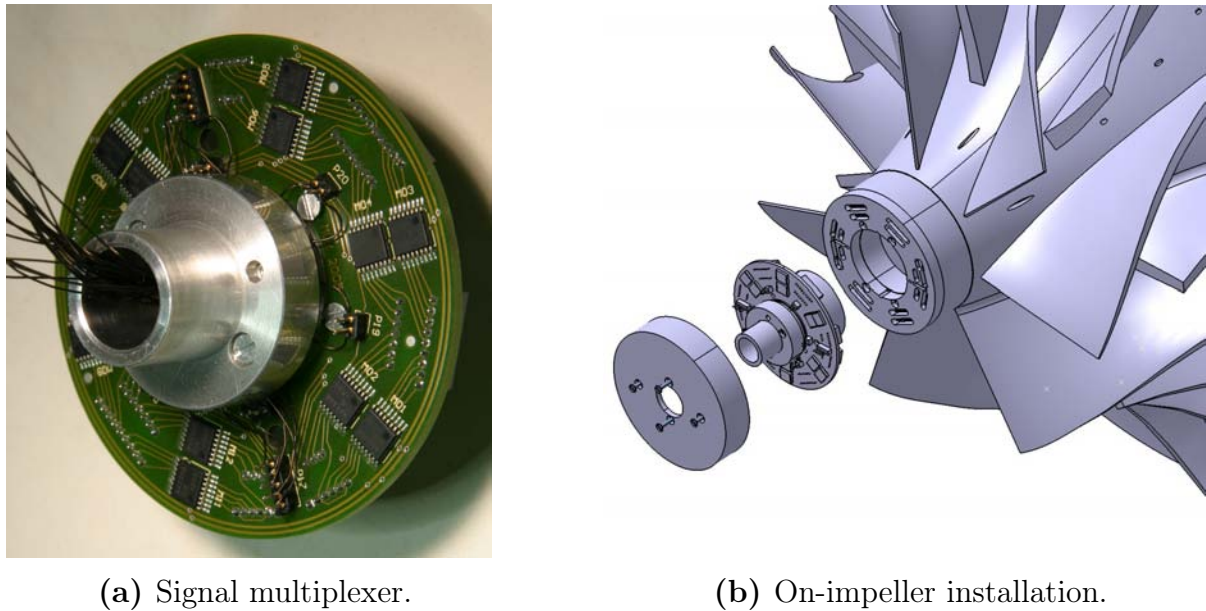


Figure 2.10.: Signal multiplexer mount.

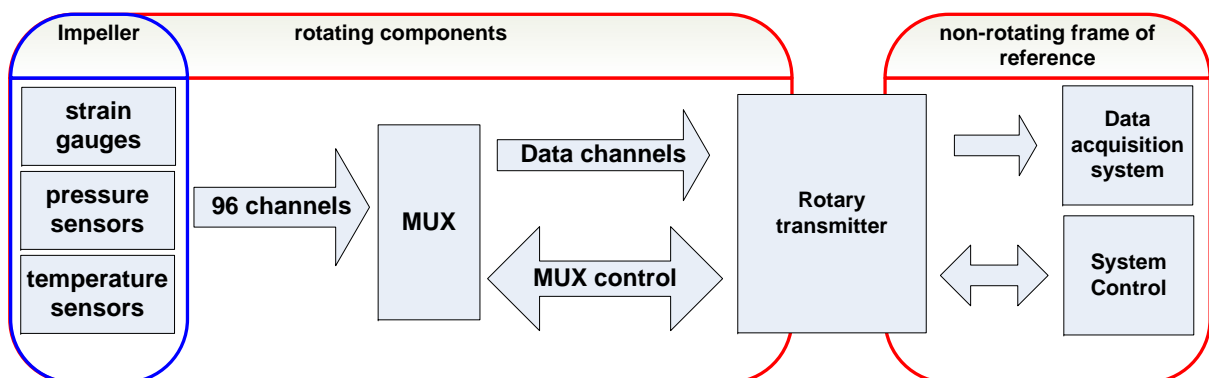


Figure 2.11.: Signal transmission and acquisition principal.

for ascending and descending rotational speeds. Strain and pressure signals acquired this way enable to compute modal damping as well as the evolution of aerodynamic work during resonance.

2.6. Measurement Cases and Pressure Levels

Measurement Cases

Measurements were performed for two differently instrumented impellers. In the case of Impeller 1 only strain gauges were installed on the blades according to figure 3.7(a). In addition piezo actuators were installed on the back side of the impeller, shown in figure 3.7(b), in order to provide dynamic excitation during near vacuum measurements. Measurements performed with this configuration were aimed at measuring strain and deriving damping properties.

In the case of Impeller 2 strain gauges and pressure sensors were installed on the impeller blades as shown in figure 3.2(a). Measurements with this configuration enabled a simultaneous acquisition of blade strain and unsteady pressure acting on the blade surface. Table 2.3 provides an overview on the measurement cases that were realized for the two instrumentation cases.

Case Dependent Inlet Pressure Conditions

Table 2.4 gives an overview on the range of pressure settings during the measurements. The pressure was varied as an independent parameter thereby allowing strain and pressure measurements at discrete pressure levels. The maximum inlet pressure is limited by the available power transmitted from the motor and decreases as the shaft speed increases.

Resonance Conditions					
screen	3 lobe	4 lobe	5 lobe	6 lobe	5 lobe
resonance case	Mode1/EO6	Mode2/EO12	Mode1/EO5	Mode1/EO6	Mode2/EO10
RPM _{res}	13500	14370	16250	13500	17400
Impeller 1					
operating line	OL1/OL2	OL1/OL2	OL1/OL2	OL1/OL2	OL1/OL2
pressure					
strain	✓	✓	✓		
damping	✓	✓	✓		✓
Impeller 2					
operating line	OL1/OL2/OL3	OL1/OL2/OL3	OL1/OL2/OL3	OL1/OL2/OL3	OL1/OL2/OL3
pressure	✓		✓	✓	
strain	✓		✓	✓	
damping	✓		✓	✓	

Table 2.3.: Measurement matrix for Impeller 1 and Impeller 2

screen	3 lobe	4 lobe	5 lobe	6 lobe	5 lobe
resonance case	Mode1/EO6	Mode2/EO12	Mode1/EO5	Mode1/EO6	Mode2/EO5
RPM _{res}	13500	14370	16250	13500	17400
inlet pressure p_{inlet}	0.1 ... 0.8bar	0.1 ... 0.8bar	0.1 ... 0.5bar	0.1 ... 0.8bar	0.1 ... 0.4bar

Table 2.4.: Case dependent inlet pressure conditions.

3. Impeller Instrumentation

Two types of sensors were applied on the blade surface. First of all flush-mounted pressure sensors were used to measure the unsteady pressure distribution along the blade mid-height. This quantity represents the forcing function of the forced response problem. Secondly, strain gauges were used to measure blade vibratory motion. This quantity represents the structural response due to external forcing. Throughout the work data reduction was performed on the alternating component of both of the signal types.

3.1. Fast Response Pressure Sensors

Unsteady pressure measurements on rotating impeller blades impose a number of requirements on pressure sensor design. On the one hand pressure sensors must be designed such that installation on impeller blades is possible and must sustain the harsh environment experienced in a rotating system. On the other hand pressure sensors must exhibit sufficient sensitivity to capture comparatively low pressure fluctuations on the blade surface. For example, *Manwaring et al.* [54] report on the difficulties encountered in measuring unsteady pressure on the blade surface. In their instrumentation sensor failure was encountered due to excessive centrifugal loads and strain due to vibration transmitted from the blade into the sensor, commonly referred to as sensor base strain.

In order to fulfil requirements of a suitable pressure sensor, the design of a new pressure sensor that can be mounted on impeller blades was accomplished. This design was based on previous in-house work undertaken in the field of fast aerodynamic probes. In particular this relates to the application of piezo-resistive semiconductors in work by *Gossweiler* [23], *Kupferschmied* [45] and *Pfau et al.* [60]. Figure 3.1(a) depicts the final design of the applied blade pressure sensor which in its core consists of a pressure sensitive die packaged into a carrier and connected to a flexible connector. The pressure sensitive die is a piezo-resistive semiconductor used for the manufacture of in-house

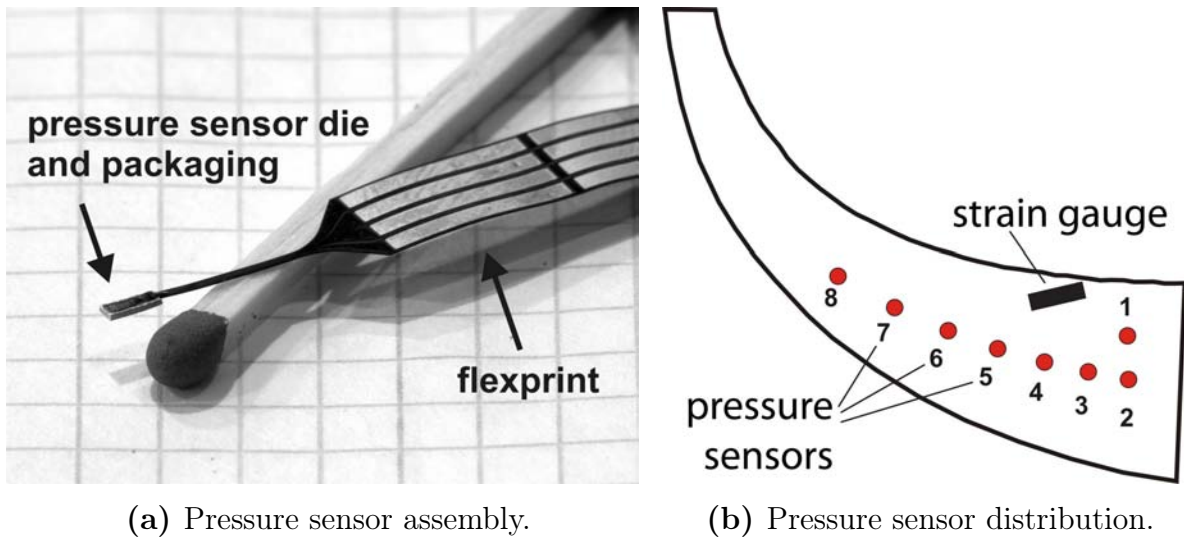
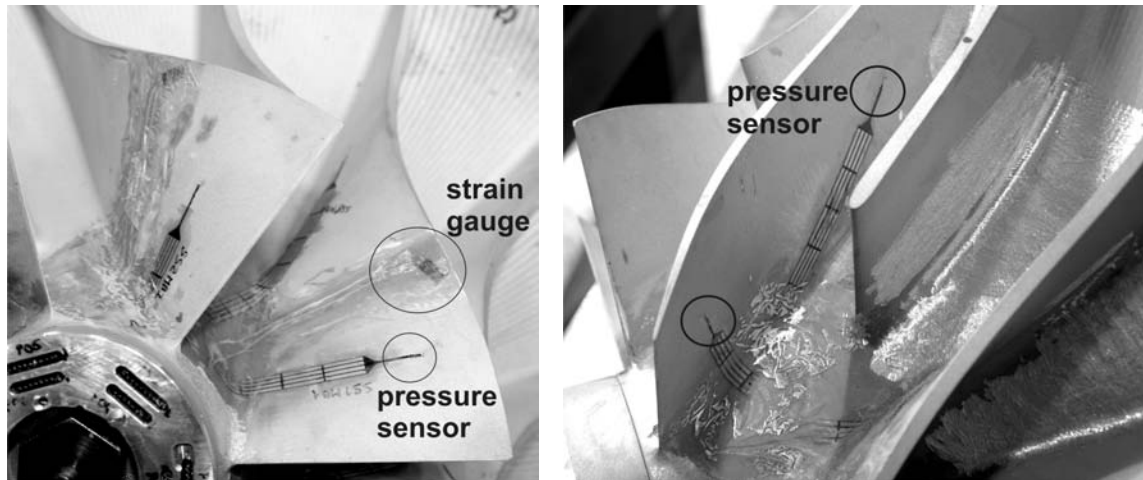


Figure 3.1.: Impeller pressure sensor and on-blade distribution.

fast response aerodynamic probes (FRAP) and is bonded to the flexible connector. Within the packaging the die is fixed and sealed using silicon such that it functions as an absolute pressure sensor. The sensitive die surface is covered by a thin layer of silicon which acts as a protective layer. The applied packaging technique enabled sensor miniaturization with dimensions as small as $1.1 \times 0.35 \times 3\text{mm}$ and with the potential for further reduction. The primary need to achieve these dimensions stems from the need to install the sensor on impeller blades with a thickness measuring only a few millimeters. Therefore, pockets that are electro-discharge machined into the blade surface for sensor placement can protrude only a limited depth into the material. Similar restrictions are encountered in axial machines for comparatively small blades, where the problem of sensor size can be partially overcome by directly placing the pressure sensitive die into a blade pocket, termed the 'chip-on' technique as described by *Ainsworth et al.* [2]. However, this necessitates removable blades where the surface and sensor pockets can be easily accessed using a microscope. In the case of an impeller, blades cannot be treated in this way, which significantly hinders the installation process and the three-dimensional blade shape imposes further complexity as shown in figures 3.2. Sensors have therefore to be packaged as a first step and then installed onto the blade surface. As can be observed from the figures, the pressure sensors are flush mounted into the pockets and the flexible connector is glued onto the blade surface.



(a) Pressure sensors and strain gauges. (b) Pressure sensors on pressure side.

Figure 3.2.: Impeller pressure and strain gauge instrumentation.

A total of 16 sensors were installed in pairs with eight sensors on each blade side. Figure 3.1(b) illustrates the sensor distribution in the meridional view. The sensors are installed in the inducer portion of the impeller at mid-height. The sensor distribution shown was chosen in order to allow for measurements of the forcing function that excites the first main blade mode. Resonant excitation occurs within the inducer portion of the blade forcing the blade to undergo its highest displacement amplitudes. On the circumference the sensors had to be distributed among all blades. This was necessary in order to reduce the risk of potential blade damage during operation resulting from excessive stress concentration. Sensor pockets were machined into a part of the material which suffers the highest stresses during resonance, thereby introducing locally additional stresses due to the notch effect. By redistributing sensors on all blades this effect could be reduced.

Overall the current sensor design was found to satisfy the problematic installation criteria. Moreover, a damaged sensor could be easily replaced within a few hours. During operation, the pressure sensors were found to be extremely robust, since none of the sensors failed due to common problems such as loss of electrical contact, membrane damage or rupture in any part of the sensor. Measurements were undertaken in a pressure range from 0.2-0.9bar, maximum centrifugal g-forces of 50k were experienced and vibratory stressing was tolerated as the blades underwent resonant vibration.

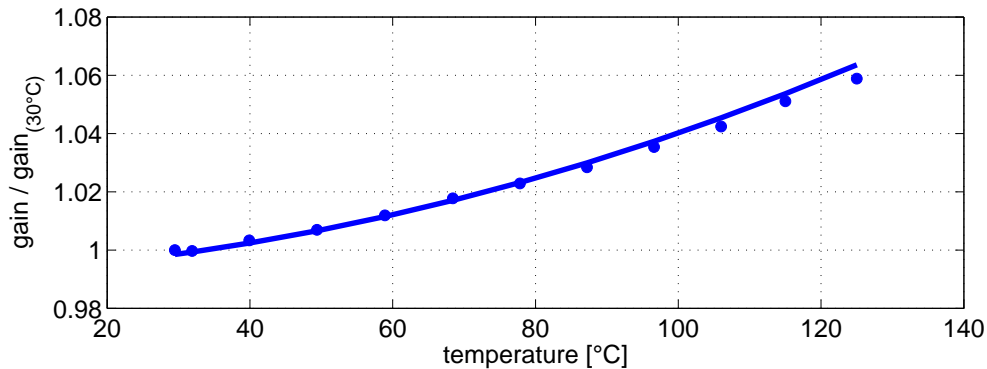


Figure 3.3.: Pressure sensor gain dependence on temperature.

3.1.1. Temperature Effects

Owing to the nature of the sensors, their pressure signal is affected by systematic error sources i.e. temperature effects, g-forces and non-linearity. Ideally, temperature and g-force effects can be calibrated in order to reduce their contribution to the measurement uncertainty. With respect to temperature, calibration in a pressure and temperature controlled chamber is required, where the pressure signal can be calibrated for a number of temperature steps. This procedure is common practice for aerodynamic probe calibrations where piezo-resistive semiconductors are employed. In the current project the necessary installations to perform simultaneous pressure and temperature calibration on an entire impeller were not available. Contamination of the pressure signal due to temperature effects had therefore to be accounted for in terms of uncertainty contribution. Figure 3.3 relates the change in gain depending on the sensor temperature. During operating pressure sensors were not exposed to temperature levels exceeding 100°C. This assessment was based on CFD. It can therefore be concluded that changes in gain due to temperature effects are of the order of 4%.

3.1.2. Centrifugal Force Effects

Centrifugal forces were shown to affect the *steady* component of the pressure signal. The works by *Dénos* [13], *Kurtz et al.* [46] and *Ainsworth et al.* [2] outline this phenomena. In the latter, the effect of g-forces on the steady portion of the signal was found to be the most significant among all the influences on the pressure signal. Centrifugal forces acting on the pressure sensitive membrane effectively alter the offset value of the linear characteristic. The gain

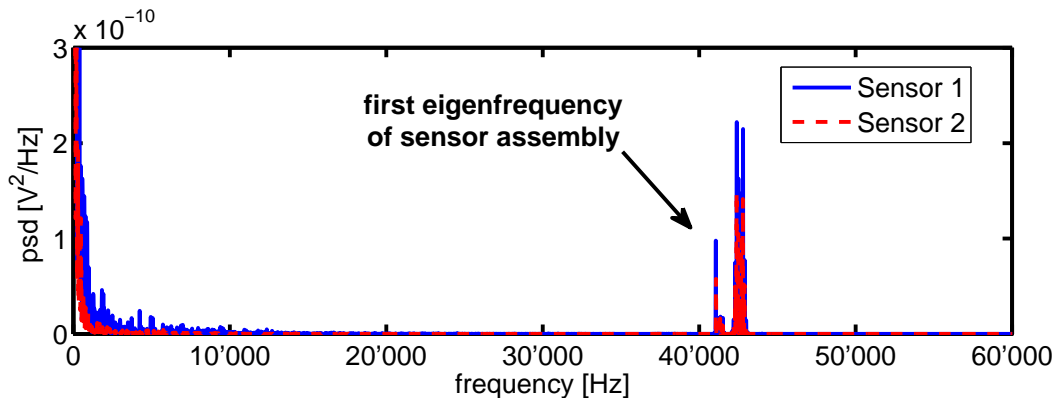


Figure 3.4.: Pressure sensor response during shock tube experiment.

value retains its amplitude and does not need to be calibrated with respect to centrifugal forces. Therefore, the *unsteady* part of the pressure signal is not affected and does not require calibration. For this reason, in the research work presented here, only the unsteady part of the pressure signal is presented and discussed.

3.1.3. Frequency Bandwidth

The frequency bandwidth of the applied pressure sensors was obtained from shock tube experiments. Here, a sensor was flash mounted on a 3mm shaft and installed within a tube. A pump was used to evacuate the tube until the burst of an elastic seal was initiated causing a step increase in pressure within the tube. The response to the step excitation on the pressure sensor was measured and is shown in figure 3.4 for two different sensors. The results show both sensors responding at 42kHz which corresponds to the first eigenfrequency of the sensor assembly. The first eigenfrequency of the membrane of the pressure die used in this work is in the range of 800kHz. Since the die is covered with silicon for packaging reasons, the added mass on the sensitive membrane reduces the overall bandwidth to approximately 40kHz. This gives a considerable margin with respect to the expected maximum frequencies during measurements which are in the range of 10kHz.

3.1.4. Sensitivity to Vibratory Strain

Within the packaging of the sensor the silicon die must in some way be mechanically connected to the blade material. As the blade vibrates, mechanical

strain can be transmitted into the pressure sensitive die and might be experienced as a change in the measured pressure. This source of contamination was of particular interest in this project since forcing function measurements in the vicinity of and during blade resonant vibration were intended. In order to assess the magnitude of stress driven error the impeller was bench mounted and the blades were periodically deformed by approximately the same amplitude as they experience during resonance of the first mode. The deformation speed was quasi-static to exclude aerodynamic effects. The signal from the pressure sensor and a strain gauge that were mounted on the same blade, as shown in figure 3.2(a), were recorded simultaneously. This way it was possible to relate the parasitic component of the pressure signal due to vibration to a meaningful quantity. Figure 3.5 shows the signal for both the strain gauge and the pressure sensor undergoing periodic variation. The procedure was repeated for a number of pressure sensor and strain gauge pairs, showing that overall the stress induced voltage within the pressure sensitive die is approximately an order of magnitude smaller than the measured change in voltage across the strain gauge. In order to assess the impact of these findings on the pressure measurement the following has to be considered: during forcing function measurements two measurement conditions have to be strictly distinguished, which are (1) off-resonance measurements and (2) resonance measurements. In the first case, blade vibration is not present and strain is therefore not induced into the pressure sensitive die. In this regime the unsteady pressure causes a voltage variation approximately ten times higher than the strain voltage shown in figure 3.5. It can therefore be concluded, that strain induced effects are insignificant during off-resonant signal acquisition. This however is not the case during resonant measurements, where the contribution from deformation effects might amount to as much as 10% of the overall pressure signal.

3.1.5. Pressure Signal Calibration and Linearity

Pressure signal calibration was performed within the test facility prior to each run. To do so, the pressure within the facility was changed within a range of 0.2-0.9bar, which corresponds to the intended operating regime during rotational operation. To relate pressure and sensor behavior a linear relation was used where the unknown gains and offsets had to be calibrated.

Piezo-resistive semiconductors exhibit a linear response characteristic within

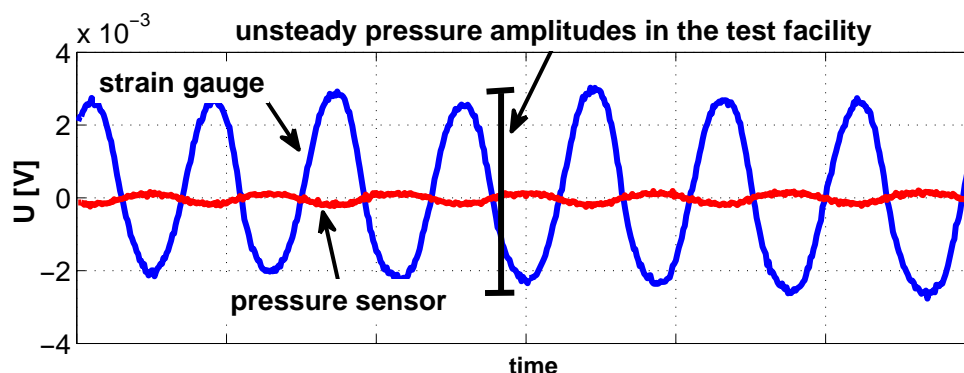


Figure 3.5.: Pressure sensor and strain gauge response to blade deformation during on-bench testing. The pressure sensor is affected by blade movement.

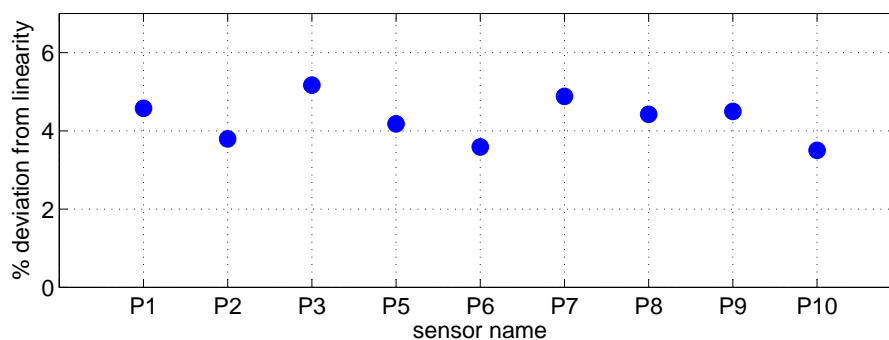


Figure 3.6.: Change in gain as pressure increases from 0.3bar to 0.9bar.

a limited range depending on the design of the pressure die. For the datum sensors linearity is guaranteed for a maximum pressure difference of 0.4bar. However, on-impeller pressure measurements require a maximum pressure range of 0.8bar and effects on deviation from linearity have to be accounted for. In the datum application the gain varies with the applied pressure as shown in figure 3.6 for a number of pressure sensors that were mounted on the impeller blades. The figure illustrates the change in gain for a linear calibration of approximately 0.9bar in comparison with a calibration of about 0.3bar. On average, the gain varies by roughly 5%. The effect is systematic and can be accounted for each sensor individually, thereby reducing the influence on the uncertainty. In practice this is done by monitoring the inlet pressure upstream of the impeller during measurements which is then used to adjust the gain to the appropriate level.

3.2. Dynamic Strain Gauges

3.2.1. Strain Gauge Installation

Dynamic strain gauges were used to measure blade vibratory strain. All gauges were applied to the suction surface of the blade due to better accessibility. Two different sensor instrumentation cases were investigated in this study. An overview on the impeller instrumentation cases and the corresponding measurement cases were given on page 35.

In the first case, Impeller 1, strain gauges only were applied to the blade surface where each blade was equally instrumented with three strain gauges, shown in figure 3.7(a). The chosen strain gauge distribution was aimed to ideally capture strain of the first four modes of the main blade and was intended to study and gain experience in the measurement of damping. Gauge positioning on the blade surface was optimized using the procedure reported by *Szwedowicz et al.* [78]. In short, the gauge positioning routine requires modal analysis results from FEM which contain non-dimensional mode dependent strain quantities. An optimization routine uses this information in a generic algorithm to identify ideal gauge positions based on the criteria of sensitivity, orthogonality, gradient and distance.

In a second case, Impeller 2, each main blade was equally instrumented with a single strain gauge that could capture response from the first two modes. Strain data from this experiment was used to obtain maximum strain, damping and in conjunction with unsteady pressure measurements the aerodynamic work. Moreover, strain gauges were used to assess pressure sensor sensitivity to blade deformation which introduces a systematic pressure measurement error.

The installation of strain gauges and the lead wires on the surface was achieved through the application of an epoxy adhesive. The lead wires were covered with a layer of fiber glass cloth. Generally, blade instrumentation introduces mistuning due to non-uniform application of adhesive and fiber glass cloth. In addition flush-mounted pressure sensors require pockets being machined into the blade surface which can be considered as an other source of blade mistuning. In any case, blade mistuning cannot be quantified, however its effect on the blade strain will be presented.

3.2.2. Resolution and Calibration

From the electronic perspective, the conventional Wheatstone bridge configuration could not be employed. Instead, a constant current power supply was used with a step response time of 60kHz. The current was optimized for optimal noise to signal ratio, taking expected strain and heating into consideration. The strain was calculated using the following equation

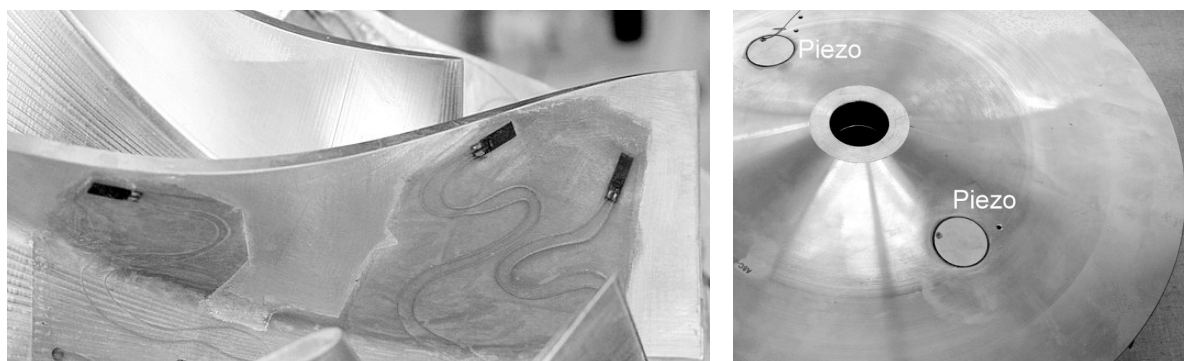
$$\epsilon = \frac{U(t)}{U_0} \frac{1}{GF} \quad (3.1)$$

where $U(t)$ is the measured voltage across a strain gauge and U_0 is the reference voltage due to strain gauge resistance of 350Ω and the constant current. The gauge factor GF represents the link between the strain a gauge experiences and the associated change in resistance. Given the above equation and the 24bit data acquisition system the strain resolution was $\Delta\epsilon_{min} = 0.08\mu m/m$. Depending on the type of the impeller sensor configuration either both signal components, i.e. static and dynamic, or only the dynamic component were recorded. For this research only the alternating component is of relevance since it represents strain due to vibratory motion. Strain gauge calibration was not performed in this study and gauge factors for the used foil nickel-chromium alloy gauges were provided by the manufacturer. A calibration approach for high sensitivity strain gauges i.e. semiconductor strain gauges, was reported by *Haupt* [27] and *Jin* [38]. In their work semiconductor strain gauges were found to exhibit considerable gauge factor variation and had to be calibrated using conventional foil gauges placed closed to them. Foil gauges were considered to have low gauge factor variation and could be used as a reference.

3.3. Piezoelectric Actuators

The use of piezoelectric actuators was crucial during measurements of modal shapes using speckle interferometry and during measurements of material damping. In both cases a source of blade excitation was required that was sufficiently strong to cause measurable blade resonant response and was also independent of the surrounding pressure conditions.

The piezoelectric actuators were mounted on the back side of the impeller shown in figure 3.7. During the experimental phase it was found that the



(a) Strain gauges mounted on impeller main blade. (b) Piezo actuators mounted on back side of impeller.

Figure 3.7.: Impeller strain gauge and piezo instrumentation.

impeller back wall is the ideal location to supply mechanical excitation for the following reasons. The impeller disk is a relatively thin structure in the inducer part of the impeller and acts as a coupling between all blades. As mechanical excitation is introduced into the disk all blades can be excited simultaneously. The experience with this approach were satisfying and data could be obtained as intended. A different approach was reported by *Jeffers et al.* [37] and *Kielb and Abhari* [40] where piezoelectric actuators were mounted directly on turbine blades. For such an installation lower excitation voltages can be realized to achieve the same blade displacement, however, the excitation would be restricted to the instrumented blade and potentially its neighboring blades. The drawback of this approach is an inevitable introduction of parasitic damping due to the actuator itself which has to be accounted for through calibration.

Some general experiences should be outlined here. During the experiment using the ESPI technique it was noted that as resonance was approached the response of those blades which were closer to the piezo location was observed first. As resonance was reached however, the modal shape characteristic interferometry pattern was equally pronounced on all blades. Examples for resonant response are shown in figures 2.9 and 2.8.

During material damping measurements strain gauges were placed on the impeller blades measuring strain caused by piezoelectric excitation. It was noted that the measured response amplitude decreased for blades further away from the piezo. The reduction in amplitude was not found to correlate with damping i.e. increase in distance did not generally cause a decrease or increase in damping.

Overall, making use of piezoelectric actuators on the back side of the impeller was found to be an effective way to study frequency, amplitude and modal shape response of an impeller. In a different experiment not reported here, a displacement sensor was used to measure blade displacement during resonance. The sensor was placed at a number of blade positions normal to the blade surface allowing to capture the modal shapes. This approach allowed to quickly verify the intended frequencies.

3.4. Uncertainty Analysis

3.4.1. Algorithm

The uncertainty analysis was carried out according to the recommendations outlined in the "Guide of Uncertainty in Measurements" (GUM) [36]. The method is standardized and converts in a first step all uncertainty information of the contributors into probability distributions. In a second step the overall uncertainty is derived based on the Gaussian error propagation formula. In DIN 1319-3 section 4.2 it is recommended to divide the evaluation process into four steps:

1. Development of the model, which describes the measurement problem in the form of a mathematical model.
2. Preparation of the input data and of additional information.
3. Calculation of the results and the associated standard uncertainty with the given input quantities and the given model.
4. Notification of the complete measurement result including the measurement uncertainty.

In the second step the uncertainty of each contributor must be determined and then converted into a probability distribution. Based on this data the expectation value and the associated variance can be calculated. The GUM method differentiates two approaches:

- Type A: Observed statistical data collected during a measurement.

- Type B: Non-statistical data, which are known prior to the measurement.

Two types of a distribution can be applied, a normal or a rectangular distribution. If the uncertainty information is given in terms of a statistical data set then the normal distribution can be applied. If the uncertainty information is provided in terms of limits then the rectangular distribution can be applied. In the latter case the standard uncertainty u of a rectangular distribution with a known half-width a is calculated from

$$u = \frac{a}{\sqrt{3}} \quad (3.2)$$

In step 3 the partial derivatives of the model function y are calculated to obtain the sensitivity of every input quantity x_i

$$c_i = \frac{\partial y}{\partial x_i} \quad (3.3)$$

The uncertainty contribution $u_i(y)$ is calculated by a multiplication of the sensitivity coefficient c_i with the standard uncertainty of the input quantity $u(x_i)$.

$$u_i(y) = c_i \cdot u(x_i) \quad (3.4)$$

The law of error propagation is given as follows:

$$u(y) = \sqrt{\sum_{i=1}^n u_i^2(y)} \quad (3.5)$$

The GUM method uses a special term called the *expanded uncertainty*. It essentially represents uncertainty limits and was introduced to allow a comparison to other kinds of uncertainty specifications. The *expanded uncertainty* U is computed from the standard uncertainty $u(y)$ multiplied by a coverage factor k .

$$U = k \cdot u(y) \quad (3.6)$$

Generally a coverage factor of $k = 2$ is used which corresponds to a confidence level of 95%.

3.4.2. Pressure Sensor Uncertainty

The measured unsteady pressure on the blade surface can be described assuming a linear sensor characteristic. The parameters m and b represent the gain and offset, respectively.

$$p(t) = mU_p(t) + b \quad (3.7)$$

In the datum application of the pressure sensors only the fluctuating component of the pressure signal is studied. For this reason the measured pressure must be separated into the steady \tilde{p} and the unsteady component p' .

$$p(t) = m \left(\tilde{U}_p + U'_p(t) \right) + b \quad (3.8)$$

$$\tilde{p} + p'(t) = \left(m\tilde{U}_p + b \right) + mU'_p(t) \quad (3.9)$$

Omitting the notations for the unsteady component, the measured unsteady pressure can be computed according to the following equation.

$$p = K_T \cdot m_{corr} U_p \quad (3.10)$$

The factor K_T represents the effect of temperature that must be taken into account in a uncertainty analysis. The equation is only valid for measurements at off-resonance conditions. In the case of measurements at resonance the factor K_S must be included in the equation.

$$p = K_T \cdot K_S \cdot m_{corr} U_p \quad (3.11)$$

The corrected gain factor m_{corr} is the result from accounting for effects due to non-linearity of the piezo-resistive semiconductor used at pressures outside the linearity range. The calibrated gain m_{cal} is obtained from calibrating the sensor signal.

$$m_{corr} = m_{cal} A_1 p_{inlet} + m_{cal} A_2 \quad (3.12)$$

$$A_1 = \frac{K_L - 1}{p_1 - p_2} \quad (3.13)$$

$$A_2 = 1 - \frac{K_L - 1}{p_1 - p_2} p_2 \quad (3.14)$$

In order to account the effect of non-linearity the factor K_L must be used. The formulations of linear fit factors A_1 and A_2 were obtained from adjusting

the gain to the known overall pressure level, in this case p_{inlet} . The pressures p_1 and p_2 represent two pressure levels at which gain was calibrated, i.e. at maximum and minimum pressure of the intended measurement range. Results on the uncertainty analysis are summarized in table 3.1 for the off-resonance case and table 3.2 for the resonance case. During the analysis the worst case scenario was estimated i.e. assuming that effects from different sources exert their strongest influence.

Uncertainty at off-resonance: The overall uncertainty was estimated to be $\pm 5.2\%$ full scale. The major contributor with $\approx 60\%$ of the overall uncertainty is temperature which affects the sensor gain. The second strongest contributor with $\approx 30\%$ stems from gain calibration and accounting for sensor non-linearity as outlined previously.

Uncertainty at resonance: The overall uncertainty was estimated to be $\pm 11\%$ full scale. Strain effects from blade vibration were included in the uncertainty analysis and were found to contribute 77% to the overall uncertainty limit.

3.4.3. Strain Gauge Uncertainty

Strain measurement signal is subject to a number of systematic error sources. To start with, (1) temperature effects and (2) effects based on the gauge factor should be considered. The former is referred to as thermal output and affects only the static component of the strain signal. As mentioned above this quantity is not considered here. The gauge factor is subject to variation and also affects the dynamic component of the signal. According to the manufacturer's technical note [81] on this subject the effect of temperature on the gauge factor is less than 1% for a temperature of 100°C . Errors due to transverse sensitivity originate from strains acting on the gauge normal to its measurement axis. An estimation of this error is given in the manufacturer's technical note [80], resulting in a uncertainty of 3% . The measured strain is obtained from the following equation

$$\epsilon = \frac{U}{R_0 I} \frac{1}{GF} K_{TS} \quad (3.15)$$

where U represents the measured voltage for a constant power supply I and strain resistance R_0 . Results for the uncertainty analysis are given in table 3.3

Quantity	Symbol	Uncertainty	Contribution
calibrated gain	m_{calib}	0.5%	3.5%
linear fit factor	A_1	35%	8.1%
linear fit factor	A_2	1.3%	23.8%
inlet pressure	p_{inlet}	0.13%	0.2%
measured voltage	U_p	0.54%	4.1%
temperature effect	K_T	2.08%	60.3%
pressure	p	5.2% full scale	
non-dim. pressure	p/p_{inlet}	5.2% full scale	

Table 3.1.: Pressure measurement uncertainty at off-resonance.

Quantity	Symbol	Uncertainty	Contribution
calibrated gain	m_{calib}	0.5%	0.8%
linear fit factor	A_1	35%	1.9%
linear fit factor	A_2	1.3%	5.4%
inlet pressure	p_{inlet}	0.13%	0.2%
measured voltage	U_p	0.54%	0.9%
temperature effect	K_T	2.08%	13.8%
strain effect	K_S	4.9%	77.0%
pressure	p	11% full scale	
non-dim. pressure	p/p_{inlet}	11% full scale	

Table 3.2.: Pressure measurement uncertainty at resonance.

Quantity	Symbol	Uncertainty	Contribution
measured voltage	U	0.54%	8.0%
gauge resistance	R_0	0.16%	0.7%
transverse strain	K_{TS}	1.73%	81.4%
feeding current	I	0.17%	0.8%
gauge factor	GF	0.58%	9.0%
strain	ϵ	3.8% full scale	

Table 3.3.: Strain measurement uncertainty.

and were obtained assuming comparatively small strain amplitudes i.e. experienced prior to resonance. The results show that the relative uncertainty of the strain measurement is approximately 3.8% and is mainly affected by effect due to transverse stresses with a contribution of 81% to the overall uncertainty.

To put this numbers into a global context, strain measurement uncertainties can be considered to be negligible in comparison to blade-to-blade strain variation experienced due to mistuning. The measured strain varied by more than 30% when comparing gauges mounted on different blades but geometrical equal position.

4. Inlet Flow Distortion

This chapter outlines an approach to generate and to experimentally quantify inlet flow distortion. First, a modeling procedure will be presented to predict the flow conditions downstream of partially blocked grids. Second, fluid flow measurements using an aerodynamic probe will be presented. Finally, measurement results will be presented and discussed for a case without distortion screens and then compared to cases where distortion screens were used.

4.1. Generation of Inlet Flow Distortion

According to the Campbell diagram in figure 2.5 the upstream flow has to be distorted such that EO4–EO12 excitations are generated. This can be achieved through the employment of distortion screens upstream of the impeller. It is crucial to measure the flow upstream of the impeller in order to visualize the resultant conditions through the quantification of flow properties. Figure 2.2 illustrates the arrangement within the inlet section of the compressor. The main components are the screens that generate the flow distortion and the aerodynamic probe that measures the flow properties. Their upstream distance is 5 and 1.5 blade heights, respectively. The transmitter is mounted and centered using two rows of adjustable struts, i.e. 3 upstream and 4 downstream. The downstream struts are covered by symmetrical airfoils in order to avoid flow separation that would otherwise be generated across the rods. As will be shown later, the given arrangement within the inlet section creates a distinct distortion pattern.

The geometry of the installed screens is shown in figure 4.2. These are essentially made of a frame holding a wire grid with specific properties, namely the wire thickness and the mesh width. The number of lobes determines the engine order excitation number. The grids are designed such that the area ratio between the blocked and the unblocked sections is equal for all screens. As the flow passes through the grid, losses are generated that block the fluid and force the mass flow to redistribute. As a result, two zones of different

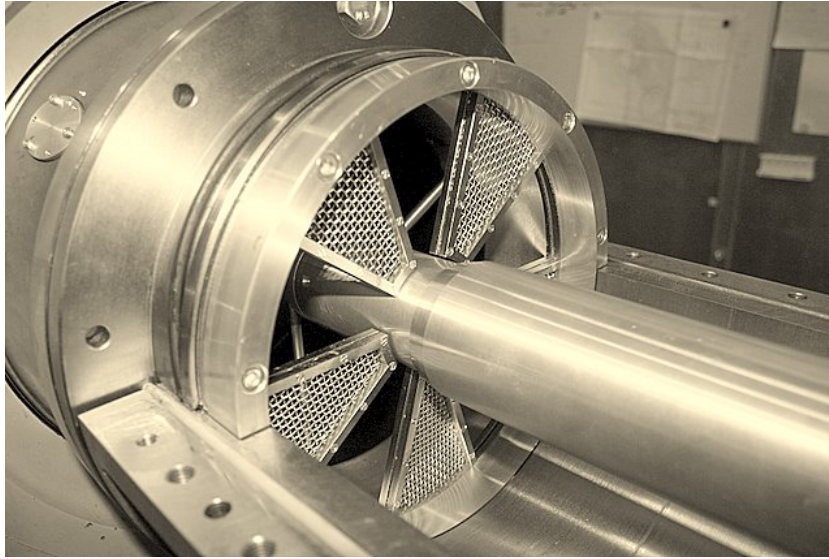
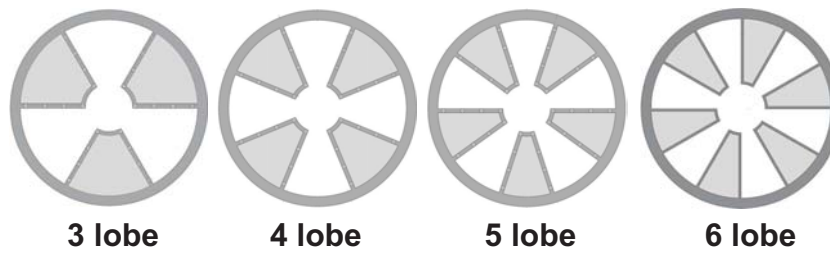


Figure 4.1.: Distortion screen installed within inlet section.



3 lobe

4 lobe

5 lobe

6 lobe

Figure 4.2.: Distortion screen geometries.

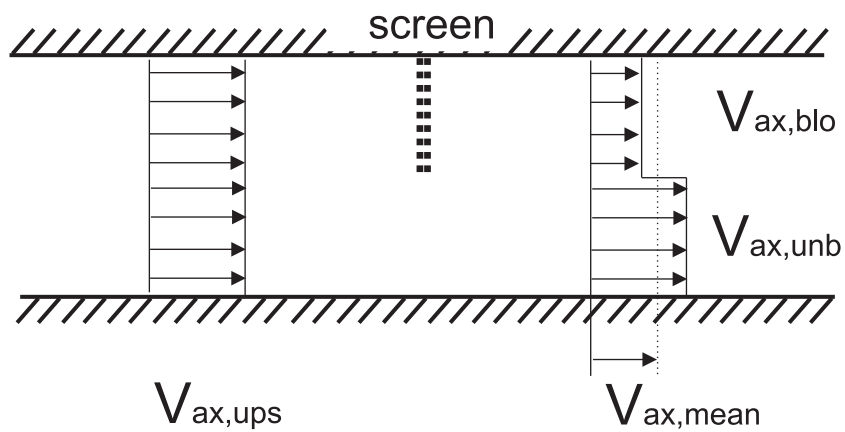


Figure 4.3.: Axial velocity definitions.

velocities and therefore total pressure are generated. The velocity distortion generated by the screens depends primarily on the uniform upstream velocity facing the screen and the grid size properties. Based on these parameters an assessment of the resultant velocities downstream of the screen can be carried out. An empirical study on the pressure drop across a grid with given wire properties was carried out by *Roach* [65] whereas *Koo and James* [43] performed measurements and calculations on the velocity distribution downstream of a blocked area for a given pressure drop. The combination of the two studies allows an assessment of the level of flow distortion due to the installed grid. To start with, *Roach* [65] examined the flow for a range of grid wires aiming to quantify pressure loss and turbulence properties. The pressure drop was found to correlate well using the following equation:

$$\frac{\Delta p}{q} = A \left(\frac{1}{\beta^2} - 1 \right)^B$$

where Δp is the pressure drop over q the dynamic head, $\beta = (1 - d/M)^2$ is the grid porosity and A depends on the Reynolds number and is given in graphical form. The parameter B is equal to unity for cylindrical wires. Further correlations are given for turbulence properties, i.e. turbulence intensity, spectra, correlation functions and length scales. These properties will not be examined in detail within this work. The study by *Koo and James* [43] examines the velocities downstream of a partially blocked flow for perpendicular and inclined grids using an analytical and a numerical approach. Measurements were conducted in order to verify the applicability of these models and were found to corroborate their applicability.

For a rapid assessment of the flow conditions downstream of a distortion screen the analytical approach was very attractive, with the advantage to simply compute a set of equations. This allowed the calculation of the far upstream velocity $V_{ax,ups}$, the downstream unblocked velocity $V_{ax,unb}$ and the blocked velocity $V_{ax,blo}$. The velocities are defined in figure 4.3. These velocities are functions of the pressure drop coefficient $\Delta p/q$ and the parameter λ . The latter represents the area split between the blocked and the unblocked part of the flow field. Figure 4.4 illustrates the velocity ratios for $\lambda = 0.5$ i.e. the blocked and unblocked area are of the same size. The unknown parameter for an arbitrarily chosen mesh is the pressure drop coefficient, which can be determined from the work by *Roach* [65].

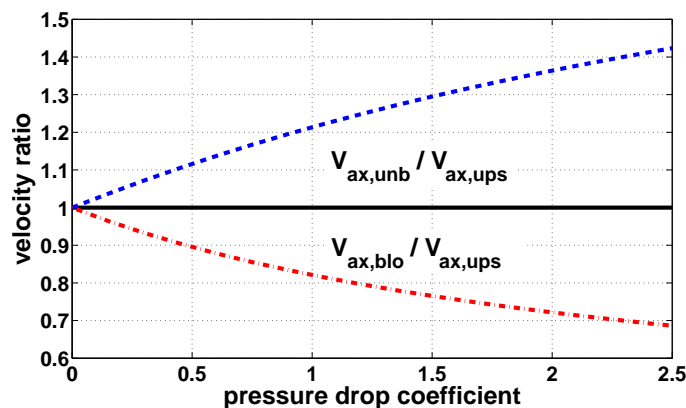


Figure 4.4.: Velocity ratio according to *Koo and James* [43].

Within the test facility the upstream axial velocity is prescribed by the operating point setting and the associated mass flow. Therefore, the expected velocity distortion is assessed for the entire mass flow range. Figure 4.5 depicts the predicted velocities upstream and downstream of the grid as a function of the non-dimensional mass flow rate. The left hand side diagram shows the velocities non-dimensionalized with the axial flow velocity at design conditions $V_{ax,des}$. The upstream axial velocity can be seen to increase nearly linearly since it is a measure of the mass flow setting. Downstream of the screen, the velocity difference between the blocked and non-blocked portion of the flow field can be seen to increase. On the right hand side the velocities are normalized using the mean axial velocity $V_{ax,mean}$. It can be observed that the velocity ratios remain constant for the entire range of mass flow settings. This quantities correspond to a pressure loss coefficient of $\Delta p/q = 0.5$ shown in figure 4.4.

4.2. Inlet Flow Field Measurement

Flow measurements upstream of the impeller were performed using a two-sensor fast response aerodynamic probe, termed FRAP. The working principals and calibration of the probe are described in detail by (*Pfau et al.* [60]). Briefly, for each measurement point the probe is revolved around the stem axis, simulating a virtual four-sensor probe and data is ensemble averaged using the one-per-revolution trigger in order to compute all necessary flow properties for a single point. The uncertainty within the total pressure is in

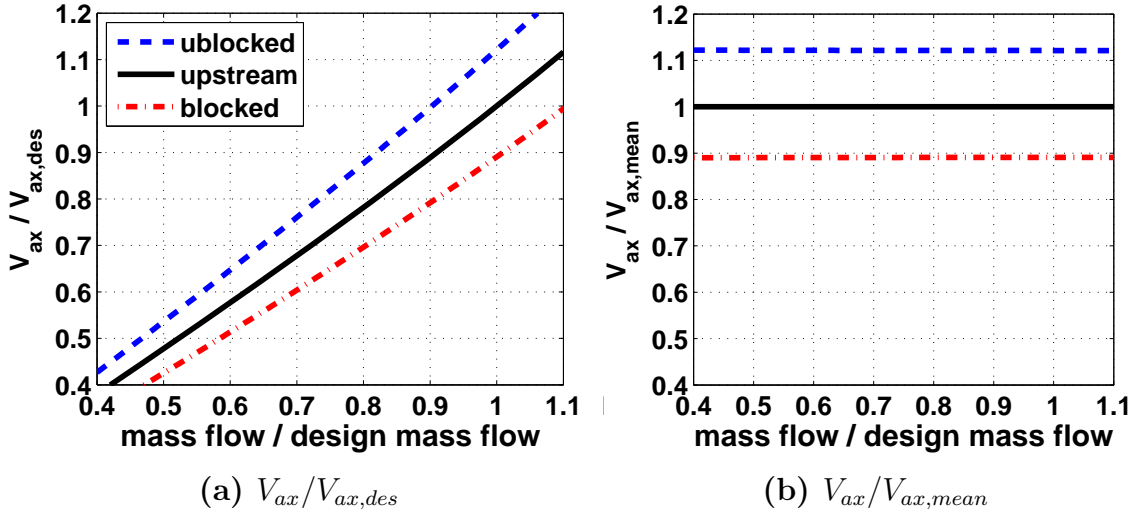


Figure 4.5.: Dependence of axial velocity distortion on mass flow.

the range of $\pm 100 Pa$, *Pfau et al.* [60]. The steady total temperature derived from the FRAP has an uncertainty of $\pm 0.5 K$ (*Kupferschmied* [45]).

Within the test section the probe was mounted in a traversing mechanism enabling automated positioning of the probe head in radial and circumferential directions. Circumferentially, traversing was limited by external struts designed to support the inlet section. White sections in figure 4.6 can be observed where measurement data is not available. The measurable inlet area consists of three sectors each with a circumferential extent of 97.5° thus covering 81% of the entire area. A typical measurement resolution consisted of 24 circumferential and 13 radial points with staggering applied near the walls and downstream of the struts where airfoil generated wakes were expected.

4.3. Flow Field without Distortion Screens

Initially, the flow field upstream of the impeller was measured with all necessary installations containing equipment to measure strain. A distortion grid was not installed. Figure 4.6 shows the time-averaged normalized axial velocity $V_{ax} / V_{ax,mean}$ and the non-dimensional pressure p_{tot} / p_{inlet} . The mean axial velocity $V_{ax,mean}$ was calculated through mass flow averaging and was found to deviate less than 2% from the axial velocity based on the measured

rig performance. The inlet static pressure p_{inlet} was measured upstream of the distortion screens in a plane shown in figure 2.2. It should be pointed out that the upstream inlet pressure is measured in a plane where the area is larger than in the place of distortion screen installation. For this reason the ratios shown later can reach values below unity.

For better visualization of the results all struts upstream of the measurement plane are indicated. As can be observed, the flow field is not uniform, with local deviation in axial velocity of $\approx 8\%$ from the mean value. Two regimes are clearly distinguishable, the bulk flow and the boundary layer at the tip of the cross section. Within the bulk flow near the hub three zones of elevated velocity $V_{ax}/V_{ax,mean} \approx 1.08$ can be observed. It can be stated that these zones are created as a result of the three upstream struts, as also seen in figure 2.2. Downstream of the four upstream struts the plot reveals wakes of comparatively small extent due to the symmetrical vanes covering the struts. Close to the hub of the central tube the boundary layers were not measured due to a required minimum probe distance from the wall. At the tip, the boundary layers are clearly developed. Also within this regime the three upstream struts exert a profound influence on the velocity distribution. The area coverage of the low momentum fluid has clearly grown.

In conclusion, although the flow was not intentionally distorted using screens, a distortion pattern was measured due to the installations housing the measurement equipment. Given this flow distribution, measurement of unsteady blade pressure identified EO2 and EO3 excitations to be contained in the upstream flow field and to amount amplitudes of the same magnitude as the intentional excitation orders.

4.4. Flow Field with Distortion Screens

Axial Velocity Distortion

The flow fields for the 3 lobe, 4 lobe, 5 lobe and the 6 lobe screen will be presented here. In all cases a mesh was used with an estimated pressure drop coefficient of $\Delta p/q = 0.5$ and area ratio of 0.5 between the blocked and unblocked portion of the grid. Due to identical design parameters between the cases, flow properties downstream of the distortion screens were expected to exhibit similar quantities in terms of velocity and pressure non-uniformity.

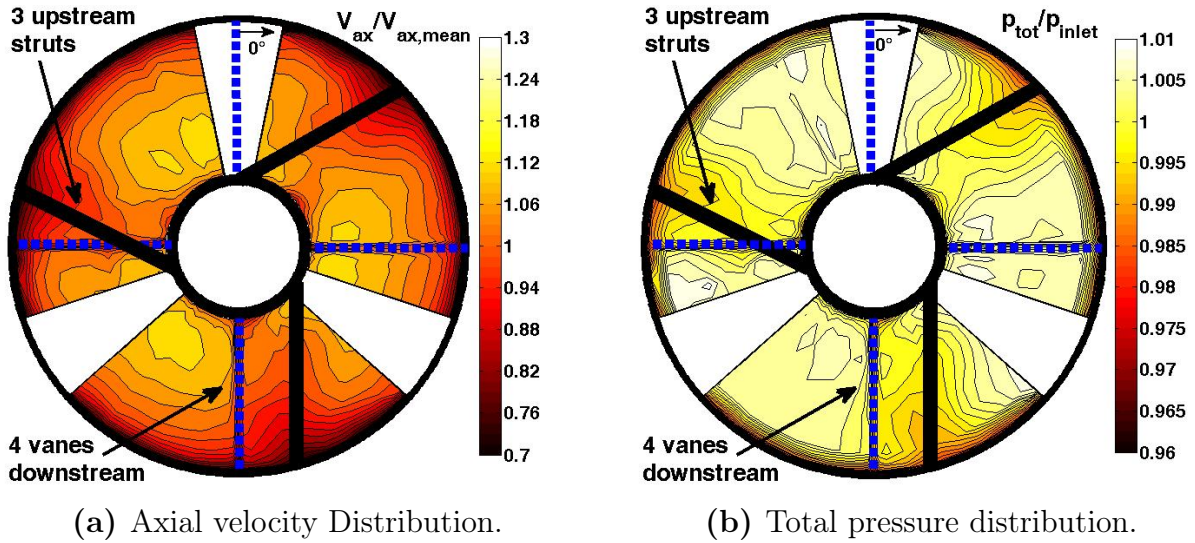
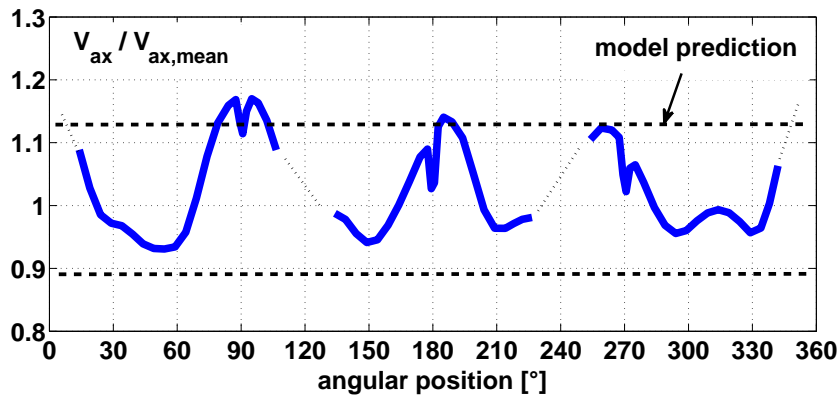


Figure 4.6.: Inlet flow properties for case without screen installation.

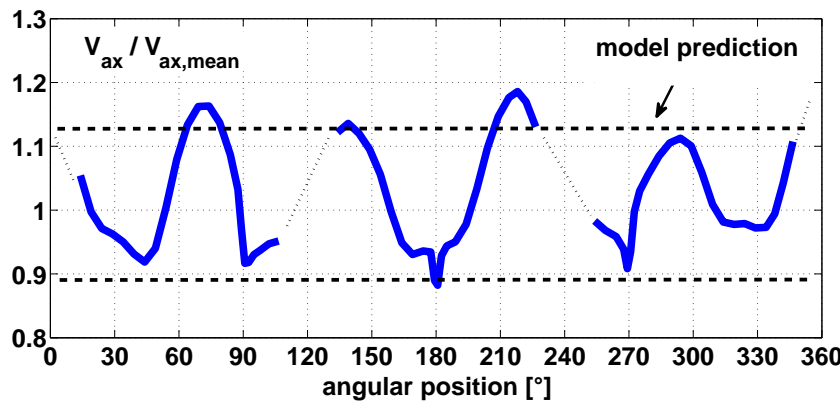
For this reason results obtained with the 5 lobe screen will be outlined in order to indicate the significant findings whereas other cases can be compared with the figures provided.

First, a comparison of the measured velocity ratio with the predicted magnitudes is given in figure 4.7 for the 4 lobe and the 5 lobe case. As will be shown later, the measured flow distribution is subject to considerable non-uniformities in the radial direction and within the distorted and undistorted part of the flow. In order to enable a comparison between the prediction and the experimental data, the axial velocity must be radially mass-averaged. Moving along the circumference in a clockwise direction the low and high momentum regimes can be identified. Both, the lower limit with $V_{ax}/V_{ax,mean} = 0.9$ and the upper limit $V_{ax}/V_{ax,mean} = 1.13$ are slightly underpredicted with respect to the minima and maxima but are considered to be sufficiently well predicted bearing in mind the simplicity of the model. The four downstream struts clearly generate local minima due to wake creation. The transition from the blocked to the unblocked area is smooth resembling a sinusoidal function rather than a step function. This indicates that sufficient mixing takes place as the fluid passes from the screen to the measurement plane.

Second, the contour plots of the axial velocity, show in figure 4.11(a), reveal



(a) 4 lobe screen



(b) 5 lobe screen

Figure 4.7.: Measured radially averaged and predicted axial velocity.

a number of interesting aspects. First of all, the distorted and undistorted lobes are not of the same shape and local minima and maxima vary. The local maximum velocities within the unblocked area amount a ratio of ≈ 1.2 i.e. being 20% above the mean value. Similar to the no-screen case presented previously, the upstream struts of the inlet section affect the flow field most apparently at around 280° seen in figure 4.11(b). The strut passes right through the high velocity fluid forcing it to decelerate. Within the blocked areas a significant amount of low momentum fluid accumulates at the tip due to the deceleration through the grid. This effect is locally attenuated by the upstream struts and the velocity ratio drops significantly below a predicted value of 0.9. Therefore the locally confined low momentum fluid is balanced by high momentum fluid within the non-blocked regime leading to values significantly above the prediction.

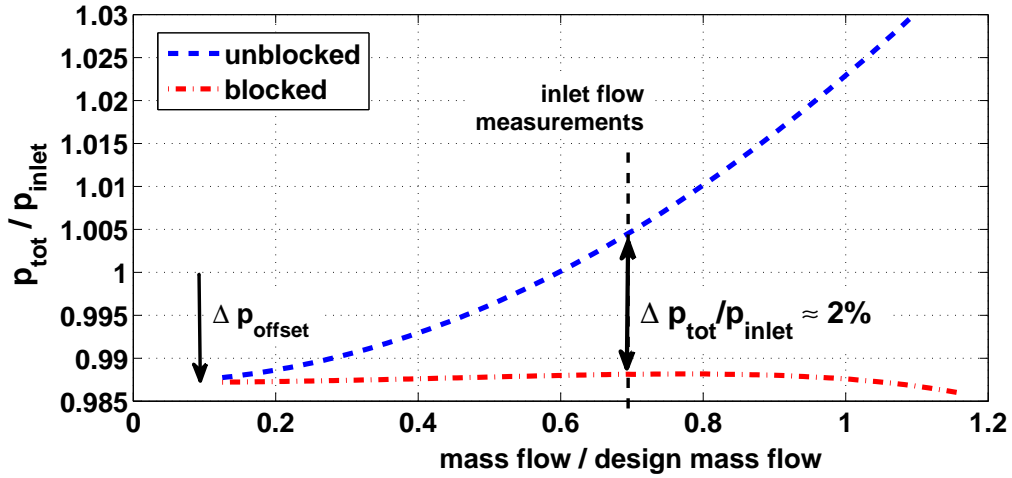


Figure 4.8.: Dependence of total pressure distortion on mass flow.

Total Pressure Distortion

The advantage of using the axial velocity over the total pressure lies in the fact that the velocity ratios $V_{ax}/V_{ax,mean}$ remain constant for the entire mass flow range. During the measurements velocity ratios for the same screen but for different mass flow settings were compared and were found to be identical. In other words, they could not be distinguished. In terms of total pressure however, a dependence of the total pressure ratio p_{tot}/p_{inlet} on the mass flow must be taken into account.

Some remarks on should be made here on the chosen non-dimensional quantity to present the data. The inlet static pressure p_{inlet} was chosen to non-dimensionalize the measured total pressure because of its significance in the measurement of resonant response and forcing function. The inlet static pressure represents a parameter which can be independently set in the test facility and thereby affects blade excitation, aerodynamic damping and maximum response amplitude. In addition, it was found that when non-dimensionalizing with inlet static pressure, p_{inlet} , the measured blade surface pressures collapse for different inlet static pressure conditions. This way the effect of the inlet static pressure could be removed from the measurement results.

Based on the previously presented model, the total pressure ratio is plotted in figure 4.8 as a function of the mass flow ratio. Downstream of the

screen it can be seen, that according to the model, the blocked portion of the grid causes a nearly constant total pressure dependence. However, downstream of the unblocked portion of the screen the total pressure increases due to a redistribution of mass flow caused by the blocked area. Redistribution of mass flow refers to the increase in mass flow passing through the blocked and the decrease in mass flow passing through the unblocked area. The local change in mass flow is viewed in reference to the uniform mass distribution far upstream of the screen. In figure 4.8, both curves are offset by about $\Delta p_{offset}/p_{inlet} = -1.1\%$. The offset was accounted in the model and was found to stem from a systematic offset between the two different measurement techniques used. The inlet static pressure, p_{static} was measured upstream of the distortion grids by the test facility performance measurement system. The total pressure p_{tot} was measured using an aerodynamic probe. The constant offset has no effect on the excitation of the blades. What affects blade excitation is the distortion level expressed in terms of $\Delta p_{tot}/p_{inlet}$. In this case the predicted and measured magnitude correspond to $\approx 2\%$ acquired at a mass flow ratio of $\dot{m}/\dot{m}_{des} = 0.7$ According to the model this magnitude increases with an increase in mass flow and reaches $\approx 4\%$ at design mass flow setting.

From the above findings it follows that the inlet total pressure distribution is a circumferential wave with an amplitude depending on the mass flow setting. In the datum study, measurements during resonance were taken at mass flow settings ranging between $0.5 < \dot{m}/\dot{m}_{des} < 1.0$ and correspond to a total pressure wave with amplitudes ranging between $1\% < \Delta p_{tot}/p_{inlet} < 4\%$.

Summary

Overall, the installed screens generated the expected distortion pattern with velocity variations in the range of $0.9 < V_{ax}/V_{ax,mean} < 1.13$. However, local variations are significant with the overall velocity ratio ranging between $0.82 < V_{ax}/V_{ax,mean} < 1.2$. Due to these local variations in the flow field it is expected that harmonics in the excitation of the blades will be observed in addition to the fundamental excitation frequency dictated by the number of screen lobes. A case-by-case comparison between the screens shows comparable flow field features. This observation applies to the regions within the bulk flow of low and high momentum flow as well as to local phenomena i.e. at the tip which is dominated by growth of boundary layer. Moreover, assembly struts affect the flow field in all cases. The total pressure distortion

depends on the mass flow setting of the test facility. In the datum forced response study, the mass flow range of interest corresponds to a total pressure distortion amplitude of 1% – 4%.

4.5. Summary and Conclusions

This chapter presented the prediction, generation and measurement of inlet flow distortion. An analytical model was derived to predict distortion amplitudes downstream of partially blocked screens installed in the flow path. The model was based on loss generation across wire meshes and flow distribution due to partial blockage. The flow field was measured upstream of the impeller using an aerodynamic probe and compared to the analytical prediction. The following summary and conclusions can be stated:

- The distortion screens consisted of blocked and unblocked parts of equal through flow area. The number of lobes corresponded to the primary excitation order they were intended to generate. The grid porosity in the blocked part was adjusted to generate a pressure drop of $\Delta p/q = 0.5$
- Fluid flow measurements without distortion screens revealed strut installations within the impeller inlet section to generate considerable flow non-uniformities. Local axial velocity reach amplitudes $V_{ax}/V_{ax,mean}$ of about 1.08. Effects due to upstream installations were found to be consistently present in all cases inlet distortion cases albeit with a reduced amplitude.
- A comparison between the predicted and the measured inlet flow distortion with a screen installed shows good agreement. The circumferential distortion distribution resembles a sinusoidal functions due to sufficient mixing within the inlet section. The average axial velocity was predicted and measured to amount amplitudes in the range of $0.9 < V_{ax}/V_{ax,mean} < 1.13$.
- Total pressure distortion amplitude expressed in terms of $\Delta p_{tot}/p_{inlet}$ increases towards higher mass flows with amplitudes ranging between 1% – 4%.
- Each distortion screen generates its intended engine order excitation. However, the flow field is subject to local variations. They were identified in the paths of struts, at the tip or within the high momentum

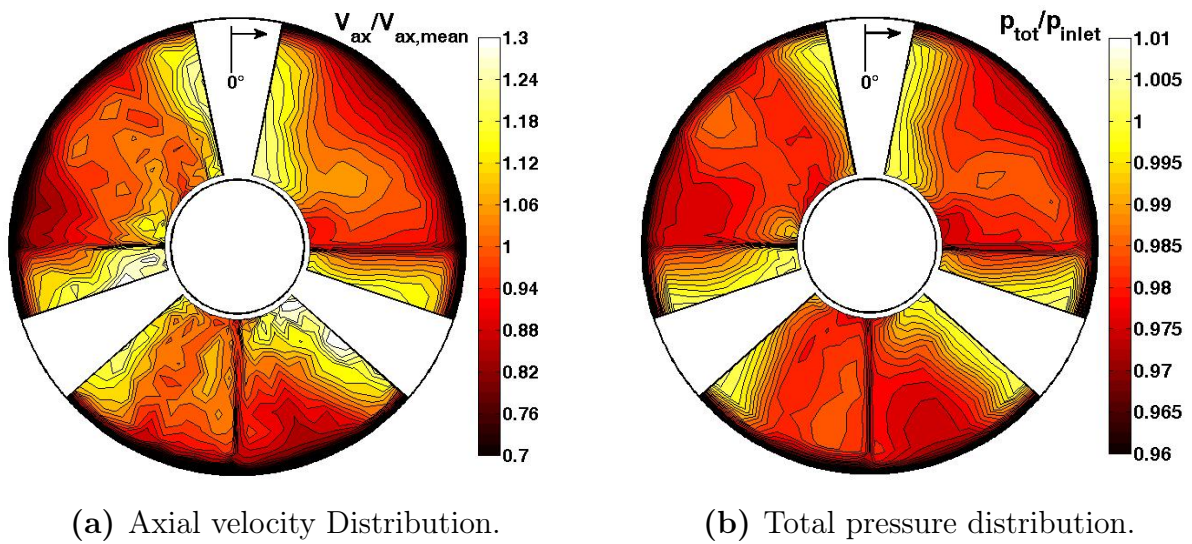


Figure 4.9.: Inlet flow properties for case with 3 lobe screen.

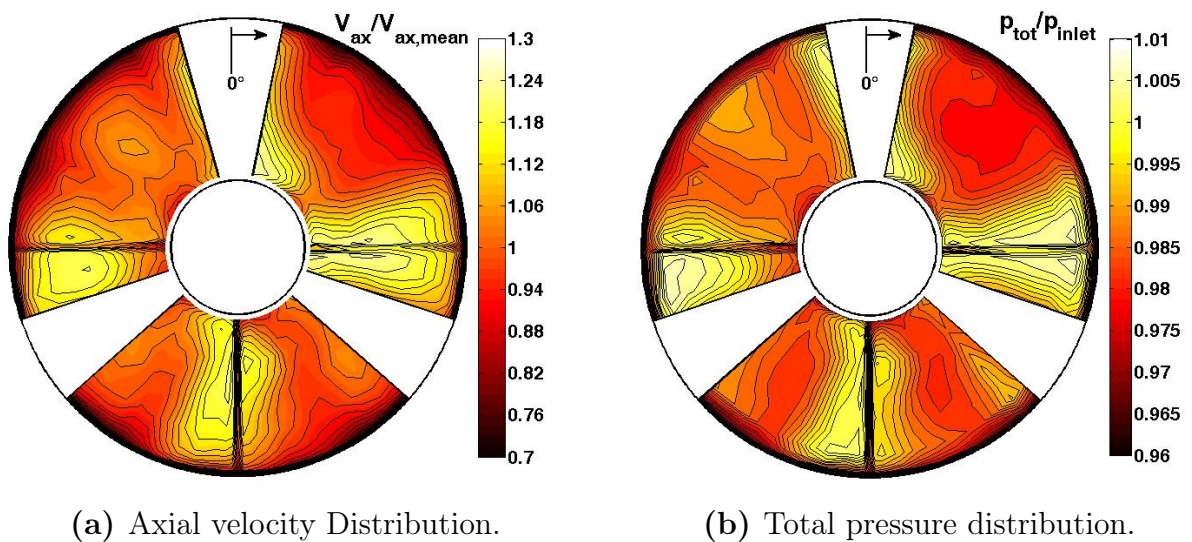


Figure 4.10.: Inlet flow properties for case with 4 lobe screen.

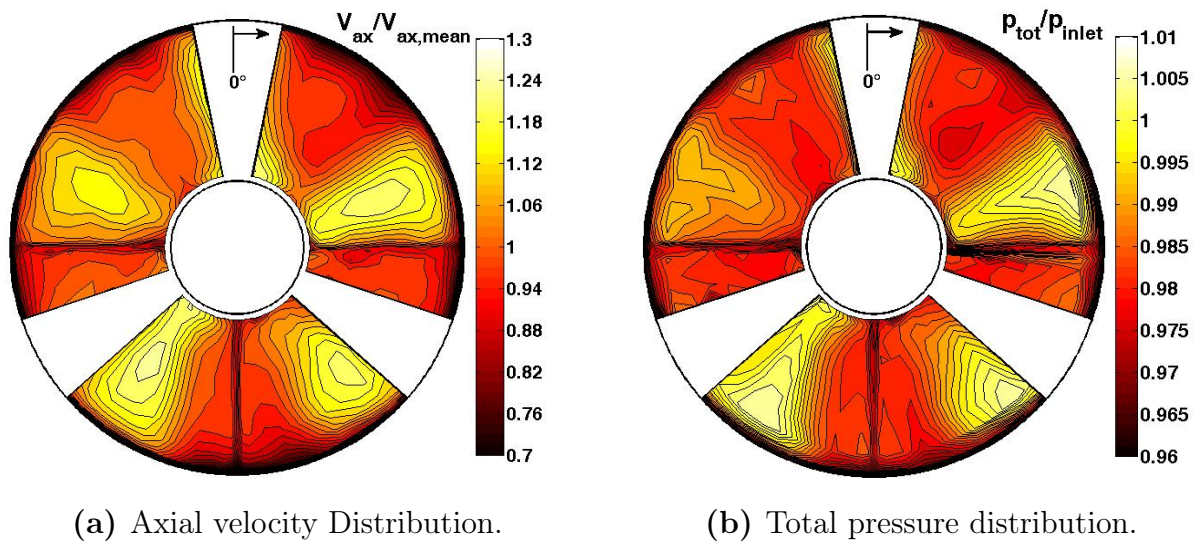


Figure 4.11.: Inlet flow properties for case with 5 lobe screen.

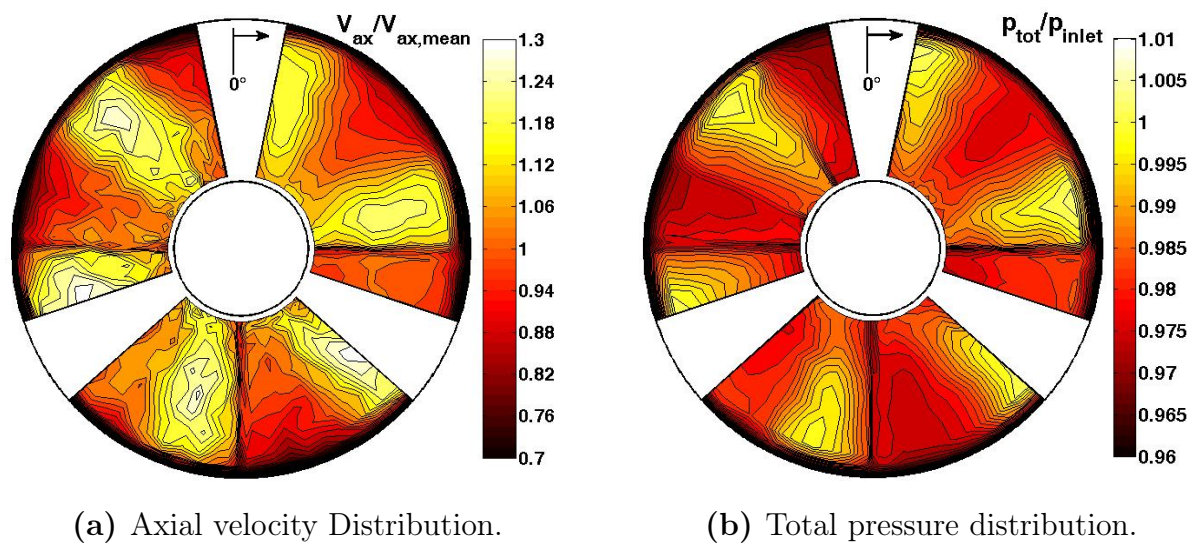


Figure 4.12.: Inlet flow properties for case with 6 lobe screen.

cores. Within these areas the local quantities can considerably exceed the predicted mean values and amount amplitudes in the range of $0.82 < V_{ax}/V_{ax,mean} < 1.2$

- The composition of the inlet flow field is expected to generate unsteady pressure fluctuations on the blade surface that consist of the intended distortion frequency superposed on lower excitation orders due to upstream installations.

5. Blade Unsteady Forcing

In the following chapter unsteady pressure measurements on the blade surfaces are presented. First, results will be analysed for the configuration case without an installed distortion screen. This allows to understand the harmonic content in the unsteady flow in the absence of any intentional flow distortion. Second, results will be presented for configuration cases with distortion screens in order to quantify blade excitation amplitude and phase. Finally, results will be presented for pressure measurements taken during resonant vibration aiming to illustrate the effect of blade motion on the measured unsteady pressure.

The objective of this chapter is to quantify the amplitude and phase of the unsteady pressure acting on the blade surfaces. For this purpose analysis of the harmonic content will be performed for a number of inlet distortion cases. Aerodynamic excitation will be shown to be affected by the inlet flow conditions, rotational speed and operating point. As such, since unsteady pressure is affected by a series of influence parameters, the scope of the following presentation must be restricted to the quantification of amplitude and phase. The scope of this chapter does not permit to analyze fluid flow features that lead to the actually measured excitation. This should be done on a case to case approach and for example applied to cases that cause hazardous increase in resonant response amplitude of the blade.

5.1. Measurement Procedure

On-blade unsteady pressure measurements presented hereafter were performed according to the approach described in section 2.5. Pressure calibration was performed on a daily basis prior each run as described in section 3.1.5. During measurements the inlet static pressure p_{inlet} was recorded at a position upstream of the impeller as shown in figure 2.2. This quantity was measured simultaneously with the blade unsteady pressure in order to provide a reference quantity with respect to the overall pressure level. The chosen approach

was necessary since it was not possible to extract steady pressure data from on-blade sensors.

The inlet static pressure was consistently used to non-dimensionalize the blade unsteady pressure. Unsteady blade pressure measured during off-resonance was found to scale with inlet static pressure. Therefore, pressure amplitudes measured at different inlet pressures were found to collapse into a single line when non-dimensionalized with inlet static pressure.

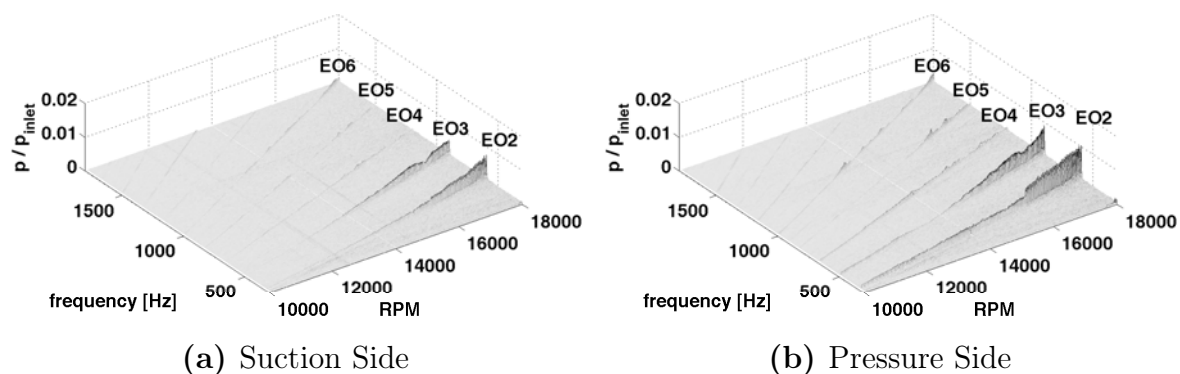
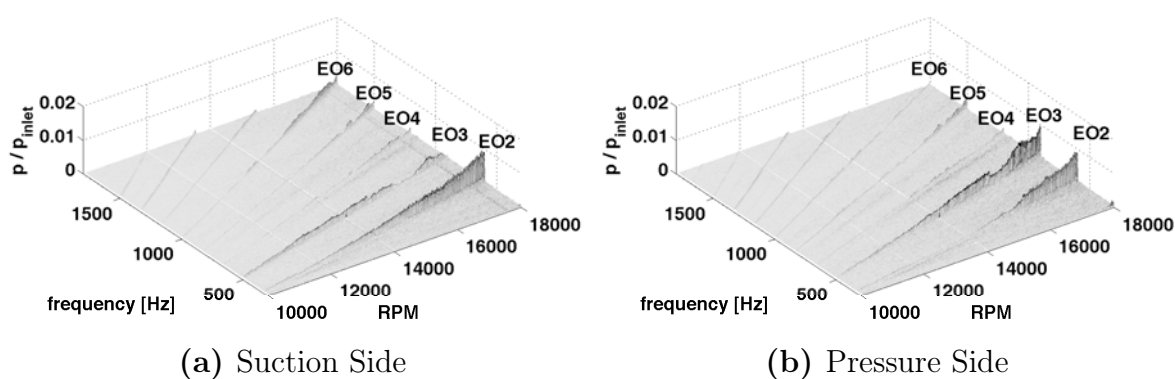
5.2. Unsteady Pressure without Distortion Screens

The measured total pressure distribution upstream of the impeller is shown in figure 4.6. A distortion screen is not installed in this case. In summary, despite the fact that a distortion screen is not installed, the flow upstream of the impeller is not uniform. The total pressure distribution can be observed to be affected by installations of the rotary transmission unit. This is particularly the case in the vicinity of the three upstream struts which generate three distinct zones of reduced total pressure.

Case near Stability Limit (OL1)

The measured spectrum of the unsteady pressure acting on the blade surface is exemplified in figures 5.1 and 5.2 for the case without a distortion screen. Here, the windowed frequency analysis was performed for the pressure difference at sensor positions 3 and 7, see figure 3.1(b). Data is shown for the operating line close to the stability limit OL1 shown in figure 2.5.

For all cases shown up to a maximum rotational speeds of 18000rpm, the unsteady pressure fluctuation amplitudes were typically in the range of 1-2% of the inlet static pressure. This gives a rough estimation of the excitation force magnitudes acting on the blade surface. With respect to the frequency content it can be observed that the unsteady pressure is composed of mainly the second and the third harmonics. Their amplitudes increase with rotational speed in particular from 14000rpm onwards. Although inlet flow distortion measurements predominantly indicate the existence of the third engine order, on-blade pressure measurements identify the second engine order to be

Figure 5.1.: Pressure excitation spectra for **sensor 3** and **OL1**Figure 5.2.: Pressure excitation spectra for **sensor 7** and **OL1**

of similar amplitude. Higher engine orders are detectable, their magnitude however does not increase as shaft speed increases.

For both sensor positions the amplitudes of the harmonics can be seen to be of very similar magnitudes. Also, comparable magnitudes can be observed for suction and pressure side.

At this stage it should be pointed out that the first excitation order is not addressed here because the obtained amplitudes are not consistent with the shown results. The following three observations were done. First, it was only the first excitation order that could not be scaled with inlet pressure. Its magnitude was found to vary independently of inlet pressure. It further varied after each new impeller/transmitter installation. Second, the first excitation order was found to remain constant over a wide range of speeds. This is contrary to all other excitation orders which generally increase in amplitude with an increase in rotational speed. Third, measurements were repeated in

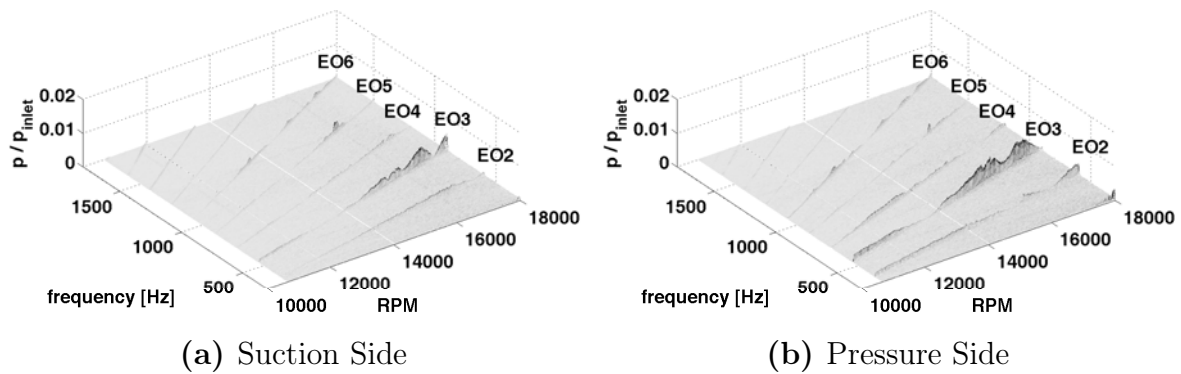


Figure 5.3.: Pressure excitation spectra for **sensor 3** and **OL3**.

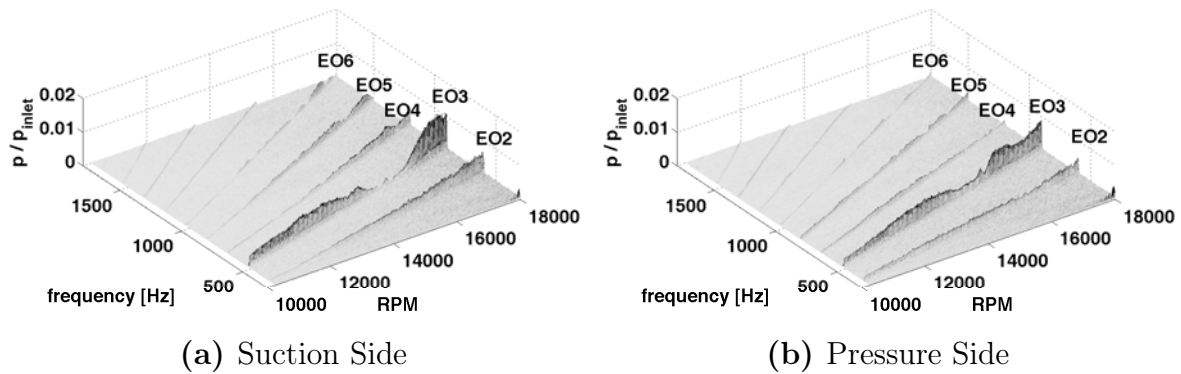


Figure 5.4.: Pressure excitation spectra at **sensor 7** and **OL3**.

order to clarify on this subject and it was found that the first excitation order could not be reproduced as opposed to higher harmonics. On this basis, further research into this problem is required.

Case for Maximum Mass Flow (OL3)

For comparison with the previous case, figures 5.3 and 5.4 illustrate the measured spectrum for the same sensors but for an operating line equivalent to the maximum mass flow setting. The major observation to make in this regard is related to an increased dominance of EO3 excitation in the flow field. This tendency can be observed for both pressure sensors equally. Also, suction and pressure side are comparably affected leading overall to a decrease of EO2 excitation and a dominant EO3 harmonic. The latter can be seen to vary considerably in amplitude with rotational speed.

The comparison between the two operating lines is a representative obser-

vation for most of the data taken and not shown here. The findings apply equally to measurements with and without distortion screens. Low engine order excitation was found to be consistently contained in the measured signal. Their amplitudes are sensitive to changes in operating line without a clear sensitivity pattern. Dependence on the rotational speed is apparent with strong local amplitude variations. In order to overcome potential doubts on the credibility of the data, measurements were repeated and were found to confirm the findings.

Generation of Higher Harmonics

From the presented spectra it becomes apparent that excitation harmonics higher than EO3 are contained in the flow field. Their amplitudes appear negligible in comparison to EO2 and EO3. With respect to EO4 excitation it can be seen that this harmonic is not affected by the four upstream struts covered with airfoils, see figure 2.2. The airfoils were observed to generate wakes independently of the screen case influencing the unsteady pressure distribution on the blade. This finding is in accordance with results presented by *Haupt et al.* [29] for a centrifugal compressor where resonant response due to carrier blades was measured but was much less than expected. On the contrary, *Manwaring and Fleeter* [53] found vane generated inlet distortion to exhibit higher excitation amplitudes than the excitation due to inlet distortion. As will be shown in the chapter on resonance response, the excitation orders of the higher harmonics were in general sufficiently high to cause response. Although this response was relatively small in comparison to the intended resonant response, its existence should cause awareness.

Forcing Function Distribution along the Blade Length

So far the frequency content of a single sensor position was shown as well as its evolution with rotational speed. The following aims to clarify the separate contributions from the blade suction and pressure sides to the resultant forcing function. Attention is given to EO2 and EO3 excitation. In the following, the pressure distribution along blade mid-height is presented for a specific shaft speed of 17600rpm which is a representative case for the speed ranges considered in the datum project.

Qualitatively, EO2 and EO3 can be identified from the unsteady pressure signal on the suction and pressure sides, figures 5.5 and 5.7. Pressure traces

are shown along the blade mid-height during a single revolution. As the blade rotates, the highest overall amplitudes are measured to be at a fixed circumferential position of approximately 20% of a revolution. This position corresponds to one of the upstream struts and appears equally for both of the operating lines. This feature was found to be consistent for all measurements and suggests the upstream struts to affect the unsteady flow field. However, the footprint of each of the three upstream struts varies significantly.

The harmonic decomposition of the unsteady pressure distribution is shown in figure 5.6 for OL1 and figure 5.8 for OL3, respectively. The data shown, was ensemble averaged for 20 revolutions. For both operating lines the amplitudes of the higher engine orders than EO3 are negligible in comparison to EO2 and EO3. This observation confirms earlier findings. For both operating lines, fluctuations on suction and pressure side are of similar amplitude. The single and most striking difference can be seen for the forcing function distribution along the blade between the two operating lines. In the first case of OL1, the highest amplitudes are experienced at the leading edge of the main blade. On the contrary, for OL3 the highest amplitudes shift downstream whereby diminishing to zero at the leading edge. These findings clearly show a dependence of the excitation function on the mass flow.

Summary

For the given flow non-uniformity due to upstream installations the harmonic content of the unsteady blade pressure is dominated by EO2 and EO3 harmonics. Higher harmonics are comparatively small. An expected effect of four vanes mounted upstream of the rotor could not be detected in the measured EO4 harmonic. The origin of the EO2 and EO3 harmonics was identified to stem from three struts mounted upstream. Generally, their amplitudes were found to be similar on suction and pressure side, and increasing with rotational speed. The excitation function along the blade surface depends on the mass flow. In order to clarify on the underlying mechanisms that lead to the measured distribution, a case-by-case analysis of the flow dynamics would be required.

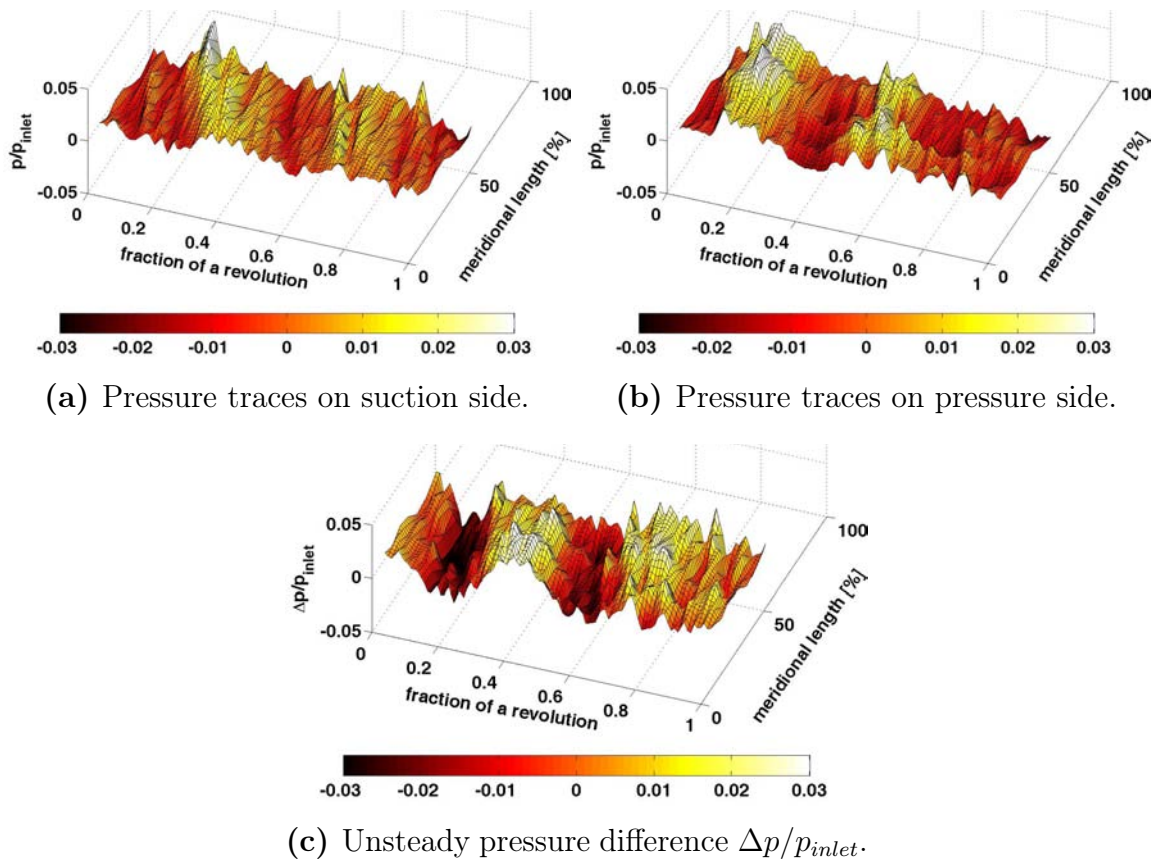


Figure 5.5.: Pressure traces at **17600rpm** for **OL1** without distortion screen.

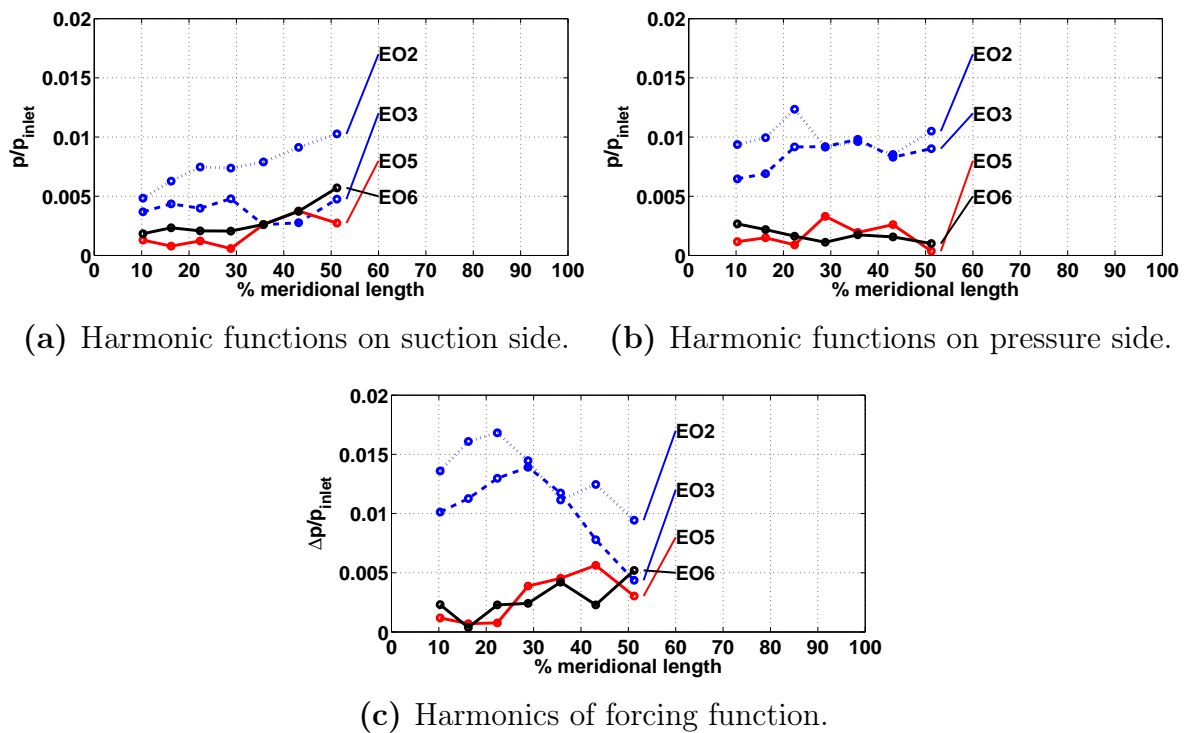


Figure 5.6.: Harmonics at **17600rpm** for **OL1** without distortion screen.

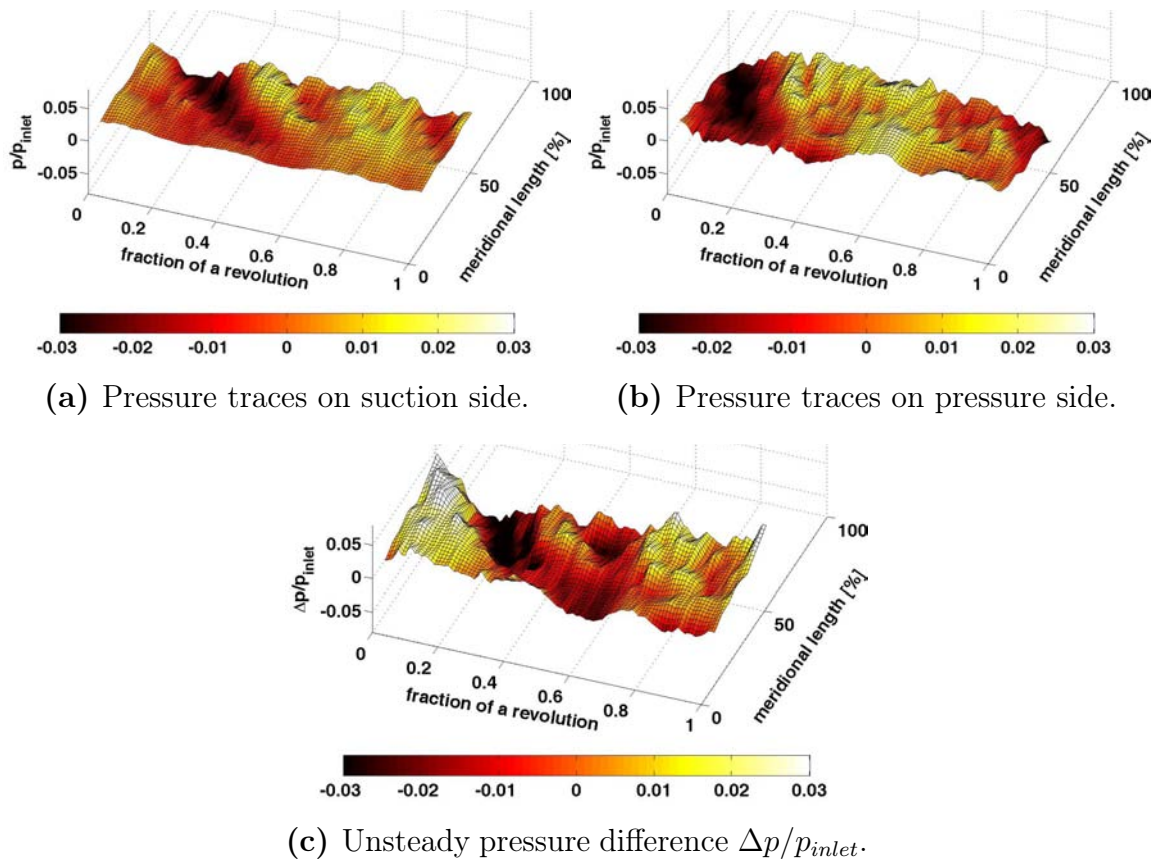


Figure 5.7.: Pressure traces at **17600rpm** for **OL3** without distortion screen.

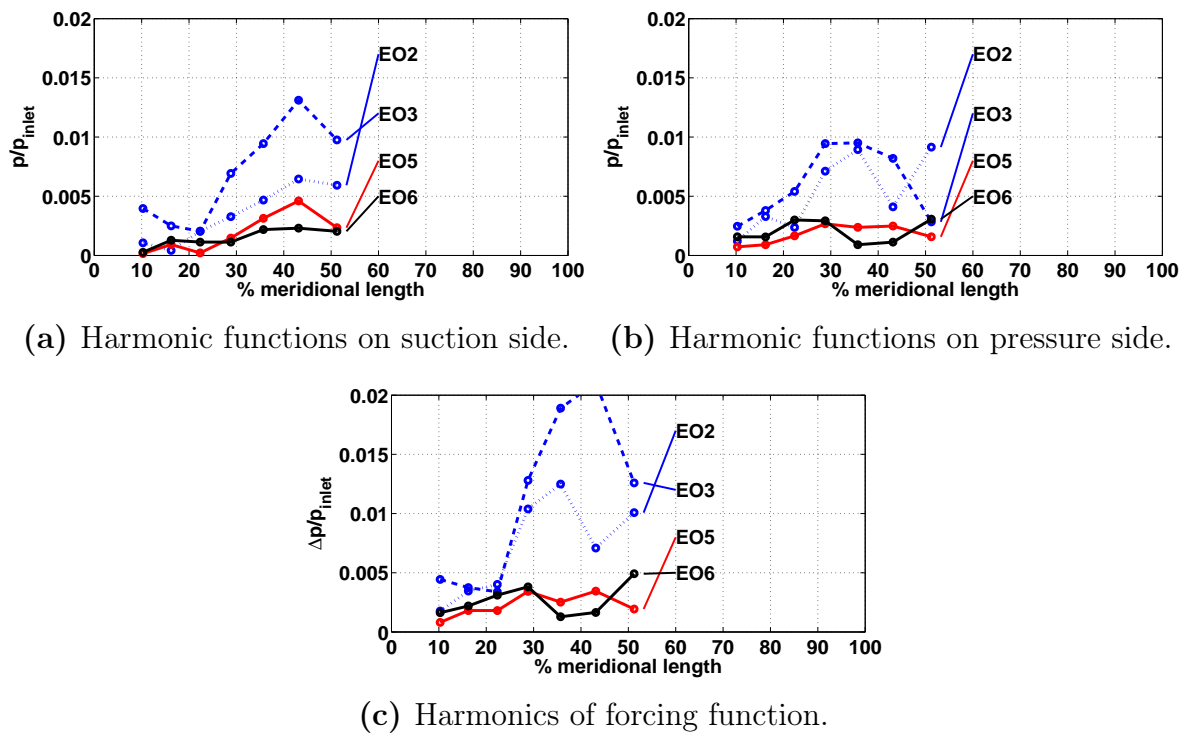


Figure 5.8.: Harmonics at **17600rpm** for **OL3** without distortion screen.

5.3. Overview on Measurement Cases

In the following sections results are presented and discussed for a number of different cases of excitation that can be distinguished depending on the distortion screen used, engine order excitation and response mode. These cases are

- **Mode1/EO5 at 16250rpm** which will be discussed first. In this case the response was caused by the fundamental excitation being generated by a 5 lobe distortion screen. Both, computational results as well as measurements will be presented.
- **Mode1/EO6 at 13500rpm** which response was generated either by the fundamental harmonic from the 6 lobe screen or by the second harmonic of the 3 lobe screen. Only measurement on the unsteady pressure distribution will be presented.
- **Mode2/EO12 at 14370rpm** which response was generated by the third harmonic from the 4 lobe screen. Only measurement on the unsteady pressure distribution will be presented.

5.4. Analysis of Resonance Case Mode1/EO5

The analysis presented hereafter focuses first on illustrating the fluid flow conditions within the blade passages during resonance. CFD was performed for this purpose. Second, unsteady pressure measurement will be presented that quantify the amplitude and phase of the excitation function. Unsteady CFD results will be used to complement the findings. The overall analysis presents and compares results for the three operating lines OL1, OL2 and OL3 according to the performance map in figure 2.3 at 16250rpm as shown in the Campbell diagram, figure 2.5.

5.4.1. Flow Field Analysis

Prior to the presentation of results on the unsteady pressure, the flow conditions within the impeller should be examined. Results from computation will be used for this purpose. The relative Mach number distribution in a plane

along the blade mid-height is shown in the figures 5.9-5.11, which correspond to the three operating lines OL1, OL2 and OL3. In all cases the rotational speed was set to 16250rpm, which represents the resonant case. At the inlet the measured flow distortion was applied as a total pressure boundary condition.

In the following the term operating line refers to the intersection of a specific mass flow setting at the constant speed of 16250rpm. The Mach number distribution for OL1 is generally in a regime below $Ma = 0.5$. Local maxima of $Ma = 0.65$ can be identified on the suction side at the exit of the impeller. The pressure side of the blade is subject to Mach numbers below $Ma = 0.3$ for almost the entire blade length. In the case of the operating line OL2, the Mach number distribution remains similar in character, however, the actual mean level is elevated to values above $Ma = 0.5$. At the exit on the suction side of the impeller local Mach numbers can be seen to reach near sonic conditions. As the mass flow increases further for operating line OL3, transonic regimes are generated at the exit. The distribution indicates half of the passage to be occupied by a zone of Mach numbers above unity. According to the impeller performance map in figure 2.3 this should be the case considering the vicinity of the operating point to the choke limit. The datum compressor with a vaneless diffuser was shown to choke within the rotor. Further upstream along the blade surface, the Mach numbers on the suction side reach values of around $Ma = 0.7$ and higher, whereas on the pressure side the Mach numbers remain around $Ma = 0.5$.

The convection of inlet flow distortion through the impeller is presented in figure 5.12. Shown is the relative total pressure distribution at impeller mid-height for the operating line OL1. At the inlet of the domain zones high and low relative total pressure alternate along the circumference. As the flow progresses towards the leading edges the different zones are chopped by the blades and convect through the impeller. The circumferential extent of each segment corresponds approximately to the blade passage width (7 main blades vs. 5lobes). Due to this circumstance the blade passages can be seen to be either fully occupied by high total pressure zones or low pressure zones. As a result, blade excitation can be generated for example due to low pressure flow on the pressure side and high pressure flow on the suction side. Moreover, as the low and high pressure zones convect through the impeller, they have the potential to affect the local Mach numbers as was observed in the Mach

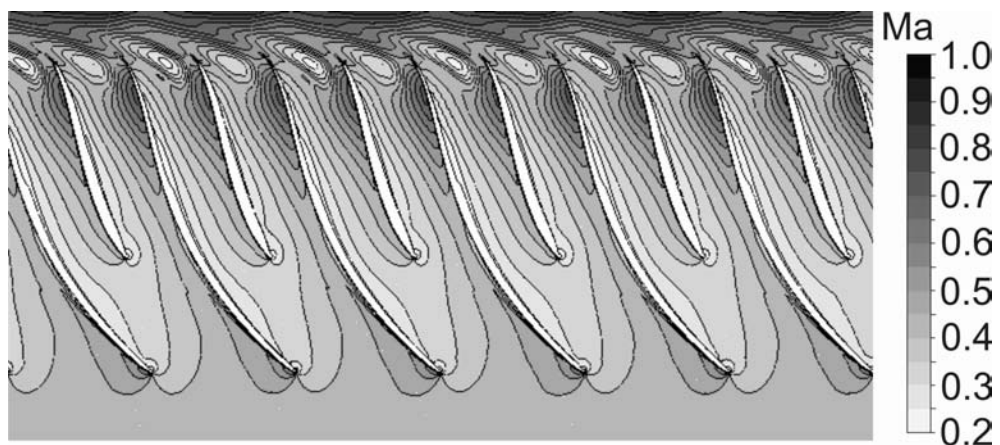


Figure 5.9.: Calculated (CFD) relative Mach number distribution for OL1.

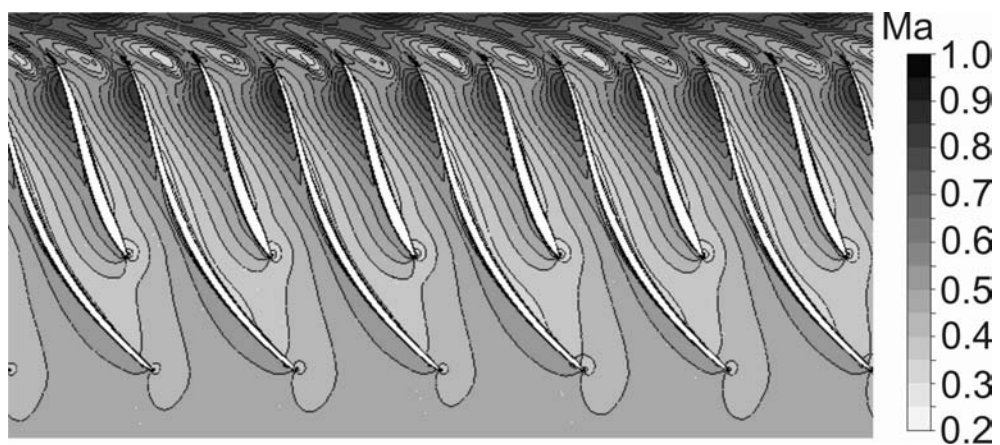


Figure 5.10.: Calculated (CFD) relative Mach number distribution for OL2.

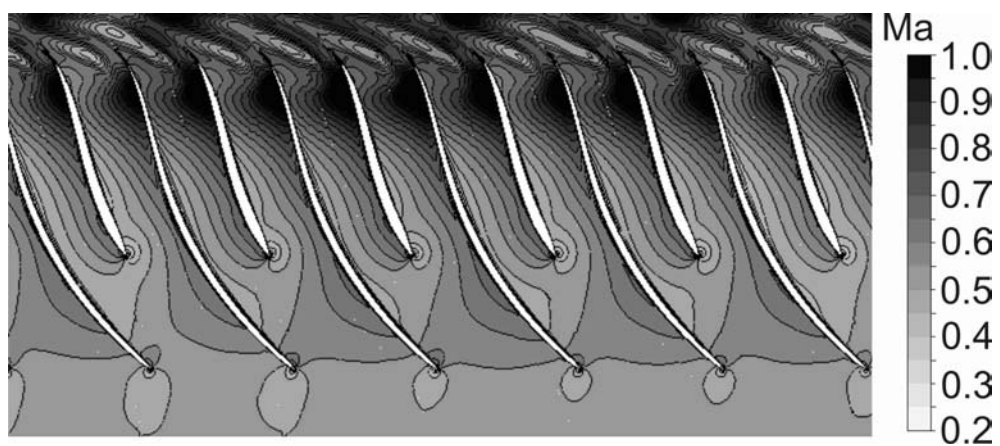


Figure 5.11.: Calculated (CFD) relative Mach number distribution for OL3.

number contours. For example, for OL3 transonic Mach number regimes may be affected such that near choking conditions within the passage may occur temporarily. Associated with this, pressure waves may be generated.



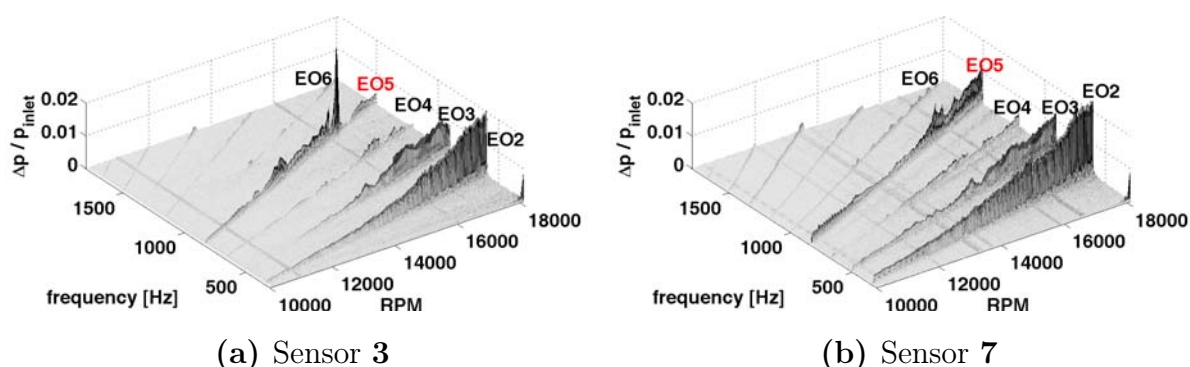
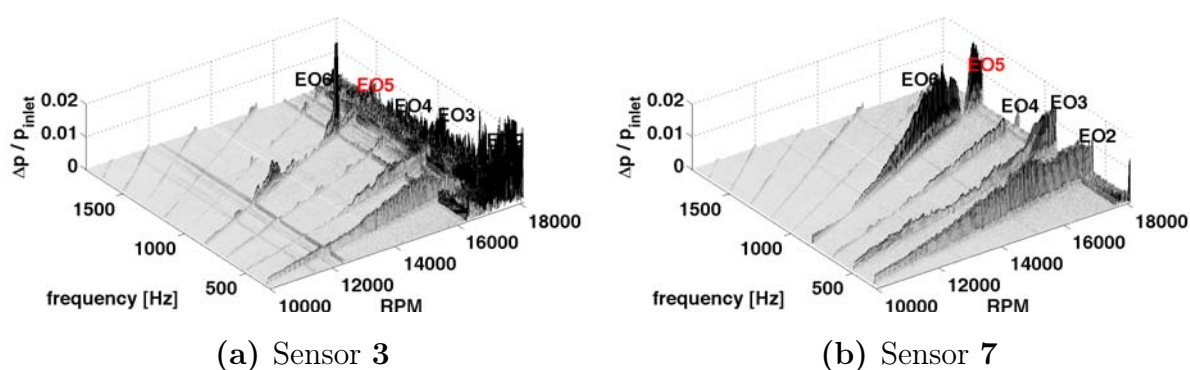
Figure 5.12.: Relative total pressure distribution for OL1.

Overall, the flow field at 16250rpm is generally subsonic within the impeller. As the mass flow increases towards choke, transonic conditions are reached at the exit of the impeller. The circumferential extent of the inlet distortion is of approximately the same size as the main blade passage and thereby either occupies an entire passage with low momentum or high momentum flow. Transonic flow at impeller exit is modulated by inlet distortion and may affect or cause unsteady pressure waves in the flow field.

5.4.2. Blade Unsteady Excitation

Spectra of Unsteady Force

The spectra of the unsteady pressure force for sensors 3 and 7 are shown in figures 5.13 and 5.14, for operating lines OL1 and OL3, respectively. The unsteady force is expressed in terms of pressure difference $\Delta p/p_{inlet}$ between the blade surfaces. For completeness, it should be noted that temporary contact losses within the rotatory transmitter can be seen as lines at constant speeds. For example, contact loss was experienced in figure 5.14(a) at 12000rpm and severe transmission problems can be identified above 17000rpm. In all cases shown the amplitudes of EO2 and EO3 are comparable and generally increasing with rotational speed. Minor modulations are apparent. These findings

Figure 5.13.: Excitation spectra for **5 lobe** screen and **OL1**.Figure 5.14.: Excitation spectra for **5 lobe** screen and **OL3**.

are consistent with the results presented for the case without distortion screen installation. It appears that EO2 and EO3 excitation persist despite the installation of a distortion screen. Their amplitudes are neither considerably reduced or amplified. EO4 excitation can be clearly identified in the spectrum whereas in previous results presented its amplitude was generally smaller.

Given the measured total pressure distributions of the inlet flow field, figure 4.11(b), it was rather surprising to discover the amplitude of EO2 and EO3 to be higher than the intended EO5 harmonic. In Chapter 4 it was shown that any distortion screen severely affected the inlet flow field. The distortion pattern was such, that the intended distortion amplitude dominated the flow field. In this cases, distortion effects due to upstream struts that cause EO2 and EO3 excitation were difficult to detect. Nevertheless, for each of the cases presented, EO2 and EO3 are the dominant unsteady forces acting on the blade and creating higher amplitudes than the intended frequencies. Only at pressure sensor position 7 for OL3 the unsteady pressure can be found to be higher than EO2 or EO3. These results indicate that lower harmonics are

better realized on the blade surface than higher harmonics. In other words, given a distorted inlet flow field composed of low and high harmonics with the same amplitudes, the low EO harmonics would cause higher amplitudes on the blade surface.

A feature particularly visible at sensor position 3 is a localized peak in the measured unsteady force at 16250rpm. The location of this maximum corresponds to resonant crossing, which causes blade vibration and induces comparatively high amplitudes. Section 5.6 deals with this problem in detail.

Pressure Distribution along Blade Mid-Height

Unsteady pressure acting on the blade surfaces is visualized in the form of traces for a single revolution. Figures 5.15-5.17 illustrate this for all three operating lines. It is important to note, that the shown pressure traces were all extracted for a measurement point at 16000rpm where blade resonance is not present and therefore the movement does not affect the measured pressure. This circumstance necessitates the need to strictly distinguish between measurements at off-resonance and measurements within resonance. Only in the former case the unsteady pressure can be measured that causes unsteady blade excitation and is therefore referred to as the forcing function.

The effect of the 5 lobe screen on the unsteady pressure can be best observed on the suction side. As the mass flow increases from OL1 to OL3, EO5 can be seen to grow in amplitude with corresponding values of $\pm 1.5\%$ to $\pm 3\%$. Particular attention should be paid to the phase relation along the blade meridional length. In figure 5.17(a) the markers T1 and T2 signify two instances in time as the blade rotates once for a full revolution. Time is expressed in terms of fraction of a revolution. As such, the markers can also be understood to represent a specific position on the circumference. As the blade rotates, it first experiences the maximum amplitude of the excitation force at the instance T1 at 50% meridional blade length. The instance T2 and the associated maximum amplitude occur later with respect to time and position along the circumference. This observation implies, that the pressure wave is traveling upstream along the blade suction side. This phenomena can be observed to occur for all operating line cases and appears to be dominant on the suction side. The travel direction of the pressure waves is contrary to what would be 'spontaneously' expected based on computational results

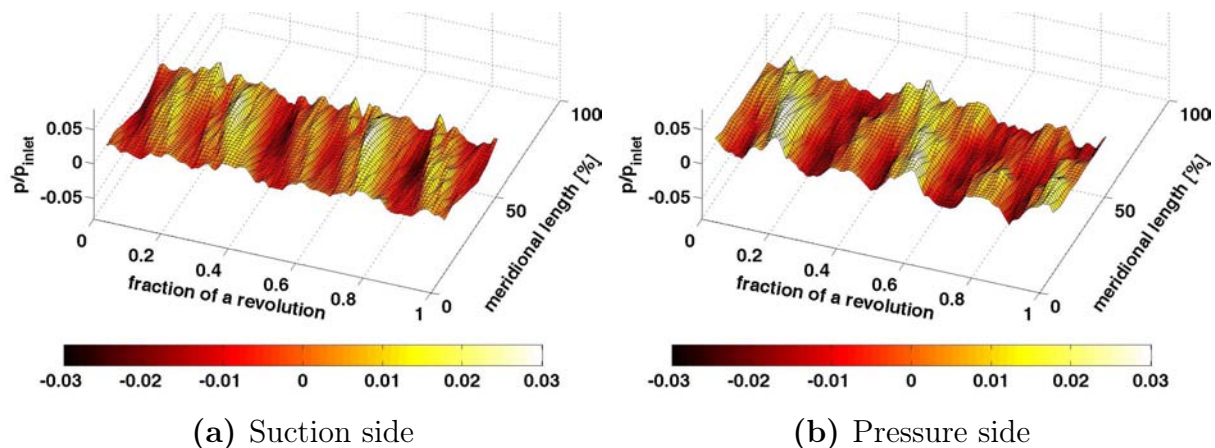


Figure 5.15.: Measured pressure traces for 5 lobe/16000rpm/OL1.

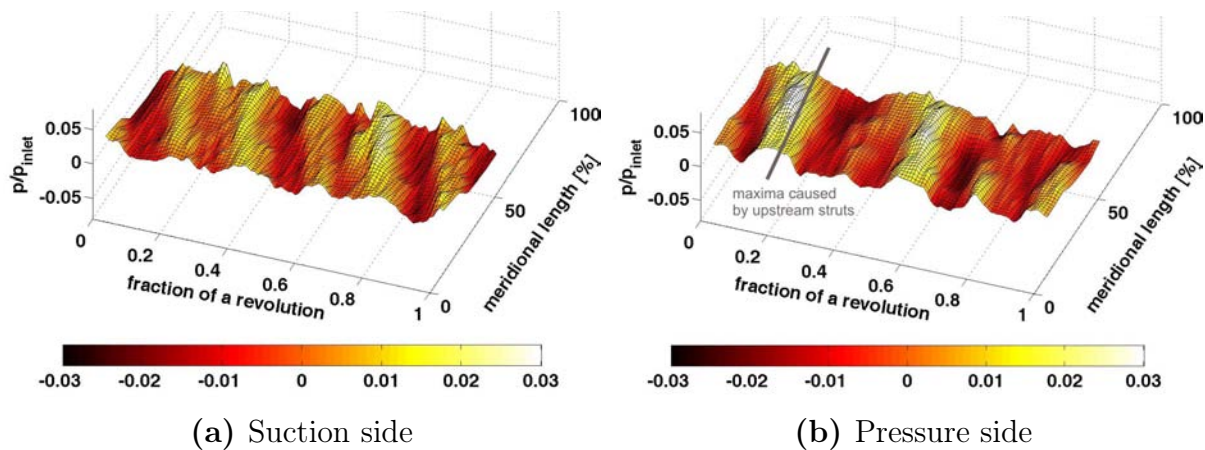


Figure 5.16.: Measured pressure traces for 5 lobe/16000rpm/OL2.

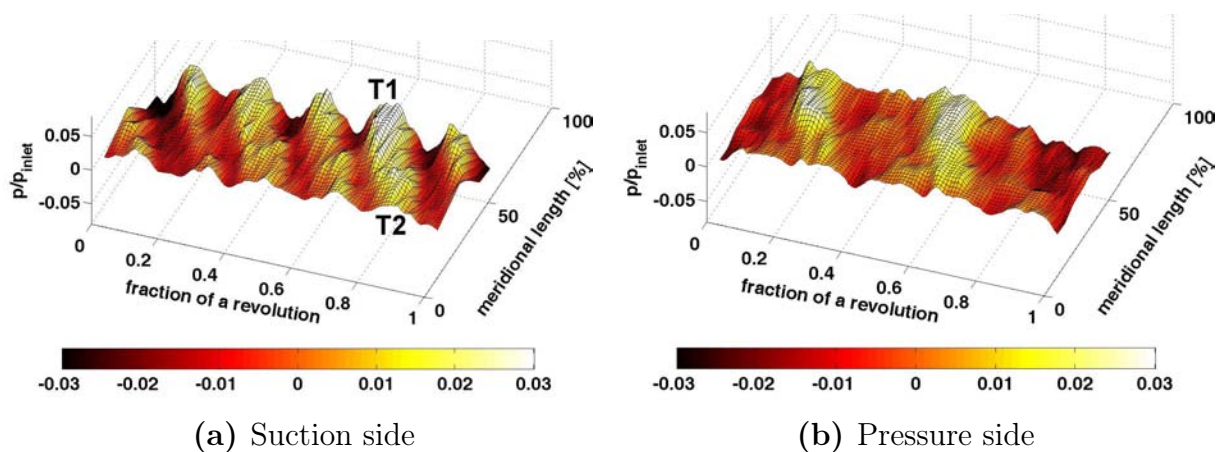


Figure 5.17.: Measured pressure traces for 5 lobe/16000rpm/OL3.

shown previously where zones of low and high total pressure are convected downstream.

Contrary to results shown for the suction side, the pressure side is dominated by the EO2 and EO3 harmonics. The shown pattern was already identified for the case without distortion screens, albeit for a different speed line. For example, in figure 5.16(b) the effect of upstream struts is indicated to cause consistent maxima and minima, which could be always found at this specific position on the circumference. The structure might have changed depending on the screen used or the impeller rotational speed, but the overall pattern remained. EO5 is visible at the leading edge only for OL1 and vanishes with an increase in mass flow. The direction of pressure wave travel is the same as for the suction side, i.e. upstream along the blade surface. However, the speed of travel as indicated by the inclination indicates to be lower on the pressure side. The maxima along the blade length appear to occur almost simultaneously.

Amplitude and Phase of EO5 harmonic

So far unsteady pressure data was presented in a qualitative manner in terms of spectral distribution and signal traces. The actual amplitude and phase that cause resonant vibration is presented here. Amplitude and phase for EO5 are shown in figure 5.18 for the suction and pressure side. Data is presented for all three operating lines at a rotational speed of 16000rpm. To start with, in all cases the unsteady pressure amplitude varies around 1% of the inlet static pressure. On the suction side the amplitude can be seen to be affected by the mass flow setting at a meridional position of 40%-50%. On the pressure side however, the amplitude is mainly affected at up to 30% of the meridional length.

The energy transferred into a blade that causes and sustains blade vibration is greatly affected by the phase of the excitation force. In general, the phase relationship expresses the time difference between a harmonic oscillation and a reference signal. The reference signal can either be an instant in time signified by a trigger signal or any other known harmonic signal. The phase relationship shown in figure 5.18 was plotted with the once-per-revolution rotor trigger as the reference signal. The main advantage of using the trigger signal as a known reference is the fact that it also references the position of

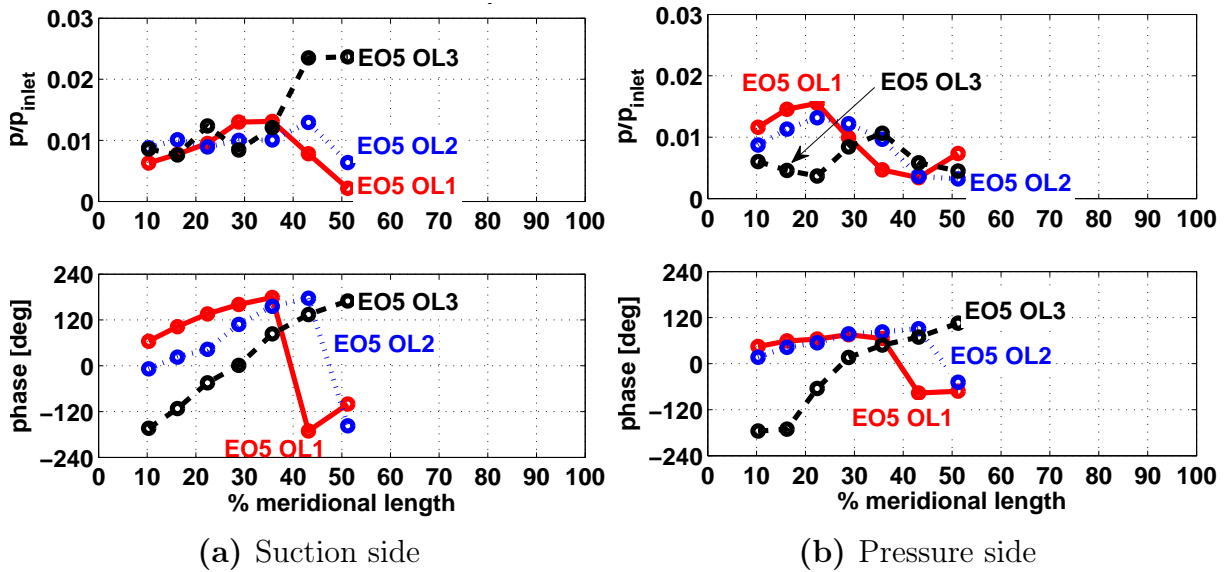


Figure 5.18.: **EO5** amplitude and phase for **5 lobe** screen at **16000rpm**.

the blade with respect to its circumferential angular position. This means the plotted phase is referenced to a blade that is always at, say 0° angular position. For example, on the suction side of the blade in figure 5.18 the phase of the EO5 harmonic for OL2 initiates at 0° at 10% meridional length. This implies that EO5 unsteady pressure harmonic initiates at the same moment as the trigger passes its mark and a blade on which the pressure is measured is at a fixed position on the circumference.

Based on the above explanation two major aspects can be observed in the phase relationship. First, the phase on the suction side can be seen to increase along the blade length for all operating lines. This implies earlier qualitative findings, that pressure waves are traveling upstream along the blade length. For example, for OL2 the phase at 10% blade length is at 0° whereas at 30% blade length the phase is already at 120° phase. This means that moving downstream along the blade length, the measured pressure phase advances compared to any location upstream. Moreover, from the inclination of the functions it can be stated that the pressure waves move at different speeds along the blade surface. For the lowest mass flow setting (OL1) the speed at which pressure waves move upstream is highest whereas the highest mass flow (OL3) causes the lowest propagation velocities. A limiting case could be imagined, in which a pressure wave would excite the blade in phase at any surface position. In this case the phase function would be horizontal.

The second main observation to make relates to the shift of the phase functions on the suction side. As the mass flow increases from OL1 to OL3 the functions can be seen to undergo an offset in the negative direction. This finding implies the following circumstance. Generally, at each measurement point along the blade the unsteady pressure can be imagined as a standing wave on the circumference. Within the flow field this pressure wave is in some way coupled to its source, in this case the inlet flow distortion. For any mass flow setting the inlet flow distortion pattern is fixed with respect to the circumference. This however does not apply to the pressure on the blade surface where an increase in mass flow causes a negative phase offset. The unsteady pressure field within the impeller can therefore be imagined as a standing wave in the absolute frame of reference that rotates with respect to the inlet flow distribution as the mass flow is changed.

In principal the same findings apply to the pressure side as to the suction side. For all operating lines the phase slope indicates pressure waves traveling upstream along the blade surface. A change in mass flow can be seen to have little effect on the phase from OL1 to OL2 but shifts the phase function for OL3 significantly.

5.4.3. Comparison with CFD (OL1 case)

Measurement of unsteady pressure on the blade surface provides valuable and rare insights into the undergoing fluid flow phenomena. However, such pressure measurements return data at discrete points whereas data would be required for an entire surface. For example, in order to compute the unsteady force acting on the blade surface, the unsteady pressure must be integrated across the entire surface. This is not possible purely on the basis of pressure measurements. In order to overcome this shortcoming, CFD results will be presented here and compared to experimental data. The aim was to support previous findings in terms of unsteady pressure distribution. Details on the CFD simulation can be found in the works by *Zemp* [84] and *Zemp et al.* [85].

The experimental results discussed hereafter are identical to those presented previously, i.e. unsteady pressure was measured with a 5 lobe screen at 16000rpm and an operating point near the stability limit (OL1). Computation was performed for the same conditions, with the only difference being the rotational speed which was set to 16250rpm corresponding to the actual

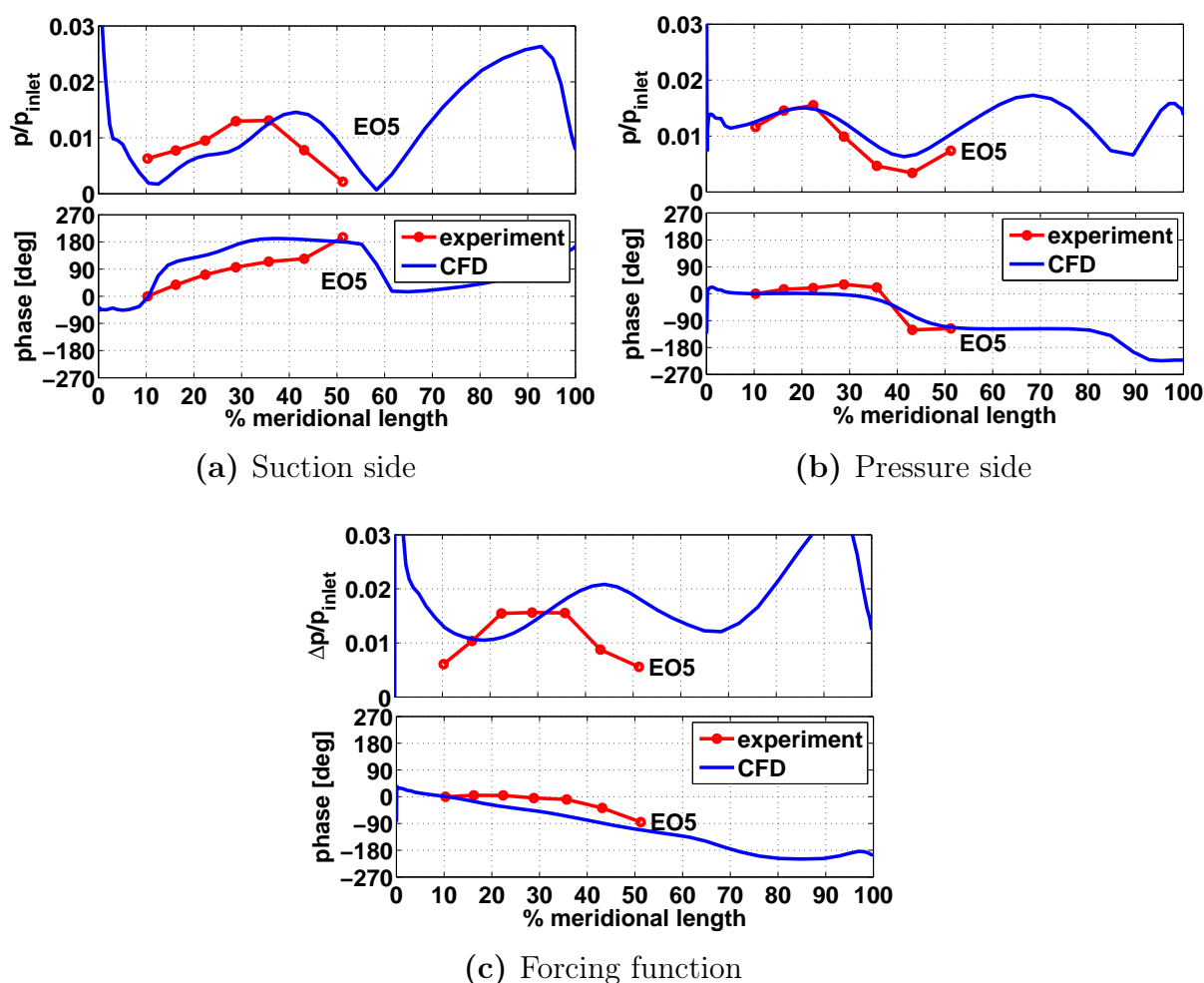


Figure 5.19.: Experiment and CFD comparison for **5 lobe** screen and OL1.

resonance point. As was mentioned previously, the experimental data had to be extracted at a speed situated at off-resonance in order to avoid modulations of the measured pressure due to vibratory motion. It should be pointed out, that in order to directly compare the phase functions, the computed and experimental phase functions had to be referenced to the phase at 10% blade length. This was required because the absolute angular position of the impeller blade did not match the experiment and would cause a considerable constant phase shift during a comparison.

Figure 5.19 compares measurement and computation for the suction and pressure side as well as the forcing functions, i.e. $\Delta p/p_{inlet}$. For both cases the EO5 harmonic is plotted. For the suction as well as the pressure side a good match can be identified for the amplitude. The computation captured flow features that lead to local maxima and minima along the blade. In terms

of phase prediction the trends were well captured. On the suction side the phase was predicted such that the direction of pressure wave propagation was predicted correctly, i.e. forward traveling waves, while the slopes are identical too. The magnitude of the phase however appears to be overpredicted and might stem from referencing both functions to 10% blade length. On the pressure side a very good match was achieved for the phase functions.

In terms of forcing function prediction the resultant pressure difference across the blade does not match when examining the excitation amplitude. The amplitude level is generally correct, however the location of the predicted maximum is shifted by about 20% of the meridional length. In terms of the phase relationship, the measurements reveal an almost all-in-phase excitation along the blade up to 40% blade length. Further downstream a fall-off can be seen. The predicted phase however, reveals a constant phase slope along the blade. Its inclination is an indication for excitation waves traveling downstream.

To conclude, the computational prediction for the datum operating point captures flow phenomena that lead to the measured unsteady pressure distribution along the blade surfaces. This in particular applies to the phase relationship. However, it was found that rather minor disagreements on the separate blade sides could have a profound impact on the resultant forcing function. Overall, the above observation render the computation valid and allow further studies of the flow field based on computation. The involved complexity of unsteady pressure distribution on the entire blade surface is presented in the following section.

5.4.4. Pressure Wave Evolution along Blade Surface

According to the measurements and the computation, in the datum case pressure waves propagate upstream along the blade surface. In order to visualize this phenomena the EO5 harmonic of the unsteady pressure distribution was plotted in figure 5.20. Shown are five successive instances in time of the fluctuating pressure component for approximately a tenth of a revolution. The time steps t_1 to t_5 were selected such that the propagation of pressure waves along the surface became visible.

Generally, multiple zones of different pressure amplitudes can be identified on the suction side. Two pressure wave fronts were marked with WF1 and WF2

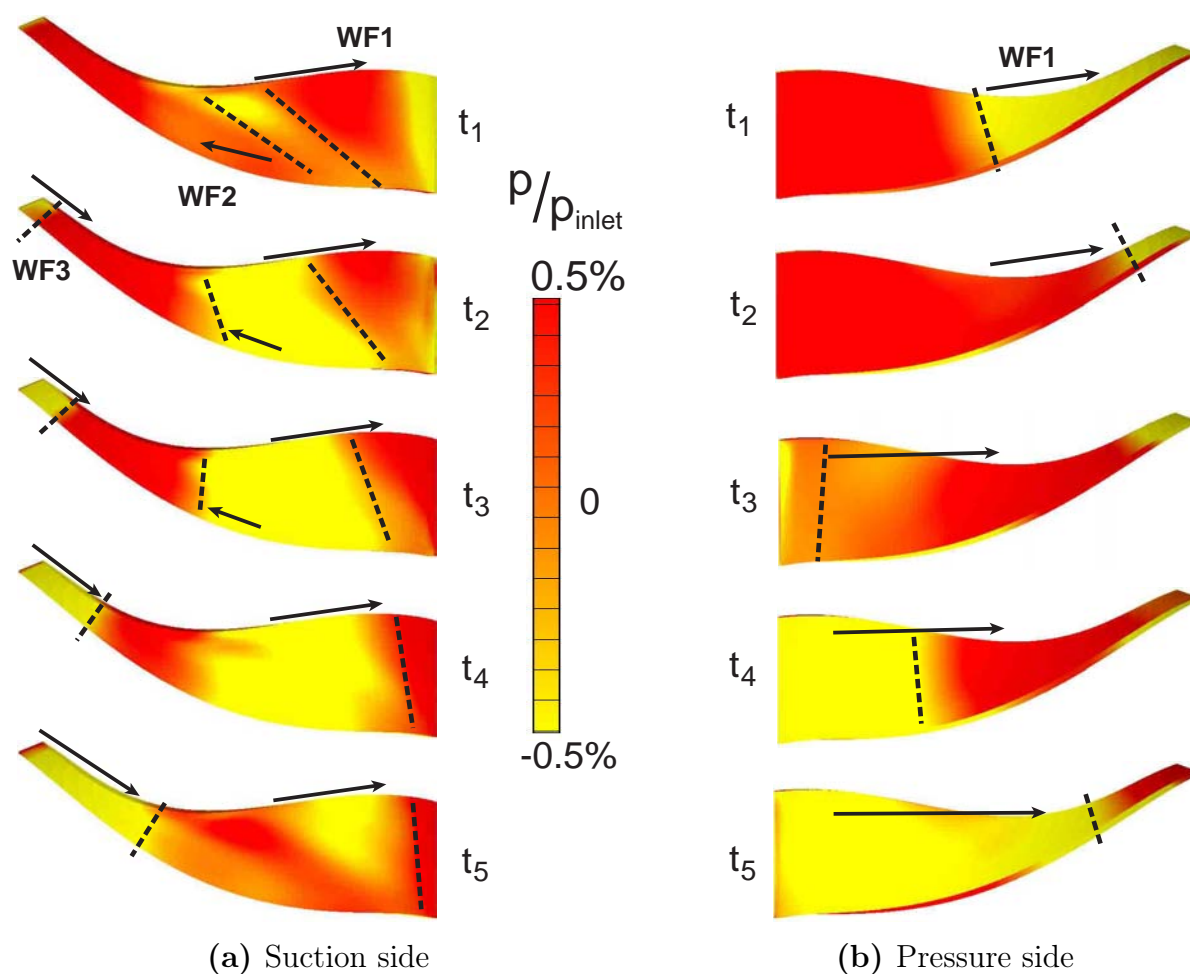


Figure 5.20.: **EO5** amplitude and phase for **5 lobe** screen at **16000rpm**.

for the first time step, t_1 . The two pressure waves are traveling into opposite direction with WF1 traveling upstream and WF2 traveling downstream. For the time step t_2 , the pressure wave fronts have drifted further apart. At the outlet of the impeller a third pressure wave front, WF3 can be identified to propagate upstream. As the time progresses, WF1 can be seen to extend from hub to tip and to move towards the blade leading edge.

The shown temporal evolution of the pressure distribution reveals the involved complexity of multiple pressure zones to propagate along the surface. With respect to pressure measurements this indicates the following problematic. As can be seen for example for the time step t_1 the zone between WF1 and WF2 exhibits maximum excitation amplitudes. This is the case in the computation as well as in the experiment. The fundamental principals to cause this pattern are not understood, but considering the relatively low amplitudes of

around 1.5% of the inlet pressure it bears the potential to be sensitive to external factors. Pressure measurements presented earlier were taken along the blade mid-height with the sensors 5 and 8 being located in the zone between WF1 and WF2. Since this is a critical zone, in the authors' opinion, mismatches between the computation and the experiment were likely to occur. In other words, the validation of computational results might be sensitive to the placement of pressure sensors. Although the overall blade pressure distribution might be well predicted, a point to point comparison between the experiment and the computation might yield a disagreement purely based on the fact that the comparison is carried out within a zone critical to predict.

On the pressure side the pressure distribution shows a single wave front to propagate from the inlet to the outlet of the rotor. Isobars extend from the hub to the tip and are perpendicular to a line along the blade mid-height. According to the phase plots presented earlier, the unsteady pressure varies simultaneously for the entire inducer portion of the blade. Towards the exit of the impeller, WF1 can be seen to propagate downstream. Overall, the pressure distribution appears to be simpler in nature compared to the suction side. It is for this reason that a better match between the experiment and the computation was found.

In summary, the unsteady pressure distribution on a blade surface is composed of pressure zones of opposing pressure wave propagation. In order to understand the origin of these zones a detailed research on the flow dynamics would be necessary. A comparison between experimental and computational data should be carried out with care for sensors that are placed on the boundaries between the pressure zones.

5.5. Analysis of Resonance Case Mode1/EO6

This section discusses results obtained for the Mode1/EO6 excitation case. This case is insofar important for this study as it enables to compare two responses for the same excitation order, EO6, which was generated using two different inlet distortion screens. In the first case a screen with 3 lobes was used to generate the second harmonic, i.e. EO6 excitation, whereas in the

second case a 6 lobe screen was employed to generate the same excitation order.

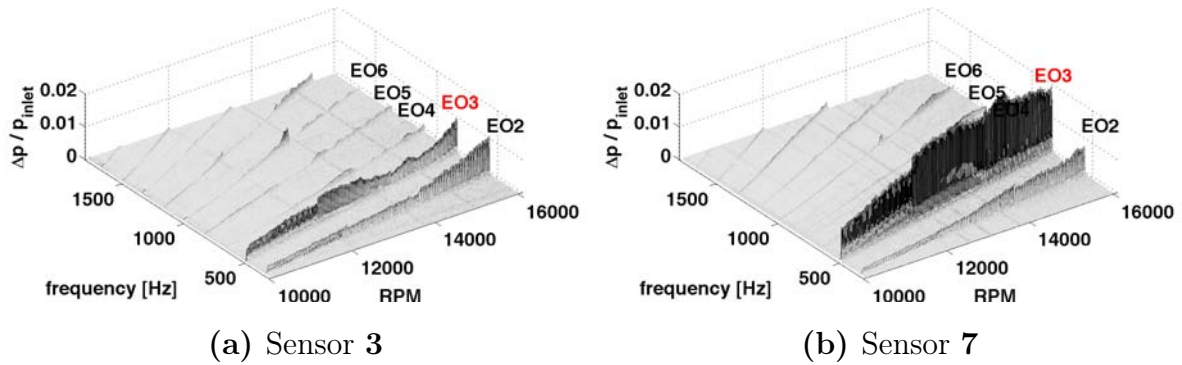
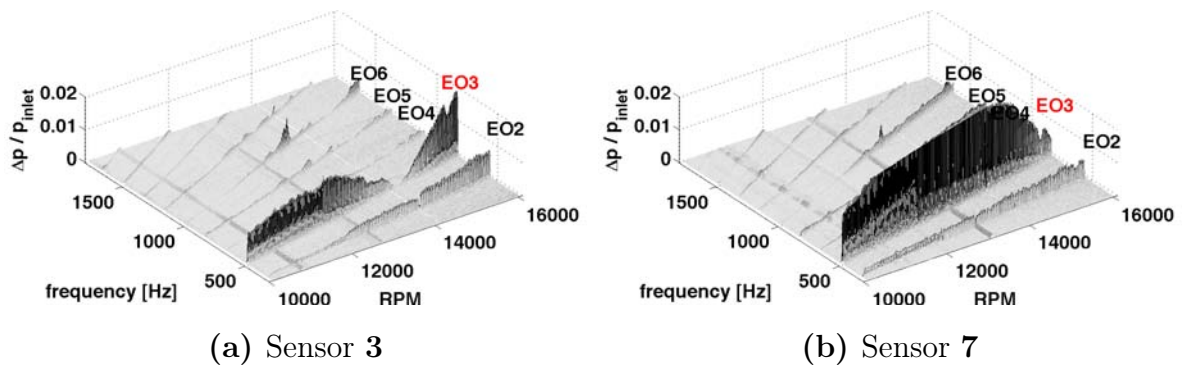
Unsteady computation was not performed for both cases, however steady results were performed to render possible an assessment of the flow conditions. Briefly, the relative Mach number at impeller inlet ranges from around $Ma = 0.3$ to $Ma = 0.35$ for the operating lines OL1 to OL3. In general, the flow field within the blade passages is of similar structure as it was shown for the 5 lobe screen presented earlier. As would be expected, the main difference was found with respect to the overall Mach number amplitudes which were smaller due to lower rotational speeds of the impeller. Relative mach numbers within the impeller passages ranged from $Ma = 0.25$ on the pressure side of the blades to $Ma = 0.6$ on the suction side at the exit of the impeller. Therefore, the flow field was within the compressible regime but with a substantial margin from localized sonic conditions.

5.5.1. Spectral Functions

Case with 3 lobe screen

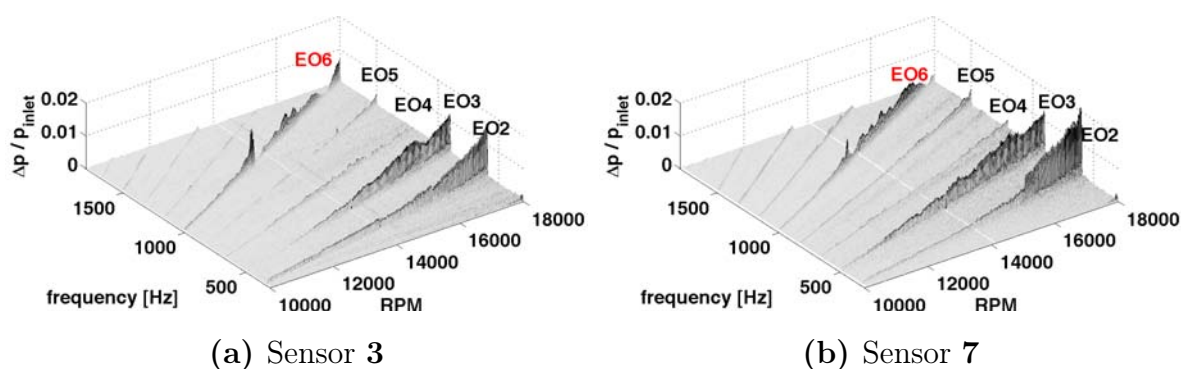
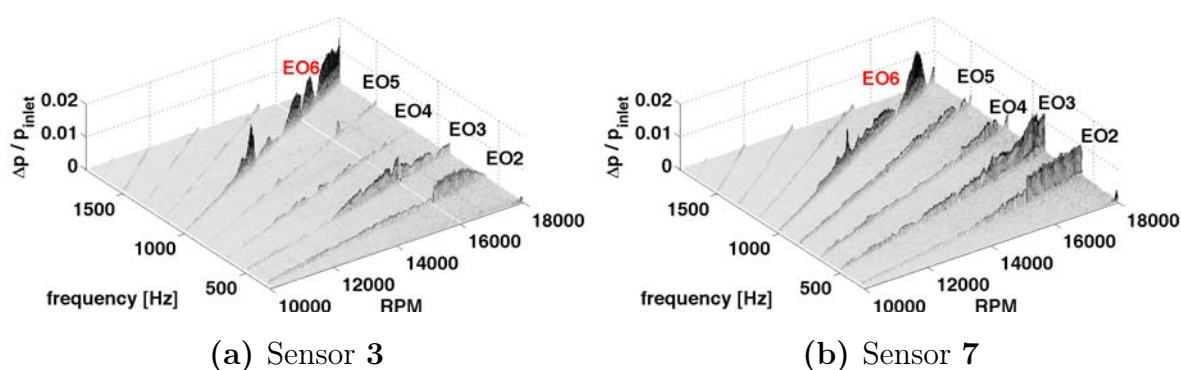
The unsteady pressure spectra for measurements with the 3 lobe screen taken at sensor position 3 and 7 are shown in figures 5.21 and 5.22 for the operating lines OL1 and OL3, respectively. The measurements cover a speed range up to 16000rpm. In comparison to the results presented earlier, the EO2 excitation is of similar amplitude. The major difference can be seen with respect to the EO3 amplitude evolution. As expected, the amplitude for this harmonic is considerably higher, in particular at sensor position 7 for both operating lines. With a 3 lobe distortion screen the EO3 harmonic reveals an evolution which does not simply increase in amplitude with rotational speed but undergoes speed dependent alternations. For example, in figure 5.22 sensor 3 shows a reduction in amplitude at 14000rpm to zero followed by a sudden increase towards higher speeds. This feature was not experienced previously for this harmonic.

Particular attention should be drawn towards relating inlet flow distortion to measured unsteady pressure, i.e. the realization of a given distortion pattern into excitation amplitude. Measurements on inlet flow distortion showed that the distortion level in terms of axial velocity or total pressure was com-

Figure 5.21.: Excitation spectra for **3 lobe** screen and **OL1**.Figure 5.22.: Excitation spectra for **3 lobe** screen and **OL3**.

comparable between all screen cases. However, the realization of inlet flow distortion in terms of measured excitation amplitude appears to be different. In the case shown here, the EO3 excitation reveals amplitudes far in excess of $p/p_{inlet} = 2\%$ whereas in the case of the 5 lobe screen the excitation amplitudes hardly exceeded this threshold. It appears, that for comparable distortion amplitudes the generation of lower harmonics, i.e. EO3, is higher than for higher harmonics, i.e. EO5. This is supported by the finding that in the case of the 5 lobe distortion screen EO5 is of comparable amplitude as EO2 and EO3, although the latter two are hardly detectable in the inlet flow distortion pattern.

In addition to the fundamental excitation order, the second excitation harmonic, EO6, was generated on the blade surface. As will be shown in the chapter on resonant response, EO6 was found to generate sufficient excitation to cause resonant response at 13500rpm. In the spectral plots of the unsteady pressure the EO6 harmonic can be identified to be contained within the flow field. Its amplitude is relatively small in comparison to the intended

Figure 5.23.: Excitation spectra for **6 lobe** screen and **OL1**.Figure 5.24.: Excitation spectra for **6 lobe** screen and **OL3**.

EO3 harmonic for all pressure sensor cases shown. In accordance with the Mode1/EO5 case, resonance can be identified at 13500rpm where the measured pressure experiences a localized peak due to blade vibratory motion.

Case with 6 lobe screen

In line with the results from the previous case, unsteady pressure spectra are shown for the operating lines OL1 and OL2 in the figures 5.23 and 5.24, respectively. The amplitude evolution of the lower harmonics EO2 and EO3 is very similar to the results obtained for the 5 lobe screen and the case without a distortion screen. The fundamental excitation order can be clearly identified in the spectra as EO6 excitation. As it was shown for previous cases, its amplitude is comparable with lower harmonics.

5.5.2. Harmonic Functions along Blade at Mid-Height

The harmonic functions for both screen cases are shown in the figures 5.25 and 5.26. The data shown was acquired at a rotational speed of 13200rpm which is below the resonant speed of 13500rpm. As was shown previously this approach was necessary in order to avoid contamination of the measurement signal by effects due to blade motion. This way purely the excitation functions could be obtained. The plots illustrate a comparison of the EO6 harmonics for the operating lines OL1, OL2 and OL3.

To start, the measured amplitudes will be discussed. In the case of the 3 lobe screen the amplitudes on the suction and pressure side reach values of approximately 0.25% of the inlet pressure. In contrast, the amplitudes for the 6 lobe screen are double in amplitude with mean values around 0.5% of the inlet pressure. This difference was already perceivable from the spectral plots. In all cases no particular difference in amplitude can be observed between the operating lines. However, what should gain attention is the similarity between the function shapes for the two screen cases. Comparing the amplitude functions between the screen cases for the same blade side and operating line shows, that their shapes are almost the same but with different amplitudes. This finding indicates, that the generation principal of the amplitude distribution of the EO6 harmonic along the blade is independent of the exact composition of inlet boundary conditions. It seems, the excitation amplitude that is realized on the blade depends only on the EO6 harmonic amplitude in the inlet flow field. It is very weakly affected by other harmonics.

For both screen cases the phase on the suction side of the blade shows pressure waves to travel upstream along the blade surface. This is in accordance with data presented for EO5 with 5 lobe inlet distortion. On the pressure side, pressure waves are almost in phase for up to 30-35% of the blade length. From 40% blade length the phase relationship shows the pressure waves to travel downstream. Also this behavior corresponds to the findings related to the phase of EO5 excitation. The amplitudes for the datum case were shown to agree between the two screen cases. This is also the case for the phase. Case to case comparison of the phase relationship reveals the phase functions to be of the same shape. This confirms the previous findings that a pressure field of EO6 excitation establishes within the impeller flow field and is only weakly coupled to the overall flow conditions.

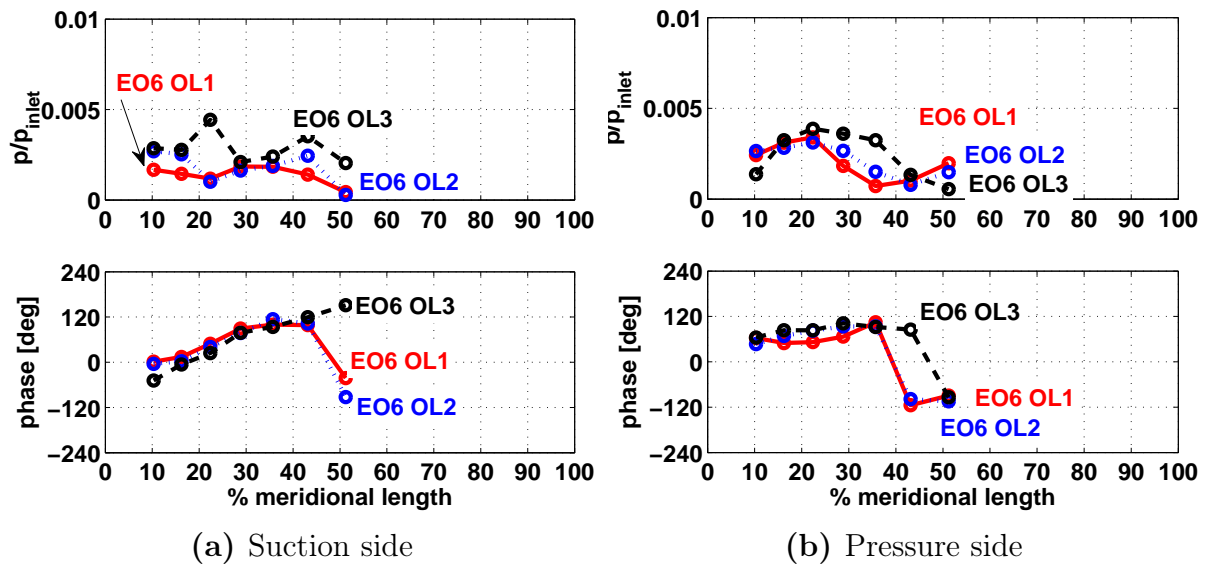


Figure 5.25.: EO6 amplitude and phase for 3 lobe screen at 13200rpm.

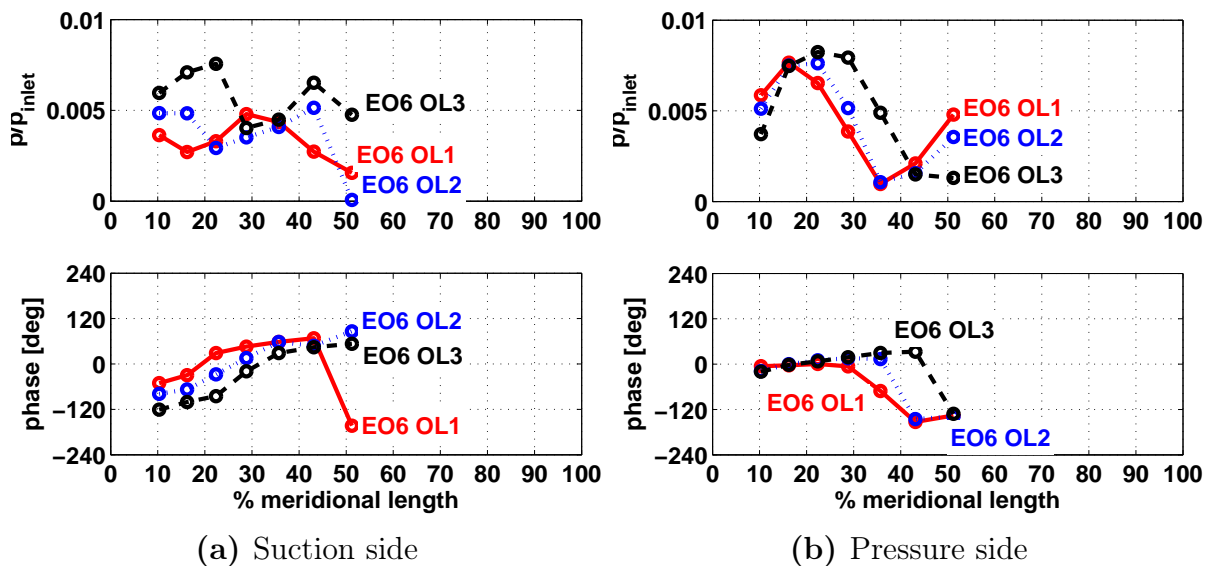


Figure 5.26.: EO6 amplitude and phase for 6 lobe screen at 13200rpm.

5.6. Unsteady Pressure during Resonant Response

In the previous sections unsteady pressure measurements were presented for off-resonance conditions which allowed to quantify the excitation amplitudes of the relevant harmonics. This section presents pressure measurement results during resonance in which case the measured pressure is affected by the blade vibratory motion. This section aims to clarify this phenomenon.

All results presented hereafter are related to data taken during resonance at 16200rpm and EO5 excitation for operating line OL1. As the impeller passes through resonance, blade deflection causes a pressure field around each blade which is superposed on the unsteady pressure caused by inlet flow distortion. The resultant pressure is measured by the sensors situated on the blade surface. In order to illustrate this phenomena, figure 5.27 shows pressure and blade displacement in the frequency domain for the suction and pressure side, respectively. In both cases the pressure sensors are situated at sensor position 1. It is crucial for this experiment that the pressure and strain gauge signals were recorded simultaneously in order to preserve their phase and amplitude relationship. Blade normal displacement at each pressure sensor position can be calculated from measured strain and transmission factors that relate strain and displacement. The transmission factors are computed on the basis of FEM modal analysis for each mode.

Figure 5.27(a) shows the measured unsteady pressure to be approximately constant up to a speed of 16000rpm. The amplitude in this range corresponds to the unsteady pressure caused by inlet flow distortion and is therefore the unsteady forcing of EO5 excitation. The blade deflection in the same speed range is comparatively small, see figure 5.27(c). It is within resonance at 16200rpm where blade deflection reaches its maximum and causes a sudden rise in measured unsteady pressure. Due to mistuning and coupling, two response peaks can be observed on the displacement spectrum. Accordingly, both peaks can be identified in the pressure spectrum.

The same response pattern as for the suction side can be observed to occur for the pressure measured on the pressure side of the blade, figure 5.27(b). In this case, the pressure and the strain sensors are mounted on blade 4. During resonance this blade was subject to the highest deflection amplitudes,

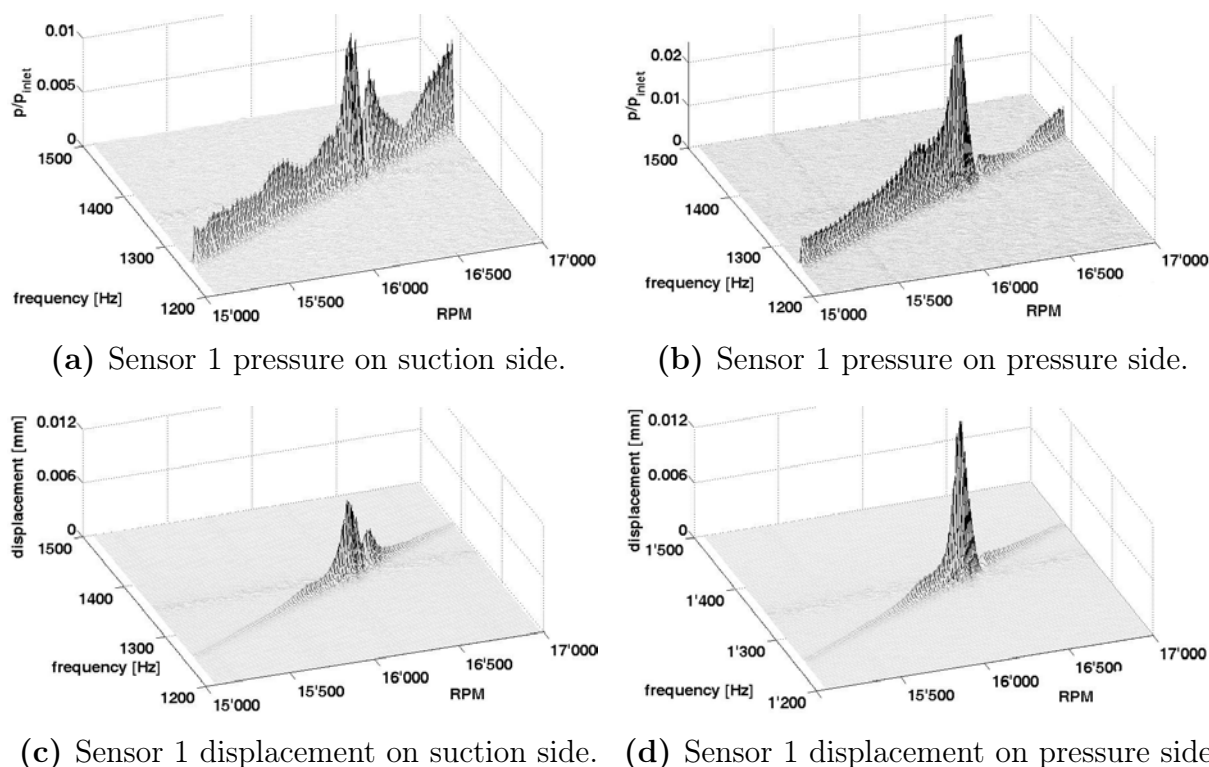


Figure 5.27.: Unsteady pressure and displacement for sensor 1 on the suction and pressure side. On the suction side (left) sensor was mounted on blade 1. On the pressure side (right) sensor was mounted on blade 4.

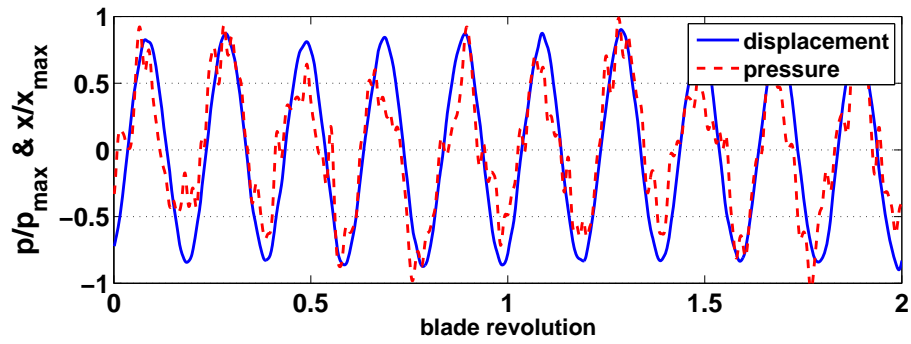
shown in figure 5.27(d), which ultimately caused the measured pressure to increase considerably during resonance. From these simple observations it can be stated that as the blade passes resonance the increase in measured pressure amplitude can be related to blade deflection. Quantification of the vibration induced unsteady pressure amplitude cannot be made, since the amplitude shown is a superposition of two signal sources and depends on the phase and amplitude of the contributors. Such an analysis would require their separation.

Further insight into the problem can be gained from examining the unsteady pressure traces taken during resonance. Figure 5.28 shows the pressure and the vibratory motion for the two cases already presented. For the given data sampling rate, each blade vibratory cycle is composed of ≈ 150 data points. In both cases vibration and pressure undergo harmonic oscillation. Observation of the signal in the time domain should be performed with care, since

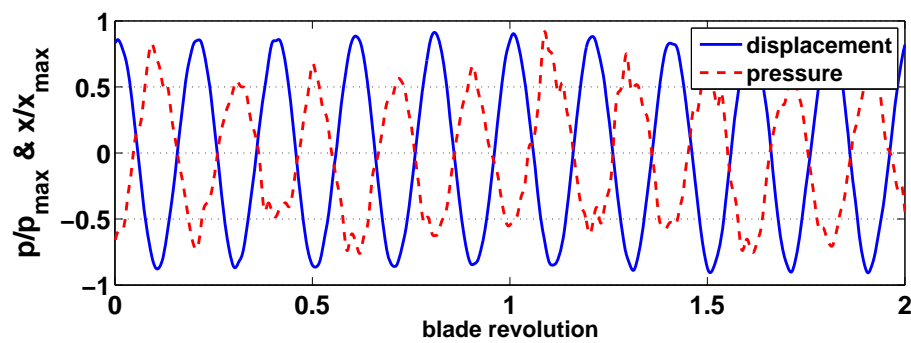
the traces shown contain information from the entire frequency bandwidth. As was shown previously, the unsteady pressure signal consists of a number of excitation orders of comparable amplitude. Observing the pressure trace shown on the suction side reveals that it predominantly follows the oscillatory blade motion. However, the amplitude is modulated due to additional frequencies contained in the flow field. On the pressure side this appears to be less the case, which can be explained by the fact that the vibratory motion is comparatively high causing an equivalent increase in unsteady pressure due to vibration.

There are a number of fundamental causes that couple the change in pressure to the blade motion, which are (1) due to fluid inertia normal to the blade surface, (2) due to incidence changes and (3) due to an increase in the through flow area. All three cases were numerically examined by *Schmitt* [70] for a turbine cascade where the third case was identified to cause unsteady pressure fluctuation that should be considered. Pressure fluctuations due to the incidence angle were found to be confined to the leading edge whereas acceleration effects caused negligible pressure amplitudes. In the datum problem the cause for blade coupled pressure fluctuations can be attributed to case (3) by identifying the phase relations on the suction and pressure sides. In the former case pressure and blade vibration are in phase, whereas in the latter case the signals are in counter phase. Considering the coordinate system in figure 5.29, it follows that as the blade moves into the positive direction this causes an increase of pressure on the suction side and a decrease on the pressure side. This relationship can only be explained by considering fluid deceleration on the suction side in the bulk flow direction due to an increase in the through flow area. The contrary manifests on the pressure side, where positive blade motion causes fluid acceleration in flow direction and a decrease in pressure. Arguing on this basis strong pressure fluctuations on the blade surface during resonance are primarily caused by local variation in through flow area thereby affecting local fluid velocity and pressure.

To conclude, the unsteady pressure measured by each pressure sensor at resonance is composed from superposing pressure fluctuations due to inlet flow distortion and pressure fluctuations due to unsteady blade motion. The latter is generally known to cause aerodynamic damping, i.e. it opposes blade motion.



(a) Suction side sensor 1 on blade 1.



(b) Pressure side sensor 1 on blade 4.

Figure 5.28.: Displacement and pressure traces during resonance.

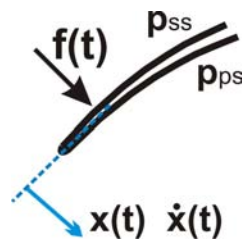


Figure 5.29.: Blade coordinates.

5.7. Summary and Conclusions

Measurement of unsteady pressure distribution was performed on the blade surfaces. Results were presented for measurements during off-resonance and during resonance conditions. The central objective of this chapter was the quantification of unsteady pressure acting on the blade surface for a number of inlet distortion cases. The following conclusions can be summarized for the case without a distortion screen, i.e. excluding the distortion effect due to a screen:

- In the case without a distortion screen the unsteady pressure acting on the blade surface is primarily composed of the EO2 and EO3 harmonics. Higher harmonics are contained in the flow field, however, their amplitudes are negligible.
- The generation of low order harmonics, i.e. EO2 and EO3, was identified to stem from wakes due to cylindrical struts positioned upstream of the impeller.
- Wakes generated by four vanes mounted upstream of the impeller had no effect on the EO4 harmonic. The EO4 harmonic was of the same amplitude as any higher harmonic measured on the blade surfaces.
- The amplitude of the unsteady pressure was found to depend on the rotational speed and the mass flow. An increase in rotational speed generally caused an increase in amplitude of EO2 and EO3 harmonics.

In the case of intentional distortion, screens with a 5 lobe, a 3 lobe or a 6 lobe pattern were employed. The conclusions can be summarized as:

- Distortion screens cause an unsteady pressure amplitude of the intended excitation order. The amplitude of the unsteady pressure amount values typically of around 1-2% of the inlet static pressure.
- Lower excitation orders in the distortion flow field are *better* realized as unsteady excitation on the blade surfaces, i.e. with an increase in engine order the excitation amplitude on the blades diminishes.
- Pressure waves on both blade surfaces travel predominantly upstream along the blade surface. The propagation speed reduced as the mass flow increases.

- The unsteady flow field in the blade passages creates zones of unsteady pressure waves that travel in opposite direction. Validation of CFD results with pressure sensors placed on the boundaries of these zones should be carried out with care.
- The distribution of the excitation amplitude and phase are independent of the overall inlet flow field. Therefore, for two different screens that generate the same engine order, the excitation distribution is the same. However, the absolute amplitude of the excitation order depends on the distortion amplitude at the inlet.

In the case of intentional distortion, the following conclusions were derived for pressure measurements during resonance:

- At resonance blades undergo vibratory motion and thereby induce an unsteady pressure component on the blade surface. This pressure component is superimposed on the unsteady pressure due to inlet flow distortion.
- In the inducer region, the vibration induced pressure was found to be higher in amplitude than the unsteady pressure due to inlet distortion.
- The cause of the induced unsteady pressure was identified to stem from local through flow area variations. As the blade vibrates, the through flow area effectively changes and thereby affects the local velocity and pressure.

6. Resonant Response

In the following chapter results on blade resonant response amplitudes are presented. First, the concept to model blade response will be outlined in order to provide an analytical formulation. The formulation is based on the Single-Degree-Of-Freedom (SDOF) modeling approach. Particular attention will be given to the importance of inlet pressure on the response amplitude. Second, the blade dynamic response will be presented for a blade passing through resonance. Third, the maximum response amplitude will be quantified and compared for a number of resonant crossing cases.

6.1. Transient Response and Maximum Amplitude

Predictions of high cycle fatigue endurance requires the quantification of the maximum alternating stress amplitude within the vibrating component. Two main scenarios can be distinguished in this matter. First, the maximum stress amplitude is constant. This is the case for a scenario where the shaft speed is constant at a frequency within the resonance regime. Second, the maximum stress amplitude varies during transient resonance crossing. In this scenario the shaft accelerates or decelerates between two operating points and thereby crosses resonant conditions. For both of the two presented scenarios, the stress amplitude and the number of cycles must be estimated for fatigue predictions. The importance of the two scenarios depends on the type of machine and its operating characteristic. For example, engines that operate at constant speeds for most of the time might experience high order resonance. In this case vibrating components are subject to a constant vibration amplitude.

For different applications, engines i.e. turbochargers, are subject to frequent changes in operating points and might therefore be subject to regular excitation during resonant crossing. The maximum response amplitude experienced during resonant crossing depends primarily on two factors. First, the over-

all blade damping and second, the exposure time to resonance. Both affect the vibratory amplitude reached during resonant crossing. In order to assess the maximum amplitude during resonance transients, models are required. Transient response models for turbomachinery blades were published in the works by *Irretier* [34, 35] and *Leul* [50]. Their methods went beyond the capabilities of a SDOF formulation of the response problem and were aimed at predicting the vibratory amplitude. The models allowed them to include the effects of changes in blade natural frequency due to stiffening and non-linear damping due to friction. For centrifugal compressor types such as used in this study, natural frequency changes are negligible and damping can be assumed independent from the rotational speed. Therefore, for reasons of simplicity, in the following a SDOF formulation was adopted and shown to agree very well with the experiment. However, it should be pointed out that the model requires calibration prior to its application.

6.1.1. Modeling Transient Blade Response

In order to understand the response characteristics of a blade under transient forcing conditions, a Single-Degree-Of-Freedom Model (SDOF) can be used to simulate the problem. The underlying concept herein is to adopt a formulation that allows to compute the response of the vibrating blade in the time domain as a function of blade damping, resonant frequency and any arbitrary excitation function. In this study the excitation function is defined in the time domain as a function of rotational speed and excitation order in order to resemble the conditions experienced during experimental testing. The critical damping ratio and resonant frequency of the SDOF model represent the modal properties of a single blade. The SDOF system is described by the second-order ordinary differential equation of the form

$$m\ddot{x} + c\dot{x} + kx = F(t) \quad (6.1)$$

with x representing the blade displacement amplitude. The forcing function herein is given by the following equation

$$F(t) = F_0 \cos[2\pi f(t)t + \phi_0] \quad (6.2)$$

where the frequency sweep $f(t)$ is modeled using the relation

$$f(t) = \frac{1}{2}\beta t + f_0 \quad \text{with} \quad \beta = \frac{f - f_0}{t - t_0} \quad (6.3)$$

The frequency as a function of time essentially resembles the constant impeller sweep rate during the measurements. The solution of the differential equation given above can be numerically obtained through interpolation of the excitation function and employment of the linear response of a SDOF system to step excitation. Details on this procedure can be found in *Craig and Kurdila* [8]. The evaluation of this approach yields the recurrence formulas

$$x_{i+1} = a_1 F_i + a_2 F_{i+1} + a_3 x_i + a_4 \dot{x}_i \quad (6.4)$$

$$\dot{x}_{i+1} = a_5 F_i + a_6 F_{i+1} + a_7 x_i + a_8 \dot{x}_i \quad (6.5)$$

where the response x_{i+1} can be calculated for a discrete time step Δt and a given forcing function. The latter is given as a vector computed by the use of the above equations. The coefficients a_1 to a_8 are functions of damping, resonant frequency and time step and are provided for a viscous lightly damped system.

In order to compute the dynamic response of a vibrating blade using the above recurrence formulas, blade damping and resonance frequency must be provided, in this case from the experiment. Both of these quantities were acquired according to the procedure outlined in Chapter 7. Blade damping and sweep rate are the major parameters to affect the dynamic response amplitude and envelope shape of the response. Therefore, both of these parameters must be adjusted according to the measurement conditions.

A simple parametric study should be presented here. Figure 6.1 shows the amplitude of the dynamic response as a function of rotational speed during transient crossing of resonance. The computation resembles conditions experienced for the Mode1/EO5 resonant case in terms of (1) rotational speed range, (2) inlet pressure, (3) eigenfrequency, (4) sweep duration Δt and (5) damping ζ . The latter two parameters were varied in this example in order to show their effect on the amplitude and shape of the response. The response amplitude was non-dimensionalized with a reference value taken from the case $\Delta t = 15s$ and $\zeta = 2\zeta_M$.

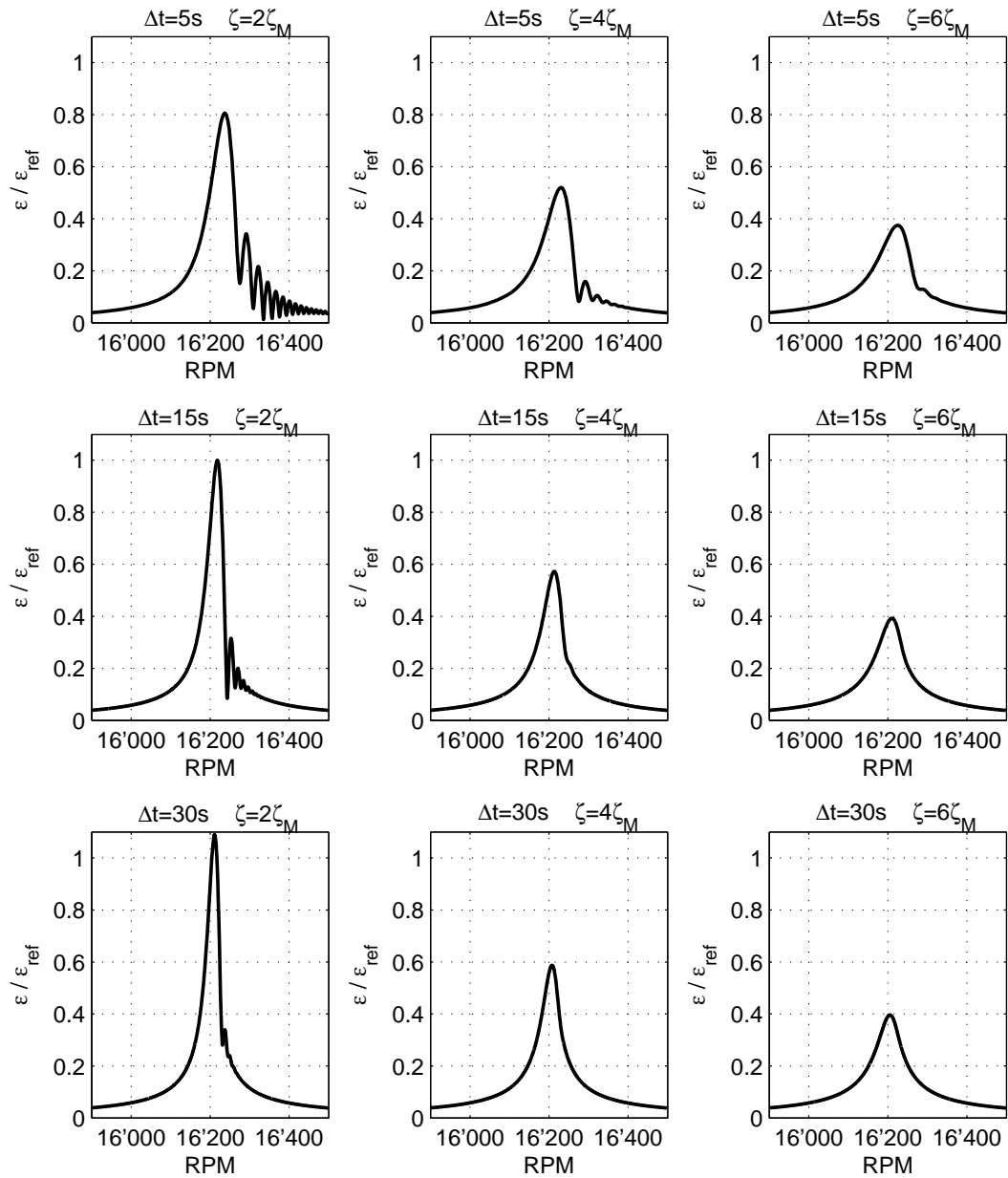


Figure 6.1.: Parametric study of dynamic response based on a SDOF model. Transition duration through resonance Δt and damping ζ are varied.

First, as would be expected the effect of damping can be observed to cause a reduction in maximum response amplitude. The excitation force was kept constant. Damping is expressed as a multiple of material damping ζ_M which is a constant value for all cases and can be ideally used as a reference quantity. An increase in damping by a factor of three, from $2\zeta_M$ to $6\zeta_M$, caused a reduction in response amplitude by 60%. Furthermore, damping affects the response envelope after resonance has occurred, i.e. above 16250rpm. Strongest amplitude alterations can be observed in this speed regime for the case $\Delta t = 5s/\zeta = 2\zeta_M$. However, the amplitudes are far below the maximum value and are therefore not relevant for high cycle fatigue assessment.

Second, the effect of sweep duration is important to be considered during measurements. According to equation 2.1 in section 2.5 a minimum sweep rate is required in order to obtain the maximum amplitude. For the datum resonant case and speed range this translates to a sweep duration of 15s. This value was used during the experiment. The effect of reducing the sweep duration to 5sec reduces the maximum response amplitude for a given damping, i.e. to approx. 80% for $\zeta = 2\zeta_M$. The effect is more pronounced for the low damping case. More important is the fact that increasing the sweep duration to 30sec does not considerably alter the experienced amplitude, i.e. approx. 10% for $\zeta = 2\zeta_M$. Therefore, from the perspective of experimental research the sweeping time can be optimized as a trade off between maximum amplitude loss and the goal to limit data recording.

6.1.2. Resonant Amplitude Dependency on Inlet Pressure

The inlet pressure is the major parameter in this study. Therefore, the experimental procedure was carried out such that each resonant crossing measurement was performed for a number of inlet pressure settings. The importance of varying the inlet pressure in this study is reflected in the fact, that both the excitation force acting on the blade surface as well as the overall critical damping ratio scale with density which depends on the inlet pressure of the test facility. In more specific terms, on the one hand unsteady forces acting on the blade surface depend on the unsteady pressure difference between the suction and the pressure side. These pressure differences scale with the inlet pressure and thereby scale the unsteady force that causes resonant response. On the other hand, damping in a centrifugal compressor is mainly composed

of aerodynamic damping, which is driven by blade vibratory motion and the resultant unsteady force that acts on the blade. Again, this force depends on the unsteady pressure distribution which scales with the overall pressure level in the facility. Under these circumstances the excitation force and the critical damping ratio are expressed in the following way

$$F(p) = F_{ref} \left(\frac{p}{p_{ref}} \right) \quad (6.6)$$

$$\zeta(p) = \zeta_M + \zeta_{A,ref} \left(\frac{p}{p_{ref}} \right) \quad (6.7)$$

The overall damping consists of two contributors, namely the material ζ_M and the aerodynamic damping ζ_A of which only the latter is subject to scaling. An in-depth investigation of this problem is presented in Chapter 7 for a number of resonant cases. For a SDOF system the maximum response at resonance x_{res} is a function of the excitation force and the damping

$$x_{res} = \frac{\frac{1}{k}F}{2\zeta} \quad (6.8)$$

The force and the damping can be substituted by the pressure dependent functions given above which yield the following function

$$x_{res} = \frac{\frac{1}{k}F_{ref} \left(\frac{p}{p_{ref}} \right)}{2 \left(\zeta_M + \zeta_{A,ref} \left(\frac{p}{p_{ref}} \right) \right)} \quad (6.9)$$

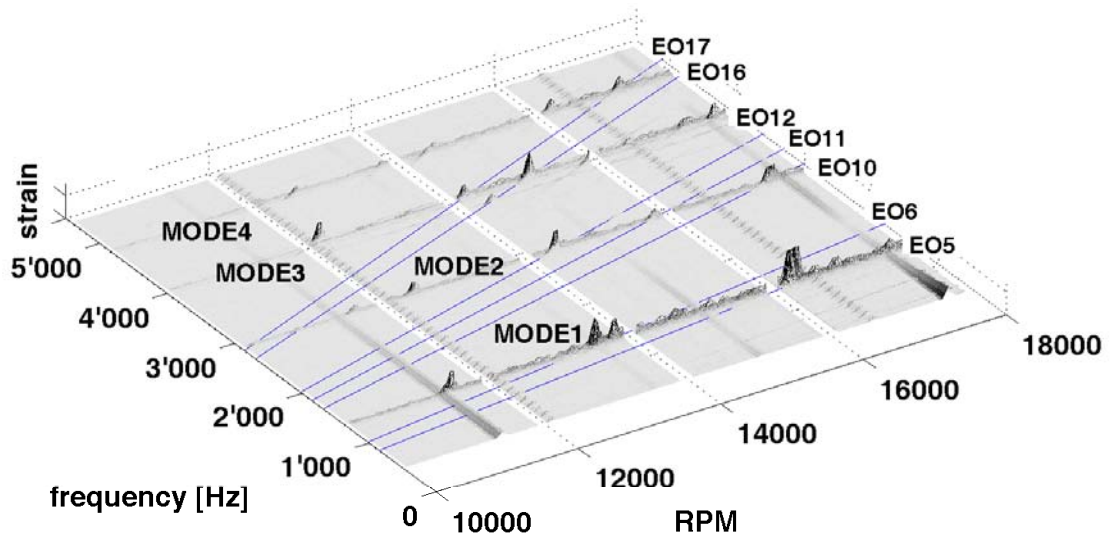
There are essentially two conclusions to draw from this relationship. First of all, as the pressure approaches vacuum conditions the force and the aerodynamic damping reduce to zero. Therefore, in this operating regime material damping has a major influence on the relationship. Secondly, towards high pressure settings the response amplitude is asymptotic since the excitation force and the aerodynamic damping are scaled equally and mechanical damping becomes negligible.

6.2. Blade Response without Installed Distortion Screens

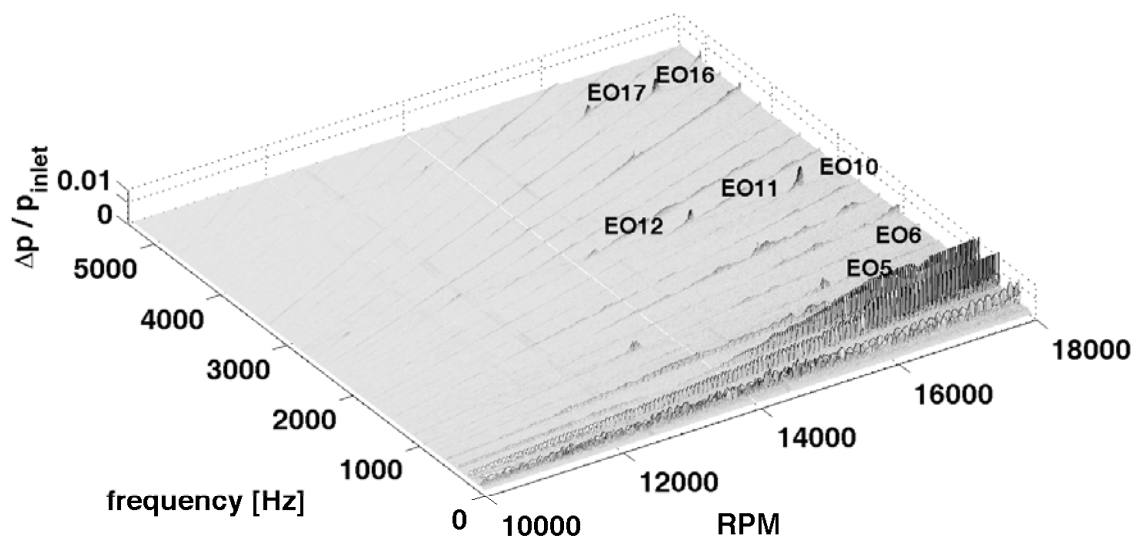
Following the measurement procedure described in section 2.5 the main blade response was measured for an inlet configuration without a distortion screen. The aim was to quantify blade response due to excitation harmonics contained in the upstream flow field although a distortion screen was not installed. The need to do so stems from the findings presented in section 5.2 on the unsteady pressure distribution. These indicated, that in the absence of a distortion screen, the unsteady blade pressure is mainly composed of the EO2 and EO3 excitation and in addition, higher harmonics were detectable and therefore represented sources for potential blade excitation. Figures 5.1 and 5.2 show the corresponding harmonics measured on the blade surface. Generally, higher harmonics than EO3 could be detected with comparatively low amplitudes.

The blade response spectrum and the corresponding unsteady pressure spectrum are shown in figure 6.2 in which case both signals were measured simultaneously for an operating line close to the stability limit (OL1). The case shown is representative for strain response experienced for a maximum rotational speeds of 18000rpm. The first main blade mode, Mode 1, can be identified to respond at 1350Hz. Measurements showed that the increase in natural frequency due to centrifugal stiffening is 1.5% over the speed range shown and is considered to be negligible. The response for Mode 2 occurs at 2875Hz. The natural frequencies for Mode 3 and Mode 4 are situated well above the 12th engine order excitation and will not be considered in detail.

The following illustrates the potential of the given system to generate a number of resonant responses for a configuration without distortion screens. In particular Mode 1 was excited by EO5 and EO6. Mode 2 resonates with an excitation stemming from the harmonics EO10, EO11 and EO12. All of the mentioned excitation orders can be identified in the pressure spectrum. The harmonics EO6 and EO12 can be assumed to stem from a distortion introduced by upstream and downstream struts within the flow field. Other harmonics, i.e. EO5, EO7 and EO11 might be combinations of lower excitation orders. Despite the fact that the maximum strain amplitude generated by these engine orders is fractional compared to the fundamental frequencies, their very existence requires awareness of a potential contributor to high cycle fatigue.



(a) Strain response spectrum.



(b) Unsteady pressure spectrum measured at sensor position 3

Figure 6.2.: Strain response and unsteady pressure spectra for the case without distortion screen.

6.3. Overview on Measured Resonant Response Cases

In the following sections results are presented and discussed for a number of different cases of excitation that can be distinguished depending on the distortion screen used, engine order excitation and response mode. These cases are

- **Mode1/EO5** at **16250rpm** response is obtained from fundamental excitation as generated by a 5 lobe distortion screen. For this case the response amplitude is the highest in comparison to all other cases considered since vibration is driven by the fundamental excitation frequency.
- **Mode1/EO6** at **13500rpm** response is obtained from the second harmonic excitation generated by a 3 lobe screen.
- **Mode2/EO12** at **14370rpm** response due to the third harmonic excitation generated by a 4 lobe screen.

For the latter two cases excitation is provided through harmonics which are contained in the flow field in addition to the fundamental excitation corresponding to the screen design.

6.4. Results

Two aspects of the results will be discussed. First, the dynamic response of the blade will be presented and compared to a SDOF system. This will make allowance to judge the capabilities of a SDOF model to predict the dynamics. Second, the maximum response amplitude will be presented as a function of inlet pressure. This quantity is important for high cycle fatigue predictions.

6.4.1. Mode1/EO5 - Dynamic Response Characteristic

Figure 6.3 shows the acquired strain amplitude for the frequency spectrum and speed range of interest. Mode 1 and 2 can be clearly identified as previously presented. The excitation stemming from EO5 is sufficiently strong to remain traceable within the entire speed range before and after resonance occurred. Resonant response can be seen to undergo at 16250rpm and will

be presented in detail.

The dynamic response of a selected blade during transient measurement for a constant sweep rate and an inlet pressure settings of 0.1bar is shown in figure 6.4. The amplitude was normalized with its maximum value. Complementary to the measured data, the calculated response is plotted using the recurrence formulas for the SDOF system introduced earlier. The amplitudes in the graph are scaled to unity since the model requires calibration in order to yield the correct amplitude. A crucial parameter for the computation is the critical damping ratio ζ which was estimated from experimental data using an amplitude-fit method, see chapter 7. As the speed during the sweep increases, the response amplitude grows to a maximum at approximately 16170rpm. For this particular blade the difference in rotational speed from the ideally expected speed of 16250rpm arises due to mistuning. Figure 6.5 shows the strain traces at resonance for all three strain gauges installed on a blade. Since the first mode shape was measured in this case, the signals are in phase and resemble a sinusoidal function. With further increase in speed the response amplitude is modulated and its envelope is characterized by successive occurrence of lobes and nodal points.

Using the Hilbert transformation the envelope of the time signal is plotted in figures 6.6(a-d) for an inlet pressure of 0.1bar – 0.4bar. Measured data was averaged across all blades of the impeller after the Hilbert transformation in order to obtain a mean response characteristic. The rotational speed axis was normalized for each blade separately with its respective resonance speed. Error bars indicate the variation of the available samples used for averaging. For all four pressure cases excellent agreement between the measurements and the SDOF dynamic model can be observed for the ascending portion of the first lobe and the resonance regime. Moreover, the sample variation, as indicated by the bars, is negligibly small before resonance indicating very good agreement between the various samples taken. Peaks within the plots, i.e. at 80rpm in the figure 6.6(b), stem from signal interferences between the system and the rotary transmitter. Their effect was generally confined to a limited speed range.

As was shown previously, there are two parameters that influence the envelope shape, the critical damping ratio and the sweep rate. Although the latter was held constant, it should be mentioned that with an increase in sweep

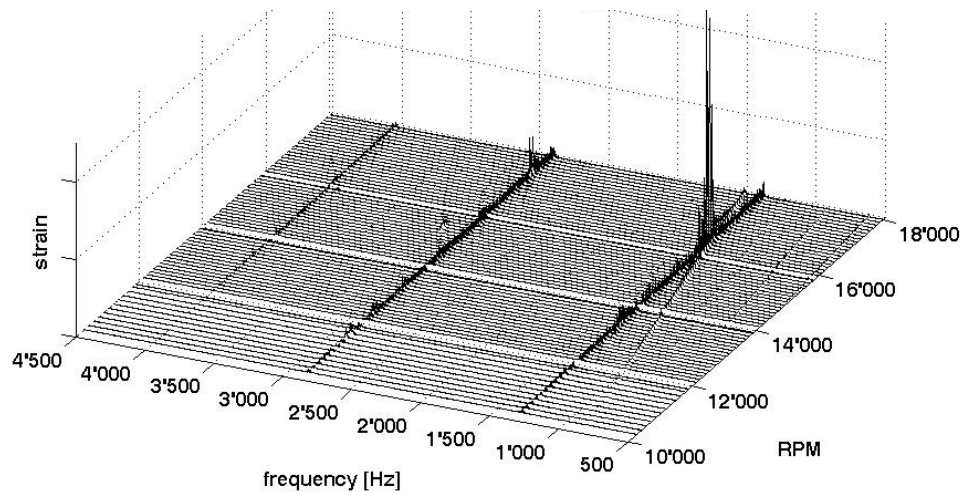


Figure 6.3.: Blade response spectrum for flow distortion with 5 lobe screen.

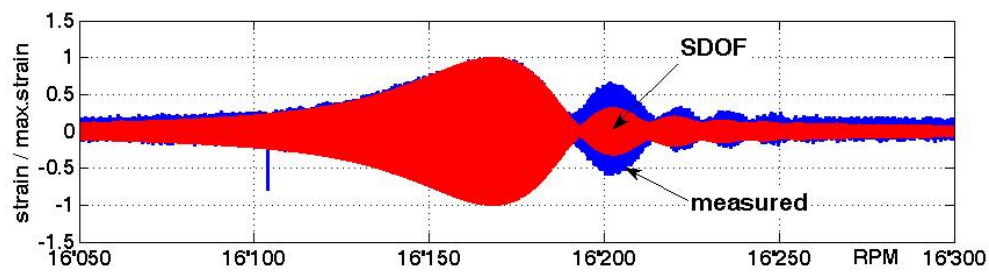


Figure 6.4.: Dynamic response at 0.1 bar inlet pressure for main blade 7 for Mode1/EO5

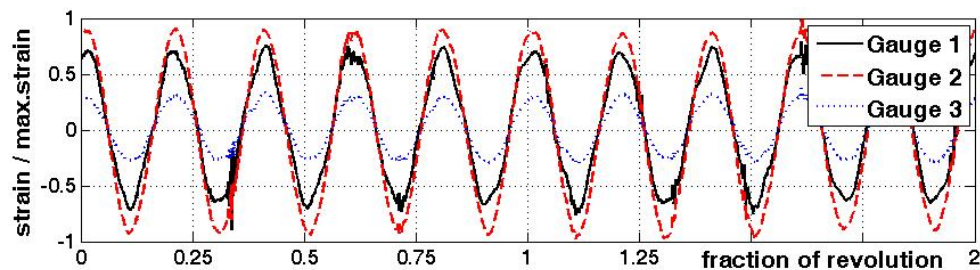
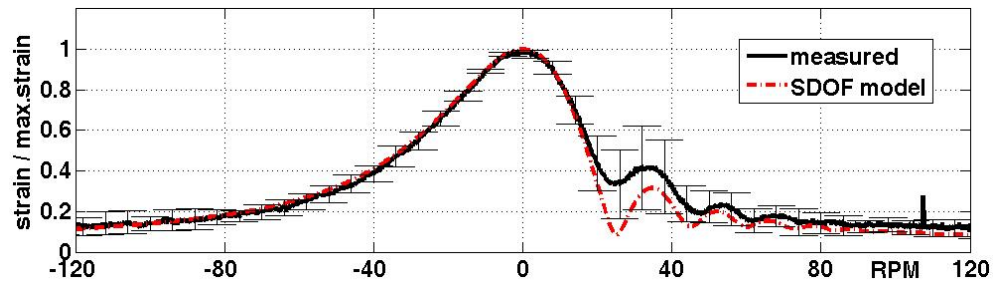
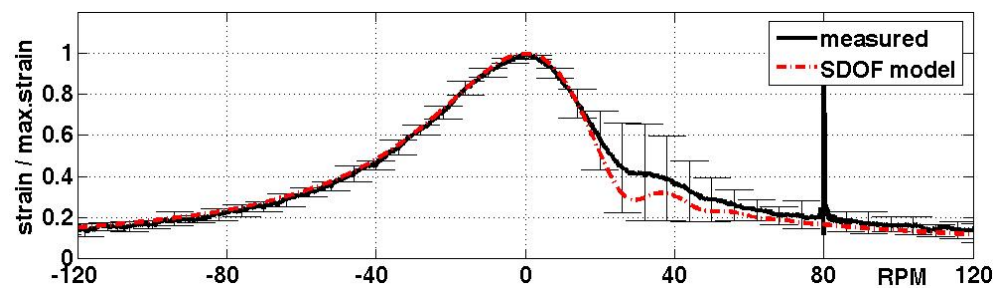


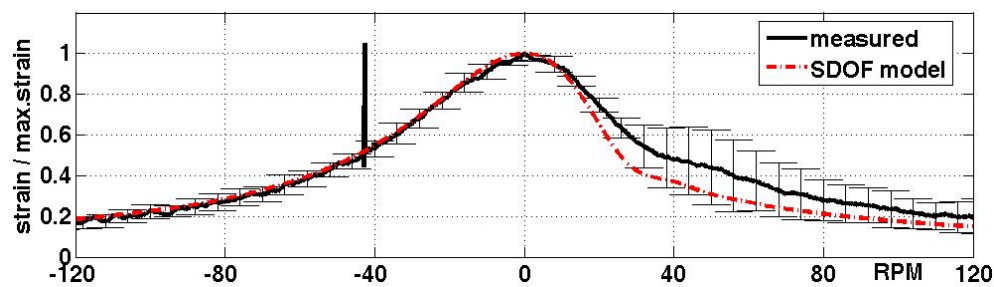
Figure 6.5.: Strain traces at resonance for two revolutions.



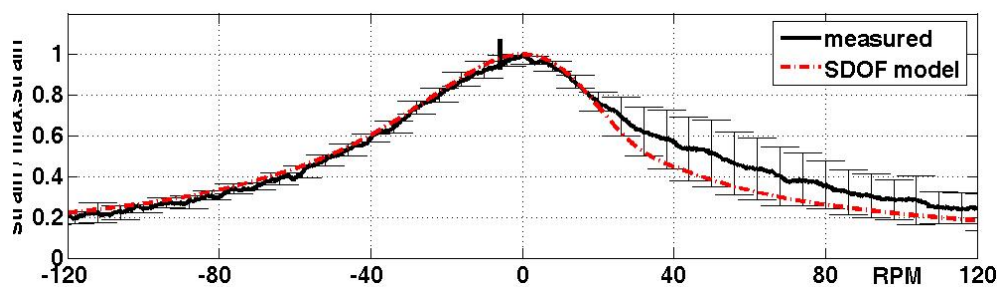
(a) Response envelope at 0.1 bar inlet pressure.



(b) Response envelope at 0.2 bar inlet pressure.



(c) Response envelope at 0.3 bar inlet pressure.



(d) Response envelope at 0.4 bar inlet pressure.

Figure 6.6.: Dynamic response envelope for Mode1/EO5 resonance.

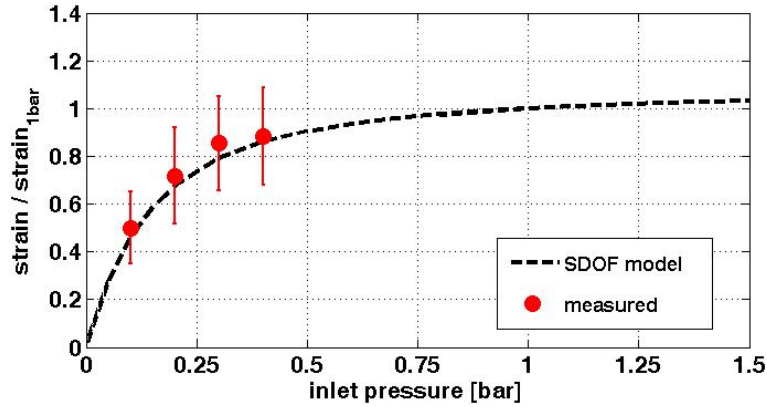


Figure 6.7.: Maximum response amplitude dependency on inlet pressure for **Mode1/EO5**.

rate the number of lobes and nodes would increase after passing the point of maximum response amplitude. The influence of the critical damping ratio on the envelope as a function of inlet pressure is also apparent in the experiment; as the pressure and therefore the damping increases, the main lobe widens while the remaining lobes diminish in amplitude. It is interesting to note an increase in blade-to-blade sample variation after resonance. Two factors are considered to cause the sample deviation for the 0.1bar and 0.2bar case. First, blade damping was found to vary from blade to blade and could therefore cause modulation of the dynamic response. Second, due to blade mistuning, coupling effects cause some of the blades to vibrate at different amplitudes. This inevitably introduces changes to the dynamic response characteristics. From results presented later in this work, it appears that the effect of blade-to-blade amplitude variation is dominating. It was found, that as the pressure increases the blade-to-blade variation also increases. However, blade-to-blade damping variation does not increase equally but is rather comparatively small. It appears therefore, that variations in response amplitude due to mistuning are primarily affected by strong blade-to-blade amplitude variations rather than by blade-to-blade damping variation.

6.4.2. Mode1/EO5 - Maximum Amplitude

In accordance with equation 6.9 the maximum response amplitude was plotted in figure 6.7. The error bars indicate the sample variation for all strain gauges considered. The SDOF curve fit was performed such that equation 6.9 was plotted using experimentally estimated damping properties, i.e. ζ_M and $\zeta_{A,ref}$. The numerator $\frac{1}{k}F_{ref}$ was then scaled in order to match the mea-

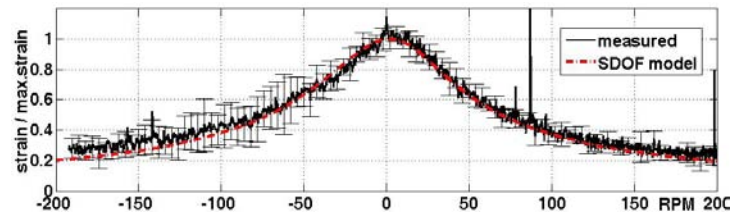
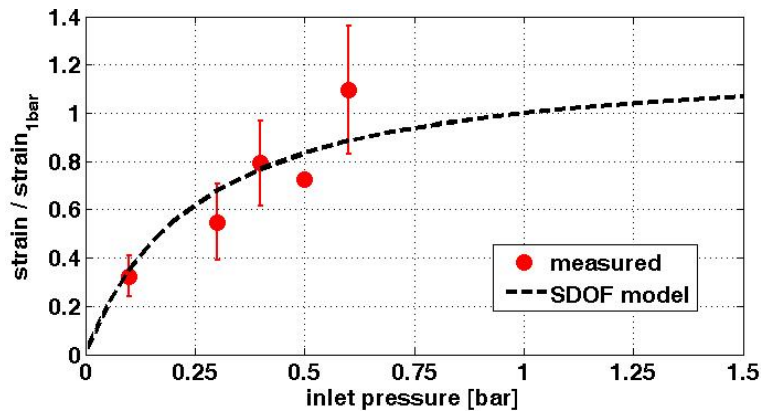
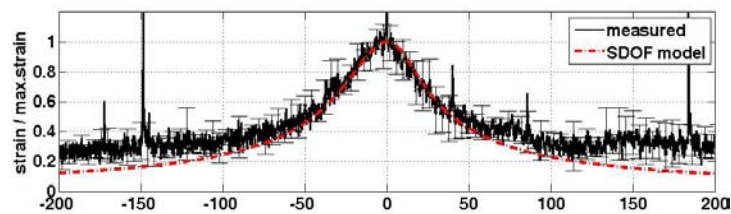
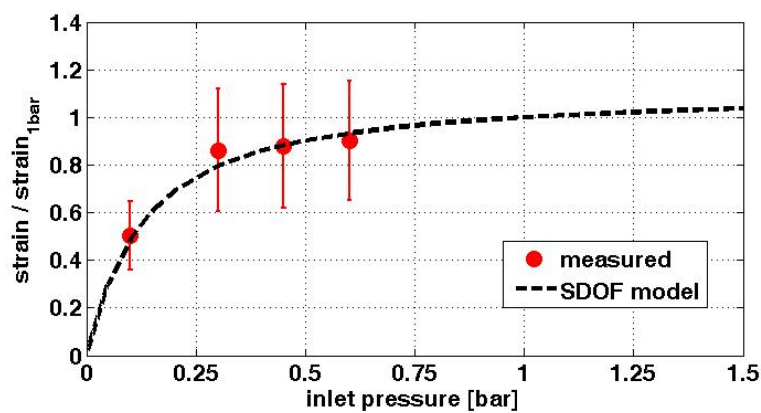
sured amplitude. The very good match between the SDOF model and the measurements essentially confirms the previous findings. Thus, for the given configuration the blade dynamics during resonant vibration can be represented by a SDOF model. The asymptotic characteristic of the maximum amplitude causes an almost constant relationship for pressure values above 0.75bar. This indicates, that the effect of material damping in the response function 6.9 becomes negligible and the increase in excitation force as well as aerodynamic damping are equal.

6.4.3. Mode1/EO6

Resonant vibration was measured for Mode 1 using a 3 lobe screen. The importance of this case lies in the fact that the excitation was provided by the second harmonic of the inlet flow distortion circumferential profile. The same analysis approach was applied as in the previous case in order to compare the dynamic response with a SDOF model. Figure 6.8(a) shows the envelope of the strain measurements as the blade resonates for 0.6 bar inlet pressure. Comparing the averaged envelope with the SDOF model, very good agreement can be observed. In contrast to the previous case presented, the plotted variance exhibits a considerable increase especially before resonance occurred. The dependency of the maximum response on the inlet pressure is given in figure 6.8(b). The general trend of the measured data is matched by the SDOF model. The cause for the rather strong deviations of the mean value from the ideal model is not understood. However, it should be added here, that the same measurements on a differently instrumented impeller yielded a very good match with the model. These results will be presented in the Chapter 8. In both cases the same procedure was applied to acquire response amplitudes as well as to compute the model predictions. The asymptotic characteristic above 0.75bar supports the reduced effect of material damping.

6.4.4. Mode2/EO12

Resonant vibration of Mode 2 was achieved through the employment of the 4 lobe screen generating EO12 excitation. The second harmonic of the distortion pattern was found to be sufficiently strong to cause amplitudes approximately an order of magnitude smaller than for the Mode1/EO5 case. Figure 6.9(a) shows the averaged dynamic response for this case at 0.6 bar inlet pressure. Also in the case of the second mode, the response under the

(a) Dynamic response envelope at $p_{inlet} = 0.6\text{bar}$ (b) Maximum response amplitude dependency on p_{inlet} Figure 6.8.: Response amplitude for **Mode1/EO6**(a) Dynamic response envelope at $p_{inlet} = 0.6\text{bar}$ (b) Maximum response amplitude dependency on p_{inlet} Figure 6.9.: Response amplitude for **Mode2/EO12**

given inlet conditions corresponds to the dynamics of a SDOF system. The variance is approximately constant for the entire speed range. The maximum response as a function of inlet pressure, figure 6.9(b), shows a good match for the available data points. Overall, the same conclusions apply here as for the cases presented above.

6.4.5. Strain Amplitude Comparison

A comparison between the maximum amplitudes should be given at this stage. Figure 6.10 compares the three cases discussed. Mode1/EO5 case shows the highest amplitudes since the excitation force in this case corresponds to the fundamental excitation frequency of the screen. As such, velocity and therefore pressure fluctuations acting on the blade surface reach their maxima. For higher harmonics contained in the forcing functions the amplitude decreases significantly. The maximum strain for the Mode1/EO6 is approximately 80% below the stress level experienced in the previous case. It should be pointed out, that damping for the two cases is comparable. Additional measurements for the same conditions and with a differently instrumented impeller confirmed the fact that damping is virtually identical. The lowest amplitudes can be observed for the Mode2/EO12 case. As will be shown in the Chapter 7 on damping, it was found that damping in this case is approximately the same as that of the Mode 1 cases. The observed reduction in maximum amplitude is therefore less affected by the increased damping than it must be by the excitation amplitude. A statement on the amplitude of the excitation force cannot be made at this point.

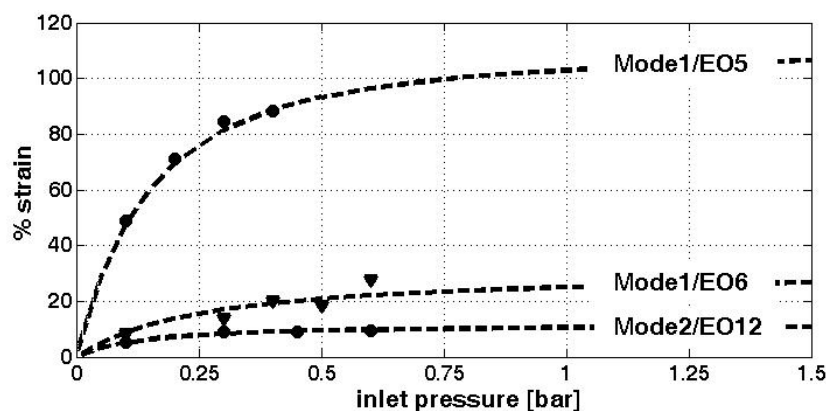


Figure 6.10.: Comparison of maximum strain amplitudes.

6.5. Effects of Mistuning

Some light should be shed on the problem of blade-to-blade response variation. Figures 6.11(a) and 6.11(b) depict the deviation of the maximum strain from the mean value used previously. The data shown was acquired from two impellers which differ in the type of instrumentation. Impeller No. 1 was instrumented only with strain gauges, whereas impeller No. 2 carried strain gauges as well as pressure sensors. In both cases the samples were acquired with strain gauges equally mounted on each blade. As can be observed, there is an offset from the mean for each blade, thus the variation is consistent and does not obey a random process. As such the error bars are a measure of the deviation of maximum strain for the given blades. The consistent offset from the mean value could either be affected by the instrumentation, which can introduce a varying degree of damping or blade mistuning. Following the work by *Whitehead* [83], the maximum factor by which the amplitude of any blade could increase is $\frac{1}{2}(1 + \sqrt{N}) = 1.8$, where $N = 7$ is the number of cyclic sectors. This gives a considerable range of amplitudes within which response could be measured due to mistuning. A comparison between the two impeller cases shows that mistuning can greatly affect the response amplitude. In the first case maximum deviations from the mean value do not exceed $\pm 60\%$ whereas in the second case values as high as 100% are reached. This effect must be taken into account during testing. It implies, that during vibration test measurements all blades must be measured in order to capture the highest response amplitude.

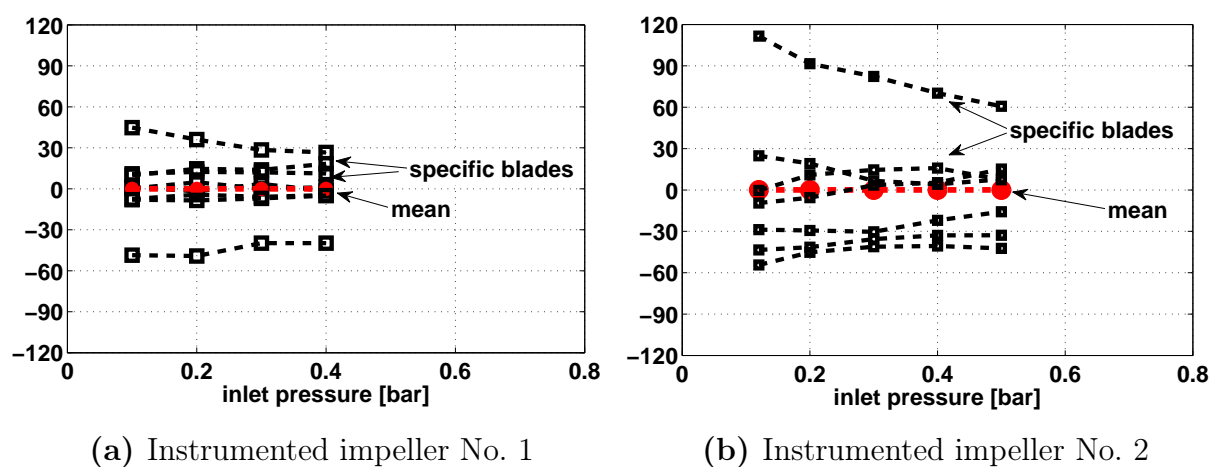


Figure 6.11.: Blade-to-blade strain variation due to mistuning.

6.6. Summary and Conclusions

In this chapter results on strain response measurements during resonance were presented. Three resonance cases were outlined. Experimental data was compared to a SDOF model in terms of dynamic response characteristic and the maximum amplitude at resonance. In all cases the inlet pressure was varied as the main parameter. The following conclusions can be derived from the analysis:

- Unsteady pressure measurements showed that the flow field upstream of the impeller contains a range of frequencies that have the potential to cause blade resonance. Strain measurements confirmed this finding at rotational speeds where resonance peaks could be identified. Although their amplitude is low compared to intentionally caused resonance, their potential to affect high cycle fatigue failure requires awareness.
- As the rotational speed traverses through resonance the dynamic response characteristic was found to exhibit a typical pattern for blades under these conditions. These are signified by a gradual increase of amplitude until resonance is reached and then an alternating fall-off in amplitude past resonance.
- Blade dynamic response predictions using a SDOF model were found to match measured blade response very well. The model was run using experimental data in terms of damping and eigenfrequency. The amplitude of the response had to be calibrated.
- The maximum response amplitude as a function of pressure was found to agree very well with the SDOF model. Best agreement was found for the Mode/EO5 case. Other cases presented exhibited deviations from the ideal character of the model. Nevertheless, it should be pointed out here, that additional measurements with a differently instrumented impeller at the same resonance cases confirmed the very good agreement with the model.
- The maximum response amplitude was compared between three resonance cases. This showed, that highest response amplitudes were generated by the fundamental excitation order of the screen. Cases where resonance was caused by the second or third harmonic of the respective distortion screen exhibited smaller amplitudes by a factor of five and more.

- The blade-to-blade amplitude variation is attributed to mistuning and coupling between the blades. Two differently instrumented impellers were compared and showed remarkable differences in terms of amplitude variation as high as 100% from the mean. This finding must be taken into account during testing and implies the need to measure all blades.

7. Damping

The work presented in this chapter outlines an experimental approach to obtain blade modal damping, expressed by the critical damping ratio. It is aimed to illustrate an approach to quantify contributions from material and aerodynamic damping to the overall damping. Two experimental studies were carried out. First, to measure material damping the impeller was bench mounted and a piezo applied to the impeller provided blade excitation. Second, aerodynamic damping measurements were performed within the test facility and blade excitation was generated by distortion screens. In both cases the pressure was initially set to near vacuum conditions and then increased. For each pressure setting the damping was estimated. The material damping could then be estimated from extrapolating to vacuum where the contribution of aerodynamic damping is zero.

7.1. Blade Damping in Turbomachinery

In general, three main contributors to damping can be identified for turbomachinery blades: material, mechanical and aerodynamic damping. Briefly, material damping is a material property which is measured by the energy dissipated during the cyclic strain in the material. This process always has a hysteresis loop where the dissipated energy and therefore the damping depend on the amplitude of cyclic strain. Mechanical damping typically accounts for the energy dissipated during contact friction between components. Applications for blades can be found at the blade root or through employment of snubbers. The mechanical damping magnitude depends on the contact geometry and the contact pressure between the parts. Aerodynamic damping accounts for vibratory energy dissipated due to the relative motion between the blade and the fluid. Main dependency parameters are the fluid density, blade mode shape during vibration and the phase relation between the forcing function and the blade mode shape. The relative contribution of the three damping mechanisms strongly depends on the kind of application and design. However, in the majority of cases material damping of turbomachinery blades

is comparatively small and therefore its contribution is often neglected. Thus, mechanical and aerodynamic damping are the main contributors to the overall damping. During the design mechanical damping represents a means to tune the damping amplitude that is required for operation.

For radial turbomachinery, where rotors are machined from a single piece, structural damping is very low and aerodynamic damping is therefore the dominant damping mechanism. Experimental measurement of aerodynamic damping can be carried out either by cascade testing or in a rotating facility. Owing to the nature of cascade testing this experimental approach to obtain aerodynamic damping values cannot be applied for three-dimensional radial compressor blades. On the other hand, available data on aerodynamic damping from rotating facilities is limited and focuses on axial machines. An estimation of aerodynamic damping was performed by *Crawley* [9] for a transonic compressor, using upstream disturbances and measuring blade response. Work on damping for a centrifugal compressor was presented by *Jin et al.* [39] where the excitation was provided by partially blocking the diffuser. In facilities where the inlet pressure can be adjusted, aerodynamic damping is obtained by measuring the overall damping and then subtracting non-aerodynamic damping measured at vacuum conditions. *Kielb and Abhari* [40] used this approach to separate the contribution of mechanical and aerodynamic damping. Their experimental approach is based on the findings described by *Jeffers et al.* [37]. Herein, the complexity is to provide blade excitation. During non-vacuum operation the excitation can either be generated by screens or blade rows, whereas at vacuum excitation requires an installation of mechanical actuators, i.e. piezoelectric actuators. Crucial for jet engines is the dependency of aerodynamic damping on the inlet pressure which is dependent on flight altitude. *Newman* [58] estimated the mode dependent aerodynamic damping in an axial transonic compressor for a number of inlet pressures. From the linear fit structural damping was derived by extrapolating to vacuum conditions.

For centrifugal compressors as they were used in this study, mechanical damping is only present due to the fixation between the impeller and the shaft. This clamping can be considered to be tight, i.e. vibratory waves propagate across the fixation into the shaft and may dissipate. This source of dissipation represents a damping mechanism, however, the associated amplitude is comparatively small and will be accounted for as a component of material

damping. Therefore, for centrifugal compressors damping during resonant vibration is considered to be composed of material and aerodynamic damping. In the following, damping will be mathematically accounted for by the critical damping ratio ζ according to a vibrating SDOF system with viscous damping. In this case the overall viscous force F_D acting on a structure is expressed by

$$F_D = -c\dot{x} = -2\zeta m\omega_n\dot{x} \quad \text{with} \quad \zeta = \frac{c}{2\omega_n m} \quad (7.1)$$

Accounting for contributions from mechanical and aerodynamic damping the corresponding forces F_{DM} and F_{DA} , the total damping force is given as

$$F_D = F_{DM} + F_{DA} \quad (7.2)$$

$$= -2\zeta_M m\omega_n\dot{x} + F_{DA} \quad (7.3)$$

Herein ζ_M is the critical damping ratio due to material damping. This quantity is assumed to remain constant. The damping force due to aerodynamic damping is dependent on the density and therefore the inlet pressure was a parameter which was altered in this project. Scaling the aerodynamic damping force with inlet pressure, the following linear relation is assumed

$$F_{DA} = F_{DA,ref} \left(\frac{p}{p_{ref}} \right) \quad (7.4)$$

$$= -2\zeta_{A,ref} \left(\frac{p}{p_{ref}} \right) m\omega_n\dot{x} \quad (7.5)$$

The applicability of this linear relationship was successfully presented by *Newman* [57] for a three stage axial compressor. Damping measurements were performed for bending and torsional modes which then could be linearly fitted as a function of inlet pressure. Finally, a relationship for the overall damping can be derived as a function of inlet pressure.

$$F_D = F_{DM} + F_{DA} \quad (7.6)$$

$$-2\zeta m\omega_n\dot{x} = -2\zeta_M m\omega_n\dot{x} - 2\zeta_{A,ref} \left(\frac{p}{p_{ref}} \right) m\omega_n\dot{x} \quad (7.7)$$

$$\zeta = \zeta_M + \zeta_{A,ref} \left(\frac{p}{p_{ref}} \right) \quad (7.8)$$

In the datum study it was more convenient to apply the damping function in the following form.

$$\zeta(p) = \zeta_M + \left(\frac{d\zeta_A}{dp} \right) p \quad (7.9)$$

It is assumed that at zero inlet pressure the aerodynamic pressure is also zero. According to the equation above, only material damping provides a means for vibratory energy dissipation at vacuum conditions. Depending on the amplitude of material damping, its influence on the overall damping increases for lower pressure levels. In an experimental approach material damping can be obtained by measuring the overall damping for a number of pressure settings and then extrapolating to zero pressure. Although damping is non-linear near vacuum conditions, i.e. at less than 0.1bar, the above approach showed excellent applicability for the datum problem to model damping as a linear function of the inlet pressure. The effect of damping can be observed in the formulation of the maximum response during resonant vibration of a SDOF system:

$$x = \frac{\frac{1}{k} F_{ref} \left(\frac{p}{p_{ref}} \right)}{2 \left(\zeta_M + \zeta_{A,ref} \left(\frac{p}{p_{ref}} \right) \right)} \quad (7.10)$$

As the inlet pressure increases, the aerodynamic damping increases from zero and may out-weight the contribution of material damping. As will be shown later, at a realistic operating pressure of 1bar the aerodynamic damping is approximately by a factor of ten higher than the material damping. The associated blade response due to inlet distortion under varying inlet pressure conditions was discussed in Chapter 6. The results showed that the SDOF model yields a very good matching with experimental data.

7.2. Damping Measurement Methods

Two analysis methods will be presented to measure damping based on a SDOF dynamic system. For both cases the time signal of the blade response was Fourier transformed and analysed in the frequency domain.

7.2.1. Frequency Analysis

The transient data acquisition procedure applied in this work requires the analysis of the signal with respect to both frequency and rotational speed. This is achieved through Short-Time-Fourier-Analysis (STFT) where the recorded signal is divided into successive windows and then Fourier transformed. Thus each window is associated with the speed range during which it was acquired. Processing the signal this way allows the identification of the change

in frequency content as the shaft speed sweeps through resonance. The choice of window length and the resultant minimum frequency resolution is limited according to the uncertainty principle, see *Qian and Chen* [61]. Owing to the nature of this problem, the window length was adjusted depending on the purpose of the analysis.

The signal analysis used to perform damping estimation through amplitude fitting requires high frequency resolution and was therefore carried out such that a frequency resolution of typically 0.2 Hz was achieved. In this case a dense resolution of the resonant peak was required. In order to visualize the frequency content during resonant sweeping, the window length was reduced resulting in a typical resolution of 2 Hz. Attention was paid to resolving the frequency content with respect to time.

7.2.2. Curve-Fit Method

The evaluation of the critical damping ratio was performed using a curve-fit procedure as described below. Applications of these methods were carried out by *Newman* [58], *Jeffers* [37] and *Kielb and Abhari* [40]. In this work the frequency response function $Y(\omega)$ was obtained by averaging the measured signal in the frequency domain. The transfer function in the frequency domain $H(\omega)$ is defined by

$$H(\omega) = \frac{Y(\omega)}{X(\omega)} \quad (7.11)$$

Data to compute the excitation function $X(\omega)$ would require measurements of the unsteady pressure fluctuations and their integration across the entire blade surface. The excitation function during resonant crossing can be assumed to be constant for the relatively narrow rotational speed range during resonance measurement. Computing the spectral density, S_y from the response function and assuming the excitation spectral density to be constant, the amplitude response $|H(\omega)|^2$ of a SDOF system is given by the following relationship

$$|H(\omega)|^2 = \frac{S_y}{S_x} = \frac{1/k^2}{\left[1 - (\omega/\omega_n)^2\right]^2 + \left[2\zeta(\omega/\omega_n)\right]^2} \quad (7.12)$$

On the basis of this model, the measured data points were curve-fitted by adjusting the numerator k , the frequency ratio ω/ω_n and the critical damp-

ing ratio ζ . In order to minimize the variation between the curve-fit and the data points a least square method was used.

A number of examples of the employment of the fitting procedure is shown for Mode 1, figure 7.1, and for Mode 2, figure 7.2. For both cases measurements for the first three blades were compared. Data was non-dimensionalized by the maximum amplitude of the spectral density. A major problem in the application of the curve-fit method in the current study is the occurrence of additional frequencies or frequency maxima within the considered band width. In particular blade no. 2 exhibits this problem, exemplified here for the first mode. The data suggests that coupling and mistuning affect the frequency response spectra. A remedy to overcome this problem is shown for blade nos. 1 and 2 for both modes. Data fitting was performed with emphasis on the ascending part of the resonance peak by limiting the frequency band. In other cases i.e. blade no. 3 mistuning and coupling was not observed enabling the curve-fit procedure to be applied for the entire frequency range.

7.2.3. Circle-Fit Method

In addition to the curve-fit procedure a circle-fit procedure was implemented, aiming to verify the estimation of damping. The circle-fit method was applied to results obtained from impeller bench testing and piezoelectric excitation as described in Chapter 3.3. The main advantage of this experimental method is the synchronized acquisition of the excitation and response spectra. Based on this, the frequency transfer function $H(\omega)$ can be computed from the cross-correlation spectrum S_{xy} and the spectral density S_x

$$H(\omega) = \frac{S_{xy}}{S_x} \quad (7.13)$$

The response amplitude as a function of frequency is exemplified for Mode 2 in figure 7.3(a). The real and imaginary components of the complex response function are shown in figure 7.3(b) for a frequency band width where resonance occurs. Due to coupling between the blade sectors, three maxima can be observed in the figure, of which the central one with the highest amplitude was selected for damping estimation. Both graphs show the dependency of the transfer function on the inlet pressure. A circle-fit was carried out in the complex domain in order to determine the center of the data points. Following the derivations given by *Ewins* [21], the critical damping ratio for a SDOF system can be computed from the following equation

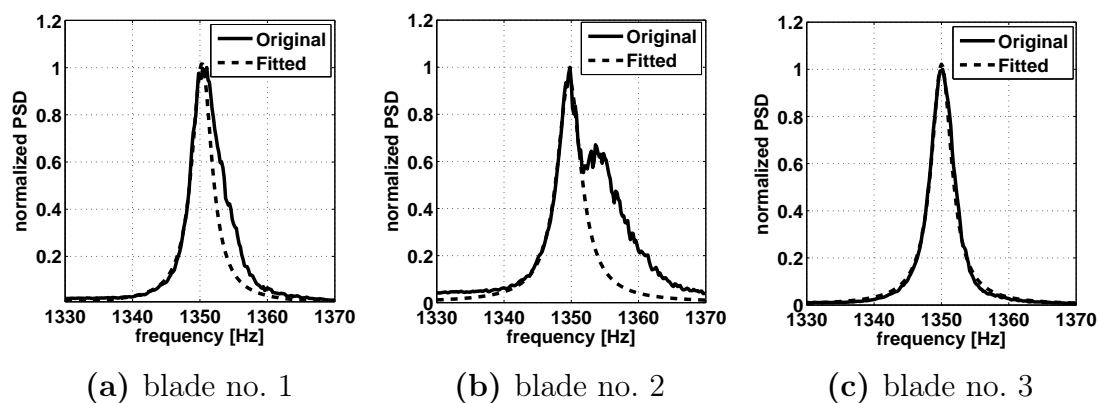


Figure 7.1.: Curve-fit method for damping estimation, Mode 1

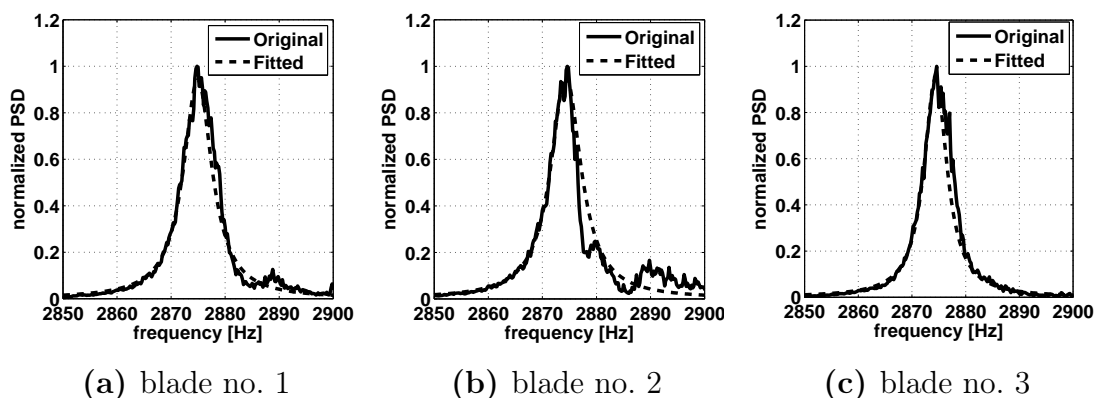
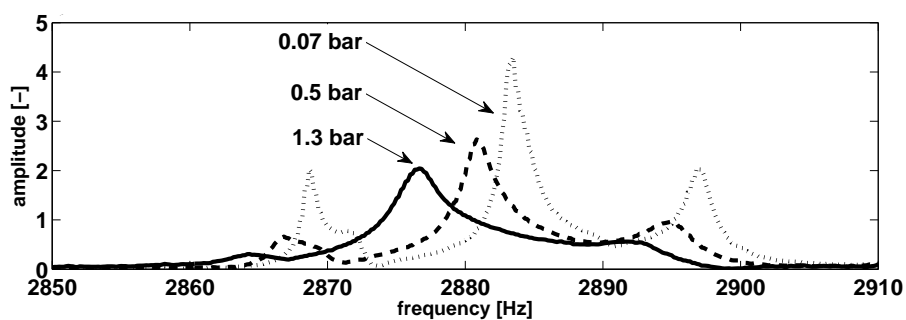
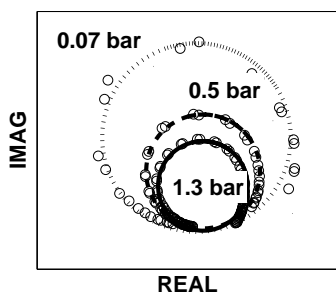


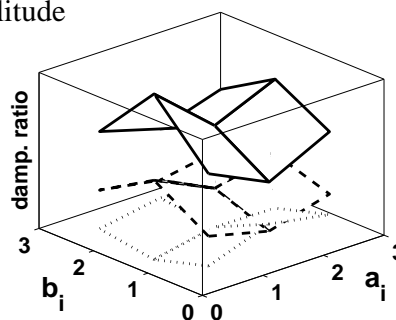
Figure 7.2.: Curve-fit method for damping estimation, Mode 2.



(a) amplitude



(b) circle-fit



(c) critical damping ratio

Figure 7.3.: Circle-fit method for damping estimation.

$$\zeta = \frac{\omega_a^2 - \omega_b^2}{2\omega_n [\omega_a \tan(\frac{1}{2}\Theta_a) + \omega_b \tan(\frac{1}{2}\Theta_b)]} \quad (7.14)$$

Herein the indices a and b signify data points before and after resonance, respectively. The angles Θ_a and Θ_b measure the angles between the resonance point and a data point a_i and b_i . Damping can therefore be calculated for a number of combinations of a_i and b_i . Figure 7.3(c) shows the estimated critical damping ratio based on this approach. Each plane represents damping for a pressure setting and the values are averaged to obtain the final damping. The employment of this procedure revealed that a maximum of six data points from resonance was applicable. Ideally this number should be significantly higher, however, in the current application the 'carpet' plots showed significant distortion for data points further away from resonance.

7.2.4. Comparison between Curve-fit and Circle-fit Methods

A comparison between the curve-fit and the circle-fit methods was carried out based on measurements performed with piezoelectric excitation. Figure 7.4 quantifies the percentage of $(\zeta_{\text{curve}} - \zeta_{\text{circle}})$ as a function of pressure. Mode 1 and Mode 2 are shown. The error bars indicate the sample variation. The mean deviation for both modes is within a range of 10%. The circle-fit method results in slightly lower damping magnitudes in comparison to the curve-fit approach. The applicability of each of the two methods was found to depend on the available data quality, which in this case was affected by the blade-to-piezo distance. On average, blades closer to the piezo exhibited higher response amplitudes. A systematic deviation, i.e. an increase in pressure, cannot be observed. Based on the findings, the overall agreement was considered to be good. Results shown later for the piezoelectric excitation case were obtained from averaging the estimates from both methods.

7.3. Damping Measurement Results

Damping measurements were carried out in two steps. In the first step, material damping was obtained through blade excitation using a piezo. The pressure was reduced towards zero in order to obtain material damping at vacuum

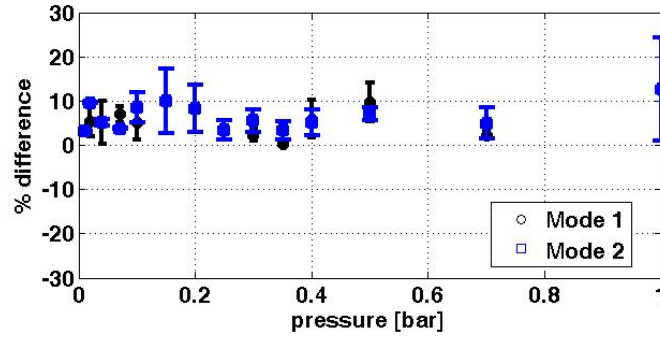


Figure 7.4.: Deviation in damping estimation, $\%(\zeta_{\text{curve}} - \zeta_{\text{circle}})$.

conditions. In the second step, damping measurements were obtained from response measurements during compressor operation under resonant conditions. Also for this step measurements were carried out for a number of discrete pressure levels in order to obtain the damping dependency on the inlet pressure.

7.3.1. Material Damping

Material damping measurements were carried out employing piezoelectric excitation as described in section 3.3. The impeller was mounted in a pressure adjustable chamber mounted on a shaft carrier representing an equivalent mount as it is the case for the rotating shaft in the testing facility. The piezo was driven by a signal generator and an amplifier with voltages typically in the range of 150V. The harmonic excitation signal was modulated in the required frequency range depending on the mode of interest. The method is commonly referred to as *chirp* excitation. The excitation signal was measured at the connectors to the piezo actuator. The resonant blade response was acquired through blade mounted strain gauges.

Both, the curve- and circle-fit methods were applied on the measured excitation and response spectra. The resultant mean critical damping ratio between the two methods is shown in figure 7.5 for Mode 1 and Mode 2. The critical damping ratio was normalized by the measured material damping given in table 7.1. The error bars in the figure indicate the sample variation of measured damping. The major goal of this experiment was to determine material damping by extrapolating a linear curve-fit to vacuum conditions where aerodynamic damping is eliminated. For this reason, measurements were refined

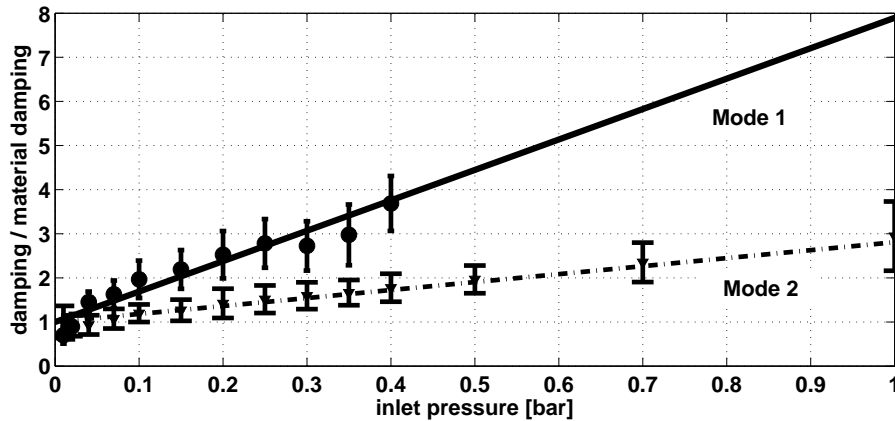


Figure 7.5.: Damping measurements using piezoelectric excitation.

main blade modes	critical damping ratio ζ_M
Mode 1	0.00035
Mode 2	0.0002

Table 7.1.: Material damping quantities.

at near vacuum. Although in the case of Mode 1 measurements were taken above an inlet pressure of 0.4bar, the application of the damping estimation procedures was uncertain due to very low response amplitudes. As mentioned previously, the excitation force exerted by the piezo at low frequencies was the limiting factor. This was not the case for the second mode. This circumstance is also reflected by the error bars, which in the case of Mode 1 increase towards higher pressure levels.

In the case of Mode 2 as compared to Mode 1, sample variation is generally lower and deviation from the linear fit is negligible. Despite the lower data quality acquired for Mode 1, for both cases a linear relationship between the critical damping ratio and inlet pressure was obtained. The extrapolation of the linear fit to vacuum yielded the critical damping ratio ζ_M due to material damping. According to table 7.1 material damping of Mode 1 was found to be approximately 40% higher in comparison to Mode 2. Though this value appears to be considerable, in absolute numbers the influence is rather small considering the increase of aerodynamic damping as the inlet pressure was

raised. Similar findings were reported by *Srinivasan et al.* [76] for a fan blade made of titanium. Here, the conclusion on material damping was that its contribution to overall damping is negligible and should not be considered during design for resonant vibration. The same reference quantifies the influence of blade stress and temperature on material damping, however, for the given application these effects were neglected. The work by *Jin et al.* [39] quotes material damping values of $\zeta_M = 0.0015$ taken at ambient pressure conditions for aluminum impeller blades. Based on the datum study it can be expected that these values were affected considerably by the surrounding air. For further comparison, *Blevins* [4] presents material damping in a range between $\zeta_M = 0.0004$ and $\zeta_M = 0.004$ for aluminum.

In conclusion, employing piezoelectric excitation enabled the measurement of material damping which is dependent on the modal shape. However, the linear fit indicates, that for on bench testing aerodynamic damping outweighs material damping as the pressure increases. In order to measure material damping of impeller blades, the surrounding pressure must be reduced to vacuum.

7.3.2. Aerodynamic Damping – Mode 1

Strain measurements through aerodynamic excitation were performed for Mode 1. Two cases will be shown. In the first case Mode1/EO5 resonance is generated due to the fundamental excitation frequency of the 5 lobe screen. In the second case Mode1/EO6 resonance is generated due to the second harmonic of the 3 lobe screen.

Mode1/EO5

Figure 7.6 exemplifies the response of a main blade as resonance occurs for 0.2bar inlet pressure. The blade natural frequency and the excitation order can be identified. The response amplitude as a function of pressure was discussed in the previous chapter. The dependency of damping on pressure is visualized in figure 7.7. The width of each slope is a measure of the level of damping, thus as the inlet pressure increases from 0.1bar to 0.4bar the width and therefore the damping increases. In order to estimate the critical damping ratio, the curve-fit method was applied to the response spectrum for data taken at the distinct operating lines, in this case OL1, OL2 and OL3 according to the performance map in figure 2.3. The critical damping

ratio obtained for each pressure setting was averaged for all blades and was then normalized by the material damping estimated for Mode 1 as listed in table 7.1. Figure 7.8 shows the results with a linear function fitted through the data according to equation 7.9. Data is presented for two differently instrumented impeller configurations as described in section 2.6. In the case of Impeller No. 1 damping for the operating lines OL1 and OL2 were measured whereas in the case of Impeller No. 2 damping for all three operating lines was acquired. The error bars indicate the sample variation. Generally, in the case of OL1 the variation is very low in comparison to OL2 and OL3. Overall, both impeller configurations exhibit comparable damping amplitudes.

Two main observations can be made. First of all, with a linear increase in damping, aerodynamic damping is the main contributor to overall damping. For instance, at an inlet pressure of about 1bar aerodynamic damping is about 10 times higher than material damping. Secondly, extrapolation of overall damping to vacuum conditions yields a very good match with material damping obtained from piezoelectric excitation. These observation shows that employing piezoelectric excitation is a valid method to estimate material damping. Prior to the experiment, concerns were raised that the piezo would not generate amplitudes sufficiently high to allow damping comparison between the experiments since material damping depends on the vibratory amplitude.

Damping comparison between the operating lines and the impeller cases shows that the gradient may vary. Particularly in the case of the OL2 in figure 7.8(a), the gradient may be influenced to some degree by the curve-fit. As can be seen, the data reveals slight deviation from a linear curve-fit and variation is considerably higher than for OL1. In the authors' opinion this variation may be introduced as a result of local modulations in aerodynamics as the mass flow varies and therefore affects the mean relative flow angle. Following the computations performed by *Zemp et al.* [85], the OL1 mean relative flow angle equals the blade metal angle whereas in the case of OL2 a reduction of $\approx 7^\circ$ was observed. Superpositioning the fluctuation introduced by the inlet distortion increases the angle deviation from the blade metal angle.

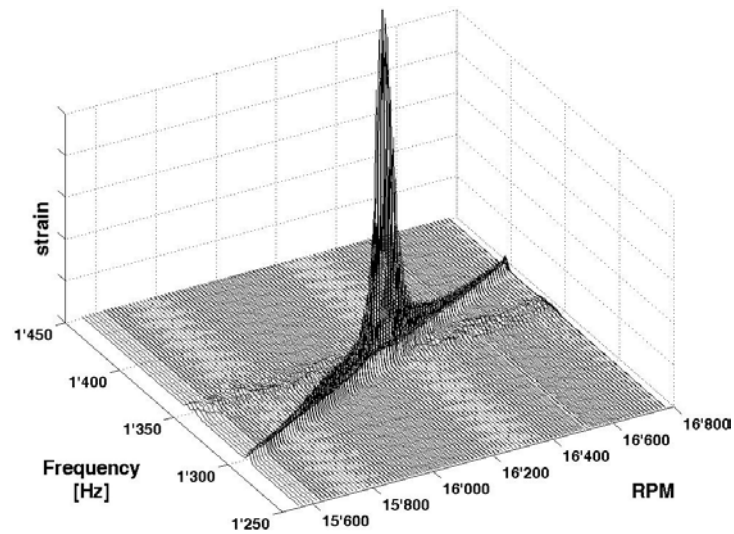


Figure 7.6.: Mode 1 response from EO5 excitation using a 5 lobe screen.

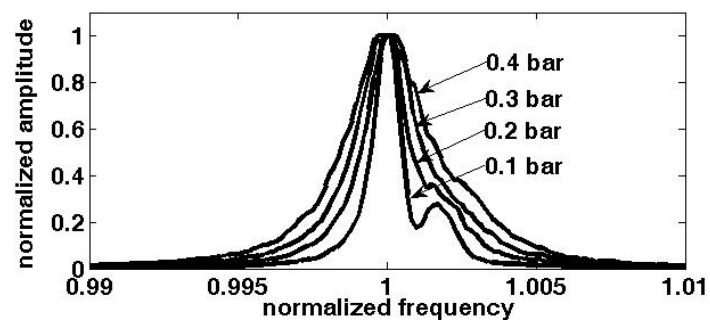


Figure 7.7.: Mode 1 response variation depending on inlet pressure.

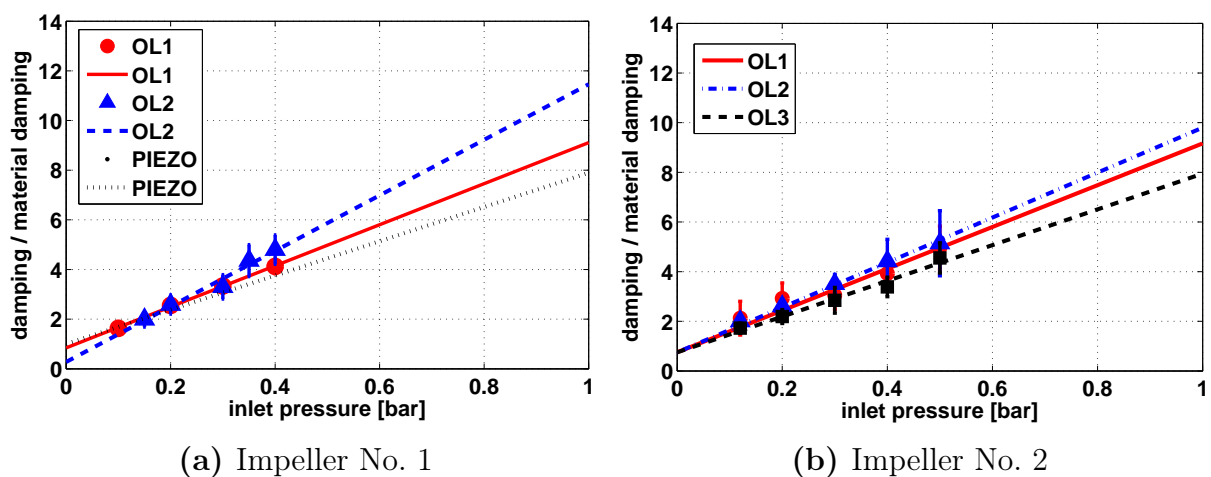


Figure 7.8.: Measured damping for Mode1/EO5.

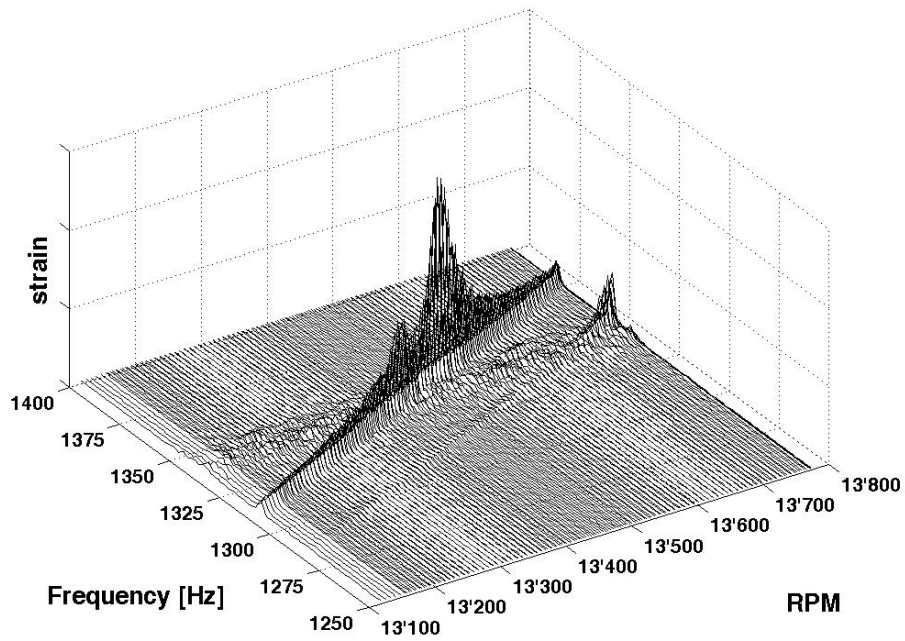
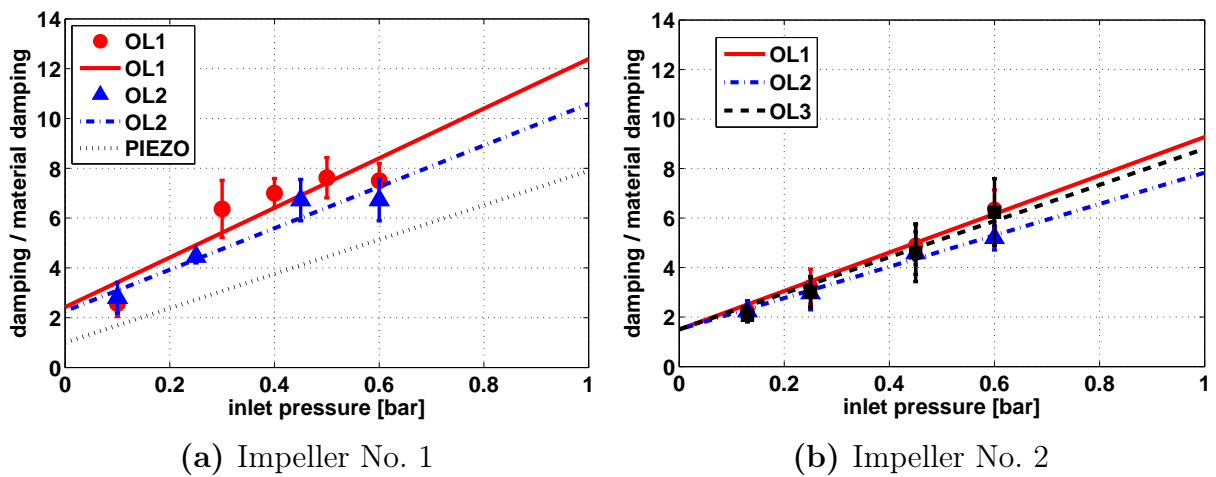


Figure 7.9.: Mode 1 response from EO6 excitation using a 3 lobe screen.



(a) Impeller No. 1

(b) Impeller No. 2

Figure 7.10.: Measured damping for Mode1/EO6.

Mode1/EO6

Figure 7.9 exemplifies a typical response spectrum of the first mode due to EO6 excitation at 0.25bar. Effects due to mistuning and coupling are visible. The damping ratios derived for both operating lines as a function of pressure are shown in figure 7.10 for both impeller cases. The first observation that can be made is that the two impeller cases exhibit slightly different levels of damping, i.e. in case of Impeller No. 1 damping seems to be higher at a given inlet pressure. Also, for the same case data points deviate more from the linear fit and variation is higher than for the Impeller No. 2 case. Two factors may affect the results. Firstly, the curve-fit procedure was found to be sensitive to the frequency band width of the spectrum that was selected to perform the fit. Secondly, for this resonance point the impeller operates at part speed with the mean flow angle being $\approx 5^\circ$ below the design incidence. This effect is in accordance with observations obtained from the Mode1/EO5 case. Ideally, the linear fits should match material damping, however due to data variation this is not the case for Impeller No. 1 whereas in the case of Impeller No. 2 the low data variation agrees very well with material damping. The increase in aerodynamic damping with pressure is comparable to data obtained for Mode1/EO5, i.e. aerodynamic damping dominates as the main contributor to overall damping.

In summary, overall Mode 1 damping is dominated by aerodynamic damping. This refers to applications with an inlet pressure of approximately 1bar. The increase in damping with the increase in pressure is comparable between the two excitation orders presented here. The magnitude of mechanical damping is generally in agreement between the experiments carried out with piezoelectric and aerodynamic excitation. Based on the overall observation damping between the two excitation orders is comparable.

7.3.3. Aerodynamic Damping – Mode 2

Damping measurements through aerodynamic excitation were performed for Mode 2. Two cases will be compared. In one case Mode2/EO12 resonance is generated due to the third harmonic excitation frequency of the 4 lobe screen. In the second case Mode2/EO10 resonance is generated due to the second harmonic of the 5 lobe screen. Both cases will be presented in parallel. Damping was measured only for the Impeller No. 1 configuration.

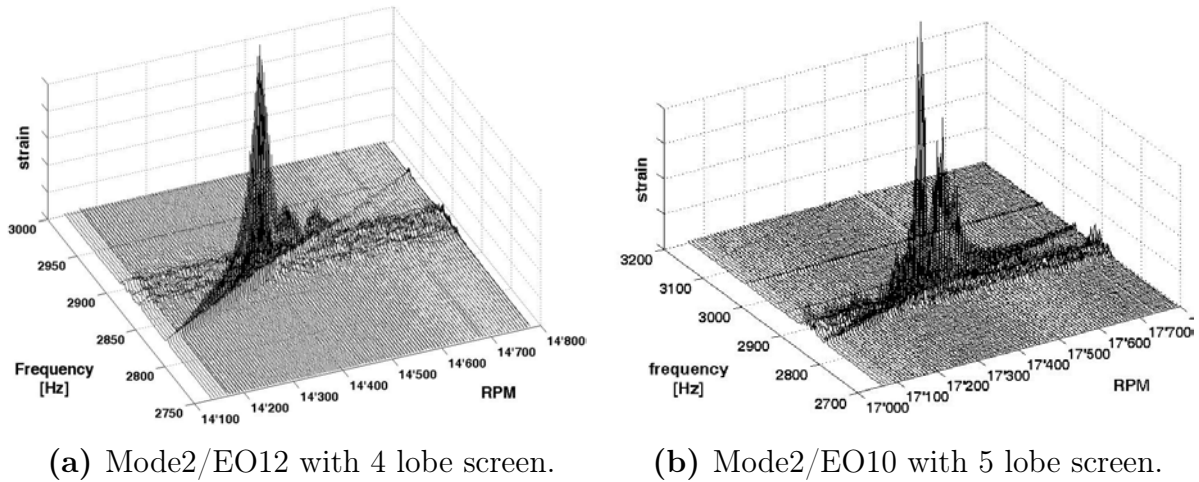


Figure 7.11.: Strain response for Mode 2

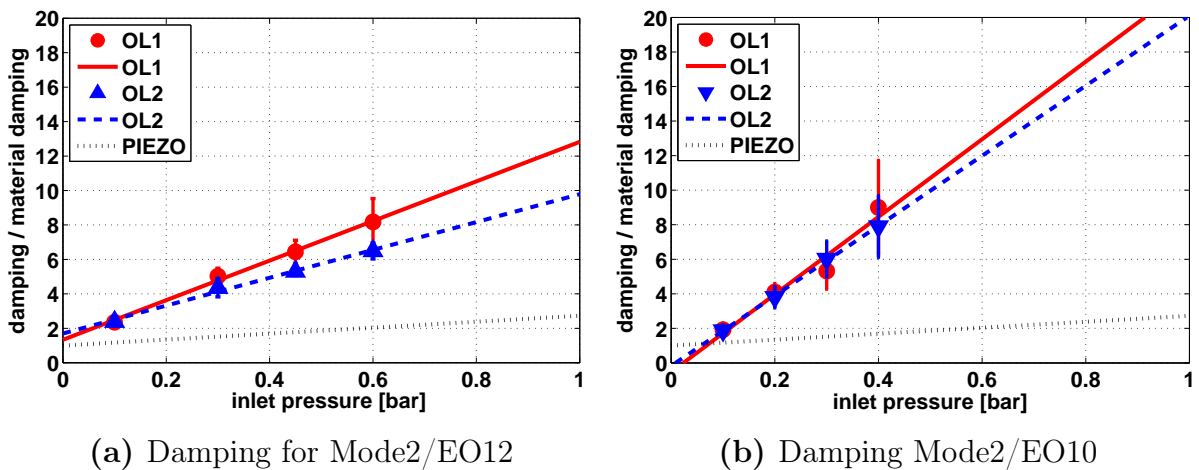


Figure 7.12.: Damping for Mode 2

Figure 7.11(a) and figure 7.11(b) exemplify the response of the second mode. For both cases mistuning and coupling are apparent due to the appearance of close frequencies at resonance. As in the cases presented earlier, damping was estimated through a curve-fit applied to the peak with the highest amplitude. Results for both cases are summarized in figure 7.12(a) for Mode2/EO12 and figure 7.12(b) for Mode2/EO10. Damping was normalized by the material damping obtained using piezoelectric excitation and summarized in table 7.1. The first observation to make is the substantially lower damping level due to piezoelectric excitation in comparison to damping obtained from aerodynamic

excitation. Moreover, in case of Mode2/EO12, material damping estimates between the experiments were found to agree reasonably well. Damping variation is comparatively low. In the case of Mode2/EO10, aerodynamic experiments yielded negative material damping. As shown previously, given the variation in damping estimates and the limited number of pressure settings at which data was acquired, the potential to affect the linear curve-fit is apparent. Overall, Mode2 damping can also be seen to be dominated by aerodynamic damping. Depending on the resonance case, damping is by a factor of 10 to 20 higher than material damping.

The dependency of damping on the operating line can be identified at least for Mode2/EO12 given the low variation. Based on the same approach, for Mode2/EO10 a statement on operating line dependency cannot be made. Overall, at this stage it is comparatively difficult to reason on the cause of damping alternation. The flow around the blade is dominated by the first harmonic of the distortion screen whereas excitation is provided by the second or third harmonics which generate lower response amplitudes.

In summary, Mode 2 damping is dominated by aerodynamic damping. The increase in damping was found to differ and to be higher in the Mode2/EO10 case. As far as data variation enables to make a judgement, material damping was predicted equally when comparing piezoelectric and aerodynamic excitation. The dependency of damping on the operating line could be identified, however, an explanation could not be given at this stage.

7.3.4. Damping Amplitude Comparison

Damping for Mode 1 and Mode 2 are summarized in terms of critical damping ratio in table 7.2 for pressure levels of 0.5bar and 1bar. A direct damping comparison can be performed with damping data published by *Jin et al.* [39] for a centrifugal compressor made of aluminum and featuring thin blades. Data was published for the first blade mode measured at ambient pressure conditions which should correspond close to 1bar. Blade forced response was generated through aerodynamic excitation. Two compressors were studied featuring equal blade geometries but different blade thicknesses. For the thin bladed compressor critical damping ratios varied between $\zeta = 0.01$ and $\zeta = 0.025$, depending on the mass flow setting. For the thick bladed compressor critical damping ratios were considerably lower and varied between

$\zeta = 0.0024$ and $\zeta = 0.0038$. Therefore, damping amplitudes depend primarily on the blade thickness. The impeller studied in this work exhibited damping amplitudes of $\zeta = 0.0032$ to $\zeta = 0.0035$ and is therefore comparable to the thick bladed compressor of *Jin et al.* The strongest discrepancy between this study and the work by *Jin et al.* is the dependency of damping on the mass flow setting, i.e. the operating line. In the datum work, damping variations were detectable but they are rather small and may be negligible from an engineering perspective. In the case of *Jin et al.* damping may vary by a factor as much as two depending on the mass flow. The major difference between the two impeller configurations is the number of blades. The datum impeller features 7+7 blades, whereas the impellers by *Jin et al.* feature 10+10 blades for the thin walled impeller and 14+14 blades for the thick walled impeller, respectively. The question that must be answered in this context is by how much does the relative blade distance alter aerodynamic damping? The displacement of fluid during vibration and the associated pressure field that opposes blade vibration maybe affected by the relative blade distance and thereby react differently to the overall mass flow passing through the blade passages.

main blade modes	overall damping ζ at 0.5bar	overall damping ζ at 1bar
Mode1/EO5	0.0018	0.0032
Mode1/EO6	0.0021	0.0035
Mode2/EO12	0.0012	0.0022
Mode2/EO10	0.0022	0.0042

Table 7.2.: Overall damping amplitudes.

7.4. Summary and Conclusions

Damping estimation during forced response for a radial compressor was carried out on the basis of experimental data. Damping measurements were performed for the first two eigenmodes of the main blade. The experimental procedure used, allowed the determination of the contributions of material and aerodynamic damping. Circle-fit and curve-fit methods were used based on the SDOF model.

In a first step, material damping was estimated using experimental data taken during piezoelectric excitation. The impeller was shaft mounted and not rotating. In this instance piezos were mounted on the impeller disk and provided synchronous excitation while strain gauges measured the blade response. Measurements were performed for a number of pressure settings ranging from vacuum and increasing to ambient conditions. The transfer function was computed and both the circle-fit and the curve-fit methods were applied.

- A comparison between the two damping measurements methods showed that the estimated damping ratios deviated by approximately 10% from each other compared to the absolute value.
- Material damping depends on the mode shape. In the case of Mode 1 material damping is by 40% higher than for Mode 2.

In a second step, the critical damping ratio was estimated based on data taken in the rotating facility. For both eigenmodes, Mode 1 and Mode 2, data was acquired for two resonant conditions. A curve-fit procedure was applied in order to determine the critical damping ratio as a function of pressure which could be curve-fitted by a linear function.

- The results showed that the estimation of material damping could be derived equally by the aerodynamic excitation experiment and also by piezoelectric excitation.
- Aerodynamic damping was found to dominate the overall damping, i.e. at 1 bar inlet pressure aerodynamic damping is higher by a factor of 10 than material damping.
- Measurement of overall damping must be undertaken under operating conditions. The results reveal, that measurement of damping differs

between the two types of experiment presented here, i.e. on-bench measurements and in the rotating facility. Measurement of material damping can be obtained from both experimental approaches

- The dependency of damping on the operating line was observed for all cases. However, the difference is marginal for both modes and can therefore be considered to be negligible. This finding opposes previous studies in the open literature for similar type of radial compressors, where damping was found to strongly depend on the operating line.
- Mode 1 damping can be considered to be independent of the resonance case. This is not the case for Mode 2 damping, where damping is dependent on the resonance.
- Depending on the resonance case, damping amplitudes between Mode 1 and Mode 2 vibration are comparable.

8. The Cumulative Aspects Of Forced Response

In the previous chapters experimental work into the understanding and the quantification of four crucial aspects of forced response were presented. These were the inlet flow distortion, the unsteady blade excitation, the resonant response and the blade damping. Where possible, computational data was used to support the process of understanding experimental findings. The separate treatment of the four aspects of forced response was necessary in order to identify their specific underlying principals. This rendered possible to quantify inlet flow distortion and measure its effect in terms of blade unsteady pressure. Also, it was found that the blade response during resonance resembles the dynamics of a SDOF model. The same argument applies with respect to damping, where the separation of aerodynamic and mechanical damping was possible.

At this stage of the research process the question arises on how the findings combine into a global picture. This problem must be viewed from a perspective relevant to engineering with focus on HCF failure. In this regard the response amplitude during resonance must be contained within a certain limit to fulfil the endurance criteria. Therefore, one must identify how excitation and damping affect the resultant response amplitude. The effects of mistuning and coupling must also be considered. An assessment of this problem can be carried out based on the available experimental data for a number of inlet distortion cases and operating lines. It will be shown, that the response amplitude can vary greatly for the same resonance case depending on the mass flow. What must be understood is the main cause of this variation. This requires a case to case comparison of blade excitation, damping and effects of mistuning.

The following sections elaborate the combined influence of measured blade excitation and damping on the blade response amplitude. It will be revealed,

that constrains exist to interpret the experimental results with respect to the excitation forces due to a limited number of pressure sensors and their position on the blade. Finally, the effect of mistuning will be related to the changes in the response amplitude and damping.

8.1. Modal Formulation

During forced vibration the dynamic behavior of a Multi-Degree-of-Freedom (MDOF) system is governed by a set of second-order ordinary differential equations representing the displacement of each degree of freedom, x

$$\underline{\underline{M}} \ddot{x} + \underline{\underline{C}} \dot{x} + \underline{\underline{K}} x = \underline{F} \quad (8.1)$$

The problematic of handling this equation is at hand due to its MDOF formulation and coupling. In order to overcome this constrain the set of coupled equations can be reduced to a set of uncoupled equations. The applied method is termed mode-superposition or normal-mode method. In the above formulation of the MDOF system the modal matrices $\underline{\underline{M}}$ and $\underline{\underline{K}}$ are diagonal matrices and the set of equations is coupled through the non-diagonal damping matrix $\underline{\underline{C}}$ in its general formulation. Therefore, in order to decouple the set of equations the damping matrix must be expressed as a diagonal matrix. The application of the normalization process is valid under the assumption of a lightly damped system, where damping can be expressed in the form of modal damping with values of $\zeta \leq 0.1$. Under these conditions the damping matrix becomes diagonal and the MDOF system can be expressed as a set of decoupled equations. Each equation within the set resembles a single mode of vibration in the modal space of the form

$$\ddot{\eta} + 2\zeta\omega \dot{\eta} + \omega^2\eta = f \quad (8.2)$$

The above equation is mass normalized and corresponds in its form to a SDOF dynamic system. The normal-mode method is presented in great detail by *Craig and Kurdila* [8]. The single degree of freedom of each mode is represented by the modal coordinate η . During steady-state vibration the dynamic system must satisfy the condition that the excitation work due to external forces and the damping work are equal, i.e. $W_E = W_D$. In order to

derive analytical expressions for both of the work terms, in the following it will be assumed that the modal force resembles a harmonic oscillation

$$f = f_0 \cos(\omega t + \Delta\varphi) \quad (8.3)$$

where the variable $\Delta\varphi$ represents the phase angle between the blade motion and the excitation force. The equation assumes that the aerodynamic excitation force is not affected by the blade motion. According to the formulation of the modal force, the modal response undergoes harmonic oscillation of the form

$$\eta = \eta_0 \cos(\omega t) \quad (8.4)$$

$$\dot{\eta} = -\omega \eta_0 \sin(\omega t) \quad (8.5)$$

$$\ddot{\eta} = -\omega^2 \eta_0 \cos(\omega t) \quad (8.6)$$

The validity of the assumption of a harmonic excitation as well as a harmonic response amplitude was outlined in the previous chapters. The aerodynamic excitation work done during a single vibratory cycle is given by the integration of the modal force f and the displacement of the structure η

$$W_E = \int_0^{\eta_c} f \, d\eta = \int_0^{T_0} f \, \dot{\eta} \, dt \quad (8.7)$$

Using the formulations for the modal force and the displacement velocity, the integration of the excitation work yields a function that depends linearly on the vibration amplitude η_0

$$W_E = -\pi f_0 \eta_0 \sin(\Delta\varphi) \quad (8.8)$$

The modal damping work for a single vibratory cycle is expressed as a function of the damping force and therefore the critical damping ratio

$$W_D = \int_0^{\eta_c} f_D \, d\eta = \int_0^{\eta_c} 2\omega\zeta \dot{\eta} \, d\eta = 2\omega\zeta \int_0^{T_0} \dot{\eta}^2 \, dt \quad (8.9)$$

and yields a quadratic relationship with respect to the vibration amplitude

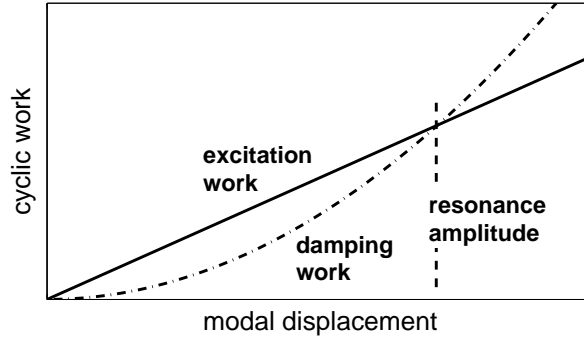


Figure 8.1.: Excitation and damping work equilibrium.

$$W_D = 2\pi\omega^2\zeta \eta_0^2 \quad (8.10)$$

The excitation work and the damping work are both plotted qualitatively in figure 8.1 as a function of the vibration amplitude. The intersection of the two functions represents the point of work equilibrium and yields the steady-state vibration amplitude at resonance. The following relationship expresses the response amplitude as a function of excitation amplitude, phase angle and modal damping

$$\eta_0 = \frac{|f_0 \sin(\Delta\varphi)|}{2\omega^2\zeta} \quad (8.11)$$

The aerodynamic excitation force distribution on the blade surface can be assumed to be independent of blade vibration, i.e. the unsteady pressure distribution is not affected by the vibratory displacement. During resonant steady-state vibration the modal shape lags behind the modal force by the phase angle $\Delta\varphi$ of 90° and represents a condition where the excitation work is at its maximum. The response amplitude becomes

$$\eta_0 = \frac{|f|}{2\omega^2\zeta} \quad (8.12)$$

In the above equation the modal damping can be directly measured according to the procedure discussed in Chapter 7. For the modal force this is not the case. In its generalized form, the modal force must be obtained from the dot product of the normalized mode shape vector, ϕ_k and the complex aerodynamic force vector, \underline{F} according to

$$f = \sum_{k=1}^n [\phi_k (F^{\Re} + iF^{\Im})_k] \quad (8.13)$$

where the real and imaginary components of the force vector act on each degree of freedom, k , and n is the number of degree of freedom. Therefore, in order to calculate the modal force the entire pressure field across the blade surface must be known as a function of time. This however is not available because pressure measurements were carried out for a discrete and limited number of points on both pressure sides. In equation 8.12 the impact of excitation can therefore be only assessed from the limited availability of measurements.

According to equation 8.12 the maximum response amplitude increases with an increase in modal force, supposed the critical damping ratio remains constant. An increase in modal force would increase the aerodynamic excitation work acting on the blade and therefore increase the slope of the linear function in figure 8.1. With constant damping, the equilibrium between excitation and damping work would occur at higher vibration amplitudes.

8.2. Blade Excitation, Damping and Response Amplitude

The central objective of the current study is to identify the impact of excitation and damping on the measured response amplitude. This evaluation must be performed according to equation 8.12. Modal damping is available from measurements. Accounting for the modal force in the equation is problematic because experimental data is not available for the entire blade surface. Due to this restriction, the excitation force must be dealt with as a distribution along the blade surface.

Prior to the presentation of results it should be pointed out that the above equation 8.12 represents the response of a single blade. This implies that the blade must be viewed as an isolated vibrating continuum which is not affected by any neighboring blades through mechanisms of mistuning and coupling. This constrain stands in conflict with measurements taken for a mistuned and coupled system of blades. A remedy to overcome this hurdle is to view

the measurement results in terms of averaged quantities across all blades. For example, blade amplitude response and damping were measured for each blade and averaging these values would enable to approximate a single blade. It should be kept in mind that the averaged quantities do not correspond to a tuned case. Mistuning and coupling are known to affect the averaged response amplitude by about $\pm 15\%$ in comparison with a tuned case.

In line with previously presented results three resonant cases will be discussed hereafter. All cases deal with resonance of the first blade mode and data was obtained with Impeller No. 2.

- **Mode1/EO5** resonance due to **5 lobe** inlet distortion
- **Mode1/EO6** resonance due to **3 lobe** inlet distortion
- **Mode1/EO6** resonance due to **6 lobe** inlet distortion

Damping

To start, the modal damping will be discussed first. Figures 8.2(a), 8.3(a) and 8.4(a) quantify damping as a function of inlet pressure. The shown results were obtained from measurements according to the procedure described in Chapter 7 for three operating lines OL1, OL2 and OL3. The shown blade damping was obtained from averaging individual values across all impeller blades and then performing a linear fit. The results are expressed in terms of damping ratio, where material damping ζ_M was taken as the reference according to the value in table 7.1. During the linear fitting material damping was found to vary by as much as $\pm 15\%$ between the three cases.

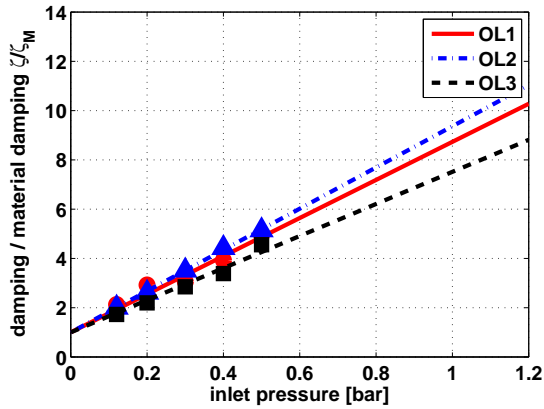
Overall, the measurements show very consistently that damping is equal for all cases. Aerodynamic damping is by a factor of 10 higher than material damping when extrapolated to an inlet pressure of 1bar. Damping variations due to operating line setting can be observed, however, the effect is comparatively marginal and might be rather affected by the linear interpolation procedure. Moreover, the results shown here were taken with Impeller No. 2 and are almost identical with results obtained for Impeller No. 1. For the evidence presented, the first blade mode damping magnitude can be considered to be equal across all excitation cases and is not affected by the operating line setting. This finding profoundly simplifies further discussions on equation 8.12 with respect to the excitation force and the response amplitude.

Blade Excitation and Response Amplitude

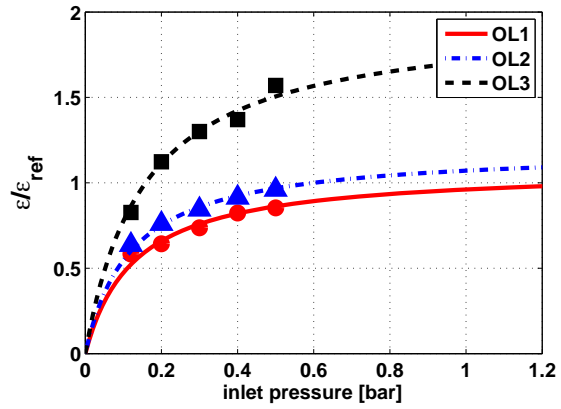
The response amplitude for the three screen cases is shown in the figures 8.2(b), 8.3(b) and 8.4(b) and is expressed in terms of non-dimensional strain measured on the blade surface. The reference strain magnitude was randomly chosen such that it allows to assess changes with reference to unity. The shown experimental values were obtained from averaging across all blades. A curve fit was performed according to the equation 6.9 in Chapter 6 using measured damping values as shown in the plots. In general, the fitting quality can be seen to be very good for all cases. This confirms previous findings on the fact that the averaged response amplitude is captured by a SDOF model.

In terms of amplitude, the response for the 5 lobe and the 6 lobe case are generally comparable, except for the OL3 response. This case will be given special attention later. In both screen cases the excitation order corresponds to the fundamental distortion order of the screen. In the case of the 3 lobe screen the second harmonic causes response amplitudes considerably smaller than in the former two cases. Since the modal damping is equal for all cases, the reason for this case dependent amplitude response must be justified by an increase in modal force according to equation 8.12. Ideally this should be reflected in the measured forcing function along the blade mid-height. Figures 8.5, 8.6 and 8.7 quantify the forcing function amplitudes along the blade mid-height expressed in terms of unsteady pressure difference. A case to case comparison shows, that the excitation amplitudes are highest for the 5 lobe case, lower for the 6 lobe case and lowest for the 3 lobe case.

Mode1/EO6 - Effect of inlet distortion: The effect of amplitude scaling can be observed for the two Mode1/EO6 cases. A straight forward comparison can be carried out here because of similarities in the excitation distribution. The shape of the EO6 phase relationship is identical for both of the operating lines cases, see figures 8.6(b) and 8.7(b). This circumstance renders the amplitude of the forcing function as the sole factor to affect the response amplitude. In the case of the 3 lobe screen the amplitudes are by a factor of 2 smaller than for the 6 lobe screen. This relationship directly translates into a change of the response amplitude of the same factor, see figures 8.3(b) and 8.4(b). It should be pointed out that the involved measured force variations are as small as 0.25% of the inlet pressure. The presented analysis supports the applicability of equation 6.9 due to the fact that the phase relationship was identical and its effect on the modal force could be eliminated.

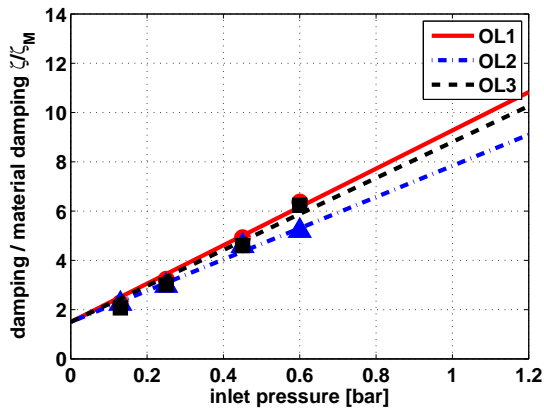


(a) Damping

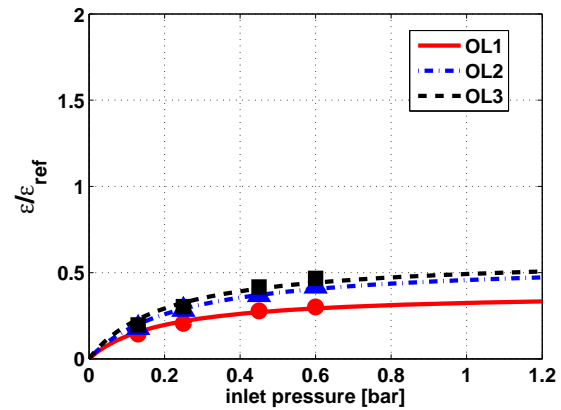


(b) Strain

Figure 8.2.: Damping and strain for Mode1/EO5 with 5 lobe screen.

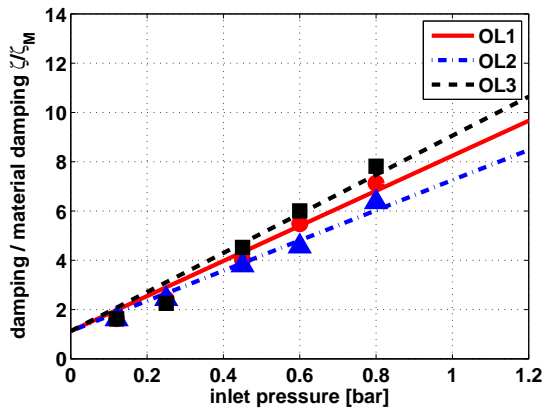


(a) Damping

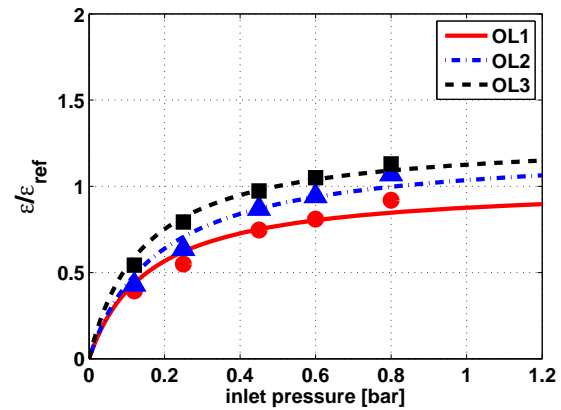


(b) Strain

Figure 8.3.: Damping and strain for Mode1/EO6 with 3 lobe screen.



(a) Damping



(b) Strain

Figure 8.4.: Damping and strain for Mode1/EO6 with 6 lobe screen.

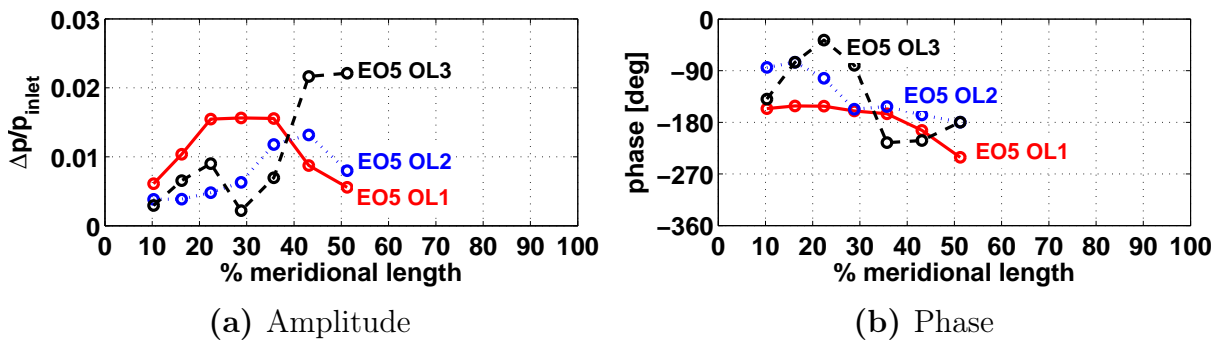


Figure 8.5.: EO5 amplitude and phase for 5 lobe screen at 16000rpm.

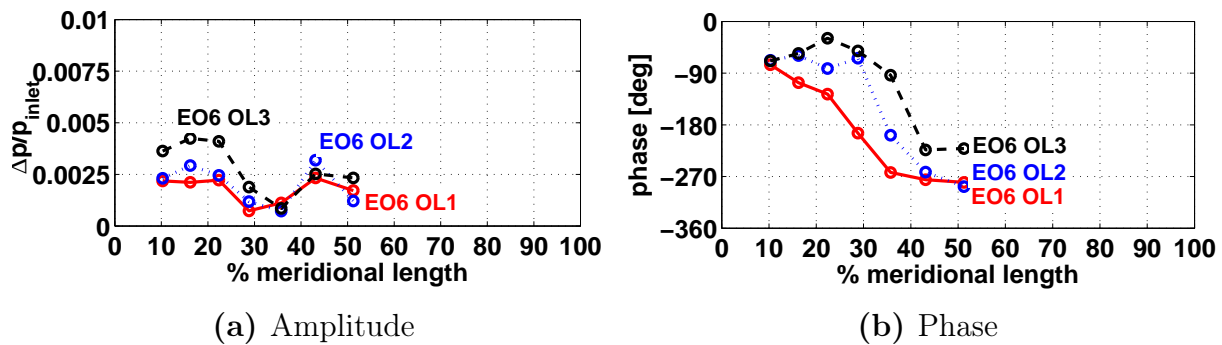


Figure 8.6.: EO6 amplitude and phase for 3 lobe screen at 13200rpm.

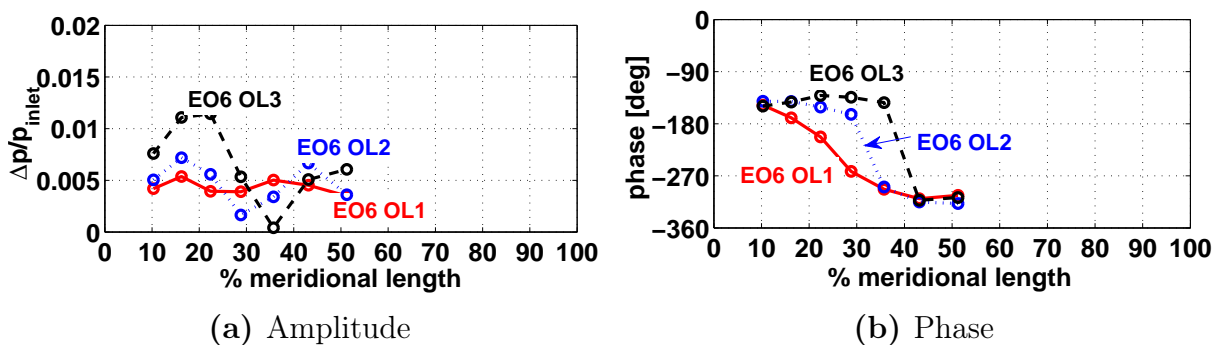


Figure 8.7.: EO6 amplitude and phase for 6 lobe screen at 13200rpm.

The analysis shows that the amplitude of the excitation must be scaled by the distortion amplitude of the inlet flow field, since all other parameters were retained constant between the screen cases. Of particular importance is

the fact that the excitation distribution, i.e. the shape of the function along the blade length, is not affected by the type of the distortion screen. This observation was achieved previously, whereas its effect to scale the response amplitude was shown here.

Mode1/EO5 - Mass flow effect on response amplitude: The case with a 5 lobe distortion screen must be treated separately. The focus will be laid on the striking increase of the response amplitude by 50% for OL3 in comparison to OL1 and OL2, see figure 8.2(b). The increase is substantial considering the fact that amplitudes in the OL1 and OL2 already reach critical levels in terms of high cycle fatigue endurance. Looking at the problem in the modal space the sudden increase can only be justified by an increase of modal force for constant damping according to equation 8.12 This argument however, is not reflected in the measured amplitude of the excitation function, see figure 8.5(a). The amplitude of the OL3 case can be seen to be actually smaller in the inducer region than for example for OL1. The amplitudes between OL2 and OL3 are comparable up to 20% meridional length. It appears that the increase in response amplitude for OL3 cannot be justified on the available measurement analysis. The following restrictions were considered to limit the judgement:

- Separate assessment of amplitude and phase. Ideally, the modal force would be computed from a pressure field distribution which combines amplitude and phase into a single value. The presented analysis however treats amplitude and phase separately for distinct points on the blade surfaces. Their combined effect can therefore not be assessed.
- The number of pressure measurement positions maybe insufficient. The analysis might not capture areas on the surface where the amplitude increases its contribution to blade excitation due to the increase in mass flow.

Based on the available data set an unambiguous answer to this problem cannot be given at this point. A remedy to overcome this shortcoming will be presented in Chapter 9. The underlying concept is to measure the aerodynamic work during resonance at each pressure sensor location which represents a measure for the energy transfer between the fluid and the blade. The strength of this analysis is the fact that computing aerodynamic work enables to combine excitation amplitude and phase into a single quantity.

In summary, in the current study of forced response of Mode 1, the presented modal damping can be considered to be constant across all screen and operating line cases. During EO6 excitation with a 3 lobe and a 6 lobe screen the measured phase relationship is identical and their difference in excitation amplitude results in an equal change in response amplitude. In the case of the 5 lobe screen however the cause of amplitude variation cannot be explained based on the available data set and requires insight into aerodynamic work as will be presented later. It must be reminded that the presented analysis derives from averaged quantities across all blades.

8.3. Mistuning Effects on Damping and Response Amplitude

In the last three decades the subject of mistuning has received an ever growing attention in the turbomachinery community. Mistuning has the potential to introduce considerable response amplitude variations, as high as 100% increase were measured in the datum research shown in section 6.5. So far, this chapter on cumulative aspects of forced response has addressed the problem of excitation, damping and response on the basis of data averaged across all blades. In the following it is aimed to quantify the effect of mistuning on damping and response amplitude on blade-to-blade basis.

Measurement data will be exemplified for the first operating line OL1. Damping and response amplitude at resonance are shown in figures 8.8-8.10 for three screen configurations. In all plots the averaged function is plotted along with bars indicating the blade-to-blade sample variation. In addition, damping and response amplitude were plotted for the blade with the maximum and minimum response amplitude among the seven main blades. In the cases presented blade 4 (MB4) and blade 7 (MB7) exhibited the maximum and minimum response amplitudes, respectively.

The 5 lobe screen case will be examined first. The first observation to make is the fact that damping was also affected by mistuning. In numbers, at 0.5bar inlet pressure damping variation reaches $\pm 20\%$ of the mean value. For the same pressure setting the response amplitude varies by about $\pm 40\%$ from mean. The maximum response amplitude was realized by blade 4 and the

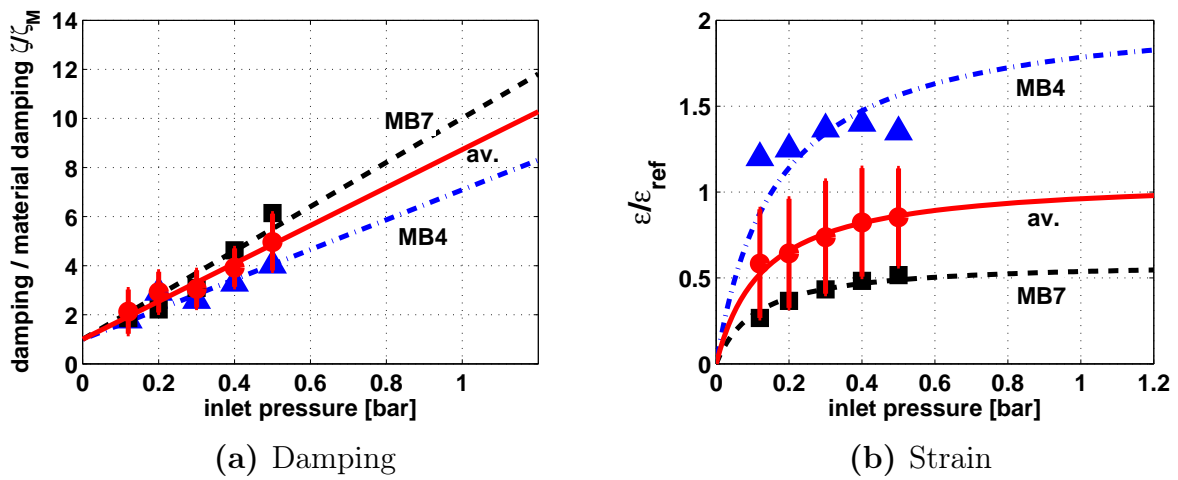


Figure 8.8.: Damping and strain variation for 5 lobe screen and OL1.

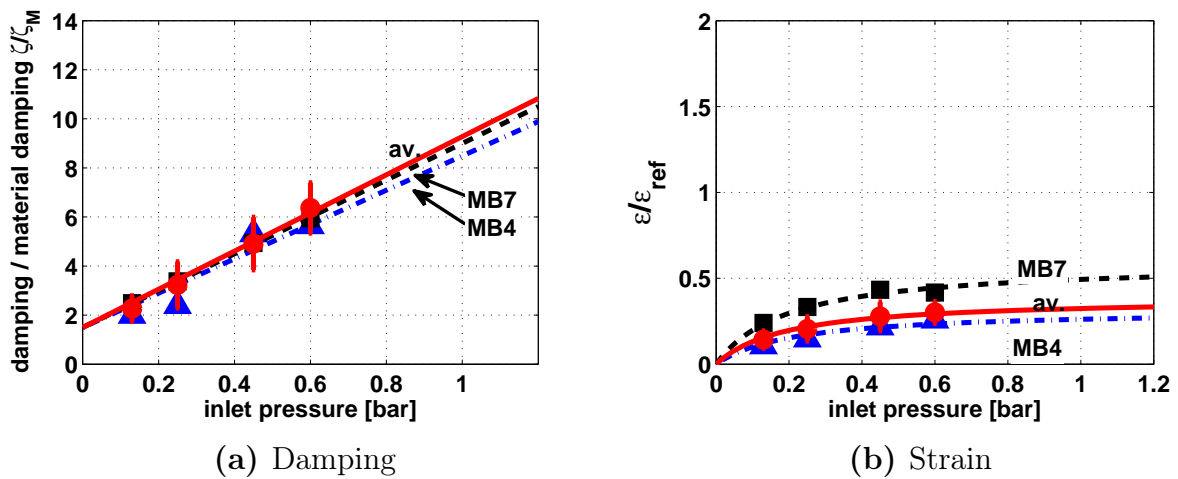


Figure 8.9.: Damping and strain variation for 3 lobe screen and OL1.

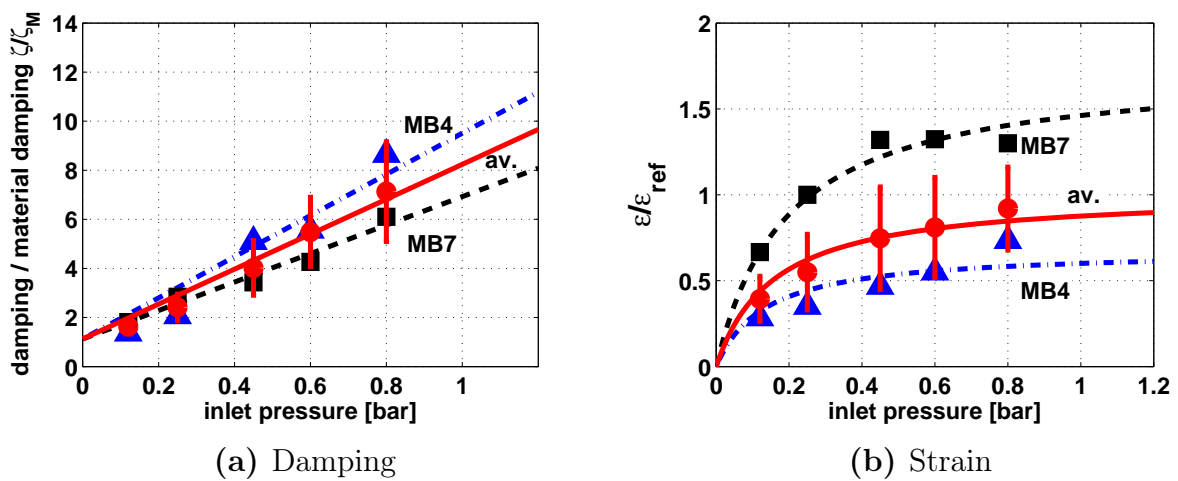


Figure 8.10.: Damping and strain variation for 6 lobe screen and OL1.

minimum by blade 7. In the case shown blade 4 can be seen to exceed the mean response level by 100% and represents thereby a dangerous source of potential failure. Damping for both blades is plotted accordingly. In the case of blade 4 damping is below whereas for blade 7 damping is above the average. The data suggests that an increase in response amplitude of a single blade is accompanied by a reduction in damping and vice versa.

A brief assessment of the numbers should be carried out here. According to equation 8.12 an increase in response amplitude can only be caused by either an increase in excitation force or a reduction in damping. For the 5 lobe case blade 4 was found to exceed the average strain level by 100% whereas its measured damping was found to reduce only by 20%. These numbers show that an increase in response amplitude is only partially justified with a decrease in damping. By far the dominating contributor must be an increase in excitation force. This simple analysis illustrates the energy redistribution mechanisms involved in cyclicly symmetric and coupled structures caused by mistuning. In the presented case excitation energy is localized on blade 4 with the effect to cause substantial increase of vibratory amplitude response in comparison to the average value.

Very similar findings can be found for the 3 lobe and 6 lobe case. In both cases it is blade 7 to respond with the highest amplitudes whereas blade 4 exhibits the smallest. This finding stands in contrast to the previous case presented and indicates that the localization of excitation energy can vary depending on the resonance case. Blade-to-blade damping variations can be seen to occur. In the case of the 3 lobe screen, damping variation was comparatively small and no trend could be identified. In the case of the 6 lobe screen, damping follows the same principal as for the 5 lobe screen, where an increase in amplitude was accompanied by a decrease in damping and vice versa. However, also in this case, the variation in damping is comparatively small and does not justify the substantial increase in vibratory amplitude.

To conclude, the presented effects of mistuning showed to affect both, damping and response amplitude. Mistuning in a coupled structure i.e. the datum impeller, is known to cause dangerous increase in response amplitude through excitation energy localization and was shown to be present for all cases discussed. Blade damping is mainly composed of aerodynamic damping and is caused by an unsteady pressure field within the blade passage. The pressure

field is induced by the blade motion itself and might also, to some unknown but not negligible degree, be affected by the neighboring blades. The presented data suggest that aerodynamic damping is affected by the alternating blade-to-blade vibratory amplitude such, that an increase in vibration amplitude causes a reduction in aerodynamic damping. However, the reduction in damping represents only a minor contribution to the increase in response amplitude of a specific blade which is primarily driven by energy localization. Depending on the resonance case, the blade affected mostly by energy localization may vary.

8.4. Summary and Conclusions

Three aspects on forced response of centrifugal compressor blades were brought together to present their properties during forced response. These aspects were unsteady pressure excitation, damping and vibratory response. Their interrelation was expressed in the modal space. In all cases the first blade mode was discussed for three operating lines. Results were presented in terms of averaged quantities across all impeller blades. In addition the effect of mistuning on damping and response amplitude was outlined. Conclusions can be summarized as follows.

- One of the major finding in this research work is the fact that damping of the first blade mode can be considered to be independent of the operating line setting and excitation order. The dependency of damping on the inlet pressure was found to be consistently equal across all cases presented.
- Owing to the fact that damping is constant for all resonant response cases, changes in response amplitude can only be justified by changes in modal force. An increase in modal force corresponds to an increase in excitation work done on the blade surface.
- Changes in mass flow setting cause a redistribution of excitation amplitude and phase and might thereby cause a profound increase or reduction in modal force. If the phase relation of the excitation between two cases remains the same, i.e. for EO6 for two different screen configurations, then an increase in excitation amplitude directly translates into an increase in response amplitude by the same factor.

-
- Due to the limited number of pressure sensors the modal force cannot be experimentally determined. Therefore, excitation expressed in terms of amplitude and phase functions may not reveal a dangerous increase of excitation work.
 - Mistuning of impeller blades causes a blade-to-blade energy localization which results in some of the blades to vibrate at particularly high or low amplitudes.
 - Blade-to-blade variation in response amplitude affects aerodynamic damping of each specific blade. Based on this mechanism an increase in excitation amplitude goes together with a decrease in damping or vice versa.
 - Blades with over-average response amplitudes exhibit a reduction in damping and vice versa. However, the reduction in damping is not equivalent to an increase in response amplitude but only a fraction of it.

9. Aerodynamic Work

The objective of this section is to present a novel analysis method that enables the measurement of energy transfer between the vibrating blade and the flow at discrete positions on the rotating blades. The motivation to incorporate the measurement of aerodynamic work was driven by the need to express the combined effects of unsteady pressure amplitude and phase as well as blade motion in the form of a single quantity. In the previous chapter the limited number of pressure sensors was shown to limit the ability to judge on the cause of response amplitude variation caused by changes in mass flow setting. Ideally, one would need to compute the modal force according to equation 8.13 for each resonance case and make a judgement based on the obtained force magnitude. Due to the limited number of pressure sensors this however is not possible. In order to overcome this limitation it was intended to compute the aerodynamic work done on the blade surface at each pressure sensor position. This procedure would essentially give a measure of energy exchange between the blade and the fluid at discrete points on the blade surface. The argumentation goes, that changes in mass flow setting would cause a redistribution of aerodynamic work along the blade and would therefore allow to identify the combined effects of pressure amplitude and phase.

The technique presented hereafter derives from simultaneous measurement of blade motion and unsteady pressure. Measurement of blade motion enables to compute the blade displacement normal to the surface at positions where pressure sensors were installed. Measurement of unsteady pressure quantifies the unsteady force acting on the blade. Due to the simultaneous measurement of this two quantities the computation of the evolution of aerodynamic work distribution could be carried out as the impeller passes through resonance. In the following, measurements of aerodynamic work will be presented alongside an analytical analysis. The purpose of the analytical procedure is to point towards the most relevant factors that determine the magnitude and sign of local aerodynamic work.

9.1. Theoretical Background

Based on the analysis presented in section 5.6 the measured unsteady pressure $p_{meas}(t)$ during resonance is composed of two harmonic oscillations, $p_d(t)$ due to inlet flow distortion and $p_m(x(t))$ due to the vibratory blade motion. The resultant measured pressure is therefore

$$p_{meas}(t) = p_d(t) + p_m(x(t)) \quad (9.1)$$

$$= p_{d,0} \cos(\omega t + \Delta\varphi_d) + p_{m,0} \cos(\omega t + \Delta\varphi_m) \quad (9.2)$$

Accordingly, the local blade displacement at each specific pressure sensor position can be modeled by a harmonic oscillation

$$x(t) = x_0 \cos(\omega t) \quad (9.3)$$

With respect to aerodynamic work only those frequencies in the measured pressure signal contribute to excitation or damping work which correspond to the vibration frequency of the blade motion. Therefore, a simplified ansatz can be made according to equation 9.2. In the case of the first term, $p_d(t)$ the relevant frequency could for example stem from EO5 excitation. In a forced response study this term is considered to cause blade vibration. In the case of the second term, $p_m(x(t))$ the unsteady pressure is coupled to the blade motion and is therefore of the same frequency as the blade motion. Motion induced pressure ideally counteracts blade vibration and is therefore a source of damping, in this case referred to as aerodynamic damping.

Particular attention should be given to the phase angles $\Delta\varphi_d$ and $\Delta\varphi_m$ which represent the phase relation between the blade motion, $x(t)$ and the unsteady pressure terms, $p_d(t)$ and $p_m(x(t))$, respectively. As will be shown hereafter, the phase angle determines the direction of energy transfer, i.e. either from the fluid to the structure or vice versa. The phase angle can therefore be used as a criterion for the direction of energy transfer. Also, considering motion dependent unsteady pressure, $p_m(x(t))$ aerodynamic damping is only present if according to equation 9.7 or 9.11 the phase angle, $\Delta\varphi_m$ is not zero.

From the perspective of measurement analysis the unsteady pressure terms, $p_d(t)$ and $p_m(x(t))$ can be superposed and treated as a single harmonic according to the following equation

$$p_{meas}(t) = p_0 \cos(\omega t + \Delta\varphi) \quad (9.4)$$

In this equation the pressure p_0 is a function of the local displacement, $x(t)$. This approach was required at this stage of the analysis since the measured pressure signal cannot be separated into its relevant contributors. It is for this reason, that in the following analysis the presented results are referred to in a more general manner as blade aerodynamic work. A more in depth elaboration would necessitate the separation of the measured pressure contribution from inlet distortion and blade motion in order to allow for the separation of aerodynamic work into excitation work and damping work. Modal damping in general and aerodynamic damping in more specific terms were presented in detail in the previous chapters. A possible approach to measure only the contribution of damping work was presented by *Crawley* [9, 10]. In his work the excitation could be turned off instantly during resonance allowing the blades to decay in their vibratory motion. This facilitated the conditions that only unsteady pressure induced by the vibratory motion of the blades was acting on the surfaces.

Aerodynamic work, W acting on the blade surface is obtained by integrating the product of the unsteady pressure force and displacement speed with respect to time.

$$W = \int_0^{2\pi/\omega} f \dot{x} dt = \int_0^{2\pi/\omega} (p_{ss} - p_{ps}) \dot{x} dt \quad \left[\frac{\text{J}}{\text{m}^2} \right] \quad (9.5)$$

In this integral the temporal limits are defined such that it yields the work done during a single blade vibration cycle. The cyclic aerodynamic work, W therefore quantifies the energy transfer between the fluid and the blade at a specific point on the blade surface for one vibration cycle. The unsteady force, $f(t)$ is defined in figure 5.29 on page 97 and represents the difference in pressure between the suction and pressure side. Using the equations from above an analytic expression of aerodynamic work can be obtained for each blade side separately. For the suction side the aerodynamic work is given by

$$W_{ss} = \int_0^{2\pi/\omega} p_{ss} \dot{x} dt \quad (9.6)$$

$$W_{ss} = -\pi p_0 x_0 \sin(\Delta\varphi_{ss}) \quad (9.7)$$

In the expression of aerodynamic work the sign of the phase angle $\Delta\varphi_{ss}$ determines the direction of energy transfer

$$\sin(\Delta\varphi_{ss}) > 0 \rightarrow W_{ss} < 0 \rightarrow \text{damping} \quad (9.8)$$

$$\sin(\Delta\varphi_{ss}) < 0 \rightarrow W_{ss} > 0 \rightarrow \text{amplification} \quad (9.9)$$

Cyclic work on the pressure side is given by

$$W_{ps} = - \int_0^{2\pi/\omega} p_{ps} \dot{x} dt \quad (9.10)$$

$$W_{ps} = \pi p_0 x_0 \sin(\Delta\varphi_{ps}) \quad (9.11)$$

Identical to the suction side, the phase angle $\Delta\varphi_{ps}$ for the pressure side determines the direction of energy transfer

$$\sin(\Delta\varphi_{ps}) > 0 \rightarrow W_{ps} > 0 \rightarrow \text{amplification} \quad (9.12)$$

$$\sin(\Delta\varphi_{ps}) < 0 \rightarrow W_{ps} < 0 \rightarrow \text{damping} \quad (9.13)$$

In the case of positive aerodynamic work, energy is fed into the structure, thus the vibratory motion is amplified. To the contrary, as the work becomes negative, energy is removed from the vibrating structure. Furthermore, the amplitude of aerodynamic work is determined by the unsteady pressure and blade vibrational amplitudes.

In the measurements the phase angle, $\Delta\varphi$ can be obtained from computing the complex frequency transfer function $H(j\omega)$. This is done on the basis of the

cross-correlation spectrum, S_{xy} between the pressure and the displacement and the spectral density S_x of the pressure signal.

$$\Delta\varphi = \arg(H(j\omega)) = \arg\left(\frac{S_{xy}}{S_x}\right) \quad (9.14)$$

On the subject of phase angle measurement it should be pointed out that the pressure signal used to compute the transfer function and hence the phase angle is always composed of two contributors to the measured pressure signal. These are the unsteady pressure due to inlet distortion and due to vibratory motion. The measured phase angle will therefore be affected by the amplitude and phase angle of the two contributors to the overall signal. For example, if the unsteady pressure due to vibratory motion dominates in terms of amplitude i.e. in figure 5.27 on page 95 then the measured phase angle will be either almost in phase or in counter-phase with the blade motion. Otherwise, if the pressure due to vibratory motion is negligible, then the measured phase angle will primarily depend on the angle of the unsteady pressure field due to inlet flow distortion and might take any arbitrary value.

General Comments on the Measurement of Aerodynamic Work

The measurement of aerodynamic work during resonant crossing represents a measure of the energy transfer between the blade and the fluid. The aerodynamic work is a specific quantity since it is derived for a single point on the blade surface and is expressed per area. Because it is not possible to separate unsteady pressure due to inlet distortion and due to vibratory motion it is also not possible to compute their separate contributions to the overall work. In other words, excitation work due to inlet distortion and damping work due to vibration cannot be separated. Following the notation presented earlier, positive work at a particular sensor position signifies net energy transfer from the fluid to the blade. For such a scenario excitation work is higher than damping work. On the contrary, damping work is higher if aerodynamic work is negative thereby removing energy from the blade.

The importance of the measured phase relationship is justified by the influence it exerts on the aerodynamic work by (1) scaling the amplitude according to the equations 9.7 and 9.11, respectively, and (2) affecting the direction of

energy transfer. In the latter case the phase angle can be used as a criterion. The scaling effect as a function of a sinus can be substantial.

9.2. Measurements of Aerodynamic Work and Phase

Figure 9.1 shows the analysis results of phase angle and aerodynamic work using experimental data. The phase angle was computed according to equation 9.14 in the frequency domain, whereas aerodynamic work was numerically integrated in the time domain according to equations 9.6 and 9.10. In order to directly compare the evolution of these two quantities, in the plots the phase angle as well as the aerodynamic work were plotted along the normalized frequency. In the measurements for the Mode1/EO5 case the shown frequency range corresponds to a change in rotational speed from 16040rpm to 16360rpm as resonance was swept. Data is presented for three different inlet pressure settings.

On the suction side, the phase can be seen to be negative and increasing towards resonance. For the same range aerodynamic work can be seen to be positive which corresponds to the criterion in equation 9.8 and energy is therefore fed into the vibrating blade. Two parameters can be identified that determine the resultant aerodynamic work as the rotational speed increases towards resonance. According to equation 9.6, aerodynamic work increases with a rise in displacement amplitude x_0 . However, as the phase approaches zero the contribution of unsteady pressure and vibration amplitudes disappears too. Past resonance, a sharp fall-off in aerodynamic work can be identified, due to a decrease in vibration amplitude and a further increase of the phase angle. As the phase angle becomes positive, aerodynamic work can be seen to locally damp blade vibration. In principal the presented mechanism of blade excitation and damping applies on the pressure as it does on the suction side, i.e. the combination of vibration amplitude and phase angle determine aerodynamic work amplitude and sign. In the case of the pressure side sensor this leads to maximum aerodynamic work at a speed and frequency ratio higher than resonance.

On the pressure side the phase angle can be seen to alternate close to 180° . This indicates that measured pressure fluctuations are dominated by contri-

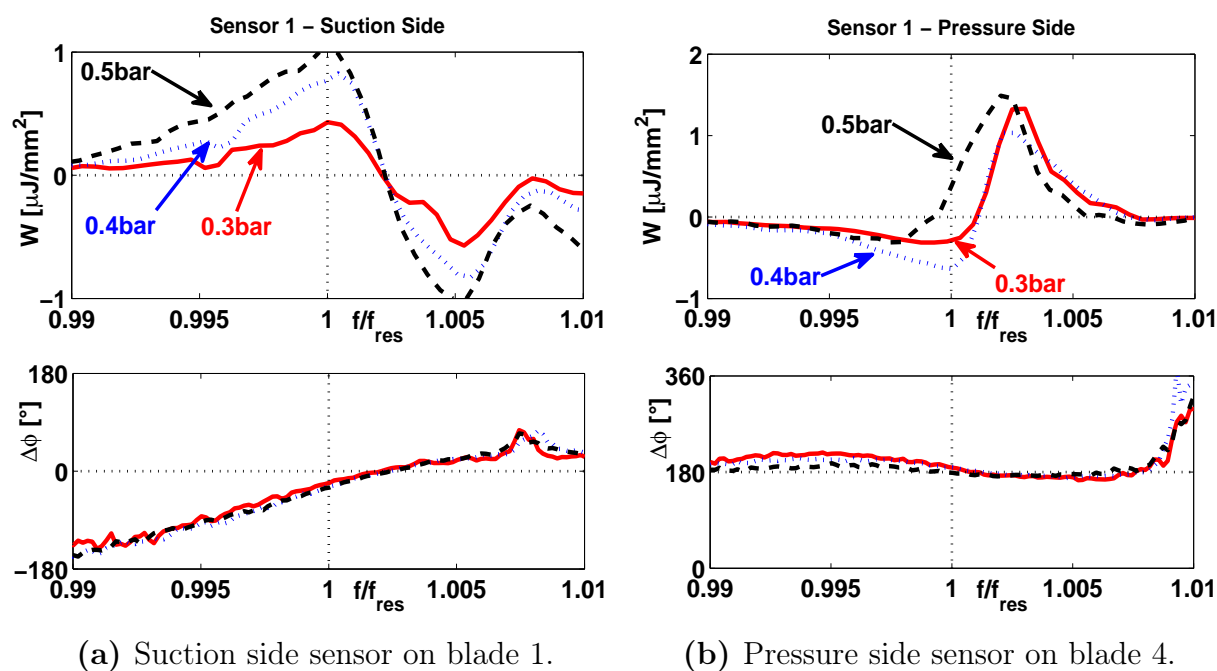


Figure 9.1.: Cyclic aerodynamic work and phase for sensor 1 for **Mode1/EO5** from 5 lobe screen excitation. Inlet pressure comparison.

tribution from blade movement whereas pressure fluctuations due to inlet flow distortion are weaker in comparison. Also, the unsteady pressure on the pressure side is in counter-phase with the blade motion. On the contrary, on the suction side blade vibration is in phase with the measured unsteady pressure since the measured phase angle at resonance passes through zero. Also in this case the unsteady pressure amplitude is dominated by the induced pressure component.

Effect of Inlet Pressure

According to figure 9.1 the inlet pressure amplitude can be observed to affect the aerodynamic work amplitude. For both blade sides the amplitude of aerodynamic work increases with increase in inlet pressure. However, the shape of the function remains similar. For example, on the suction side, the aerodynamic amplitude changes, but because the flow angle remains approximately independent of the inlet pressure, the aerodynamic work function was retained with respect to the position of the maxima and minima. These observations in principal also apply to the pressure side.

The measured dependency of the aerodynamic work function on the inlet pressure was in agreement with expectations for the following reason. Off-resonance measurements showed that unsteady pressure functions along the blade collapsed when non-dimensionalized with inlet static pressure. Therefore, prior to resonance the flow field structure can be considered to be independent of the inlet pressure range that is considered in this study. As such, the distribution pattern of the unsteady pressure excitation on the blade remains constant and only varies in amplitude as a function of inlet pressure. The effect of the excitation amplitude can be studied in equation 9.7 where the increase in response amplitude causes an increase in aerodynamic work.

Variation in phase angle can be clearly seen to occur on the pressure side accompanied by shifts of the aerodynamic work function along the frequency axis. For the pressure side, an increase in inlet pressure from 0.3bar to 0.5bar, causes a shift of the amplitude functions towards lower frequencies. At resonance this effect causes excitation at 0.5bar instead of damping. Nevertheless, the functions at different amplitudes can be considered to be similar.

Overall, the inlet pressure appears to primarily affect the amplitude of energy transfer between the blade and the fluid, whereas the structure of the excitation pattern, signified by the phase angle, remains similar between the cases. This means, that zones on the blade of positive or negative energy exchange retain their character.

Effect of Modal Shape

An overview of aerodynamic work evolution for sensor positions 1-5 is shown in the figures 9.2 and 9.3 for the suction and pressure sides, respectively. Data is plotted for three operating lines OL1, OL2 and OL3. The plots are presented such that aerodynamic work is centered around resonance indicating the moment of maximum displacement of the blade. The main general observation to make is a reduction in maximum aerodynamic work along blade mid-height from sensor position 2 to 5. This is primarily due to a reduction in blade displacement according to the first mode of the blade as illustrated in figure 2.9(a) on page 31. The same principal applies to sensors positioned near the leading edge which exhibit the highest aerodynamic work amplitudes, in particular at sensor position 1, where sensors are offset outwards in a radial direction. According to equation 9.7, the displacement amplitude affects aerodynamic work linearly. Since the displacement amplitude is af-

ected by the modal shape, for Mode 1 sensors positioned near the leading edge will exhibit the highest displacement amplitudes. For higher modes this means, that sensors positioned near nodal lines would capture near zero energy transfer.

To conclude, the magnitude of energy transfer between the blade and the fluid is considerably affected by the local displacement which is mode shape dependent. Areas associated with high vibratory displacement generally translate into high amplitudes of excitation or damping work.

Effect of Operating Line

The previous section 8.2 on excitation, damping and response amplitude was concluded with the finding that in the case of the 5 lobe screen the cause of amplitude variation due to changes in operating line cannot be explained on the available data analysis. Inclusion of aerodynamic work distribution into the argumentation were considered to remedy the encountered deficiency and will be presented in the following.

The aerodynamic work amplitude and phase are shown in figures 9.2 and 9.3 for three operating lines. To start, it should be reminded that the response amplitude of OL1 and OL2 were found to be similar whereas OL3 response was by about 50% higher. However, in the OL3 case the measured forcing function was comparable or even smaller than in the OL1 or OL2 cases. The previous conclusions on aerodynamic work identified the sensor positions 1-3 where aerodynamic excitation or damping is comparatively high. On the suction side the aerodynamic work can be seen to be positive for OL1 and OL2 due to the corresponding phase angle relationship. As the impeller passes through resonance along OL3 the phase angle for sensors 1-3 becomes positive and causes damping at the measurement positions. On the pressure side the contrary occurs. For OL3 the unsteady pressure feeds energy into the vibrating blade. In particular at sensor position 1 the aerodynamic work increases substantially. The analysis of the datum cases shows, that the aerodynamic work is redistributed between suction and pressure side. This is caused by changes in unsteady pressure phase relationship.

The following question must be answered at this stage: How do the above findings on aerodynamic work reconcile with the fact that blade resonant response experiences a substantial increase for OL3 in comparison to the op-

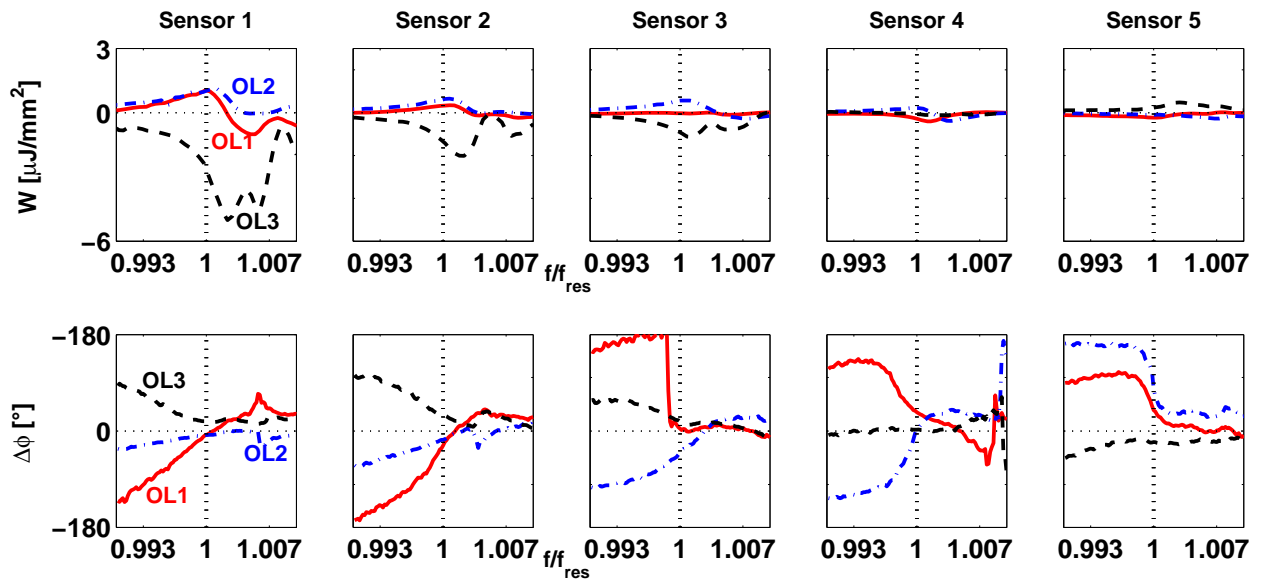


Figure 9.2.: Cyclic aerodynamic work and phase on **suction side** for **Mode1/EO5** from 5 lobe screen excitation and $p_{inlet} = 0.5\text{bar}$.

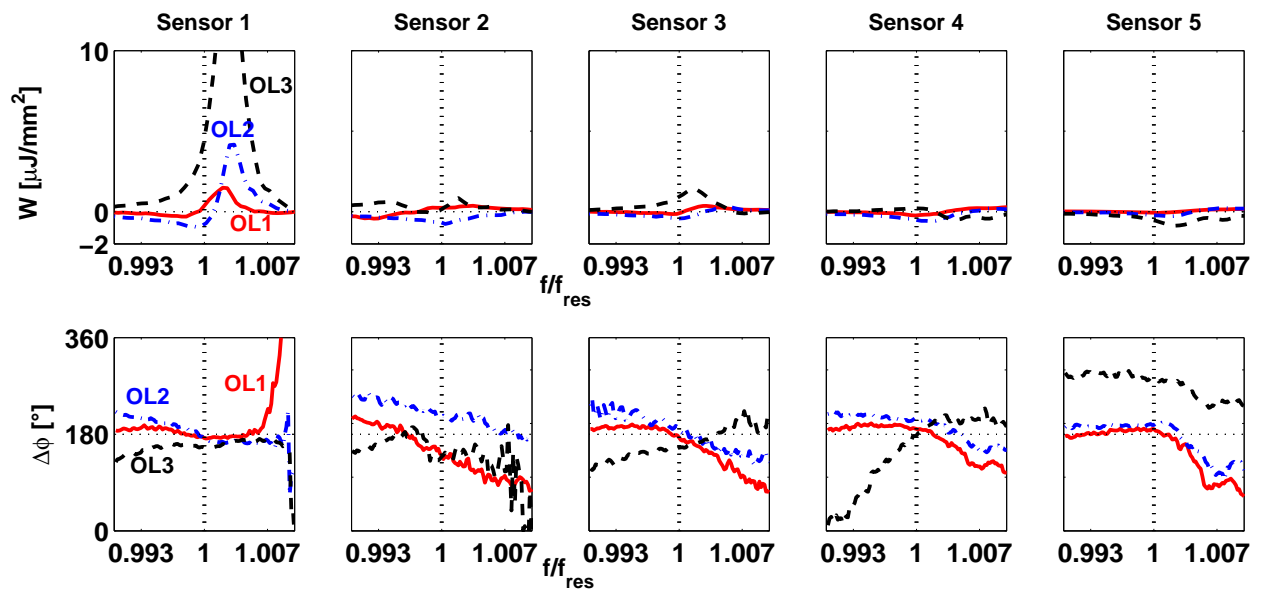


Figure 9.3.: Cyclic aerodynamic work and phase on **pressure side** for **Mode1/EO5** from 5 lobe screen excitation and $p_{inlet} = 0.5\text{bar}$.

erating lines at lower mass flow settings? In the previous findings it was stated that the change in response amplitude can only be justified by an increase in modal force since modal damping remains constant. This in turn implies an increase in excitation work according to the integral formulation of equation 8.7. Despite the limited number of measurement positions on the blade surface the data suggests, that an increased energy transfer into the structure can only be justified to occur on the pressure side in the region of sensor 1. The excitation work done in this part of the blade is balanced by the damping work done on the suction side for sensors 1-3.

The findings presented lead to the conclusion that energy transfer between the blade and the fluid is a very localized phenomenon on the blade surface. Changing the operating line and therefore the mass flow causes a redistribution of the excitation phase angle and thereby affects the magnitude of excitation work.

9.3. Summary and Conclusions

A method was presented to measure the aerodynamic work on the blade surface. The approach is based on simultaneous measurements during resonance of unsteady surface pressure and blade displacement. The aerodynamic work represents a measure of energy transfer between the vibrating blade and the fluid.

- Measurement of aerodynamic work enables to experimentally identify zones on the blade surfaces that suffer from high excitation work amplitudes. This capability is of great relevance to applications where blades are subject to forced response vibration or flutter. Passive or active flow modulation techniques could be introduced in order to specifically target areas of higher excitation work.
- The presented method does not separate excitation and damping work but measures their combined contributions.
- The phase angle between blade vibration and unsteady pressure determines the direction of energy transfer and thereby classifies the resultant work into excitation or damping work.

- Parametric variation of inlet pressure primarily affects the amplitude of excitation work. The flow structure approximately retains its characteristic. Generally, increasing the inlet pressure causes an increase in aerodynamic work.
- Damping work amplitude strongly depends on the modal shape. For the first mode, measured damping work amplitude reduces along the blade due to reduction in displacement amplitude. Regions of higher displacement ultimately cause higher transfer of energy.
- Changes in operating line and the associated mass flow variation affects the phase angle distribution on the blade surfaces. Even if the measured excitation amplitudes might reduce in amplitude the phase angle might considerably affect the excitation work.
- Measurement of aerodynamic work show that energy transfer between the blade and the fluid is a very localized phenomenon on the blade surface. Certain areas on the blade surface show high levels of energy transferred into the blade whereas other areas are dominated by damping. The distribution varies with the operating line setting and are consequently affected by the phase angle.
- Measurement of aerodynamic work provides a means to gain valuable information in the field of forced response. The method combines variables that are commonly examined independently of each other, i.e. excitation amplitude, phase and vibration amplitude, into a single parameter. The method thereby enables to judge on their combined effects.

10. Conclusions, Summary and Future Work

10.1. Conclusions

Experimental investigations into forced response for blades of a centrifugal high-speed compressor was undertaken. Resonance of the first two blade modes was generated by introducing inlet flow distortion. For the first time for centrifugal compressors, all aspects of forced response were experimentally acquired: inlet flow properties, unsteady forcing function and blade resonant response. The measurement conditions of the testing facility were representative for real engine applications. Based on the experimental data the following conclusions were derived:

- Upstream strut installations generate EO2 and EO3 blade excitation of comparable amplitude as the intended excitation order, i.e. EO5 or EO6. The amplitude of the lower harmonics was affected by the distortion screens.
- Circumferential inlet total pressure distortion of 1% – 4% was sufficient to generate dangerous forced response amplitudes.
- Unsteady excitation is characterized by zones of pressure waves propagating either upstream or downstream along the blade surfaces.
- Excitation forces increase in amplitude towards higher rotational speeds. For a constant shaft speed, the excitation amplitude and phase depend on the mass flow setting, which predominantly affects the unsteady pressure on the pressure side of the blade.
- The amplitude and phase functions of a specific excitation order is independent of the installed distortion screen as long as this specific harmonic is generated. The distortion screen affects the amplitude of the excitation not the distribution. Therefore, the underlying mechanisms

to cause a specific excitation distribution must be similar for different screen cases.

- The response of a centrifugal compressor blade vibrating either with first or the second eigenfrequency can be modeled using a single-degree-of-freedom system.
- Blade-to-blade response amplitudes are considerably affected by mistuning. Response amplitudes of specific blades were exceeded the mean amplitudes by as much as 30% for one test impeller and 100% for a differently instrumented impeller.
- Material damping can only be measured at vacuum conditions and is a mode depend quantity.
- Aerodynamic damping is the dominating contributor to overall damping and exceeds the latter by approximately a factor of 10 for the first mode at ambient pressure conditions of 1bar.
- For the first mode, blade damping can be considered constant for any operating point on the compressor map. However, damping scales linearly with inlet pressure.
- During resonance, the unsteady pressure acting on the blade surface is composed of unsteadiness due to inlet flow distortion and unsteadiness induced by the blade movement.
- An analysis method was developed to experimentally quantify the transfer of excitation energy from the fluid to the blade or vice versa. The method combines the influence if excitation amplitude and phase and vibratory motion into a single quantity.
- During resonance, depending on the amplitude and phase of the unsteady excitation and the blade motion, zones of positive or negative energy transfer are created. In the former case excitation work is done on the blade, in the latter case damping occurs.
- Zones particularly prone to transfer high excitation energy were identified that lead to an increase in vibratory response amplitudes.

10.2. Summary

Experimental Setup

The centrifugal compressor facility RIGI was successfully redesigned in order to integrate a series of measurement techniques and flow distortion devices. Important in the work was the adaptation of blade modal properties for an existing centrifugal compressor in order to guarantee low engine order excitation. For this purpose the blade thickness was reduced thereby decreasing the modal frequencies. As a result, a number of resonant crossing cases were realized between the first two main blade modes with engine excitation orders of up to 12. Primarily, resonant cases between the first main blade mode and EO5 and EO6 excitations were studied. These case scenarios are engine representative. Typically, measurements were performed for maximum rotational speeds of 18000rpm at inlet pressures ranging from 0.1bar to 0.8 bar depending on the case. Three operating lines were chosen to build up a measurement matrix, one along the stability limit, one half way between the stability limit and the maximum mass flow and the final along the maximum mass flow.

The adaptation in blade thickness was performed iteratively using FEM until the first and second main blade frequencies were sufficiently low. The results were experimentally verified by employing an optical technique based on speckle interferometry. For both modes the predicted and measured results agreed very well in terms of modal shapes and frequencies. This is generally the case for the first modes where coupling between the blades has negligible influence on the modal shapes.

On Blade Sensor Instrumentation

Crucial to the accomplishment of this work was the development and application of dynamic sensors on the blade surface. Two types of sensors were used. Fast pressure sensors were installed along the blade mid-height in order to quantify the excitation functions acting on the blade. The design and realization of the pressure sensors was based on existing in-house techniques applied for fast aerodynamic probes, termed FRAP, and involved miniaturization of the pressure sensitive head. Pressure sensor properties were measured through a series of experiments including the estimation of temperature effects, linearity, frequency bandwidth and sensitivity to vibratory strain. The

measurement uncertainty of the pressure sensor at off-resonance conditions was found to be $\pm 5\%$ full scale, whereas during resonance the uncertainty is $\pm 11\%$ full scale. A calibration for the effects of centrifugal forces could not be performed and the pressure sensors could therefore not be used for the measurement of the steady (DC) component of the pressure signal.

Inlet Flow Distortion

An experimental technique was setup to generate and measure flow distortion upstream of the impeller. First, a model was developed based on loss generation across wire meshes and mass distribution due to blockage. The model enabled to predict the change in velocities between the blocked and non-blocked portions of the inlet flow field depending on the screen porosity. Model prediction was in good agreement with radially averaged measurement data. Inlet distortion screens consisted of separate lobes equal in number to the intended excitation order. Each of the lobes was made of a wire mesh to partially block the flow. Measurements upstream of the impeller showed that the flow field predominantly consisted of the intended excitation order. The total pressure distortion depends on the mass flow setting of the test facility. In the datum forced response study, the mass flow range of interest corresponded to a total pressure distortion amplitude of $1\% - 4\%$. However, local maxima and minima of the total pressure or velocity were found to exceed considerably the predicted averaged levels. The installed distortion amplitudes were sufficient to create resonance response. Upstream of the impeller, installations within the flow path locally reduced or increased the velocity ratios. This feature was consistently present and was independent of the installed distortion screen.

Unsteady Blade Surface Pressure Measurements

Viewed on a global scale, the general consensus is that the forcing function acting on the blade must be examined and judged on a case to case approach. Generalization of features in the forcing function is inherently complex due to their dependency on too many parameters, i.e. rotational speed, excitation order and mass flow. Their cumulative effect alters fluid flow features on the blade and would require a case to case examination. Realistically, such an approach can only be justified in cases where excitation is not tolerable and may cause failure.

Unsteady pressure measurements on the blade surface were performed during off-resonant and resonant conditions. These two regimes must be strictly distinguished during signal processing. At off-resonance, the unsteady pressure acting on the blade surface originates from inlet distortion and represents the forcing function known to cause resonant vibration. During resonant conditions the measured pressure signal is composed of unsteady pressure due to inlet flow distortion and an additional contribution due the blade vibratory motion. Therefore, measurements within the resonant regime cannot be used to examine the excitation function. For this reason the forcing function must be examined for speeds outside the influence of vibratory motion.

Unsteady Blade Surface Pressure without Distortion Screens

In the case that a distortion screen was not installed upstream of the impeller, the harmonic content of the unsteady pressure acting on the blade surface was found to be primarily composed EO2 and EO3 harmonics. Their origin was associated with upstream installations protruding into the flow field. Along the blade meridional length amplitudes for both harmonics varied in the range between 1% to 1.5% of the inlet static pressure. Both harmonics were found to depend on the operating line which corresponded to a change in mass flow. Higher harmonics, i.e. EO4 and above, were generally detected in the flow field, however with negligible amplitudes in comparison. An additional observation was that the amplitudes of EO2 and EO3 harmonics increased steadily with increase in rotational speed.

Unsteady Blade Surface Pressure with Distortion Screens

In any case where a distortion screen was installed the measured unsteady pressure on the blade surfaces was primarily composed of EO2, EO3 and the intended harmonic, i.e. EO5 or EO6. The lower harmonics EO2 and EO3 persisted independently of the installed screen, albeit their amplitudes were affected by the screen and typically caused an increase in comparison to the case without a screen.

A 5 lobe screen was used to generate Mode1/EO5 excitation. In this case the unsteady pressure on the suction side was primarily affected by the number of screen lobes. The amplitude was found to remain constant along the blade length in the inducer region for the entire mass flow range. On the pressure side the amplitude of EO5 harmonic varied depending on the operating line.

On both of the blade sides the phase relationship revealed EO5 pressure waves moving upstream along the blade length. The phase relationship was mainly affected on the pressure side of the blade. Consequently, the dependency of the forcing function on the mass flow and the associated change was dominated by the flow conditions on the pressure side.

Unsteady, three-dimensional fluid flow computations were performed to complement the measurement findings. Measured inlet flow quantities were applied as boundary conditions. Measurements and computation were compared for results for a mass flow setting near the stability limit. The computation was judged to capture the measured flow features on the separate blade surfaces. However, minor mismatches on the separate surfaces lead to disagreement for the resultant forcing function. The unsteady pressure distribution on the suction side consisted of multiple zones where pressure waves propagated in opposing directions. The relatively complex unsteady pressure field in conjunction with low amplitudes of excitation represent a source of uncertainty during validation. That means, that pressure sensors situated on the borders between the pressure zones might disagree with the prediction, although the flow field in general might be captured well by the computation.

The 3 lobe and the 6 lobe screens were used to generate the Mode1/EO6 excitation. This comparison represented a case where the same excitation harmonic, EO6, could be compared for two different inlet boundary conditions. The conclusion was, that the measured unsteady pressure distribution is very similar for both cases. The amplitude shape and the phase angle distribution agreed between the two cases. The amplitude was by a factor of two higher in the 6 lobe case since EO6 is the fundamental excitation and for the 3 lobe screen the second harmonic. Therefore, the underlying mechanisms to cause the resultant excitation must be similar in nature between the screen cases. Also the unsteady pressure propagation mechanisms must be weakly coupled to the overall flow field. Consequently, the installed screen only affects the amplitude of the same excitation order but not the shape and phase angle.

Blade Response during Resonance

The blade response during resonance was experimentally examined with respect to two aspects, the dynamic response characteristic and the maximum amplitude. A SDOF model was formulated in order to compare data against

the model. Data was obtained for a number of resonance cases depending on the excitation order and blade mode. It was concluded, that the response of a single blade can be modeled by a SDOF model. Very good agreements between the model and the measurements were achieved for the response dynamics as a function of time. The dependency of the maximum response amplitude as a function of inlet pressure was captured by the model. The SDOF model is a valid tool to study transient response characteristics and the maximum amplitude once the model is calibrated. Mistuning was shown to introduce substantial blade-to-blade variation in maximum response amplitudes as much as 100% above the average. Sensor instrumentation on the blades affects mistuning and the resultant blade-to-blade amplitude variation.

Blade Damping

Blade damping was obtained from resonant response measurements and was expressed in terms of critical damping ratio based on a SDOF model. Curve-fit procedures were applied on the data in order to derive the damping magnitude. Material damping was obtained from on-bench experiments near vacuum conditions where blades were excited using piezo-electric actuators mounted on the disk. Material damping is a mode dependent quantity and exhibited values for Mode 1 to be by 40% higher than for Mode 2. Material damping cannot be measured at ambient conditions because the added damping due to surrounding air exceeds material damping. Damping measurements taken within the facility during resonance showed that aerodynamic damping is the dominating damping mechanism. Aerodynamic damping is by a factor of 10 higher than material damping at ambient conditions. Aerodynamic damping can only be measured during operation where engine representative conditions can be met. Based on experiments taken for two differently instrumented rotors and a number of resonant cases it was concluded that damping of the first mode of the datum impeller could be considered to be constant. This finding greatly simplified judgements on resonance response of centrifugal compressors. For the second mode, damping was found to vary between the resonance cases.

Cumulative Aspects of Forced Response

The cumulative aspects of forced response combine blade excitation, damping and response and aim to conclude on the governing mechanisms that lead to potentially hazardous blade failure. The conclusions were derived for the first

main blade mode. Owing to the fact that damping is constant for all resonant response cases, changes in response amplitude could only be justified by changes in modal force. An increase in modal force corresponded to an increase in excitation work done on the blade surface. However, the modal force cannot be obtained from a limited number of pressure sensors since it represents the integral of the pressure distribution. For this reason it may not be sufficient to express excitation in terms of amplitude and phase distribution. A method was developed in order to overcome this limitation by examining the aerodynamic work. This quantity reflects the energy transfer between the blade and the fluid during resonance at each pressure sensor position. The method enabled to identify zones on the impeller blade which were subject to either damping or excitation. The cumulative conclusion was that the energy transfer between the blade and the fluid is primarily affected by the phase angle between the blade motion and the unsteady pressure. This causes the creation of zones on the blade surface where the blade is either excited or damped. Changes in mass flow setting altered the phase angle distribution of the excitation force and thereby caused a redistribution of energy transfer zones. The evidence shown, suggested that zones of particularly high excitation energy could be generated leading to a sudden increase in vibratory response.

At this point the conclusions should be brought to a closure by referring to the objectives of this work as stated in section 1.5 on page 17. The governing parameters in forced response of centrifugal compressors to determine the response amplitude are the modal damping and the modal force. However, modal damping can be considered to be constant for the first mode and is therefore independent of any changes that affect the aerodynamics of the rotor. It follows, that the modal force is the sole parameter to affect the resonant response amplitude. The effect of two contributors to the modal force must be weighted, i.e. the sensitivity to the amplitude and the phase angle distribution. In terms of resonant response prediction, computation of the forcing function through CFD must be undertaken with great care to accurately model the amplitude and phase angle distribution. Finally, mistuning bears a substantial potential to cause blade failure due to localized blade excitation. Modeling and predicting blade mistuning effect is of paramount importance.

10.3. Future Work

This study has presented and quantified a number of fundamental forced response principals of centrifugal compressor blades. Also, novel measurement techniques were introduced for the quantification of damping and unsteady pressure and should be applied in further studies. A meaningful continuation of the present work should address the following three fields related to resonant response: (1) High order excitation and (2) Mistuning

High Order Excitation

The results presented in this work were limited to the first blade mode. Damping was also provided for the second mode. However, in industrial practice a common case of resonant response occurs due to interaction with diffuser vanes. Their potential field propagates upstream and causes excitation of the rotor blades. Typical for this scenario is the excitation of higher blade modes where blades may not be treated as single entities due to strong coupling with the rotor disk. Blade modes may not be isolated but may be sufficiently close to cause interaction. The forcing function acting on the blade could be studied using blade mounted pressure sensors. This would represent considerable advantage over conventional application of pressure sensors installed in the shroud of the compressor. A parametric study could involve radial gap variation between the rotor and the diffuser vanes in order to track changes in excitation and also response amplitude.

Mistuning

In the datum study mistuning was shown to introduce severe increase in response amplitude. Although this was partially affected by the applied blade sensors, the problem is of paramount importance to forced response. A continuation of research into this field should aim at predicting the increase of response amplitude due to mistuning in comparison to a tuned rotor. This would involve structural modeling of the coupled system and random variation of blade section properties.

Bibliography

- [1] R. W. Ainsworth, A. J. Dietz, and T. A. Nunn. The use of semiconductor sensors for blade surface pressure measurement in a model turbine stage. *Journal of Engineering for Gas Turbines and Power*, 113(2):261–268, 1991.
- [2] R. W. Ainsworth, R. J. Miller, R. W. Moss, and S. J. Thorpe. Unsteady pressure measurement. *Measurement Science & Technology*, 11(7):1055–1076, 2000.
- [3] B. H. Anderson and D. J. Keller. Considerations in the measurement of inlet distortion for high cycle fatigue in compact inlet diffusers. *NASA TM*, 211476, 2002.
- [4] R. D. Blevins. Flow-induced vibration. 1990.
- [5] J. A. Busby, R. L. Davis, D. J. Dorney, M. G. Dunn, C. W. Haldeman, R. S. Abhari, B. L. Venable, and R. A. Delaney. Influence of vane-blade spacing on transonic turbine stage aerodynamics: Part II—time-resolved data and analysis. *Journal of Turbomachinery*, 121(4):673–682, 1999.
- [6] J. W. H. Chivers. Blade pressure measurements. In *VKI Lecture Series 1981-7*, volume Measurement Techniques in Turbomachines, VKI, Belgium, 1981. VKI.
- [7] J.-S. Choi, D. K. McLaughlin, and D. E. Thompson. Experiments on the unsteady flow field and noise generation in a centrifugal pump impeller. *Journal of Sound and Vibration*, 263(3):493–514, 2003.
- [8] R. R. Craig and A. J. Kurdila. *Fundamentals of structural dynamics*. John Wiley, Hoboken, NJ, 2nd edition, 2006.
- [9] E. F. Crawley. Aerodynamic damping measurements in a transonic compressor. *Journal of Engineering for Power – Transactions of the ASME*, 105:575–584, 1983.

-
- [10] E. F. Crawley, J. L. Kerrebrock, and J. Dugundji. Priliminary measurements of aerodynamic damping of a transonic compressor rotor. In *Measurement methods in rotating components of turbomachinery; Proceedings of the Joint Fluids Engineering Gas Turbine Conference and Products Show*, pages 263–271, New Orleans, 1980.
- [11] H. P. Dickmann, T. S. Wimmel, J. Szwedowicz, D. Filsinger, and C. H. Roduner. Unsteady flow in a turbocharger centrifugal compressor: Three-dimensional computational fluid dynamics simulation and numerical and experimental analysis of impeller blade vibration. *Journal of Turbomachinery-Transactions of the ASME*, 128(3):455–465, 2006.
- [12] G. Dimitriadis, I. B. Carrington, J. R. Wright, and J. E. Cooper. Blade-tip timing measurement of synchronous vibrations of rotating bladed assemblies. *Mechanical Systems and Signal Processing*, 16(4):599–622, 2002.
- [13] R. Dénos. Influence of temperature transients and centrifugal force on fast-response pressure transducers. *Experiments in Fluids*, 33(2):256–264, 2002.
- [14] R. Dénos, T. Arts, G. Paniagua, V. Michelassi, and F. Martelli. Investigation of the unsteady rotor aerodynamics in a transonic turbine stage. *Journal of Turbomachinery*, 123(1):81–89, 2001.
- [15] R. Dénos, C. Sieverding, T. Arts, J. Brouckaert, G. Paniagua, and V. Michelassi. Experimental investigation of the unsteady rotor aerodynamics of a transonic turbine stage. *Proceedings of the Institution of Mechanical Engineers, Part A: Journal of Power and Energy*, 213(4):327–338, 1999.
- [16] M. G. Dunn. Phase and time-resolved measurements of unsteady heat transfer and pressure in a full-stage rotating turbine. *Journal of Turbomachinery*, 112:531–538, 1990.
- [17] M. G. Dunn. Convective heat transfer and aerodynamics in axial flow turbines. In *ASME Gas Turbine Conference and Exhibit*, volume 2001-GT-0506, New Orleans, Louisiana, USA, 2001.
- [18] M. G. Dunn, W. A. Bennett, R. A. Delaney, and K. V. Rao. Investigation of unsteady flow through a transonic turbine stage: Data/prediction

- comparison for time-averaged and phase-resolved pressure data. *Journal of Turbomachinery*, 114(1):91–99, 1992.
- [19] M. G. Dunn, H. L. Martin, and M. J. Stanek. Heat-flux and pressure measurements and comparison with prediction for a low aspect ratio turbine stage. *Journal of Turbomachinery*, 108:108–115, 1986.
- [20] Y. El-Aini, R. deLaneuville, A. Stoner, and V. Capece. High cycle fatigue of turbomachinery components - industry perspective. In *33rd AIAA/ASME/SAE/ASEE Joint Propulsion Conference*, volume AIAA 97–3365, Seattle, WA, 1997.
- [21] D. J. Ewins. *Modal testing theory, practice and application*. Research Studies Press, Baldock, Hertfordshire, England, 2nd edition, 2000.
- [22] K. Gallier. *Experimental Characterization of high Speed Centrifugal Compressor Aerodynamic Forcing Function*. 2005.
- [23] C. R. Gossweiler. *Sonden und Messsystem für schnelle aerodynamische Strömungsmessung mit piezoresistiven Druckgebern*. Diss. ETH Nr. 10253. Zürich, 1993.
- [24] J. H. Griffin. Optimizing instrumentation when measuring jet engine blade vibration. *Journal of Engineering for Gas Turbines and Power*, 114:217–221, 1992.
- [25] D. Hagelstein, H. Hasemann, and M. Rautenberg. Coupled vibration of unshrouded centrifugal compressor impellers. Part 2: Computation of vibration behavior. *International Journal of Rotating Machinery*, 6(2):115–128, 2000.
- [26] H. Hasemann, D. Hagelstein, and M. Rautenberg. Coupled vibration of unshrouded centrifugal compressor impellers. Part 1: Experimental investigation. *International Journal of Rotating Machinery*, 6(2):101–113, 2000.
- [27] U. Haupt. *Untersuchung des Schaufelschwingungsverhaltens hochbelasteter Radialverdichterlaufräder*, volume 7 of *Fortschrittsberichte der VDI Zeitschriften*. Verein Deutscher Ingenieure VDI-Verlag GmbH Düsseldorf, Hannover, 1984.

- [28] U. Haupt, A. N. Abdelhamid, N. Kaemmer, and M. Rautenberg. Blade vibration on centrifugal compressors - fundamental considerations and initial measurements. In *ASME Gas Turbine Conference and Exhibition*, volume 86-GT-283, Duesseldorf, Germany, 1986.
- [29] U. Haupt, K. Bammert, and M. Rautenberg. Blade vibration on centrifugal compressors - fundamental considerations and initial measurements. In *ASME Gas Turbine Conference and Exhibition*, volume 85-GT-92, Houston, Texas, 1985.
- [30] U. Haupt and M. Rautenberg. Investigation of blade vibration of radial impellers by means of telemetry and holographic-interferometry. *Journal of Engineering for Power-Transactions of the ASME*, 104(4):838–843, 1982.
- [31] U. Haupt and M. Rautenberg. Blade vibration measurements on centrifugal compressors by means of telemetry and holographic-interferometry. *Journal of Engineering for Gas Turbines and Power-Transactions of the ASME*, 106(1):70–78, 1984.
- [32] U. Haupt, M. Rautenberg, and A. N. Abdelhamid. Blade excitation by broadband pressure fluctuations in a centrifugal compressor. In *ASME Gas Turbine Conference and Exhibition*, volume 87-GT-17, Anaheim, California, 1987.
- [33] U. Haupt, U. Seidel, A. N. Abdelhamid, and M. Rautenberg. Unsteady flow in a centrifugal compressor with different types of vaned diffusers. In *ASME Gas Turbine Conference and Exhibition*, volume 88-GT-22, Amsterdam, The Netherlands, 1988.
- [34] H. Irretier. The maximum transient resonance response of rotating blades with regard to centrifugal force and non-linear damping effects. In *International Gas Turbine & Aeroengine Congress & Exhibition*, volume 97-GT-116, Orlando, Florida, USA, 1997.
- [35] H. Irretier and D. B. Balashov. Transient resonance oscillations of a slow-variant system with small non-linear damping—modelling and prediction. *Journal of Sound and Vibration*, 231(5):1271–1287, 2000.
- [36] ISO. Guide to the expression of uncertainty in measurement (gum). Technical Report ISBN 92-67-1011889, 1993.

- [37] T. R. Jeffers, J. J. Kielb, and R. S. Abhari. A novel technique for the measurement of blade damping using piezoelectric actuators. In *ASME Turbo Expo*, volume 2000-GT-0359, Munich, Germany, 2000. ASME.
- [38] D. Jin. *Untersuchung von Schaufelschwingungen und ihrer Erregungsur-sachen an Radialverdichtern*. Dissertation. Hannover, 1990.
- [39] D. Jin, H. Hasemann, U. Haupt, and M. Rautenberg. *Untersuchung der Schaufeldämpfung hochbelasteter Radialverdichterlaufräder*. Schwingungen in rotierenden Maschinen: Referate der Tagung an der Universität/Gesamthochschule Kassel. Braunschweig, Vieweg cop. 1991, Kassel, 1991.
- [40] J. J. Kielb and R. S. Abhari. Experimental study of aerodynamic and structural damping in a full-scale rotating turbine. *Journal of Engineering for Gas Turbines and Power – Transactions of the ASME*, 125(1):102–112, 2003.
- [41] R. E. Kielb. Unsteady flows: An aeroelastic blade design perspective. In *ERCOFTAC Turbomachinery Seminar and Workshop*, Aussois, France, 1998.
- [42] R. E. Kielb and M. Imregun. Aerolasticity in axial flow machines - damping characteristics. In *VKI Lecture Series 1999-05*, Belgium, 1999. von Karman Institute for Fluid Dynamics.
- [43] J. K. Koo and D. F. James. Fluid flow around and through a screen. *Journal of Fluid Mechanics*, 60(3):513–538, 1973.
- [44] P. D. Köppel. *Instationäre Strömung in Turbomaschinen: Analyse zeitabhängiger Sondenmessungen*. Dissertation ETH Nr. 13500. Zürich, 2000.
- [45] P. Kupferschmied. *Zur Methodik zeitaufgelöster Messungen mit Strömungs-sonden in Verdichtern und Turbinen*. Diss. ETH Nr. 12474. Zürich, 1998.
- [46] A. D. Kurtz, R. W. Ainsworth, S. J. Thorpe, and A. Ned. Further work on acceleration insensitive semiconductor pressure sensors for high bandwidth measurements on rotating turbine blades. In *Kulite Semiconductor Products, Inc., NASA 2003 Propulsion Measurement Sensor Development Workshop*, Huntsville, Alabama, 2003.

- [47] F. Kushner. Rotating component modal analysis and resonance avoidance recommendations. In *Proceedings of the thirty-third turbomachinery symposium*, pages 143–162. Turbomachinery Laboratory, Texas A&M University, College Station, Texas, 2004.
- [48] B. Lakshminarayana. Techniques for aerodynamic and turbulence measurements in turbomachinery rotors. *ASME Journal of Engineering for Gas Turbines and Power*, 103:374–392, 1981.
- [49] C. P. Lawson and P. C. Ivey. Tubomachinery blade vibration amplitude measurement through tip timing with capacitance tip clearance probes. *Sensors and Actuators A: Physical*, 118(1):14–24, 2005.
- [50] F. Leul. *Zum transienten Schwingungsverhalten beim Resonanzdurchgang linearer Systeme mit langsam zeitveränderlichen Parametern*, volume Dissertation of *Bericht 4/1994*. IFM, Kassel, 1994.
- [51] Y. K. Lin. Dynamics of disordered periodic structures.
- [52] S. R. Manwaring and S. Fleeter. Inlet distortion generated periodic aerodynamic rotor response. *Journal of Turbomachinery-Transactions of the ASME*, 112(2):298–307, 1990.
- [53] S. R. Manwaring and S. Fleeter. Forcing function effects on rotor periodic aerodynamic response. *Journal of Turbomachinery-Transactions of the ASME*, 113(2):312–319, 1991.
- [54] S. R. Manwaring, D. C. Rabe, C. B. Lorence, and A. R. Wadia. Inlet distortion generated forced response of a low-aspect-ratio transonic fan. *Journal of Turbomachinery-Transactions of the ASME*, 119(4):665–676, 1997.
- [55] R. J. Miller, R. W. Moss, R. W. Ainsworth, and N. W. Harvey. Wake, shock, and potential field interactions in a 1.5 stage turbine—Part I: Vane-rotor and rotor-vane interaction. *Journal of Turbomachinery*, 125(1):33–39, 2003.
- [56] R. J. Miller, R. W. Moss, R. W. Ainsworth, and N. W. Harvey. Wake, shock, and potential field interactions in a 1.5 stage turbine—Part II: Vane-vane interaction and discussion of results. *Journal of Turbomachinery*, 125(1):40–47, 2003.

- [57] F. A. Newman. Experimental determination of aerodynamic damping in a three-stage transonic axial-flow turbine. Technical Report NASA-TM-100953, NASA, 1988.
- [58] F. A. Newman. Experimental vibration damping characteristics of the third-stage rotor of a three-stage transonic axial flow compressor. In *24th Joint Propulsion Conference AIAA, ASME, SAE, ASEE*, Boston, Massachusetts, 1988. AIAA-88-3229.
- [59] J. E. T. Penny, M. I. Friswell, and S. D. Garvey. Automatic choice of measurement locations for dynamic testing. *AIAA Journal*, 32(2):407–414, 1994.
- [60] A. Pfau, J. Schlienger, A. I. Kalfas, and R. S. Abhari. Unsteady, 3-dimensional flow measurement using a miniature virtual 4 sensor fast response aerodynamic probe (FRAP). In *ASME Turbo Expo*, volume GT2003–38128, Atlanta, Georgia, USA, 2003.
- [61] S. Qian and D. Chen. *Joint time-frequency analysis methods and applications*. Prentice Hall PTR, Upper Saddle River, N.J., 1996.
- [62] D. C. Rabe, A. Bolcs, and P. Russler. Influence of inlet distortion on transonic compressor blade loading. In *AIAA/ASME/SAE/ASEE Joint Propulsion Conference and Exhibit, 31st*, volume AIAA 95-2461, San Diego, CA, 1995.
- [63] K. V. Rao, R. A. Delaney, and M. G. Dunn. Vane-blade interaction in a transonic turbine, Part I: Aerodynamics. *Journal of Propulsion and Power*, 10(3):305–311, 1994.
- [64] B. Ribi. *Radialverdichter im Instabilitätsbereich*. Dissertation ETH Nr. 11717. Zürich, 1996.
- [65] P. E. Roach. The generation of nearly isotropic turbulence by means of grids. *International Journal of Heat and Fluid Flow*, 8(2):82–92, 1987.
- [66] C. H. Roduner. *Strömungsstrukturen in Radialverdichtern, untersucht mit schnellen Sonden*. Dissertation ETH Nr. 13428. Zürich, 1999.
- [67] H. Roth. Measurement methods in rotating components of turbomachinery. In B. Lakshminarayana, editor, *Joint Fluids Engineering Gas Turbine Conference and Products Show*.

- [68] M. Schleer. *Flow structure and stability of a turbocharger centrifugal compressor*. Dissertation ETH Nr. 16605. VDI-Verlag, Düsseldorf, 2006.
- [69] M. Schleer, T. Mokulys, and R. S. Abhari. Design of a high pressure-ratio centrifugal compressor for studying Reynolds number effects. In *International Conference on Compressors and their Systems*, London, 2003. IMechE.
- [70] S. Schmitt. *Simulation von Flattern und aerodynamischer Zwangserregung in Turbomaschinenbeschaufelungen*. Dissertation. Institut für Antriebstechnik, Köln, 2003.
- [71] M. D. Sensmeier and K. L. Nichol. Minimizing vibratory strain measurements error. 98-GT-257, 1998.
- [72] J. C. Slater, G. R. Minkiewicz, and A. J. Blair. Forced response of bladed disk assemblies - a survey. AIAA-1998-3743, 1998.
- [73] K. P. Sälzle. *Schwingungsverhalten der Laufräder von Radialventilatoren*. Dissertation Universität Stuttgart. Stuttgart, 2001.
- [74] A. V. Srinivasan. Vibrations of bladed-disk assemblies - a selected survey. *Journal of Vibration, Acoustics, Stress and Reliability in Design*, 106:165–168, 1984.
- [75] A. V. Srinivasan. Flutter and resonant vibration characteristics of engine blades. *Journal of Turbomachinery – Transactions of the ASME*, 119:741–775, 1997.
- [76] A. V. Srinivasan, D. G. Cutts, and S. Sridhar. Turbojet engine blade damping. Technical Report NASA-CR-165406, NASA, 1981.
- [77] D. Stahlecker. *Untersuchung der instationären Strömung eines beschaufelten Radialverdichterdiffusors mit einem Laser-Doppler-Anemometer*. Dissertation ETH Nr. 13228. Zürich, 1999.
- [78] J. Szwedowicz, S. M. Senn, and R. S. Abhari. Optimum strain gage application to bladed assemblies. *Journal of Turbomachinery*, 124(4):606–613, 2002.
- [79] B. L. Venable, R. A. Delaney, J. A. Busby, R. L. Davis, D. J. Dorney, M. G. Dunn, C. W. Haldeman, and R. S. Abhari. Influence of vane-blade

- spacing on transonic turbine stage aerodynamics: Part I—time-averaged data and analysis. *Journal of Turbomachinery*, 121(4):663–672, 1999.
- [80] VISHAY. Errors due to transverse sensitivity in strain gages. Technical report, VISHAY MICRO-MEASUREMENTS, 2007.
- [81] VISHAY. Strain gage thermal output and gage factor variation with temperature. Technical report, VISHAY MICRO-MEASUREMENTS, 2007.
- [82] D. S. Whitehead. Effect of mistuning on the vibration of turbomachine blade induced by wakes. *Journal of Mechanical Engineering Science*, 8(1):15–21, 1966.
- [83] D. S. Whitehead. The maximum factor by which forced vibration of blades can increase due to mistuning. *Journal of Engineering for Gas Turbines and Power*, 120:115–119, 1998.
- [84] Zemp. *CFD investigation on inlet flow distortion in a centrifugal compressor*. Master Theses ETH Zürich. 2007.
- [85] A. Zemp, A. Kammerer, and R. S. Abhari. Unsteady CFD investigation on inlet distortion in a centrifugal compressor. In *ASME Turbo Expo*, volume GT2008–50744, Berlin, Germany, 2008.
- [86] M. Zielinski and G. Ziller. Noncontact vibration measurements on compressor rotor blades.

A. Nomenclature

Abbreviations

CFD	Computational Fluid Dynamics
FEM	Finite Element Method
FRAP	Fast Response Aerodynamic Probe
GF	Gauge Factor used for strain gauges
GUM	Guide of Uncertainty in Measurements
EO	Engine Order
ESPI	Electronic Speckle Pattern Correlation Interferometry
HCF	High Cycle Fatigue
LDV	Laser Doppler Velocimetry
MDOF	Multi-Degree-of-Freedom
Mode 1, Mode 2	first, second main blade mode
Mode1/EO5	resonance between Mode 1 and EO5 excitation
OL1, OL2, OL3	Operating Line 1, 2 and 3
PSD	Power Spectral Density
PIV	Particle Image Velocimetry
RPM	Revolutions per Minute
SDOF	Single-Degree-of-Freedom
WF	Wave Front

Symbols

A	factor depending on Reynolds number
B	shape factor
GF	gauge factor
H	frequency transfer function
F, F_0	forcing function, force amplitude
F_D, F_{DM}, F_{DA}	damping force, material, aerodynamic
I	current
K_L, K_T, K_S	factor for linearity, temperature and stress effects

K_{TS}	factor for transverse sensitivity effects
M	mesh width
ND	nodal diameter
R	resistance
RPM	revolutions per minute
S_{max}	maximum sweep rate
S_x	spectral density of excitation function
S_y	spectral density of response function
S_{xy}	cross-correlation spectrum
T_0	duration of a cycle
U	voltage or expanded uncertainty
V_{ax}	axial velocity
W, W_E, W_D	aerodynamic work, excitation or damping work
X	frequency function of excitation
Y	frequency function of system response
a	half-width for standard uncertainty
b	offset
c	viscous damping coefficient
c_i	sensitivity coefficient
d	wire diameter
f	frequency, local force or modal force
k	spring constant
m	mass or gain
p	pressure
psd	power spectral density
Δp	pressure difference
q	dynamic head
t	time
u	standard uncertainty
x, \dot{x}, \ddot{x}	displacement, speed, acceleration
x_i	input quantity during uncertainty estimation
y	model functions during uncertainty estimation

Greek Symbols

α	area ratio
β	grid porosity function or frequency gradient

Δ	difference between suction and pressure side
ϵ	strain
Ω	angle
ω	frequency in radians
ω_n	natural frequency in radians
ϕ	modal shape vector
φ	phase angle
$\eta, \dot{\eta}, \ddot{\eta}$	modal displacement, speed, acceleration
$\zeta, \zeta_M, \zeta_A,$	critical damping ratio, material, aerodynamic

Subscripts

\sim	steady component
'	unsteady component

Subscripts

<i>a</i>	data point before resonance
<i>b</i>	data point after resonance
<i>blo</i>	downstream of screen in the blocked area
<i>cal</i>	calibrated quantity
<i>corr</i>	corrected quantity
<i>d, m</i>	inlet distortion or vibratory motion dependent quantity
<i>in,out</i>	at inlet, outlet of the impeller
<i>inlet</i>	plane at inlet of impeller inlet section
<i>mean</i>	mean velocity
<i>max</i>	maximum value
<i>meas</i>	measured quantity
<i>min</i>	minimum value
<i>0</i>	time independent or reference quantity
<i>t</i>	total quantity
<i>ref</i>	reference quantity
<i>res</i>	at resonance
<i>ss, ps</i>	suction, pressure side
<i>tot</i>	total quantity
<i>ups</i>	upstream of screen
<i>unb</i>	downstream of screen in the unblocked area

B. List of Publications

A. Kammerer, R. S. Abhari. The Cumulative Effects of Forcing Function, Damping and Mistuning on Blade Forced Response in a High Speed Centrifugal Compressor With Inlet Distortion. *Journal of Engineering for Gas Turbines and Power*.

A. Kammerer, R. S. Abhari. Blade Forcing Function and Aerodynamic Work Measurements in a High Speed Centrifugal Compressor With Inlet Distortion. *Journal of Engineering for Gas Turbines and Power*.

A. Kammerer, R. S. Abhari. Experimental Study on Impeller Blade Vibration During Resonance Part 1: Blade Vibration Due to Inlet Flow Distortion. *Journal of Engineering for Gas Turbines and Power*, 131(2):022508–11, 2009.

A. Kammerer, R. S. Abhari. Experimental Study on Impeller Blade Vibration During Resonance Part 2: Blade Damping. *Journal of Engineering for Gas Turbines and Power*, 131(2):022509–9, 2009.

A. Zemp, A. Kammerer, R. S. Abhari. Unsteady CFD Investigation on Inlet Distortion in a Centrifugal Compressor. *ASME Gas Turbine Conference and Exhibit*, Berlin, Germany, GT2008–50744, 2008.

G. Cassina, B. H. Beheshti, A. Kammerer, R. S. Abhari, Parametric Study of Tip Injection in an Axial Flow Compressor Stage. *ASME Gas Turbine Conference and Exhibit*, Montreal, Canada, GT2007-27403, 2007".

C. Curriculum Vitae

Personal Data

Albert Kammerer, born October 7, 1976 in Issyk, Alma-Ata, Kazakhstan

Professional Experience

- 2006-2009 Research assistant and doctoral student at the Laboratory for Energy Conversion at ETH Zürich
- 2003-2006 Development engineer at ETH Zürich
- 2002-2003 Diploma Project at Rolls-Royce Aeroengines, Derby
- 2002 Research Project with Rolls-Royce Aeroengines, Bristol

Education

- 1997-2003 Diploma studies in Aerospace Engineering at Technical University of Braunschweig, Germany
- 2001-2002 Master of Science studies in Thermal Power at Cranfield University, UK